Eindhoven University of Technology

MASTER

The influence of collisions on trapped-electron modes in fusion plasmas

Morren, Maikel C.L.

Award date:
2022

Link to publication

Disclaimer
This document contains a student thesis (bachelor's or master's), as authored by a student at Eindhoven University of Technology. Student theses are made available in the TU/e repository upon obtaining the required degree. The grade received is not published on the document as presented in the repository. The required complexity or quality of research of student theses may vary by program, and the required minimum study period may vary in duration.

General rights
Copyright and moral rights for the publications made accessible in the public portal are retained by the authors and/or other copyright owners and it is a condition of accessing publications that users recognise and abide by the legal requirements associated with these rights.

- Users may download and print one copy of any publication from the public portal for the purpose of private study or research.
- You may not further distribute the material or use it for any profit-making activity or commercial gain

EINDHOVEN UNIVERSITY OF TECHNOLOGY

Department of Applied Physics

Science and Technology of Nuclear Fusion -

The influence of collisions on trapped-electron modes in fusion plasmas

A thesis presented for the degree of *Master of Science*

Maikel Cornelis Leonard Morren (1002099)

Under supervision of
dr. ir. J. van Dijk[1]
dr. J.H.E. Proll[1]

Committee members
dr. B. Bagheri[1]
dr. J. Citrin[1,2]
dr. M. Curti[3]

1 Department of Applied Physics, Eindhoven University of Technology
2 Dutch Institute for Fundamental Energy Research
3 Department of Electrical Engineering, Eindhoven University of Technology

June 24, 2022

Acknowledgements

During the past year that I have I worked on this thesis I have been able to learn a lot more about plasma turbulence, kinetic theory and numerical/mathematical nitty gritty than I initially hoped when I reached out for doing a project on gyrokinetics. However it was not just the interesting physics itself that kept me enticed to continue working on the project but also the kind and helpful people of the small research community. In particular I appreciate the willingness of the various authors I contacted to share their data, which allowed to ground this fairly abstract theoretical project within the bounds of realistic experimental settings.

I am grateful for my supervisors Jan van Dijk and Josefine Proll for allowing me the freedom I took to dive deep in the material to build a thorough understanding of the subject matter, and to carry out the ideas/approaches I came up with. Writing a thesis about such a touch subject which remains exciting yet comprehensible for both the general physicist and seasoned fusion scientist audiences would not have been possible without the feedback and discussion from my supervisors.

Besides my supervisors I would also like to thank Paul Mulholland for teaching me the ropes of working with GENE which is notorious for having a steep learning curve, as well as MJ Pueschel who was a huge help in getting GENE initially up and running on the Marconi HPC and has been my life-line for fixing the many errors that popped up as the simulations were gradually built up from the simple default settings to the collisional simulations presented in this thesis. My gratitude also extends to Ralf Mackenbach, who shared and explained his code for finding the populations of trapped particles and calculating the bounce averages over their orbit which allowed me to complete the perturbative calculation by taking into account the actual magnetic geometry, and made a part of his CPU hours available to do the final simulations when my own budget on the supercomputer ran out.

In addition to the numerical aspects, I would also like to thank Paul Costello with whom I had some nice discussions on the relatively overshadowed Universal Instability and has been of great help in the process of identifying this mode in the stellarator simulations. Despite only making it into the thesis as a mediocrely written appendix, I am grateful for the lengthy discussions I had with Tom Vredenbregt on the variational principle and in particular how its complex variant is applied in other fields of physics, as I was unfamiliar with the method.

I would like to make a tribute to my small test panel of non-expert people who proofread my science communication product and provided valuable feedback which helped to explain the indisputably hard subject matter of my research in layman terms. But perhaps most important I appreciate my fellow graduating students that I worked side-by-side on a daily basis and with whom I shared many a laugh, many a struggle, copious amounts of caffeine and the occasional drink. Before closing off, I feel obligated to honour the many unsung heroes from *stack exchange* which had provided answers to the many question boards I visited which enabled me to do what I wanted to on the UNIX based console interface of Marconi and make the many complex yet colourful and visually appeasing figures.

Last but definitely not least I would like to thank my parents and friends for being understanding of my ever increasing absence as I got more engulfed in the project, while always being supportive and providing a nice distraction from the work whenever I did the find the time for a visit or a social call.

Abstract

Turbulence on the electron- and ion gyroradii scales is the main cause of particle- and energy losses in fusion plasmas. A proper understanding of turbulence is thus necessary to increase their confinement time to make a self-burning plasma as needed for a fusion power plant possible.

A plethora of different microinstabilities exist in a fusion plasma, with typically the Ion Temperature Gradient (ITG) mode and the Trapped Electron Mode (TEM) causing the most transport in present day devices. Most theoretical/numerical investigations of these instabilities have been carried out in the collisionless limit, as the collision frequency under fusion reactor conditions is typically small. However especially for TEMs a small but non-zero collisionality could have a substantial effect due to collisional (de)trapping mechanism.

The (linear) stability properties of TEMs in the presence of collisions are investigated using the gyrokinetic framework through a combination of analytical theory and simulations in both the DIII-D tokamak and HSX/W7-X stellarator geometries, the latter of which is stable against collisionless TEMs.

Analytically a perturbative approach is used to find scaling laws for the TEM growth rate, which show that at high collisionality there is a universal stabilising influence of collisions. At low collisionality, however, the collisionless growth rates are unaffected in the tokamak whereas a destabilising influence of collisions is found at low wavenumbers for both stellarator cases.

Simulations with the GENE code show the same qualitative behaviour of the growth rate with increasing collisionality, which can be attributed to particle de-trapping by collisions. In addition these simulations show that collisions do not spoil the stability of W7-X against TEMs, but promote a change of the dominant instability towards the so-called *Universal Instability*. This new instability, which is predicted to be important in low-shear devices like W7-X, is observed to appear over a substantantially larger wavenumber range than recently found in collisionless simulations which established their existence at low wavenumber in stellarators.

List of Figures

Contents

1 Introduction

In this section the motivation for the research and goals of the research are presented. To accommodate for the mixed audience of fusion specialists and general physicist first a brief motivation is provided in Section 1.1 leading to the overarching research question of this thesis. Then to bridge the gap between these audiences, an exposition of the relevant aspects about magnetic confinement confusion needed to fully grasp the concepts introduced during the brief introduction and later used throughout the thesis is presented in Sections 1.2 to 1.5, which is therefore lengthier than the reader familiar about these concepts is used to. With everyone aboard, the state-of-the-art is then presented in Section 1.6 followed by the scope and outline of the remainder of the thesis in Section 1.7.

1.1 Research motivation

One of the most most pressing challenges for humanity to overcome during this century is to transition our energy generation from traditional fossil fuels to sustainable alternatives, all the while the global energy demand will increase to facilitate energy access to developing countries [1]. Not only will the remaining energy reserves run out before the end of the century, but the energy generation by traditional burning of fossil fuels will have to be gradually phased out to limit their harmful effect on climate change to the "acceptable" levels of the Paris agreement [2].

Nuclear fusion could be a promising solution to this energy problem. In a nuclear fusion process two relatively light nuclei merge, forming a heavier nucleus and some elementary particles as byproducts to satisfy conservation laws. Because this process occurs under influence of the strong nuclear force, the energy released in this process is enormous and is typically in the range of tens of MeV [3]. This in contrast to the chemical reactions which occur under the much weaker electromagnetic interaction and typically release only a handful of eV of energy [3], which form the basis for the majority of our present day energy production. Furthermore as the fuel used in nuclear fusion is significantly lighter than the hydrocarbons burnt in combustion power plants the energy density of nuclear fusion is unprecedented. Combined with the fact that no harmful greenhouse gasses or radioactive waste (in contrast to nuclear fission) is produced in a fusion reaction, nuclear fusion presents a sustainable and clean alternative energy source that could help to fill up the gap in the energy problem.

A fusion power plant would then consist of a dense plasma which is heated up to reach fusion conditions and kept in place by strong magnets [3] (explained in more detail in Section 1.2). There are two[1] "flavours" of magnetic fields that can be used to get this confinement, which result in the two reactor types of a tokamak and stellarator whose most important difference lies in the rotational symmetry and lack thereof of the magnetic field. These reactor types will be further discussed in Section 1.3. The confinement by the magnetic is not perfect[2] such that over time heat and particles will leak out, which is one the hand desired as it allows to extract the energy released by the fusion reactions from the plasma, but on the other hand undesired as it cools down the plasma. For magnetic confinement confusion to be successful as an energy source these energy losses should not exceed the energy generated by the fusion reactions, such that the fusion conditions of the plasma can be sustained. which leads to the so called fusion triple product criterion [5]

[1] These are the common options for magnetic confinement fusion, some other alternatives exist like a levitated dipole, spheromak and reversed field pinch devices however these have significantly less matured than the two schemes discussed here [3].

[2] This is similar to the finite quality factor $\mathcal{Q}$ of a resonant microwave cavity used to store electromagnetic energy. As a result of the finite conductance of the metal walls, the fields can penetrate into the surface layer of the materials where they generate eddy currents which will be dissipated by the finite resistivity [4]. Over time this depletes the energy content of the fields in the cavity.

$$nT\tau_E \geq \frac{12T^2}{E_{f,c}\,\langle\sigma v\rangle} \tag{1}$$

where n, T are the plasma density and temperature respectively, τ_E the energy confinement time, $E_{f,c}$ the energy of the magnetically confined fusion products[3], and $\langle\sigma v\rangle$ the reaction rate. In the context of fusion it is common to express in the temperature not in Kelvin but in terms of an average particle energy, defined by $\hat{T}[\mathrm{J}] = k_b T[\mathrm{K}]$, and throughout the full thesis whenever temperature is mentioned it will refer to this temperature as an energy unit and the hat will be omitted (although in practical units this energy is typically expressed in keV instead).

One problem of particular importance is the prediction of particle and energy fluxes, as these determine the energy confinement time. A fusion plasma has a hot and dense core region to maximise the triple product Equation (1), but gradually transitions to a cold and dilute[4] edge region such that the reactor walls are not exposed to the extreme plasma conditions and can survive, see Figure 1a. As a consequence there is a strong pressure gradient in the plasma which prevents the plasma from being in thermal equilibrium and drives outward transport in an attempt to flatten the pressure profile [6]. This transport is driven by particle collisions (described by Fick's and Fourier's law), the drifts caused by the nonuniform magnetic geometry (as is explained Section 1.3) in and plasma turbulence. In present day tokamaks and stellarators this transport is completely dominated by turbulence [3, 7]. This turbulence leads to chaotic fluctuations in density and temperature at multiple scales in the plasma which lead to mixing between the core and edge plasma regions thereby cooling the core region and reducing the energy confinement time [8]. This turbulence is believed to be driven by microinstabilities, which are spontaneous perturbations of the plasma on the scale of the electron- and ion gyroradius [9–11]. These perturbations can grow over time by tapping into the free energy of the plasma, which mainly consists of the pressure gradient [12], thus making turbulence an unavoidable issue fusion plasmas. A proper understanding of these microinstabilities is therefore imperative to increase the energy confinement time and pave the way towards fusion power plants which beat the triple product requirement Equation (1).

Many microinstabilities can simultaneously exist in the plasma on the same scale, and they can be identified by their respective driving mechanisms, spatial scale and frequencies [15]. The most important microinstabilities that are believed to cause the majority of the observed transport in present day experiments are the ion temperature gradient (ITG) and the trapped electron mode (TEM) [16–19]. The latter is an instability which is driven by the trapped particles (this will be explained in detail in Section 1.5), which exist in a fusion device because the confining magnetic field is inhomogeneous and functions like a magnetic bottle [5, 12]. The influence of particle collisions is often neglected in the investigation of these microinstabilities, since the collision frequency scales as $\nu \propto n/T^{3/2}$ [20] and is typically much lower than any other characteristic frequency in the plasma core [7]. Under typical reactor conditions, the collision frequency only becomes appreciable near the edge region where the temperature drops significantly, as seen Figure 1a. However present day experiments do not yet achieve the plasma parameters comparable to reactor conditions, with temperature typically being an order of magnitude lower, such that collisions are not totally negligible and could have an influence on the turbulence observed in these experiments, as supported by the various favourable scalings

[3]This is the fraction of the total energy released per fusion reaction which remains stored in the plasma and can be used to compensate for the energy losses of finite confinement by reheating the plasma. As only charged particle are confinemened by the magnetic field, the energy stored in the neutron of the D-T reaction does not account for this as it will leave the plasma before redistributing its energy.

[4]The edge region is not completely dilute of particles, as a result of the colder temperature most plasma particles recombine into neutral gas particles which gives rise to a high neutral particle density. For the discussion of the outward heat and particle fluxes however the relative densities are those of the charged particles.

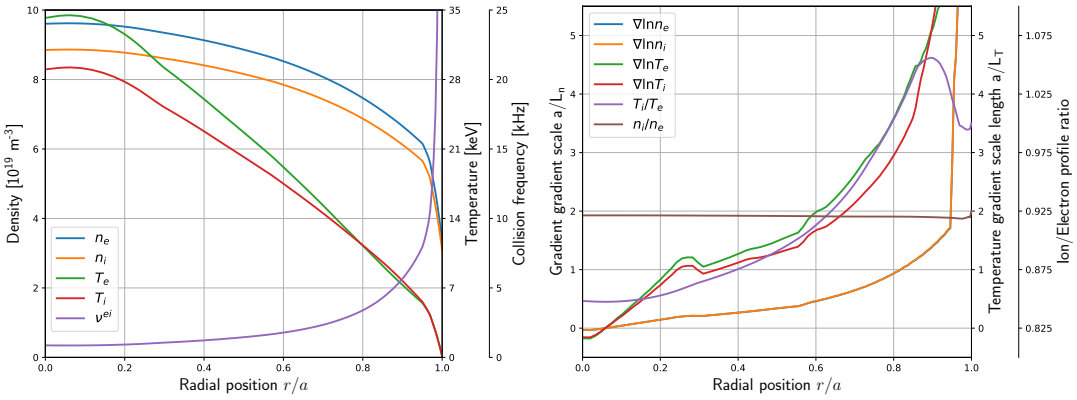

(a) *(b)*

Figure 1: Plasma profiles for the EU-DEMO baseline 2018 scenario [13], which form a representative set of reactor conditions for power plant purposes. Shown are (a) density- and temperature profiles for electrons and ions, and the electron-ion momentum scattering frequency according to Equation (17)*, and (b) normalised profile gradients and profile ratios as important for the theory developed in Chapters 2 and 3. Density and temperature data are reproduced from [14] with permission from the author.*

of the confinement with decreasing collision frequency [21–24]. Collisions are expected to have a particularly large influence on instabilities that rely on the existence of trapped particles, since collisions lead to trapping of previously "free" particles (referred to as passing particles as explained in Section 1.5) or detrap previously trapped particles [3]. There it is of interest to know how collisions would affect turbulence as a result of TEM microinstability, which will be the main topic of this thesis.

1.2 Basic principle of magnetic confinement fusion

Nuclear fusion occurs in nature only under the very exotic conditions of stellar cores [25] (light elements) and supernovas [26] (heavier elements). This is because two nuclei can only fuse if they come within the interaction range of the strong force [27], which has roughly the same dimension as the nuclei themselves [5], while overcoming their long range repulsion by the Coulomb force, otherwise they will simply scatter. This classical picture places an energy barrier of a few 100 keV to the fusion process, however neglects the quantum mechanical nature of the nuclei which results in a finite probability for the reaction to occur below this threshold energy due to tunnelling [3]. Nevertheless a fair amount of energy far above the ionisation is still required for fusion to occur, and consequently any matter undergoing fusion will be in the plasma state.

It is possible to reproduce fusion conditions on Earth in laboratories by simply directing a beam of high energy hydrogen on a hydrogen target as first achieved in 1934 [28]. This is however not a feasible method to use fusion for energy generation, since a significant fraction of the high energetic beam particles will be lost due to scattering on the high density target. Therefore a feasible method of energy generation will require to confine the hot plasma. The stars confine the plasma by their high gravitational pressure, but this method is not feasible on Earth[5]. Rather, the plasma can be confined using strong magnetic fields. This confinement works twofold. On the macroscopic level, the hot plasma will have a natural tendency to expand which is counteracted by the magnetic pressure, as determined by the magnetohydrodynamic

[5]Furthermore, even if they could be realised, the exact stellar fusion conditions would not be desirable, since stars convert protons into helium through the p-p chain, which is a slow multi-stage process [29], whereas a quick single-stage reaction is desirable for energy generation.

(MHD) force balance [30]

$$\boldsymbol{J} \times \boldsymbol{B} = \boldsymbol{\nabla} p \tag{2}$$

where $\boldsymbol{J}$ denotes the current density, $\boldsymbol{B}$ the magnetic field and p the thermal plasma pressure. Meanwhile on the microscopic level the presence of the magnetic field constrains the motion of the charged particles to align itself with the field lines while gyrating in the plane perpendicular to the field line as a result of the Lorentz force. This creates a strong anisotropy in the plasma w.r.t. the magnetic field which significantly reduces the energy transport across the field lines.

In principle any light nuclei can be fused together if the temperature is high enough. But in view of the limited confinement time as a result of turbulence and the high input power needed to reach fusion conditions [31], a feasible nuclear power plant should pick its fuel such that the triple product requirement is easiest to achieve. Minimising the threshold value at the right-hand side of Equation (1) then leads to the choice of the deuterium-tritium reaction

$$D + T \rightarrow \alpha(3.5\,\mathrm{MeV}) + n(14.1\,\mathrm{MeV})$$

as the most proper candidate to achieve fusion conditions since it has the highest reaction rate at the lowest temperature [12].

1.3 Magnetic confinement devices: tokamak and stellarator

From the MHD force balance Equation (2) it follows that both the current density and magnetic field must lie on isobars, which span surfaces in 3D space. The requirement[6] that both $\boldsymbol{B}, \boldsymbol{J}$ must lie on these surfaces constraints the geometry of the confinement devices that can be made, since according to the "hairy ball theorem" it is only possible to smoothly spread out a vector field on a toroidal surface [32]. There are two classes of such toroidal confinement devices: the tokamak and the stellarator which will be discussed below.

1.3.1 The tokamak

The tokamak, originally pioneered by Russians scientists in the early '50s [33], is the straightforward and intuitive realisation of a magnetic confinement device, consisting of a vacuum vessel in the shape of a torus around which several planar coils are placed to create an axisymmetric toroidal (long way around the torus) magnetic field.

Such a toroidal field alone cannot properly confine the charged particles since as a result of the geometry the coils sit closer together on the inboard- than outboard side of the torus, which result in a non-uniform magnetic field strength. This gradient in the magnetic field strength will perturb the circular orbits of the gyration in the plane perpendicular to the magnetic field, and result in a net particle drift called the $\boldsymbol{\nabla} B$ drift [12]. As this drift is opposite for ions and electrons the magnetic inhomogeneity drives charge separation, and causes the plasma to collectively move toward the outer wall due to the resulting $\boldsymbol{E} \times \boldsymbol{B}$ drift. This issue is remedied by adding an additional poloidal (short way around the torus) magnetic field which makes the effective magnetic field helical and forces particles to sample both low- and high magnetic field regions to average out the $\boldsymbol{\nabla} B$ drift.

[6] A more handwaving argument for the need of a toroidal geometry follows from the microscopic influence of the magnetic field; as the motion of charged particles along a magnetic field line is not constraint, the magnetic field lines have to close back on themselves in order to prevent enormous end losses of particles and energy in a simple linear geometry such as a plasma column. The easiest way to mitigate is by bending the plasma column in the shape of a torus.

The necessary poloidal magnetic field is introduced by driving an inductive current in the plasma by a solenoid in the center of the torus, which also renders the poloidal field axisymmetric. A schematic tokamak configuration[7] highlighting the above elements is shown in Figure 2a.

Although the tokamak idea is simple and intuitive, it has some drawbacks. First since the current is driven inductively, it only makes pulsed operation of the device possible which is undesirable from a power plant perspective. Although it is possible to drive this current through non-inductive methods, this would be inhibit the reactor efficiency as these methods require a lot of input power [35]. Additionally, the required plasma current to generate the poloidal field is large, typically in the MA range, which is unfavourable for the macroscopic stability of the plasma as the plasma current is one of the driving factors for MHD instabilities [5].

1.3.2 The stellarator

The issue of the resulting drifts from the non-uniform magnetic field discussed above is not unique to the tokamak, but is present in all toroidal magnetic confinement systems. However, what differentiates between the confinement methods is how the required helical magnetic field to average out the drift is generated. The stellarator in contrast does not rely on a plasma current, but generates its helical magnetic field directly from its external coils.

The stellarator idea was originally proposed by Spitzer [37] and created its effective helical field by bending a torus into the shape of a figure eight, but suffered from poor plasma confinement. The confinement properties of stellarators were later improved by first using helically shaped coils wound around the vacuum vessel to directly generate a helical field (the so called classic stellarator), but modern stellarators typically use an optimised modular coil design [38]. For simplicity in their design, stellarators are typically made with a discrete toroidal symmetry n, such that the magnetic field structure repeats itself n times through the torus [39]. A schematic (classical) stellarator configuration highlighting these elements is shown in Figure 2b.

The coil configuration of stellarators breaks the axisymmetry present in tokamaks and result in an inherently 3D magnetic geometry. Although the geometry has become significantly more

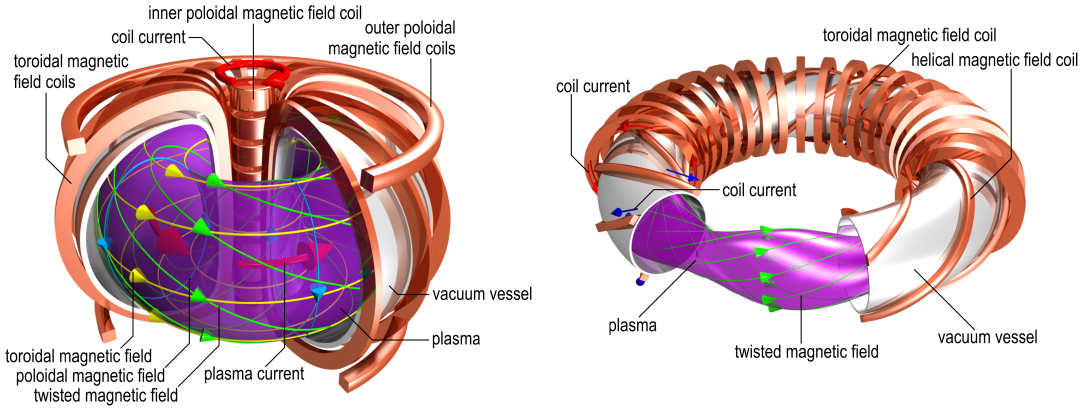

(a) *(b)*

Figure 2: Schematics showing the coils, plasma shape, currents and magnetic field lines for (a) the ideal tokamak and (b) the classical stellarator. Notice how the stellarator configuration does not require a plasma current, and how the shape of the plasma volume is non-axisymmetric. Adapted from [36].

[7]Note that this concerns a simplified ideal tokamak where the poloidal cross section is circular, whereas modern tokamaks employ plasma shaping techniques which create deformed poloidal cross sections to increase the plasma stability and confinement time [34].

complex, breaking with axisymmetry gives stellarators about 50 degrees of freedom in the magnetic field which is an order of magnitude more than for tokamaks [40]. As it is already possible to reduce the turbulent transport to appreciable levels by tweaking the magnetic configuration in the limited parameter space available to tokamaks [41], it seems feasible that the additional freedom present in stellarators could be used to completely optimise for turbulence as well [42]. Furthermore, the stellarator concept has the obvious advantage that does not require a plasma current to generate its magnetic field[8] which is favourable for MHD stability and also makes steady-state operation possible. Additionally, it has also been observed that stellarators do not suffer from stringent operational limits on the plasma density and pressure, which are the source of violent plasma disruptions in tokamaks [43]. The obvious disadvantage of the stellarator is the complexity of the design and manufacturing of the coils [38, 44].

1.4 Magnetic field in general geometry

Regardless whether a tokamak or stellarator is used for the confinement, the magnetic field lines will be helical. In so-called magnetic coordinates such a helical magnetic field can be represented as [45]

$$\boldsymbol{B} = \boldsymbol{\nabla}\psi \times \boldsymbol{\nabla}\theta + \boldsymbol{\nabla}\zeta \times \boldsymbol{\nabla}\chi \tag{3}$$

where ψ, χ denotes the toroidal- and poloidal magnetic flux respectively, and ζ, θ are the so called toroidal and poloidal Boozer angles. These magnetic coordinates do not coincide with the physical poloidal- and toroidal angles in the torus, but are closely related to them, and are defined such that magnetic field lines are straight in the (θ, ζ) plane [46]. The helical twisting of the magnetic field can be described by rotational transform ι, which in magnetic coordinates is equivalently defined by [47]

$$\iota = \frac{\mathrm{d}\theta}{\mathrm{d}\zeta} = \frac{\mathrm{d}\chi}{\mathrm{d}\psi} = \frac{\boldsymbol{B}\cdot\boldsymbol{\nabla}\theta}{\boldsymbol{B}\cdot\boldsymbol{\nabla}\zeta} \tag{4}$$

and describes the number of poloidal turns a field line makes per toroidal turn, as well as the ratio between fluxes and magnetic field components. In case ι is a rational number a magnetic field line will "bite its own tail" after an finite number of round trips through the torus, but otherwise a field line will traverse the torus indefinitely and trace out a full surface. In tokamak physics it is more common to describe the field line twisting by the safety factor q, which is the inverse of the rotational transform $q = 1/\iota$, since important macroinstabilities set operational limits to integer values of q at the core and edge plasma [3]. Using the rotational transform the magnetic field can also be written in Clebsch representation as

$$\boldsymbol{B} = \boldsymbol{\nabla}\psi \times \boldsymbol{\nabla}\alpha \tag{5}$$

where $\alpha = \theta - \iota\zeta$. From the Clebsch representation it follows that $\boldsymbol{B}\cdot\boldsymbol{\nabla}\psi = \boldsymbol{B}\cdot\boldsymbol{\nabla}\alpha = 0$, that is the magnetic field lines lie in a surface of constant enclosed magnetic flux, which are therefore called flux surfaces. Together with the MHD force balance Equation (2) it then follows that the isobars correspond to surfaces of constant magnetic flux which are therefore called flux surfaces, and the pressure is referred to as a flux function $p = p(\psi)$. Since the flux grows with increasing distance from the magnetic axis, this creates a set of nested flux surfaces in the torus and the flux ψ can thus be used as a radial coordinate. Lastly, $\boldsymbol{B}\cdot\boldsymbol{\nabla}\alpha = 0$ implies that also α is constant along a field line, such that α can be used as a field line label to identify different field lines on a given flux surface. For completeness, the magnetic field can also be written in the less illustrative form $\boldsymbol{B} = B\boldsymbol{e_b}$ by separating its magnitude $B = \|\boldsymbol{B}\|$ and direction $\boldsymbol{e_b} = \boldsymbol{B}/B$, which will be convenient later to identify the unit vector $\boldsymbol{e_b}$ with the parallel direction.

[8] Note that this not mean that the stellarator is completely devoid of current. The MHD force balance Equation (2) requires a plasma current to balance the pressure gradient, however this current is significantly smaller than the MA currents present in tokamaks.

1.5 Charged particle motion and adiabatic invariants

In a magnetically confined fusion plasma, there are a handful of periodic motions present in the trajectories of individual particles. With each periodic motion, there is an associated approximately conserved quantity, called an adiabatic invariant, because there is a separation of scales [30]. These adiabatic invariants are very fundamental for the behaviour of the particles in a fusion plasma, as they give rise to the existence of trapped particles and determine the confinement on a microscopic level.

Firstly, there is the gyration of the particles perpendicular to the magnetic field lines which occurs at the gyrofrequency $\Omega = qB/m$ and gryoradius $\rho = v_\perp/\Omega$, where m and q denote the particle's mass and charge, B the magnetic field strength and $v_\perp$ the component of the velocity perpendicular to the field. Associated with this periodic motion is the magnetic moment

$$\mu = \frac{mv_\perp^2}{2B} \tag{6}$$

which is approximately conserved if the variations of the magnetic field strength remain small over the course of a gyro-orbit, which requires $\omega/\Omega \ll 1, \rho/L_B \ll 1$ where ω is the frequency of fluctuations in the magnetic field and L_B is the characteristic length scale of spatial variations in the magnetic field [12]. These conditions generally hold under fusion conditions, and conservation of the magnetic moment has an enormous impact on the particle trajectories. Since μB is just the perpendicular kinetic energy, the region of the magnetic geometry that is accessible to a particle is limited to $B \leq E/\mu$ where $E = 1/2mv^2$ is the equally conserved total kinetic energy. Since the magnetic field in both tokamaks and stellarators is non-uniform, this gives rise (local) minima and maxima of magnetic field strength along a field line which define "magnetic wells". If the maximum magnetic strength along a field line exceeds this E/μ threshold value, then a particle cannot escape the well(s) along the field line and will be deflected back to regions of lower magnetic field[9]. Such particles are referred to as trapped particles, and will perform a bounce motion along the magnetic field line between the bounce points defined by $\mu B = E$. In contrast particles whose E/μ threshold value is higher than the maximum field strength along a field can follow the field through the full torus and are called passing/circulating particles. This distinction between trapped and passing particles is visualised in Figure 3 for the LHD stellarator.

The bounce motion of trapped particles is also periodic with an associated bounce frequency ω_b, and is related to the second adiabatic invariant $\mathcal{J}$, defined by [46]

$$\mathcal{J} = \int_a^b mv_\parallel \, \mathrm{d}l \tag{7}$$

where the integration is along the field line and the integration boundaries are the bounce points where $v_\parallel = 0$. This invariant is related to the motion of the so-called guiding center, which can be considered as the average position of the particle during gyration, and to lowest order simply follows the field line. To next order the guiding center will experience small drifts perpendicular to the field lines due to magnetic inhomogeneity. If these perpendicular excursions remain small w.r.t. to length scale of variations in the magnetic geometry L_B, it can be shown that $\overline{\frac{\mathrm{d}\mathcal{J}}{\mathrm{d}t}} = 0$, with the bar denoting an average over the bounce motion, which implies that the guiding center of trapped particles will remain on the same field line in between deflections [48]. The

[9] This situation is analogous to the analysis of one dimensional motion in classical mechanics under the influence of a potential, where $mv_\parallel^2/2$ has the role of the 1D kinetic energy, and μB has the role of potential energy. This analogy also makes clear why the particle is deflected rather than coming to a standstill along the field line, since the potential energy can be associated with a force $F_\parallel = -\mu \boldsymbol{\nabla}_\parallel B$ aptly called the mirror force. A formal calculation shows that this mirror force from this simple analogy argument is the exact parallel force a particle experiences in an inhomogeneous field properly averaged over the gyromotion [3].

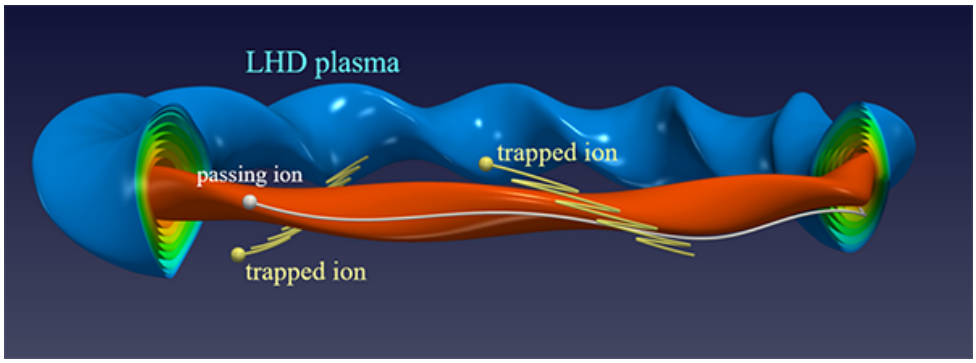

Figure 3: Characteristic orbit of a trapped and passing ions in the Large Helical Device (LHD) stellarator, showing the contrast between the field line following trajetory of the passing ion and the bounce motion of trapped ions along with the precession drift of their guiding center. Also indicated in the poloidal cuts are the isobar surfaces. Image courtesy National Institute for Fusion Science (NIFS).

requirement for the excursions to remain small enough w.r.t. changes in background magnetic geometry is that the drift- and fluctuation frequency satisfy $\omega_d/\omega_b \ll 1, \omega/\omega_b \ll 1$, and is also typically satisfied under fusion conditions [12, 46].

The conservation of $\mathcal{J}$ defines a surface of possible field lines to which the particle must stick, and constrains the drifts to cause only a slow precession of the particle within this surface [48, 49], which is shown in Figure 4 for the case of a tokamak. If the frequency of variations in the magnetic field also satisfies ω/ω_{pc} where ω_{pc} denotes the precession frequency, then there is also a third adiabatic invariant associated with this drift velocity $\boldsymbol{v_d}$, which is proportional to the magnetic flux enclosed by the orbit of a particle [5].

Although the conservation of adiabatic invariants have an enormous influence on the trajectories of particles, violation of the conditions has even bigger consequences as these are associated losses of confinement [12]. Typically the frequencies of these three periodic processes are ordered as $\Omega \gg \omega_b \gg \omega_{pc}$ such that the third adiabatic invariant is most easily violated due to fluctuations in the magnetic field [49]. Good confinement requires that the average radial drift vanishes to keep particles and their energy at their original flux surface. For passing particles the average cross field drifts vanish by design of the helical field as they sample both low- and high field regions. For trapped particles the average drifts depend on the second adiabatic invariant as [36]

$$\overline{\dot{\psi}} = \frac{1}{q\tau_b}\frac{\partial \mathcal{J}}{\partial \alpha} \qquad \overline{\dot{\alpha}} = -\frac{1}{q\tau_b}\frac{\partial \mathcal{J}}{\partial \psi} \tag{8}$$

where the bar denotes averaging over a single bounce period τ_b of a trapped particle (this averaging procedure will be properly defined in Section 3.1). It can be shown that the bounce time is given by $\tau_b = \frac{\partial \mathcal{J}}{\partial E}$ [50], further emphasising the importance of the second adiabatic invariant for trapped particles. Consequently, to make the average radial displacement of trapped particles vanish, the second adiabatic invariant $\mathcal{J}$ should be identical for all field lines on a flux surface such that $\frac{\partial \mathcal{J}}{\partial \alpha} = 0$. Magnetic fields that achieve this are called omnigeneous, and a special case of this are quasi-isodynamic fields which cause the trapped particles to precess around the flux surface poloidally rather than toroidally, as is the case for tokamaks. It is however not possible to create magnetic fields that are exactly globally omnigeneous, but realistic fields can achieve omnigeneity to a high degree of approximation [46].

For omnigeneous fields, the conservation of the second adiabatic invariant $\mathcal{J}$ identifies interesting configurations that could reduce the energy losses associated with fluctuations in the field [43]. For omnigeneous configurations $\mathcal{J} = \mathcal{J}(\psi, E, \mu)$ and a perturbation that causes excursions

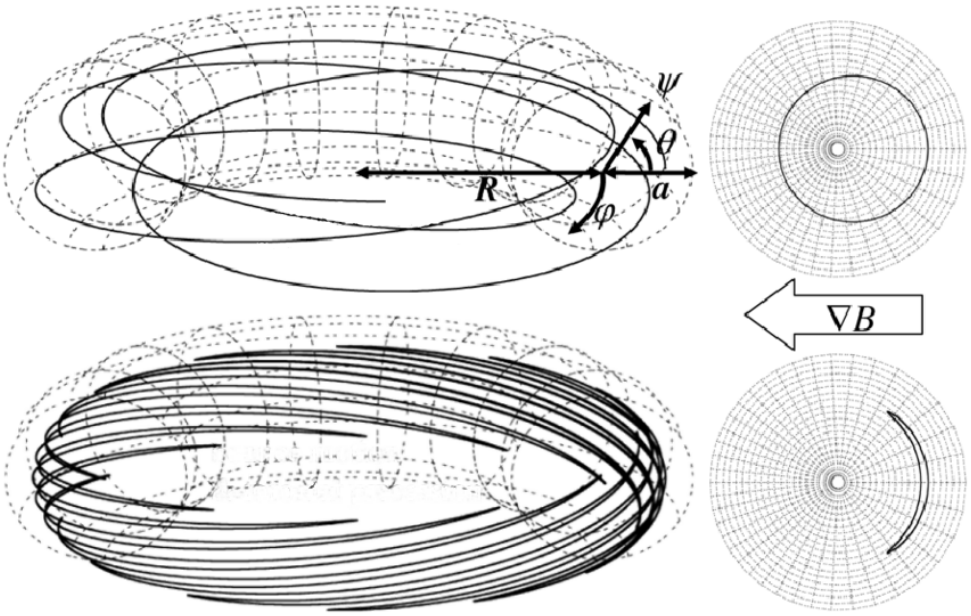

Figure 4: Characteristic trajectory of a passing particle (top) and trapped particle (bottom) in a tokamak, and the projection of their orbit in the poloidal plane. Note how the passing particle traverses both the high and low magnetic field regions and traces out the full field line along a flux surface, whereas the trapped particle is constrained to the low field region at the outboard side while precessesing around toroidally, which results in a banana shaped orbit in the poloidal plane. Also indicated in the top plot are the definitions of the physical poloidal and toroidal angles θ, φ, the radial direction indicated by the magnetic flux ψ, as well as the major- and minor radius R, a. Adapted from [7].

$\delta\psi, \delta\alpha, \delta E, \delta\mu$ in the particle trajectory result in a change of second adiabatic invariant of

$$\delta J = \frac{\partial J}{\partial \psi}\delta\psi + \frac{\partial J}{\partial E}\delta E + \frac{\partial J}{\partial \mu}\delta\mu.$$

If however the perturbation frequency $\omega/\omega_b \ll 1$ than $\mathcal{J}$ and consequently since $\omega_b/\Omega \ll 1$ also μ remain conserved such that $\delta\mu = \delta\mathcal{J} = 0$, which results in an energy change due to radial excursion of

$$\delta E = -\frac{\frac{\partial \mathcal{J}}{\partial \psi}}{\frac{\partial \mathcal{J}}{\partial E}}\delta\psi = -\frac{\frac{\partial \mathcal{J}}{\partial \psi}}{\tau_b}\delta\psi.$$

Since $\tau_b = \frac{\partial \mathcal{J}}{\partial E} > 0$ by definition, it follows that whether a particle gains or loses energy for a radially outward excursion $\delta\psi > 0$ depends completely on the sign of $\frac{\partial \mathcal{J}}{\partial \psi}$. As any gains in particle energy have to come at the expense of the energy in the perturbations, it follows that radially outward excursions corresponding to confinement losses are suppressed if $\frac{\partial \mathcal{J}}{\partial \psi} < 0$. Such configurations are called maximum-$\mathcal{J}$ configurations as the second adiabatic invariant peaks on the magnetic axis, which is the innermost flux "surface" which becomes a single degenerate magnetic field line.

1.6 State of the art

"Nuclear fusion will deliver power in 50 years from now" has been an ongoing jab at the prospects of the fusion community [51], since it seems that the code towards a working controlled fusion reactor is almost cracked, but the progress is advancing at a snail's pace. This statement however does undermine the enormous progress that has been made over the past 70 years: the fusion

triple product has increased by 5 orders of magnitude to a record value of $1.6 \times 10^{21}\,\mathrm{m}^{-3}\,\mathrm{keV\,s}$ held by the JT-60 tokamak [52], and the plasma duration has increased from several milliseconds to a record value of over 15 minutes of steady-state operation at the EAST tokamak [53]. Furthermore a recent DT plasma campaign in the JET tokamak in preparation of the new ITER tokamak has shown a sustained fusion output power of 10 MW for five seconds [54]. Although all existing records have been made in tokamak devices, stellarators are also catching up with the recent W7-X device holding the stellarator triple product record of $6.8 \times 10^{19}\,\mathrm{m}^{-3}\,\mathrm{keV\,s}$ with an energy confinement time of 0.22 s [55]. Despite the advances, nuclear fusion still faces several physics and engineering challenges which are the focus of active research. To name a few besides turbulence, there is the issue of high heat- and neutron loads on materials [56,57], the control of macroscopic plasma instabilities in the edge [58], the understanding of plasma detachment [59], and the breeding of sufficient tritium [60,61].

Returning to the issue at hand of plasma turbulence, a significant effort has been put towards understanding the microinstabilities which cause them. Experimentally microturbulence is investigated by measuring the frequency spectra [62,63], and phase differences/correlations [64–66] of the plasma fluctuations, but it is generally much harder to experimentally distil information about the underlying microinstabilities since the experiments exist in a fully developed chaotic turbulent state. To gain insight in the microinstabilities which exist on much shorter timescales than experiments, a mixture of theory and simulations are performed based on the framework of *gyrokinetics* [6,7], in which the dynamics of the gyromotion is removed from the evolution of the perturbations as the gyrofrequency far exceeds the frequency of the fluctuation, which reduces the dimensional complexity of the problem [8,67]. This which will be explained in much more detail in Section 2.3. The different types microinstabilities correspond to certain limits/simplifications of the governing equations from this framework [68]. Neglecting collisions within this framework does simplify the analytical theory and reduces computation time, but it creates a fundamentally physically incorrect picture of the plasma. Collisions facilitate the interaction between particles and is responsible for establishing an equilibrium amongst electrons and ions (Maxwellisation of the distribution function) and between them (thermal equilibration $T_e \approx T_i$ and quasi-neutrality $n_e \approx n_i$, as achieved under reaction conditions, see Figure 1b). Obviously, without ion-ion collisions there also would not be any fusion reactions.

There have been some investigations on the role of collisions on plasma turbulence, but the majority of this work has focused on the non-linear regime of the turbulence to assess the influence of the collisionality[10] on the heat and particle fluxes, which are determined by the saturated turbulent state [71]. Since non-linear physics is notoriously difficult, most work has been carried out numerically and the relevant physics is then deduced from simple models that can explain the results. Different results have been obtained for different microinstabilities, showing an increase in heat flux with collisionality for the ion temperature gradient (ITG) mode [72,73]. A similar but less strong increase in heat flux for electron temperature gradient (ETG) mode [74], but a decrease in heat flux with collisionality was found for trapped electron modes (TEM) [75]. These different microinstabililites type will be discussed in Section 2.1. Meanwhile linear investigations have revealed contrasting results for the influence of the collisionality on the growth rate, showing a stablising effect at moderate driving gradients [76] but a destabilising effect at strong gradients [77].

The above research has been limited to tokamak geometries and fairly little is known about the effect of collisionality in stellarators. The onset of microinstabilities depends critically on the magnetic geometry [78], so it is not evident that the results obtained in tokamaks also apply to

[10]The collisionality $\nu_\star$ is a commonly used dimensionless measure for the collision frequency in transport theory defined as the ratio between collision frequency and bounce frequency ($\nu_\star = \nu/\omega_b$) [20, 69, 70], however as the latter is fixed by the geometry the collisionality and collision frequency are used interchangeably throughout this work.

stellarators. For the ITG mode, a preliminary investigation on the role of collisions in different geometries has shown that the growth rate is hardly affected by collisions in both tokamak and the LHD stellarator, but strongly affected in a slab geometry where the magnetic field lines are straight and uniform [79]. In case of the W7-X stellarator, an extensive scan over the driving gradients has been performend, which show an overall reduction in growth rates when collisions are taken into account [11]. This has however only been assessed for a single, and particularly high collisionality and is the only investigation of the effects of collision in W7-X to date, so it remains unknown whether this growth rate stabilisation in W7-X is monotonous in collisionality.

Analytical investigations of the role of collisionality on microinstabilities are even less common. Early investigations of the role of collisions in the literature use simplified fluid rather than kinetic models and find the collisions have a damping effect in a slab geometry [80, 81], but a destabilising effect in a tokamak [82]. More recent investigations use either a fully kinetic approach [83] in tokamaks, or a hybrid approach of cold fluid ions and kinetic electrons [84, 85] in stellarators but consider low and high collisionality limits from the outset. Most analytical work on collisions is dedicated to formulating approximate collision operator models which retain the essential physics of the full collision operator, but are more numerically efficient to implement in gyrokinetic codes [86–91].

1.7 Scope and outline of the thesis

As highlighted above much remains unknown about what the influence of collisions is on microinstabilities in stellarators. For the collisionless case at least, the stellarator ITG seems to have a comparable growth rates [92] and turbulent transport levels [93] as in tokamaks. The same cannot be said for TEMs, as these heavily rely on the structure of magnetic wells along the field line. In tokamaks due to axisymmetry, there is a single but repeated magnetic well along the field line caused by closer the proximity of coils on the inboard side. Consequently, there is strong localisation of where the trapped particles reside. For stellarators in contrast, there can be multiple local maxima/minima along the field line creating magnetic wells of varying depths along a field line, and consequently there will be multiple spatially separated populations of trapped particles [16]. This difference is illustrated in Figure 5. Therefore the response of trapped electrons, and hence the levels of turbulence, to an identical initial plasma perturbation will be fundamentally different in stellarators.

Since the TEM is believed to be responsible for the majority of turbulent electron transport in present day experiments [7, 94], extremely sensitive to the details of the magnetic geometry, and the TEM is the microinstability expected to be most affected by collisions as a result of the (de)trapping mechanism it is therefore of interest to find out how TEM turbulence in stellarators is influenced by collisions. Already in the collisionless case, important differences between stellarators arise, where maximum-$\mathcal{J}$ devices like W7-X have been shown to be resilient against trapped particle instabilities both analytically [95] and numerically [96]. It remains to be seen however if this favourable property of maximum-$\mathcal{J}$ devices would extent to collisional TEM.

A full characterisation of TEM turbulence in different geometries is not feasible within a single thesis. In particular the transport fluxes are determined by the final turbulent state and described by the full non-linear physics which is notoriously difficult to solve especially analytically but also numerically. As it is still unclear what the effects of collisions on the underlying microinstability would be, this should be examined first to warrant a full investigation of changes to the transport fluxes compared with their collisionless values. Therefore this thesis will focus on the role of collisions on the linear stability properties of the TEM. To be able to isolate the influence of collisions on the TEM the investigations will be limited to instabilities driven by density gradient only, which rules out the ITG/ETG instabilities mentioned above (as will

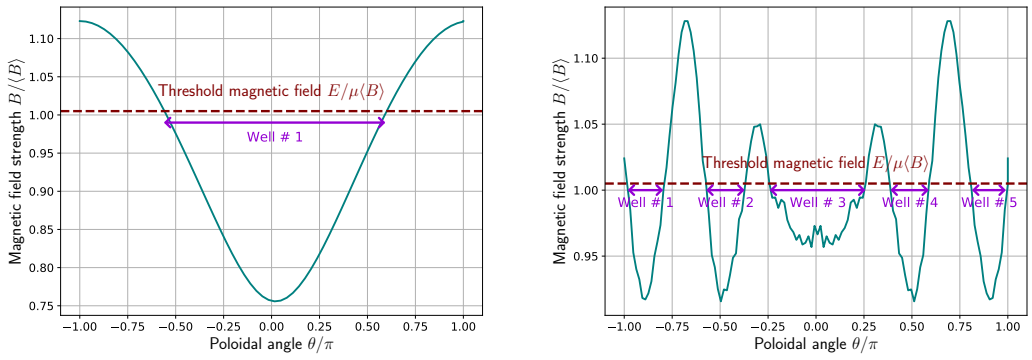

(a) *(b)*

Figure 5: Variation of the magnetic strength along a field line in the poloidal plane for (a) the tokamak and (b) the standard configuration of W7-X stellarator. Also indicated are the trapping wells along the field line for a particle with the same normalised threshold field. In these plots $\theta = 0$ corresponds to the outboard side of the torus, where magnetic field of tokamaks have their absolute minimum.

become clear in Section 2.1).

As the stability analysis is analytically tractable, the approach will be mainly to see if any a priori influence can be obtained from theory, rather than inferring trends from simulations, even if only qualitatively. Because of the sensitivity of the TEM on geometry, it will be interesting to see if this behaviour is universal, or differs between tokamak and stellarators. A general survery of every possible stellarator configuration among the vast possiblities will be infeasible, and therefore two realistic geometries from experimental devices will be considered: the HSX stellarator [97] and the W7-X [98] stellarator. This choice allows to assess possible differences due to the maximum-$\mathcal{J}$ property of the geometry, which is achieved in the high-mirror configuration of W7-X [11] but not in HSX. To facilitate fair comparison with a tokamak, the realistic DIII-D [99] geometry will be considered rather than the idealised case of a circular plasma cross section.

Besides this theoretical investigation, numerical simulations for the above geometries will also be performed to facilitate a comparison with the theory, which is expected to break down at some point due to the inevitable approximations that have to be made. Furthermore, this will also allow for quantitative results whereas theory is expected to yield primarily qualitative results. For the simulations the GENE code [17] will be used to numerically investigate plasma microinstabilities, which can be used for both linear stability analysis and full non-linear turbulence simulations.

The remainder of the thesis is then outlined as follows. In Chapter 2 a basic description of the instability mechanism and the necessary background theory needed to describe plasma microturbulence as well as collisional process in a plasma will be discussed. This framework is then applied to TEMs analytically in Chapter 3 and numerically in Chapter 4 to find how the stability of TEMs is changed by the inclusion of collisions. This is followed by a comparison of the results obtained from theory and simulations in Chapter 5. Lastly a summary of the findings and outlook for future research is presented in Chapter 6.

2 Background theory

The present chapter will introduce the necessary theoretical background needed to describe and understand the microinstabilities in fusion plasmas. First, the instability mechanisms introduced in Chapter 1 will be briefly explained in Section 2.1 using only basic physics to gain an intuitive understanding of the process leading to instability without the need of a thorough mathematical analysis. Then with a clear picture of the TEM instability mechanism in mind, the remainder of this chapter is dedicated to formulating physical framework and mathematical machinery used to rigorously describe these microinstabilities. In Section 2.2 the need for a approach kinetic approach to plasma turbulence is argued and briefly explained. As collisions form a central part of this thesis, Section 2.2.1 in particular will discuss the kinetic description of collisional processes in the plasma in terms of the *collision operator*. Then in Section 2.3 the gyrokinetic equation will be derived in detail as it introduces much of the of the concepts and terminology which are used throughout the later work in this thesis. To close the gyrokinetic framework, the quasi-neutrality condition is then introduced in Section 2.4 which together with the gyrokinetic equation forms the foundation for the analytical work and simulations that follow in Chapters 3 and 4 respectively. Lastly in Section 2.5 an alternative model for the collision operator is introduced and motivated, which will be used in Chapter 3 to account for collisions in an analytically tractable way.

2.1 Microinstability mechanisms

A plethora of plasma instabilities can occur on the scale of the gyroradius, and can be distinguished by means of how perturbations in the plasma profiles couple to perturbations in the electromagnetic fields. The ITG/TEM instabilities which are most important for transport in present day experiments can be described by perturbations in the electric field alone, and therefore throughout the thesis the electrostatic limit will be considered where perturbations in the magnetic field are neglected. This is a valid approximation for low β plasmas where $\beta = p/(B^2/2\mu_0)$ is the normalised plasma pressure and the total energy content is dominated by the equilibrium magnetic field [30]. Within the electrostatic limit, the electric field can be completely described in terms of the electrostatic potential ϕ as $\boldsymbol{E} = -\boldsymbol{\nabla}\phi$. These different microinstabilities can all be interpreted in terms of unstable variations of the fundamental plasma *drift wave*, which describes the interaction between plasma- and electric field perturbations, as result from the magnetic field inhomogeneity in the torus [12]. Therefore the drift wave is discussed first in terms of a simple and original waveform analysis which avoids the more mathematical descriptions given in plasma physics textbooks [5, 12, 30] (which is reproduced in Appendix E for completeness), and then the changes to this model which lead to the different instabilities are introduced.

2.1.1 The drift wave

The fundamental interaction between plasma- and potential perturbations is characterised by the so-called drift wave, which can be understood by considering a simplified plasma slab geometry with a uniform magnetic and straight field. The basic ingredient is the existence of a gradient in the background density $\boldsymbol{\nabla} n_0$ perpendicular to the magnetic field. In the slab geometry the magnetic field is taken in the z direction, and the density gradient is taken in the x direction, which would correspond to the toroidal and radial directions in a torus respectively. This leaves a third direction determined by $\boldsymbol{e_y} = \boldsymbol{e_z} \times \boldsymbol{e_x}$ which is referred to as the binormal direction, which roughly corresponds to the poloidal angle in a torus [5].

If a wave-like perturbation of the particle guiding centers $\delta x(y) = A\sin(ky)$ is superimposed on the existing background density, then these radial excursions effectively "take" plasma particles from a position x at density $n_0(x)$ and "displace" those particles at constant density to $x +$

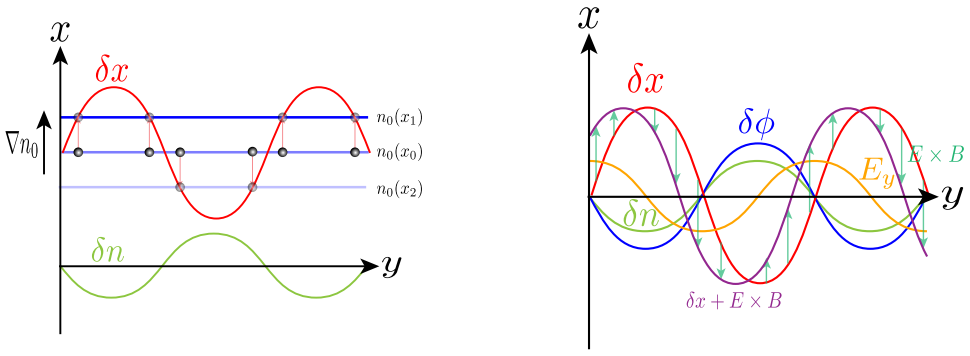

(a) (b)

Figure 6: Schematic mechanism of the drift wave showing (a) how the guiding center displacement leads to a density perturbation and (b) the waveforms of all perturbed quantities along with the effect of the $\boldsymbol{E} \times \boldsymbol{B}$ drift on the initial displacement.

$\delta x(y)$ where the equilibrium density is $n_0(x + \delta x(y)) \approx n_0(x) + \delta x(y)\frac{\mathrm{d}n_0}{\mathrm{d}x}$, resulting in a density perturbation $\delta n(y) = -\delta x(y)\frac{\mathrm{d}n_0}{\mathrm{d}x}$ which is π out of phase with the guiding center perturbation, as shown in Figure 6a. As the electrons are much lighter than the ions and can freely move along the field line, they will quickly "communicate" with the unperturbed electrons and diffuse out to re-establish equilibrium along the field line, which is called the adiabatic electron response. Within the same time frame, the much heavier displaced ions will not have moved much along the field line and are left behind at their initial density. As these ions are now balanced by electrons at the background this results in a net charge density of $\rho = e\delta n$, which creates an electrostatic potential $\phi \propto \rho$ in phase with density perturbation. This potential difference creates an electric field $\boldsymbol{E} = -\boldsymbol{\nabla}\phi$, which in the presence of the magnetic field results in an $\boldsymbol{E} \times \boldsymbol{B} \propto \frac{\mathrm{d}\delta x(y)}{\mathrm{d}y}\boldsymbol{e_x}$ drift that causes an additional guiding center displacement which is $\pi/2$ out of phase with the initial guiding center displacement, see Figure 6b. This drift also affects the guiding centers of previously unperturbed particles and will result in an additional density perturbation which is shifted w.r.t. the initial density perturbation. This cycle continues and causes the density perturbation to propagate along the y direction rather than grow in amplitude and thus corresponds to a stable perturbation called the drift wave.

2.1.2 The trapped-particle mode

One major influence of an inhomogeneous magnetic field is the existence of trapped particles, which are absent in the simple drift wave picture above. The second key element that is introduced by an inhomogeneous magnetic field is the $\boldsymbol{\nabla}B$ and curvature drifts (these will be elaborated in Section 2.3). As this drift vanishes on average for passing particles, the response of passing particles to density perturbations is essentially that described by the drift wave model. Therefore, it is the non-vanishing average drift of trapped particles that could introduce an instability mechanism.

To investigate this, two changes will be made to the basic drift wave model: the electron response is no longer assumed to be adiabatic and the effect of trapped particles is simulated by adding a constant drift velocity v_d which is opposite for ions and electrons, see Figure 7a. This drift moves trapped particles originally at position (x, y_0) to $(x, y_0 \pm \delta y)$ where the plus sign is taken for ions. In absence of a density perturbation this does not lead to the accumulation of charge since the density gradient is in the x direction. If however there is also a wavelike radial excursion of guiding centers like before, then these drifts will now move trappped particles at the locally perturbed density $n(x, y) = n_0(x) + \delta n(y)$ which results in an imbalance between the in/out

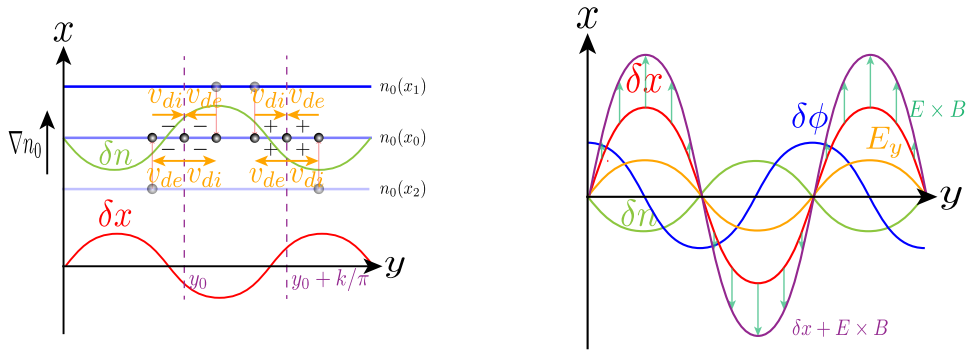

(a) (b)

Figure 7: Schematic mechanism of the trapped particle mode showing (a) how the oppositely directed magnetic drifts of electrons and ions result in a charge density and (b) the waveforms of all perturbed quantities along with the effect of the $\boldsymbol{E} \times \boldsymbol{B}$ drift on the initial displacement.

fluxes of electrons and ions. This leads to the build up of a net charge density of

$$\begin{aligned}\rho(y_0) &= +e\left[n(x, y_0 - \delta y) - n(x, y_0)\right] - e\left[n(x, y_0 + \delta y) - n(x, y_0)\right] \\ &\approx -2e\left.\frac{\partial n(x,y)}{\partial y}\right|_{y=y_0} \delta y = +2e\frac{\mathrm{d}n_0}{\mathrm{d}x}\frac{\mathrm{d}\delta x(y_0)}{\mathrm{d}y}\delta y.\end{aligned}$$

which is now $\pi/2$ out of phase with the initial density perturbation in contrast to the drift wave mechanism, see Figure 7b. Completely analogous to the analysis of the drift wave mechanism, this charge density will result in an $\boldsymbol{E}\times\boldsymbol{B}$ drift given by $\boldsymbol{E}\times B \propto -\frac{\mathrm{d}^2\delta x(y)}{\mathrm{d}y^2}\boldsymbol{e_x}$ which is completely in phase with the initial guiding center perturbation. This drift will thus add to the already existing radial excursion of the trapped particle guiding centers thereby enhancing its amplitude, see Figure 7b. As the density perturbation $\delta n = -\delta x(y)\frac{\mathrm{d}n_0}{\mathrm{d}x}$ is proportional to the guiding center perturbation this will also be enhanced creating a feedback loop which leads to instability. Since the amplitude of the density perturbation is directly proportional to the density gradient, this instability mechanism will be more dangerous at high density and is thus referred to as the density-gradient-driven trapped-particle mode.

By comparing with the basic drift above, it is thus the phase between the density and potential perturbation which is of importance for determining whether an instability occurs. This makes the direction of the drift velocity crucial, as it is easily verified that a reversal of the drift velocities would lead to a potential which is $-\pi/2$ out of phase with the density perturbation and an $\boldsymbol{E} \times \boldsymbol{B}$ drift that is π out of phase with the initial radial excursion of guiding centers, which would quench rather than enhance the amplitude of the guiding center displacement corresponding to damping of the perturbations.

2.1.3 Temperature gradient modes

The above analysis only considers the situation with a density gradient and implicitly assumes a uniform temperature, but in general a fusion plasma also has a temperature gradient which could drive instabilities. As the average drifts of trapped particles depend on temperature, a temperature perturbation can also result in an imbalance between in/out fluxes of charged particles, such that temperature-gradient-driven trapped-particle also modes exist [36].

Although temperature gradient effects are not discussed in this thesis, since it is so important for present day transport the instability mechanism of the ITG mode is sketched in Appendix A using the same waveform based model as above. The fundamental change w.r.t. the basic drift

wave is that ions are considered to respond to the perturbations with a temperature dependent drift velocity, while the electrons are treated adiabatically again. Analogous to the trapped particle mode, an instability occurs when there is a $+\pi/2$ phase difference between the temperature fluctuations and potential fluctuations, although this instability is largely a passing particle effect [5]. For completeness, it will be mentioned that an electron temperature gradient (ETG) mode also exists which is completely isomorphic[11] to the ITG with the roles of ions and electrons reversed [102], although it is generally considered less important for the overall transport [19].

2.2 Kinetic description of a plasma

In order to describe the plasma dynamics, in principle one would have to solve the equations of motion for all plasma particles. As plasma microturbulence occurs on the gyroradius scale, at bare minimum this means that particle trajectories have to be evolved within a box which spans several gyroradii in each direction to correctly resolve the spatial structure of the fluctuations. Under the typical reactor conditions of Figure 1a this corresponds to tracking $\mathcal{O}(10^{13})$ particles which is beyond the capabilities of modern super computers. On the other hand, the involved spatial- and temporal scales of the microinstabilities are not sufficiently collisional for the plasma to re-establish well defined "fields" like density, velocity and temperature such that a reduced fluid description of the plasma cannot be used to describe plasma microturbulence [8].

Thus an intermediate statistical approach has to be taken, which describes the ions and electrons in terms of a distribution function. This distribution function can be very complicated if the particles are strongly coupled. Fortunately, at the reactor conditions the average potential energy can be estimated as a few meV whereas the thermal energy is a few tens of keV, such that the particles can be considered as weakly coupled and the single-particle distribution function $f(t, \boldsymbol{q}, \boldsymbol{p})$ describes the full ensemble[12]. This distribution function is defined such that the number of particles occupying a small volume in six dimensional phase-space is given by $f\mathrm{d}^3\boldsymbol{q}\mathrm{d}^3\boldsymbol{p}$ where $\boldsymbol{q}, \boldsymbol{p}$ are the canonical position and momentum respectively. The evolution of this distribution function is described by the kinetic equation [5]

$$\frac{\partial f_s}{\partial t} + \dot{\boldsymbol{q}} \cdot \boldsymbol{\nabla}_{\boldsymbol{q}} f_s + \dot{\boldsymbol{p}} \cdot \boldsymbol{\nabla}_{\boldsymbol{p}} f_s = C_s(f_s) \tag{9}$$

where the subscript s indicates the species, t denotes time, $\boldsymbol{\nabla}_{\boldsymbol{q}}, \boldsymbol{\nabla}_{\boldsymbol{p}}$ represent the gradient w.r.t. phase-space coordinates $\boldsymbol{q}$ and $\boldsymbol{p}$ respectively, the dot indicates a derivative w.r.t. time and C_s is the collision operator. The left-hand side of Equation (9) is the phase-space analogue of the material derivative, such that in absence of collisions Equation (9) represents conservation of the distribution function along a trajectory in phase-space. The collisions can then be considered as a perturbation resulting from the neglected weak particle interactions which cause discrete jumps in phase-space [103]. Since the particle interactions are the result of the local microscopic electromagnetic fields generated by individual particles, the unperturbed trajectories are completely determined by the macroscopic electromagnetic fields [20], and consequently the canonical position $\boldsymbol{q}$ is just the real position $\boldsymbol{x}$ and the canonical momentum is just the normal momentum $\boldsymbol{p} = m\boldsymbol{v}$. Then the kinetic equation can be simplified to[13]

[11] At least conceptually the instability mechanisms are isomorphic being described by a kinetic response of one species and an adiabatic response of the other. Mathematically there is a subtle difference in the adiabatic response as due to their much smaller gyroradius electrons cannot respond adiabatically to perturbations which cross the flux surface by several ion gyroradii, as this would correspond to unphysical transport [100, 101]. Nevertheless the isomorphism holds at least for the linear onset of instability discussed by the waveform model, although there is still debate whether the isomophism also carries over non-linearly [17, 74].

[12] In other words the complete N particle distribution function f^N describing the full ensemble of particles can be factorised into the individual particle distribution functions $f^N = \prod_{j=1}^{N} f_j(t, \boldsymbol{q_j}, \tilde{\boldsymbol{p}}_{\boldsymbol{j}})$.

[13] Gravitational effects are neglected, as even for ions for which gravity is strongest, the Lorentz force is already dominant over gravity for electric fields as weak as $\mathcal{O}(0.1\,\mu\mathrm{V\,m^{-1}})$ and magnetic fields as weak as $\mathcal{O}(0.1\,\mathrm{pT})$, which are always exceeded in fusion plasmas.

$$\frac{\partial f_s}{\partial t} + \boldsymbol{v} \cdot \boldsymbol{\nabla}_{\boldsymbol{x}} f_s + \frac{q_s}{m_s} \left(\boldsymbol{E} + \boldsymbol{v} \times \boldsymbol{B} \right) \cdot \boldsymbol{\nabla}_{\boldsymbol{v}} f_s = C_s(f_s) \tag{10}$$

where q_s, m_s denote the charge and mass of a particle from species s respectively, $\boldsymbol{E}, \boldsymbol{B}$ represent the macroscopic electric and magnetic field respectively.

2.2.1 The collision operator

As collisions are central for this thesis, a couple of words on the collision operator are due. Collisions in a plasma are in stark contrast with the usual picture of a "billiard ball" collisions in neutral gasses [104]. This is because charged particles interact by the long range Coulomb force, such that essentially a single collision involves the interaction between many particles, which makes a complete description of collisions intractable. Nevertheless because the $1/r^2$ dependence of the Coulomb force between a pair of charged particles, most of these interactions are weak and cause only a small deflection in the trajectory of a particle, such that the reaction on particles in the direct vicinity to this small scattering will be negligible compared to the interaction they experience with all other unscattered particles, and consequently there will be no correlations between the small deflections of particles [105]. In other words, this means that the small deflections can be considered as random walk in the velocity of the scattered particle [20]. Because of the high densities, repulsive[14] nature and $1/r^2$ dependence of the Coulomb force, there will only be relatively few strong interactions which cause a significant deflection to the trajectory, such that the accumulated effect of the small deflections from long-range interactions will be dominant [70]. This allows to consider the collisions in a plasma as independent random binary scattering events which result in small velocity deflections, such that the influence of collisions can be around $\boldsymbol{\Delta v} \approx \boldsymbol{0}$.

The mathematical details of this process are quite lengthy and the derivation can be found in Appendices B.1 to B.3. This derivation results in a Fokker-Plank equation for the collision operator which describe the effective drag- and diffusive forces that collisions have on the distribution function. The collision operator describing collisions between particles from species a with species b can then be compactly expressed as

$$C_{ab}(f_a, f_b) = L^{ab} \frac{\partial}{\partial v_k} \left[\frac{m_a}{m_b} \frac{\partial \varphi_b}{\partial v_k} f_a - \frac{\partial^2 \psi_b}{\partial v_k \partial v_l} \frac{\partial f_a}{\partial v_l} \right] \tag{11}$$

where $L^{ab} = (q_a q_b / m_a \epsilon_0)^2 \ln \Lambda$ is a measure of the interaction strength, with $\ln \Lambda$ the Coulomb logarithm which is related to the number of particles in the Debye sphere[15] [30], $f_{a,b}, m_{a,b}, q_{a,b}$ are the distribution function, mass and charge of species a and b respectively, ϵ_0 the vacuum permittivity, $v_{k,l}$ denote velocity components with repeated indices l, k implying Einstein summation, and φ_b, ψ_b are the so-called Rosenbluth potentials determined by

$$\begin{aligned} \varphi_b(\boldsymbol{v}) &= -\frac{1}{4\pi} \int \frac{f_b(\boldsymbol{v'})}{\|\boldsymbol{v} - \boldsymbol{v'}\|} \mathrm{d}^3 \boldsymbol{v'} \\ \psi_b(\boldsymbol{v}) &= -\frac{1}{8\pi} \int \left\|\boldsymbol{v} - \boldsymbol{v'}\right\| f_b(\boldsymbol{v'}) \mathrm{d}^3 \boldsymbol{v'} \end{aligned} . \tag{12}$$

[14] The repulsive nature sets a clear distance of closest approach and thus limits the number of large deflections as a result of close proximity pair interactions. In case of attractive interactions, there is no limiting distance. However the number of particles that fall within a handful of interparticle distances is negligibly small compared to the total number of particles within the Debye sphere. Consquently the accumulated effect effect of small deflections in the scattered trajectory as a result from long-range interactions will outweigh the effect of the few large deflections in the scattered trajectory as result from nearest-neighbour interactions. Therefore the argument for repulsive interactions is easily extended to collisions between ions and electrons.

[15] This can be taken as the region over which the electric field of a single charged particle can influence those around it, as beyond the Debye length the microscopic electric fields get shielded by collective rearrangements of the bulk plasma. See any introductory textbook to plasma physics, e.g. [3]

This Fokker-Planck collision operator Equation (11) is valid provided that the Coulomb logarithm $\ln\Lambda \gg 1$ as otherwise the effect of large angle deflections and correlations become dominant, and the collisions can no longer be considered binary [106]. The Coulomb logarithm depends weakly on plasma parameters as [70]

$$\ln\Lambda = 17.25 - \frac{1}{2}\ln n[10^{19}\mathrm{m}^{-3}] + \ln T[\mathrm{keV}] \tag{13}$$

where the quantities in square bracket indicate the proper unit for density and temperature, and is typically between $\ln\Lambda \sim 15 - -20$ for fusion plasmas, making the Fokker-Planck approach valid. In principle the Fokker-Planck collision operator is derived in the absence of a magnetic field where the particle motion is isotropic. Nevertheless Equation (11) can still be used in a magnetised plasma provided that the gyroradius is larger than the Debye length [107], such that the effects of gyration are not noticeable at the spatial scales where the particle is scattered. This condition is also typically satisfied under reactor conditions.

Although Equation (11) is generally valid for collisions between any charged particle species a, b with arbitrary distribution functions, it is not very illustrative. In particular the Rosenbluth potentials are hard to evaluate as they involve integrals over the relative velocity between particles. If species b is taken to have Maxwellian distribution, then the calculation of the Rosenbluth potentials is analytically tractable. In Appendix B.4 it is shown that in this case the collision operator takes the more comprehensible form of

$$C_{ab}(f_a, f_{Mb}) = \nu_D^{ab}\mathcal{L}\{f_a\} + \frac{1}{v^2}\frac{\partial}{\partial v}\left[v^3\left(\frac{m_a}{m_a+m_b}\nu_s^{ab}f_a + \frac{1}{2}\nu_\parallel v\frac{\partial f_a}{\partial v}\right)\right] \tag{14}$$

where $\mathcal{L}$ is the Lorentz scattering operator

$$\mathcal{L} = \frac{1}{2}\left(\frac{1}{\sin\theta}\frac{\partial}{\partial\theta}\left(\sin\theta\frac{\partial}{\partial\theta}\right) + \frac{1}{\sin^2\theta}\frac{\partial^2}{\partial\varsigma^2}\right) \tag{15}$$

with v, θ, ς are spherical velocity coordinates[16], and $\nu_D^{ab}, \nu_s^{ab}, \nu_\parallel^{ab}$ are the so-called test-particle collision frequencies

$$\nu_s^{ab} = \hat{\nu}^{ab}\left(1+\frac{m_b}{m_a}\right)\frac{T_a}{T_b}\frac{2G(x_b)}{x_a} \quad \nu_\parallel^{ab} = \hat{\nu}^{ab}\frac{2G(x_b)}{x_a^3} \quad \nu_D^{ab} = \hat{\nu}^{ab}\frac{\mathrm{erf}(x_b) - G(x_b)}{x_a^3} \tag{16}$$

where the special functions are $G(x) = (\mathrm{erf}(x) - x\,\mathrm{erf}'(x))/(2x^2)$ and $\mathrm{erf}(x) = \frac{2}{\sqrt{\pi}}\int_0^x \exp\left(-\xi^2\right)\mathrm{d}\xi$ is the error function, $x_s = v/v_{Ts}$ is the velocity normalised to thermal speed of each species $v_{Ts} = \sqrt{2T_s/m_s}$, and the characteristic collision frequency $\hat{\nu}^{ab}$ is given by

$$\hat{\nu}^{ab} = \frac{n_b}{4\pi v_{Ta}^3}\left(\frac{q_a q_b}{\epsilon_0 m_a}\right)^2 \ln\Lambda = \nu_{90^\circ}^{ab}\frac{3\sqrt{\pi}}{4}. \tag{17}$$

Here $\nu_{90^\circ}^{ab}$ is the so-called 90° scattering frequency, such that $1/\nu_{90^\circ}^{ab}$ is the time it takes for the accumulated effect of small angle collisions with species b to decorrelate the velocity[17] of a typical thermal particle from species a and essentially make the particle "forget" about its history and become part of the background plasma [3].

When writing the collision operator in the form of Equation (14) the different effects that the collisions have on a particle become clear. As the Lorentz scattering operator $\mathcal{L}$ essentially describes diffusion of the velocity vector on a surface of constant speed[18] $v = \|\boldsymbol{v}\|$, the first term

[16] Following the physics convention where θ indicates the polar angle and ς the azimuthal angle.

[17] This should be interpreted in the sense that the velocity autocorrelation function $\langle \boldsymbol{v_a}(t)\cdot\boldsymbol{v_a}(t+\tau)\rangle \to 0$.

[18] Speed is typically only used in traffic regulations in everyday life, however to distinguish between processes that depend only on the magnitude of the velocity rather than its full vectorial details (like the collision frequencies of Equation (16)), the notion of speed will also be used throughout this thesis.

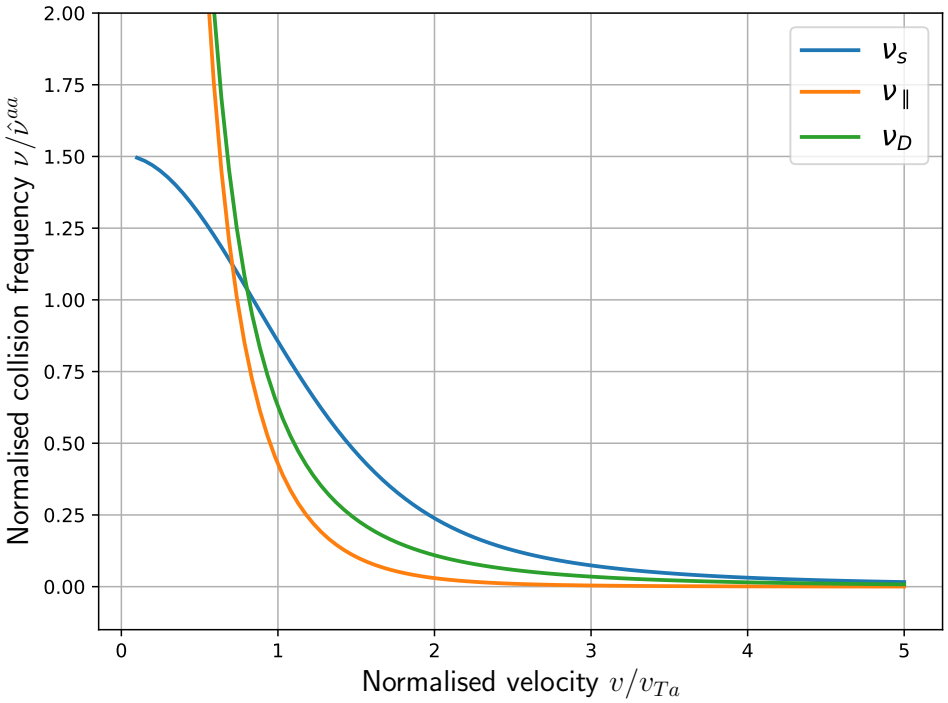

Figure 8: Dependence of the test particle collision frequencies Equation (16) *on particle velocity in case of self collision when* $b = a$.

describes the how collisions change the direction of the velocity of a particle which result in the small deflection of the trajectory, and is referred to as pitch-angle scattering. The second term in Equation (14) all contain terms that affect the speed of a particle and are in contrast to the Lorentz scattering operator thus not energy conserving. Therefore this part of the collision operator describes energy scattering due to energy exchanges in a collision. The energy scattering is a balance between drag forces that slow the particle down and diffusive forces in the same direction as the initial velocity, which can be identified by the first and second speed derivatives of the distribution function. The test particle collision frequencies $\nu_s^{ab}, \nu_\parallel^{ab}, \nu_D^{ab}$ then simply give the rates at which a particle is slowed down by drag, accelerated by parallel diffusion and deflected by perpendicular diffusion respectively. The velocity dependence of these frequencies in the case of self-collisions $b = a$ is shown in Figure 8, which shows that at low velocity diffusion is more important while at high velocity drag dominates.

The interspecies collisions when $a \neq b$ are special in plasma because of the enormous mass difference between electrons and ions. Because of this mass difference the thermal velocities v_{Ti}, v_{Te} will be on disparate scales when the temperatures are similar. This effects the behaviour of the test-particle collision frequencies Equation (16) through the velocity dependence of $G(x_b), \phi(x_b)$, where the particle velocity is normalised to the thermal speed of the other species, such that they can be expanded for small and large arguments

$$\phi(x \ll 1) \approx \frac{2}{\sqrt{\pi}}x - \frac{2}{3\sqrt{\pi}}x^3 + \mathcal{O}(x^5) \qquad \phi(x \gg 1) \approx 1$$

$$\phi'(x \ll 1) \approx \frac{2}{\sqrt{\pi}} - \frac{2}{\sqrt{\pi}}x^2 + \mathcal{O}(x^4) \qquad \phi'(x \gg 1) \approx 0$$

$$G(x \ll 1) = \frac{\phi(x \ll 1) - x\phi'(x \ll 1)}{2x^2} \approx \frac{2x}{3\sqrt{\pi}} + \mathcal{O}(x^3) \qquad G(x \gg 1) = \frac{\phi(x \gg 1) - x\phi'(x \gg 1)}{2x^2} \approx \frac{1}{2x^2}$$

where for small arguments the next order terms in the Taylor expansion of $\phi(x), \phi'(x)$ are needed to prevent an indeterminate limit $0/0$ in G. Writing $x_b = x_a v_{Ta}/v_{Tb}$ and performing an expansion in the electron-ion mass ratio give the relevant collision frequencies between ions and electrons as

$$\begin{aligned}
\nu_s^{ei} &\approx \hat{\nu}^{ei} \frac{1}{x_e^3} & \nu_s^{ie} &\approx \hat{\nu}^{ie} \frac{4}{3\sqrt{\pi}} \sqrt{\frac{m_e}{m_i}} \left(\frac{T_i}{T_e}\right)^{3/2} \\
\nu_\parallel^{ei} &\approx \hat{\nu}^{ei} \frac{m_e}{m_i} \frac{T_i}{T_e} \frac{1}{x_e^5} & \nu_\parallel^{ie} &\approx \hat{\nu}^{ie} \frac{4}{3\sqrt{\pi}} \sqrt{\frac{m_e}{m_i}} \sqrt{\frac{T_i}{T_e}} \frac{1}{x_i^2} \\
\nu_D^{ei} &\approx \hat{\nu}^{ei} \frac{1}{x_e^3} & \nu_D^{ie} &\approx \hat{\nu}^{ie} \frac{4}{3\sqrt{\pi}} \sqrt{\frac{m_e}{m_i}} \sqrt{\frac{T_i}{T_e}} \frac{1}{x_i^2}
\end{aligned} \tag{18}$$

where the electron collision frequencies now only depend on the v/v_{Te} and vice versa for the ions. From the ratio of these frequencies it follows that the electrons are easily deflected and slowed down by ions, but the energy exchange between them proceeds much slower by the mass ratio, which is exactly the same conclusion as reached when working out the momentum and energy conservation laws using basic classical mechanics [108]. In contrast ions predominantly only experience a net drag from the "sea" of electrons, as the mass difference makes it impossible to change the ion momentum or energy by a significant amount, completely analogous to how a cyclist only experiences an effective drag from the many collisions with air molecules they make, without being thrown off course.

2.3 The gyrokinetic equation

In principle the kinetic equation Equation (10) could be used to solve for the distribution function of electrons and ions to study the effect of fluctuations in a magnetised fusion plasma. However this equation has the full details of the plasma evolution "encoded" within it, which spans a wide range of spatial scales between the microscopic gyroradius and macroscopic plasma size and an even wider range of temporal scales between the fast gyration and total pulse duration [6].

Experimental observation of microturbulence across many fusion devices have revealed however that the fluctuations in the plasma obey the scaling [7]

$$\frac{\omega}{\Omega_s} \sim \frac{k_\parallel}{k_\perp} \sim \frac{v_E}{v_{Ts}} \sim \frac{\delta n_s}{n_{0s}} \sim \frac{\delta B}{B_0} \sim \frac{\rho_s}{L_n} \sim \delta \ll 1 \tag{19}$$

where ω is the perturbation frequency, $\Omega_s = q_s B/m_s$ the gyrofrequency of each species s, $k_\parallel, k_\perp$ denote the wave number parallel and perpendicular to the direction magnetic field, v_E is the magnitude of the perturbed $\boldsymbol{E}\times\boldsymbol{B}$ drift velocity, v_{Ts} is the thermal velocity of species s, $\delta n_s, n_{0s}$ are the density perturbation and equilibrium density of species s, $\delta B, B_0$ are the strengths of the perturbed- and equilibrium magnetic field, $\rho_s = v_\perp/\Omega_s$ is the gyroradius of each species and $L_n = \|\boldsymbol{\nabla} \ln n_0\|^{-1}$ is the gradient length scale of the plasma profile, which can be regarded as a measure of the macroscopic plasma size. For typical microinstabilities the wavenumber scales with $k_\perp \rho_s \sim \mathcal{O}(1)$. Together with the scaling for the $\boldsymbol{E}\times\boldsymbol{B}$ drift Equation (19) implies that the electrostatic potential fluctuations have the scaling

$$\delta \sim \frac{v_E}{v_{Ts}} \sim \frac{k_\perp \phi}{B v_{Ts}} \sim \frac{\phi}{B \rho_s v_{Ts}} \sim \frac{q_s \phi}{T_s} \tag{20}$$

where $\rho_s \Omega_s \sim v_{Ts}$ was used, such that the particle energy remains dominated by its thermal kinetic part.

The perturbations are observed to be highly elongated[19] along the magnetic field but compressed

[19] This does not mean that perturbations with short correlation lengths along the magnetic field cannot exist in the plasma, as spontaneous fluctuations are naturally generated at all scale. Such perturbations will however by quickly subdued to Landau damping from passing particles, and consequently after some initial transient only the elongated fluctuations will survive [7].

perpendicular to it, which is expressed by the $k_\parallel/k_\perp \ll 1$ scaling of Equation (19) since the wavenumbers follow as inverse correlation lengths $k_{\parallel,\perp} \sim 1/L_{\parallel,\perp}$. This reflects the length scales in the in the helical particle orbits, where the anisotropy between the motion along the field line and the perpendicular gyration forms the basis of magnetic confinement (see Section 1.2). Furthermore, the oscillation period has been observed to be much slower than the gyrofrequency, as expressed by $\omega/\Omega_s \ll 1$ in Equation (19) which shows there is a clear disparity between the timescales. This means that the gyration of the particles cannot couple to the evolution of the instabilities, and it is the slower motion of the guiding centers that is responsible for driving the perturbations unstable[20]a which motivates the removal of the details of the gyration from the kinetic equation.

This can be achieved by a change of phase-space variables[21] $(\boldsymbol{x}, \boldsymbol{v}) \to (\boldsymbol{R}, E, \mu, \vartheta)$ defined by

$$\begin{aligned} \boldsymbol{R} =& \boldsymbol{x} - \frac{\boldsymbol{e_b} \times \boldsymbol{v}}{\Omega_s} & \vartheta =& \arctan\left(\frac{\boldsymbol{v}\cdot\boldsymbol{e_1}}{\boldsymbol{v}\cdot\boldsymbol{e_2}}\right) \\ \mu =& \frac{m_s v_\perp^2}{B} & E =& \frac{m_s v_\parallel^2}{2} + \mu B + q_s\phi \end{aligned} \tag{21}$$

where $\boldsymbol{R} = \boldsymbol{x} - \boldsymbol{\rho}$ is the position of the guiding center, $\boldsymbol{e_b} = \boldsymbol{B}/B$ the unit vector in the direction of the magnetic field, E, μ the particle energy and magnetic moment, $\boldsymbol{e_1}, \boldsymbol{e_2}$ are orthogonal unit vectors locally defined at the guiding center such that $\boldsymbol{e_1} \times \boldsymbol{e_2} = \boldsymbol{e_b}$ and thus ϑ is the gyrophase angle which contains all information of the fast gyromotion [110]. The time derivatives of the new velocity variables are given by $\dot{\vartheta} = \Omega_s$ since it defines the gyromotion, $\dot{\mu} \approx 0$ as the frequency ordering $\omega/\Omega_s \sim \delta$ makes μ a proper adiabatic invariant, and lastly

$$\begin{aligned} \dot{E} =& m_s \boldsymbol{v}\cdot\dot{\boldsymbol{v}} + q_s \left.\frac{\partial\phi}{\partial t}\right|_{\boldsymbol{x}} + q_s\left(\boldsymbol{v}\cdot\boldsymbol{\nabla}\right)\phi \\ =& m_s\boldsymbol{v}\cdot\frac{q_s}{m_s}(\boldsymbol{E} + \boldsymbol{v}\times\boldsymbol{B}) + q_s\left.\frac{\partial\phi}{\partial t}\right|_{\boldsymbol{x}} + q_s\left(\boldsymbol{v}\cdot\boldsymbol{\nabla}\right)\phi = q_s\left.\frac{\partial\phi}{\partial t}\right|_{\boldsymbol{x}} \end{aligned}$$

where the last step follows from $\boldsymbol{E} = -\boldsymbol{\nabla}\phi$ and it has been made explicit that the potential ϕ is a function of the particle position $\boldsymbol{x}$ rather than the guiding center position $\boldsymbol{R}$ since ϕ is not a formal phase-space variable. Consequently the transformed kinetic equation takes the form

$$\frac{\partial f_s}{\partial t} + \dot{\boldsymbol{R}}\cdot\boldsymbol{\nabla}_{\boldsymbol{R}} f_s + q_s\left.\frac{\partial\phi}{\partial t}\right|_{\boldsymbol{x}}\frac{\partial f_s}{\partial E} + \Omega_s\frac{\partial f_s}{\partial\vartheta} = C_s(f_s). \tag{22}$$

Note that although μ does not appear explicitly, the distribution function still depends critically on μ as it distinguishes between trapped and passing particles.

In Equation (22) all the fast time scale dynamics are in the $\frac{\partial}{\partial\vartheta}$ term, and in Appendix C.1 it is shown using an order of magnitude estimate that this term is unbalanced, making the

[20]Note that this is in line with the explanation of the basic instability mechanisms discussed in Section 2.1, where only excursions of the guiding centers is considered and the details of the gyration have been completely left out.

[21]Formally such a change of variables should be performed through perturbative Lie transforms, since the new coordinates are not canonical and therefore do not conserve the original phase-space properties such as symmetries and conserved quantities [109]. This transformation method involves an asymptotic expansion of the new coordinates in the small order parameter δ, where the lowest order terms simply correspond to the unperturbed particle trajectories in absence of the turbulent fluctuations, and the higher order terms ensure that the magnetic moment is an adiabatic invariant to all orders in δ [110]. These additional terms would result in $\mathcal{O}(\delta^2)$ corrections to the gyrokinetic equation, since the perturbations in the distribution function and fields themselves are already $\mathcal{O}(\delta)$. As the goal of this thesis is linear stability analysis, such corrections can be neglected and a simple substitution of variables will suffice, although the additional corrections are important for non-linear simulations which determine the turbulent transport fluxes [6].

distribution function to leading order isotropic. In Appendix C.2 this leading order distribution function is shown to be the Maxwellian distribution

$$F_{Ms} = n_{0s}(\psi)\left(\frac{m_s}{2\pi T_{0s}(\psi,t)}\right)^{3/2}\exp\left(-\frac{m_s v_s^2}{2T_{0s}(\psi,t)}\right) \tag{23}$$

with equilibrium density and temperature profile depending only on ψ as a result that the plasma isobars are flux surfaces. The equilibrium temperature has a weak time dependence to allow for temperature equilibration between electrons and ions as in general $T_{0e} \neq T_{0i}$, and a slow energy exchange due to collisions will take place to make the plasma isothermal [90] (a concrete example of this appears in Appendix G.3.2). This process is however slow and within the gyrokinetic ordering occurs on a timescale $\tau_{eq} \sim \mathcal{O}(1/\delta^2\omega)$ [111], such that the equilibrium contribution can be considered as "frozen" in the gyrokinetic framework.

To next order, the influence of the potential fluctuations ϕ on the distribution function is then obtained by splitting the distribution in an equilibrium and perturbed part $f_s = F_{Ms} + \delta f_s$. In Appendix C.3 it is shown that that this perturbed distribution can be split as

$$\delta f_s = -\frac{q_s\phi}{T_{0s}}F_{Ms} + g_s \tag{24}$$

where the first part is the so-called adiabatic response which arises due to the tendency of particles to re-establish equilibrium by quickly redistributing along the field line in an attempt to cancel the perturbed electric field [67], and the second part is the gyrophase independent kinetic response which obeys the gyrokinetic equation

$$\frac{\partial g_s}{\partial t} + \left\langle \frac{\boldsymbol{E}\times\boldsymbol{B}}{B^2}\right\rangle_{\boldsymbol{R}}\cdot\boldsymbol{\nabla}_{\boldsymbol{R}}F_{Ms} + \left\langle \dot{\boldsymbol{R}}\right\rangle_{\boldsymbol{R}}\cdot\boldsymbol{\nabla}_{\boldsymbol{R}}g_s + q_s\left\langle \left.\frac{\partial\phi}{\partial t}\right|_{\boldsymbol{x}}\right\rangle_{\boldsymbol{R}}\frac{\partial F_{Ms}}{\partial E} = \left\langle C_s^L(g_s)\right\rangle_{\boldsymbol{R}}. \tag{25}$$

In Equation (25) the gyroaverage operator

$$\langle\cdots\rangle_{\boldsymbol{R}} \equiv \frac{1}{2\pi}\oint\cdots \mathrm{d}\vartheta \tag{26}$$

has been introduced which averages any quantity over the fast gyromotion of the particles while keeping their guiding centers fixed, thus effectively filtering out any remaining details of the fast gyration such that the kinetic description has been completely reduced from a $6D$ to a $5D$ phase-space. Conceptually, this reduction in the dimensionality of phase-space effectively means that the helical orbit of charged particles is reduced to the motion of a charged ring with radius ρ_s moving along the gyrocenter[22], which is the average position of the particle during a gyration, see Figure 9. Also introduced in Equation (25) is the linearised collision operator[23]

$$C_s^L(g_s) = C_s(g_s, F_{Ms}) + C_s(F_{Ms}, g_s)$$

where the first term describes particles from the perturbed distribution colliding with the background "sea" of equilibrium particles, and vice versa for the second term, which are respectively referred to as the "test" and "field" part of the collision operator in literature [88].

[22] Although sometimes used interchangeably with guiding center, it is a matter of terminology. Formally the guiding center $\boldsymbol{R}$ and the gyrocenter $\langle\boldsymbol{R}\rangle_{\boldsymbol{R}} = \langle\boldsymbol{x}\rangle_{\boldsymbol{R}}$ are formally different quantities, as $\boldsymbol{R}$ rapidly changes it direction in the perpendicular plane as the particle gyrates, while $\langle\boldsymbol{R}\rangle_{\boldsymbol{R}}$ is only affected by the slow cross field drifts.

[23] The non-linear part of the collision operator, taking into account collisions between particles from the perturbed distribution function are hardly ever accounted for in literature, even non-linearly. The $\boldsymbol{E}\times\boldsymbol{B}$ non-linearity which facilitates interaction between the different modes is the main non-linear feature which determines the heat fluxes, and a linear collisional operator still captures the essential physics of particle, momentum and energy conservation while providing sufficient to ensure the dissipation required to for the fluxes to reach a statistically steady state [86, 89].

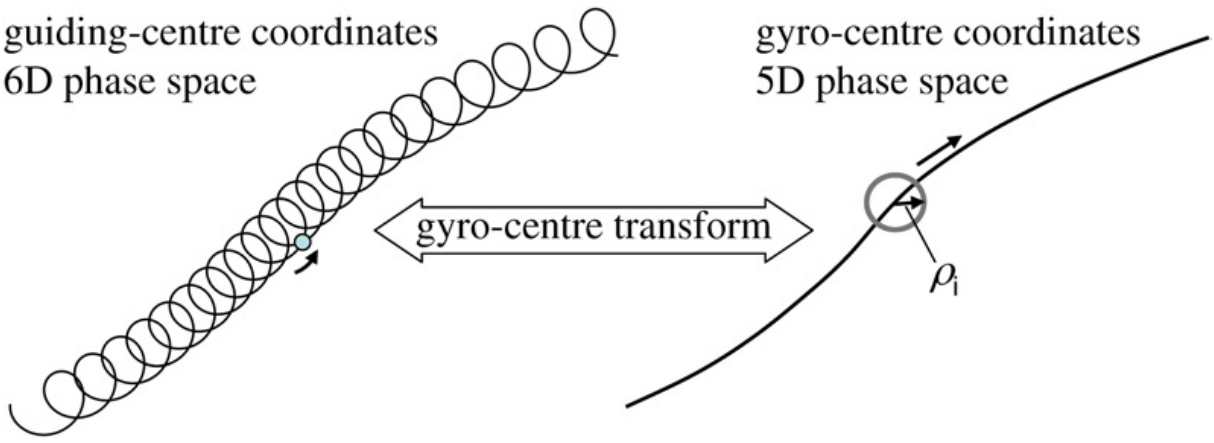

Figure 9: As a result of the gyroaveraging operator Equation (26) *and the coordinate transformation of phase-space Equation* (21) *and the timescale separation* $\omega, \Omega_s \sim \delta$ *the details of the fast gyration is completely removed from the plasma dynamics, which reduces the helical particle particles orbits to the motion of a charged ring along the gyrocenter particle's helical trajectory into the motion of a charged ring along the guiding center. Adapted from [7].*

All that remains is to evaluate the gyroaverages. In Appendix D it is shown that the gyrocenter drift is given by

$$\left\langle \dot{\boldsymbol{R}} \right\rangle_{\boldsymbol{R}} = v_{\parallel} \boldsymbol{e_b} + \underbrace{\frac{\boldsymbol{e_b} \times \langle \boldsymbol{\nabla} \phi \rangle_{\boldsymbol{R}}}{B}}_{= \langle \boldsymbol{v_e} \rangle_{\boldsymbol{R}}} + \underbrace{\frac{\boldsymbol{e_b}}{\Omega_s} \times \left(v_{\parallel}^2 \boldsymbol{\kappa} + \frac{v_{\perp}^2}{2} \boldsymbol{\nabla} \ln B \right)}_{= \boldsymbol{v_{ds}}} \tag{27}$$

where the first term is simply the unaffected parallel motion along the field line, the second term is the gyroaveraged $\boldsymbol{E} \times \boldsymbol{B}$ velocity $\boldsymbol{v_E}$ and the last term is the magnetic drift velocity $\boldsymbol{v_{ds}}$ which consists of a gradient driven part and a curvature driven part where $\boldsymbol{\kappa} = (\boldsymbol{e_b} \cdot \boldsymbol{\nabla}) \boldsymbol{e_b}$ is the magnetic curvature vector. Thus indeed as claimed, the guiding center mainly consists of the motion along the field line superimposed by slow cross field drifts which are $\mathcal{O}(\delta)$ smaller.

To evaluate the remaining gyroaverages of the electrostatic potential fluctuations, the $k_{\parallel}/k_{\perp} \ll 1$ spatial scale anisotropy of the perturbations w.r.t. the magnetic field Equation (19) can be used to separate the slow variation along the field line from the fast variation perpendicular to the field by means of a WKB approximation [112]

$$\phi(\boldsymbol{x}, t) = \hat{\phi}(\boldsymbol{x}) \exp\left(i \left\{ \frac{S(\boldsymbol{x})}{\delta} - \omega t \right\} \right) \tag{28}$$

where both $\hat{\phi}(\boldsymbol{x})$ and $S(\boldsymbol{x})$ vary on the large equilibrium scale and ϕ has also been Fourier transformed in time. In Equation (28) the fast variation across the field is contained in the exponential factor as a result of the $\rho/L_n \sim \delta$ scaling. The gyroaveraging procedure of all terms involving the potential perturbation in Equation (25) is then fairly straightforward, but still quite tedious. This step of the derivation is therefore deferred to Appendix C.4 and here only the important physical consequences are highlighted below. This procedure then reduces Equation (26) to

$$\frac{\partial g_s}{\partial t} + \left(v_{\parallel} \boldsymbol{e_b} + \boldsymbol{v_E} + \boldsymbol{v_{ds}} \right) \cdot \boldsymbol{\nabla}_{\boldsymbol{R}} g_s - \left\langle C_s^L(g_s) \right\rangle_{\boldsymbol{R}} = -i \frac{q_s}{T_s} J_0(k_{\perp} \rho_s) \hat{\phi} \left(\omega - \omega_{\star s}^T \right) F_{Ms} \tag{29}$$

where all terms involving g_s have been collected on the left-hand side and the gyrocenter drift Equation (26) has been explicitly substituted. In Equation (29) a perpendicular wavevector is introduced according to $\boldsymbol{k}_{\perp} \approx \boldsymbol{\nabla} S(\boldsymbol{x})/\delta$ which allows to interpret the WKB approximation as if

Equation (28) were a single Fourier mode in a spatial Fourier series of the electrostatic potential. The wavenumber $k_\perp$ appearing in the zeroth order Bessel function J_0 is then simply defined as its magnitude $k_\perp = \|\boldsymbol{k}_\perp\|$. This Bessel function reflects the effect that as the particle undergoes its fast gyration it will sample different phases of the perturbation which is practically "frozen" in time. If the potential varies over distances much longer than the gyroradius ($k_\perp \rho \ll 1$) then the effective electric field $\langle \boldsymbol{E} \rangle_{\boldsymbol{R}}$ the charged ring in Figure 9 experiences, will be roughly just its local value at the centre $\boldsymbol{E}(\boldsymbol{R})$ (recall that in the electrostatic approximation $\boldsymbol{E} = -\boldsymbol{\nabla}\phi$). If, however, the potential varies on distances much shorter than the gyroradius ($k_\perp \rho_s \gg 1$) than this phase mixing between positive and negative electric field regions makes that the effective electric field that acts on the charged ring will be roughly zero. Also introduced in Equation (26) is the temperature-dependent diamagnetic frequency $\omega_{\star T}$ which is defined by

$$\begin{aligned} \omega_{\star s}^T =& \omega_{\star s}\left(1 + \eta_s\left[\frac{E}{T_s} - \frac{3}{2}\right]\right) \\ \omega_{\star s} =& \frac{T_s}{q_s}\frac{(\boldsymbol{k}_\perp \times \boldsymbol{e_b})\cdot\boldsymbol{\nabla}\psi}{B}\frac{\mathrm{d}\ln n_s}{\mathrm{d}\psi}. \\ \eta_s =& \frac{\mathrm{d}\ln T_s}{\mathrm{d}\psi}\Big/\frac{\mathrm{d}\ln n_s}{\mathrm{d}\psi} \end{aligned} \tag{30}$$

where $\omega_{\star s}$ is the frequency of the fundamental drift wave due to density gradient in a slab geometry showcased in Section 2.1.1 (as proven in Appendix E), $\omega_{\star s}^T$ is its straightforward extension to the case of a temperature gradient, and η_s is the ratio between density and temperature gradient scale lengths which are defined by[24] $L_n = \|-\boldsymbol{\nabla} n\|^{-1}$, $L_T = \|-\boldsymbol{\nabla} T\|^{-1}$, such that $\eta_s = L_{n_s}/L_{T_s}$ measures the competition between density- and temperature gradient drive of the instabilities.

In principle the kinetic response g_s will have the same spatial scale anisotropy as ϕ, as it is also a perturbation, so a similar WKB approximation can be made for the spatial part of g_s

$$g_s(\boldsymbol{R}, E, \mu, t) = \hat{g}_s(\boldsymbol{R}, E, \mu)\exp\left(i\left\{\frac{S(\boldsymbol{R})}{\delta} - \omega t\right\}\right). \tag{31}$$

The remaining derivatives on the right-hand side of Equation (29) can then be evaluated with the same methods from Appendix C.4. One point of attention, however, is that the right-hand side of Equation (29) contains the convective $\boldsymbol{v_E}\cdot\boldsymbol{\nabla}_R g_s$ non-linearity, since both ϕ, g_s are perturbations. This results in results in the crossing of the generally different phase factors between g_s, ϕ and creates either rapidly oscillating or near-constant terms. Because of the analogy with the WKB approximation and a Fourier series made above, this is a manifestation of the multiplication-convolution property of Fourier transforms. As the goal of this thesis is linear stability analysis to study how collisions affect the onset instability, the amplitudes of the perturbations are small during the time period of interest and the convective non-linearity will thus typically be $\mathcal{O}(\delta)$ smaller compared with the other terms in Equation (29) and can thus be neglected.

With the gyrokinetic equation subsequently linearised, if the WKB expansion for the perturbations is substituted in Equation (29) all terms except for the collision operator would have the same rapidly varying phase factor. Were it not for the collision operator, this phase factor could then be cancelled on both sides of the equation to yield an algebraic equation for the amplitude coefficients $\hat{\phi}, \hat{g}_s$ only, as shown below

$$\begin{aligned} v_\parallel \boldsymbol{\nabla}_\parallel \hat{g}_s - i(\omega - \omega_{ds})\hat{g}_s =& -i\frac{q_s}{T_s}J_0\hat{\phi}\left(\omega - \omega_{\star s}^T\right)F_{Ms} \\ &+ \exp\left(-i\left\{\frac{S(\boldsymbol{R})}{\delta} - \omega t\right\}\right)\left\langle C_s\left[\hat{g}_s\exp\left(i\left\{\frac{S(\boldsymbol{R})}{\delta} - \omega t\right\}\right)\right]\right\rangle_{\boldsymbol{R}} \end{aligned} \tag{32}$$

[24] The minus sign accounts for the peakedness of the profiles in the plasma core such that the gradients are typically negative.

where for illustrative purposes the collision operator has been transferred to the right-hand side and given its private line. In Equation (32) the parallel derivative $\boldsymbol{\nabla}_\parallel = \boldsymbol{e_b} \cdot \boldsymbol{\nabla}_{\boldsymbol{R}}$ which acts only on the $\hat{g}_s$ and not on the phase factor by means of $\boldsymbol{k}_\perp \approx \boldsymbol{\nabla} S/\delta$, and the magnetic drift frequency $\omega_{ds} = \boldsymbol{k}_\perp \cdot \boldsymbol{v_{ds}}$ which gives the rate at which the particle orbits precess through the torus, have been introduced. The complicated term involving the collision operator arises because $\langle C_s \rangle_{\boldsymbol{R}}$ has not (yet) been WKB expanded like the other terms. If the collision operator could be written as $\langle C_s \rangle_{\boldsymbol{R}} = \hat{C}_s \exp(i\{S(\boldsymbol{R})/\delta - \omega t\})$, then the phase factor would be cancelled an a purely algebraic equation in $\hat{\phi}, \hat{g}_s, \hat{C}_s$ remains. Because of the operator property of C_s and the fact that it has been linearised in g_s, such a WKB expansion does not have to be carried out explicitly but follows from the WKB expansion of g_s. Some care in this expansion has to be taken however, as the kinetic response g_s is defined at the guiding center position $\boldsymbol{R}$, and so is the gyroaveraging operator, but the collision operator involves derivatives of the distribution at fixed particle position $\boldsymbol{x}$. This nuance can be taken care of by expressing the phase factor iS/δ both in $\boldsymbol{x}$ and $\boldsymbol{R} = \boldsymbol{x} - \boldsymbol{\rho_s}$ by expanding about the gyroradius [86]

$$\begin{aligned} &\left\langle C_s \left[\hat{g}_s \exp\left(i \left\{ \frac{S(\boldsymbol{R})}{\delta} - \omega t \right\} \right) \right] \right\rangle_{\boldsymbol{R}} \approx \left\langle \exp\left(i \left\{ \frac{S(\boldsymbol{x})}{\delta} - \omega t \right\} \right) C_s \left[\hat{g}_s \exp(-i \boldsymbol{k}_\perp \cdot \boldsymbol{\rho_s}) \right] \right\rangle_{\boldsymbol{R}} \\ &\approx \exp\left(i \left\{ \frac{S(\boldsymbol{R})}{\delta} - \omega t \right\} \right) \langle \exp(+i \boldsymbol{k}_\perp \cdot \boldsymbol{\rho_s}) C_s \left[\hat{g}_s \exp(-i \boldsymbol{k}_\perp \cdot \boldsymbol{\rho_s}) \right] \rangle_{\boldsymbol{R}} \end{aligned} \tag{33}$$

where the $\exp(-i\omega t)$ factor can be taken out of the collision operator and the gyroaveraging operator by realising that the binary collisions between particles have to occur simultaneously as particles scatter on the instantaneous and not future/past Coulomb fields, and that the oscillation frequency is fixed a property of the perturbations and therefore gyrophase independent. The gyroaverage itself still has to be evaluated and depends on the detail of the collision operator [91, 107]. Finally then, the phase factor of Equation (33) will cancel against its conjugate in front of the gyroaveraged collision operator in Equation (32), which yields the linearised gyrokinetic equation (GKE)

$$v_\parallel \boldsymbol{\nabla}_\parallel \hat{g}_s - i(\omega - \omega_{ds}) \hat{g}_s - \langle \exp(i \boldsymbol{k}_\perp \cdot \boldsymbol{\rho_s}) C_s \left[\hat{g}_s \exp(-i \boldsymbol{k}_\perp \cdot \boldsymbol{\rho_s}) \right] \rangle_{\boldsymbol{R}} = -i \frac{q_s}{T_s} J_0 \hat{\phi} \left(\omega - \omega^T_{\star s} \right) F_{Ms} \tag{34}$$

which describes the dynamics of the plasma under influence of small-amplitude low-frequency perturbations with elongated structures along the field line and short perpendicular structures comparable to the gyroradius perpendicular to the magnetic field.

2.4 Quasi-neutrality condition

In order to solve the linearised gyrokinetic equation Equation (34) for the kinetic response g_s the electrostatic potential ϕ has to be known. The electrostatic potential is however determined by the charge densities in the plasma which are defined as the first velocity moment of the distribution functions. Consequently for any physically correct description of microturbulence, the gyrokinetic equation will have to be solved in tandem with Poisson's equation[25]

$$\nabla^2 \phi = - \frac{\sum_s q_s n_s}{\epsilon_0} \tag{35}$$

where the sum is over all plasma species and plasma dielectric effects are neglected. In order for the plasma to be in equilibrium a macroscopic electric field is not allowed as this would pull the ions and electrons apart. This leads to the concept of quasi-neutrality, which expresses the

[25] In the specific case of the electrostatic limit considered in this thesis, it is sufficient to solve Poisson's equation. In the more general case when perturbations to the magnetic field are also taken into account, one must also solve Ampère's equation as the perturbations in the plasma current will self-consistently determine the magnetic field perturbations [109].

tendency of a plasma to distribute its ions and electrons in a way such that over an intermediate scale the effective charge density vanishes and there is no equilibrium electric field $\boldsymbol{E_0}$. This requires the electron density to be approximately equal to the total density of all ion species, weighted by their charge state, i.e. $n_{0e} \approx \sum_{s'} Z_{s'} n_{0s'}$ where $Z_{s'} = q_{s'}/e$ is the charge number of the ions and the sum is only over ion species. This intermediate scale beyond which electric fields will be shielded is the Debye length [113]

$$\lambda_D = \sqrt{\frac{\epsilon_0 T_{0e}}{n_{0e} e^2 \left(1 + \sum_{s'} Z_{s'}^2 T_{s'0}/T_{e0}\right)}}$$

which under the typical fusion conditions $T_i \approx T_e$ of a simple hydrogen plasma is up to a numerical factor of unity determined by its electron part $\lambda_{De} = \sqrt{\epsilon_0 T_{0e}/n_{0e}e^2}$ [3].

If a density perturbation now occurs in the plasma this can create a non-vanishing electric field which is determined by Poisson's equation Equation (35) by letting $n_s \to n_{0s} + \delta n_s$

$$\nabla^2 \phi = \frac{e\left(\delta n_e - \sum_{s'} Z_{s'} \delta n_{s'}\right)}{\epsilon_0}$$

where ϕ contains only the perturbed part and the equilibrium contribution cancels due to quasi-neutrality. By introducing the dimensionless potential $\Phi = e\phi/T_{e0}$ this can be rewritten in terms of the Debye length as[26]

$$\frac{n_{0e}e^2}{\epsilon_0 T_{e0}} \nabla^2 \Phi = \lambda_{De}^2 \nabla^2 \Phi = \frac{\delta n_e - \sum_{s'} Z_{s'} \delta n_{s'}}{n_{0e}} \tag{36}$$

An order of magnitude estimate of the middle term of Equation (36) gives $\lambda_{De}^2 \nabla^2 \Phi \sim \delta \times (\lambda_{De} k_\perp)^2 \sim \delta \times (\lambda_{De}/\rho_s)^2$ which follows from using the WKB form of the potential Equation (28), considering $\boldsymbol{k}_\perp$ as a constant property of the instability and the scalings Equation (19) together with the microturbulence property $k_\perp \rho_s \sim \mathcal{O}(1)$. Consequently unless $\lambda_{De}/\rho_s \sim \delta^{-1/2} \gg 1$ the perturbations cannot cause significant deviations from quasi-neutrality as both density perturbations on the right-hand side of Equation (36) are of $\mathcal{O}(\delta)$ according to the scaling Equation (19). Under the typical reactor conditions of Figure 1a the ratio between Debye length and gyroradius is $\mathcal{O}(1)$ for electrons and $\mathcal{O}(0.01)$ for ions, such that the density perturbations obtained from solving the gyrokinetic equation must satisfy $\sum_s q_s \delta n_s \approx 0$ where the sum is again over all species.

The density perturbations can be expressed in terms of the distribution function as

$$\delta n_s = \int f_s \mathrm{d}^3\boldsymbol{v} - \int F_{Ms} \mathrm{d}^3\boldsymbol{v} = \int \delta f_s \mathrm{d}^3\boldsymbol{v}$$

where the perturbed distribution function is given by Equation (24). The density perturbation due to the adiabatic response is straightforward to calculate, since all velocity dependence is in the isotropic Maxwellian F_{Ms} such that

$$\delta n_{s,ad} = \int -\frac{q_s \phi}{T_s} F_{Ms} \mathrm{d}^3\boldsymbol{v} = -\frac{q_s \phi}{T_s} n_{0s}.$$

The density perturbation due to the kinetic response involves another subtlety. By the choice of new phase-space coordinates g_s is formally a function of guiding center position $\boldsymbol{R}$ such that a velocity integration would give a perturbed guiding center density $\delta n(\boldsymbol{R})$. The electrostatic potential in contrast "lives" in real space and it is the local charge densities in real space

[26] Formally speaking $\nabla^2 \Phi \neq \frac{e}{T_{e0}} \nabla^2 \phi$ as the equilibrium electron temperature is not constant. However this electron temperature varies over the macroscopic length L_{Te} whereas the perturbed potential will vary over the gyroradius such that the changes in ϕ will be the dominant contribution to the Laplacian.

which determine the perturbed electric fields, so a particle density $\delta n(\boldsymbol{x})$ is required for the quasi-neutrality condition [67, 111]. Just as with the collision operator, this is remedied by[27] expanding the rapidly varying phase factor of the WKB decomposition Equation (31) between $\boldsymbol{x}, \boldsymbol{R}$

$$\begin{aligned}\delta n_{s,kin} &= \int \hat{g}_s(\boldsymbol{R}+\boldsymbol{\rho_s}, E, \mu) \exp\left(i\frac{S(\boldsymbol{R}+\boldsymbol{\rho_s})}{\delta} - i\omega t\right) \mathrm{d}^3\boldsymbol{v} \\ &\approx \exp\left(i\frac{S(\boldsymbol{x})}{\delta} - i\omega t\right) \int \hat{g}_s(\boldsymbol{R}, E, \mu) \exp(-\boldsymbol{k}_\perp \cdot \boldsymbol{\rho_s}) v_\perp \,\mathrm{d}v_\perp \,\mathrm{d}v_\parallel \,\mathrm{d}\vartheta \\ &= \exp\left(i\frac{S(\boldsymbol{x})}{\delta} - i\omega t\right) \int \hat{g}_s(\boldsymbol{R}, E, \mu) J_0\left(\frac{k_\perp v_\perp}{\Omega_s}\right) 2\pi v_\perp \,\mathrm{d}v_\perp \,\mathrm{d}v_\parallel\end{aligned}$$

where the definition of the Bessel function Equation (C.5) and cylindrical velocity coordinates $\mathrm{d}^3\boldsymbol{v} \to v_\perp \,\mathrm{d}\vartheta \,\mathrm{d}v_\perp \,\mathrm{d}v_\parallel$ have been used, and the velocity dependence of the gyroradius is made explicit for the remaining integrals. Compiling these results then gives the quasi-neutrality condition for the perturbed densities

$$\sum_s n_{s0}\frac{q_s^2}{T_s}\hat{\phi}(\boldsymbol{x}) = \sum_s q_s \int \hat{g}_s(\boldsymbol{R}, E, \mu) J_0\left(\frac{k_\perp v_\perp}{\Omega_s}\right) \mathrm{d}^3\boldsymbol{v} \tag{37}$$

where the WKB decomposition for the potential Equation (28) has been used to cancel the fast varying phase factor again, and the 2π factor resulting from integrating the rapid phase factor over ϑ has been reabsorbed into the velocity differential $\mathrm{d}^3\boldsymbol{v}$ and the implied integration boundaries.

2.5 Simplified BGK collision operator model

The inclusion of a Fokker-Planck collision operator Equation (11) makes finding solutions to the kinetic equation Equation (10) nearly impossible. Even when neglecting collisions, the right-hand side is a non-linear partial differential equation since the sources of the electromagnetic fields are determined by moments of the distribution function. Meanwhile the collision operator itself involves both derivatives and integrals of the distribution function through the Rosenbluth potentials, making the collision operator an integrodifferential equation for the distribution function [114]. This is highly intractable for doing any analytical theory. The problem is made even worse in the gyrokinetic framework, as the gyroaverage of the collision operator operator in Equation (34) introduces additional spatial diffusion terms of the gyrocenters proportional to $(k_\perp\rho_s)^2$ wich is referred to as a Finite Larmor Radius (FLR) effect [7,86]. Therefore a simplified collision operator is needed to make any analytical work feasible. Fortunately in the limit of low β plasmas, the resulting physics is rather insensitive to the model of the collision operator that is used, provided that the model is physically reasonable [115].

The main role of collisions is to make particles aware that they do not exist in a vacuum but are embedded in a medium consisting of a background "sea" of many other particles. By exchanging small amounts of momentum and energy in a conservative way, a particle is slowly integrated into this collective of other particles eventually leading to equilibration of the distribution function which becomes stationary. A simplified collision model that describes this equilibration process is the Bhatnagar-Gross-Krook (BGK) operator [116]

$$C_{BGK} = -\frac{1}{\tau_{rel}}\left(f - M[f]\right) \tag{38}$$

[27] At least up to linear accuracy it is, non-linearly there will be $\mathcal{O}(\delta^2)$ corrections due to the expansion of new coordinates which give rise to a polarisation charge density and magnetisation current in case of magnetic fluctuations [109].

where τ_{rel} is the characteristic time scale for relaxation towards the equivalent Maxwellian[28]

$$M[f] = n[f]\left(\frac{m}{2\pi T[f]}\right)^{3/2}\exp\left(-\frac{m}{2T[f]}\left(\boldsymbol{v}-\boldsymbol{q}[f]\right)^2\right) \tag{39}$$

where the density, mean flow velocity[29] and temperature functionals are defined as moments of the distribution function f

$$\begin{aligned} n[f] &= \int f(\boldsymbol{x},\boldsymbol{v},t)\mathrm{d}^3\boldsymbol{v} = n(\boldsymbol{x},t) \\ \boldsymbol{q}[f] &= \int \boldsymbol{v} f(\boldsymbol{x},\boldsymbol{v},t)\mathrm{d}^3\boldsymbol{v}/n[f] = \boldsymbol{q}(\boldsymbol{x},t) \\ \frac{3}{2}T[f] &= \int \frac{m}{2}\left(\boldsymbol{v}-\boldsymbol{q}[f]\right)^2 f(\boldsymbol{x},\boldsymbol{v},t)\mathrm{d}^3\boldsymbol{v}/n[f] = \frac{3}{2}T(\boldsymbol{x},t) \end{aligned} \quad . \tag{40}$$

In this way, the BGK operator captures the essential physics of particle, momentum and energy conservation and describes the relaxation towards a steady Maxwellian distribution just like any other collision operator would [104]. In Appendix F it is shown that in absence of gradients and electromagnetic fields the BGK collision operator Equation (38) causes any arbitrary initial distribution function to exponentially relax towards the Maxwellian $M[f]$ with a rate given by $1/\tau_{rel}$, which expresses the thermodynamic irreversibility of collisions [117]. There are however two drawbacks to the BGK collision operator. Firstly it is an empirical model where the relaxation time τ_{rel} is a constant free model parameter, whereas any rigorous derivation of collision rates result in velocity dependent relaxation rates such as those in Equation (16). If a velocity dependent relaxation rate would be used instead, then the BGK operator no longer conserves particles, momentum and energy. A comparative study by Livi & Marsch between the BGK operator and the full Fokker-Planck operator has, however, shown that when using the physical collision rates of Equation (16) the density, momentum and temperature are only non-conserved on a 1% level, making this issue not very severe [118]. Secondly, because the BGK model is less sensitive to the shape of the distribution than the Fokker-Planck collision operator, this will results in erroneous velocity moments of the distribution function higher than the temperature, starting with the heat flux [104, 119]. This means that the BGK operator cannot be used for transport studies. The same study by Livi & Marsch has also shown that the errors in higher order moments are smaller using velocity dependent relaxation compared to constant relaxation rate [118]. As it is not the aim of the thesis to determine transport coefficients, the BGK model can be thus used as a proxy for the exact collision operator for the purpose of analytical linear stability analysis, using velocity dependent relaxation rates as done in the literature [84, 85, 120–122].

2.5.1 Linearisation of the BGK model

The BGK model is, in principle, valid for any distribution function f_s that is arbitrarily far from equilibrium. For the case of interest it will be applied to a distribution function that is nearly an isotropic Maxwellian Equation (23) superimposed by small fluctuations given by Equation (24), so the functionals for density, mean velocity and temperature that determine the equivalent Maxwellian can be calculated as[30]

[28] In the form of Equation (38) the effect of scattering is described by particles being "absorbed" from the distribution function f and then being "re-emitted" at a Maxwellian distribution with the same properties as f, such that scattering will establish a local thermodynamic equilibrium situation.

[29] This represents the velocity with which each plasma species as a collective would move if it were described a as a fluid rather than statistically by their distribution function. Typically the symbol $\boldsymbol{u}$ is used for this, but to prevent confusion with Appendices B and H where $\boldsymbol{u}$ denotes the relative velocity for a collision pair the symbol $\boldsymbol{q}$ is used here instead to honour the notation of the original BGK article [116].

[30] In these equations g_s is still a guiding center distribution expressed in $\boldsymbol{R}$ which for the evaluation of the integrals have to be formally transformed to $\boldsymbol{x}$, just as was done in Section 2.4.

$$
\begin{aligned}
n[f] =& n_{0s}\left(1-\frac{q_s\phi}{T_{0s}}\right)+\int g_s(\boldsymbol{v})\mathrm{d}^3\boldsymbol{v}\\
\boldsymbol{q}[f] =& \frac{\int \boldsymbol{v} g_s \mathrm{d}^3\boldsymbol{v}}{n[f]}\\
\frac{3}{2}T[f] =& \frac{\frac{3}{2}T_{0s}\left(1-\frac{q_s\phi}{T_{0s}}\right)n_{0s}+\frac{m}{2}\int v^2 g_s \mathrm{d}^3\boldsymbol{v}}{n[f]}-\frac{m}{2}\boldsymbol{q}[f]\cdot\boldsymbol{q}[f]
\end{aligned}
$$

where $(\boldsymbol{v}-\boldsymbol{q})^2$ has been expanded in the temperature functional and the velocity moments of the Maxwellian $\int F_{Ms}\mathrm{d}^3\boldsymbol{v}=n_{0s}$, $\int \boldsymbol{v}F_{Ms}\mathrm{d}^3\boldsymbol{v}=\boldsymbol{0}$, $\int v^2F_{Ms}(v)\mathrm{d}^3\boldsymbol{v}=3n_{0s}T_{0s}/m_s$ have been used. For small perturbations of the distribution $\delta f/F_{Ms}\sim\delta$ it is expected that the moments of the distribution will are also only slightly perturbed. Indeed, the density can be written as $n[f]=n_{0s}(1-\delta n[f]/n_{0s})$ where $\delta n/n_{0s}\sim\delta$, which invites a similar expression for the temperature $T[f]=T_{0s}\left(1+\delta T[f]/T_{0s}\right)$ where $\delta T/T_{0s}\sim\delta$. The same cannot be done for $\boldsymbol{q}[f]$ as there is no equilibrium flow. However, for the distribution to be only slightly perturbed from Maxwellian, the mean flow should be small compared to the RMS velocity such that $\boldsymbol{q}[f]/v_{RMS}\sim\delta$ as otherwise the perturbed distribution will be a strongly shifted Maxwellian which no longer satisfies $\delta f/F_{Ms}\sim\delta$. Consequently the temperature and flow velocity functionals can be appropriately linearised by expanding $1/n[f]$ as a harmonic series, and neglecting all $\mathcal{O}(\delta^2)$ contributions. This procedure leads to

$$
\begin{aligned}
\frac{\delta n[f]}{n_{0s}} =& -\frac{q_s\phi}{T_{0s}}+\frac{\int g_s\mathrm{d}^3\boldsymbol{v}}{n_{0s}}=-\frac{q_s\phi}{T_{0s}}+\frac{\int g_s\mathrm{d}^3\boldsymbol{v}}{\int F_{Ms}\mathrm{d}^3\boldsymbol{v}}\\
\frac{\boldsymbol{q}[f]}{v_{RMS}} \approx& \frac{\int \boldsymbol{v}g_s\mathrm{d}^3\boldsymbol{v}}{n_{0s}\sqrt{\int v^2F_{Ms}\mathrm{d}^3\boldsymbol{v}/n_{0s}}}=\frac{\int \boldsymbol{v}g_s\mathrm{d}^3\boldsymbol{v}}{\sqrt{\int F_{Ms}\mathrm{d}^3\boldsymbol{v}\int F_{Ms}v^2\mathrm{d}^3\boldsymbol{v}}}\\
\frac{\delta T[f]}{T_{0s}} \approx& -\frac{q_s\phi}{T_{0s}}+\frac{m\int v^2g_s\mathrm{d}^3\boldsymbol{v}}{3n_{0s}T_{0s}}-\frac{\delta n_s[f]}{n_0}=\frac{\int \frac{mv^2}{2}g_s\mathrm{d}^3\boldsymbol{v}}{\int \frac{mv^2}{2}F_{Ms}\mathrm{d}^3\boldsymbol{v}}-\frac{\int g_s\mathrm{d}^3\boldsymbol{v}}{\int F_{Ms}\mathrm{d}^3\boldsymbol{v}}
\end{aligned}
$$

where in the second step the equilibrium parameters are rewritten as moments of the Maxwellian to be symmetric with the similar integral over g_s. Note that for the temperature perturbation $\delta T[f]$, two $\mathcal{O}(\delta)$ appear with opposite signs such that near cancellation occurs. In fact in the low β limit the temperature perturbation can be safely be taken as $\delta T/T_{0s}\to 0$ [115]. The only way to consistently make the perturbation in the temperature functional vanish is if all integrals involving the kinetic response vanish from the other functionals as well[31]. Consequently the linearised equivalent Maxwellian $M[f]$ becomes

$$
M[f]\approx n_{0s}\left(1-\frac{q_s\phi}{T_{0s}}\right)\left(\frac{m}{2\pi T_{0s}}\right)^{3/2}\exp\left(-\frac{mv^2}{2T_{0s}}\right)=F_{Ms}\left(1-\frac{q_s\phi}{T_{0s}}\right)
$$

that is the actual Maxwellian with a corrected density due to adiabatic response, which is exactly what one would expect for the local thermodynamic equilibrium that $M[f]$ represents. The linearised BGK model then trivially follows as

$$
C_{BGK}\approx\frac{1}{\tau_{rel}}g_s \tag{41}
$$

[31]To see why the kinetic response can be written as $g_s=\delta n_{kin}(\boldsymbol{x})G(\boldsymbol{v})$ in analogy with the Maxwellian $F_{Ms}=n_{0s}(\boldsymbol{x})F(\boldsymbol{v})$, where the densities satisfy the scaling $\delta n_{kin}/n_{0s}\sim\delta$ such that the velocity dependent parts must satisfy $G(\boldsymbol{v})/F(\boldsymbol{v})\sim\mathcal{O}(1)$ such that the perturbation in the distribution remains $g_s/F_{Ms}\sim\delta$. Then the vanishing of $\delta T/T_{0s}$ for arbitrary velocity dependent part of the kinetic response $G(\boldsymbol{v})$ is only possible if $\delta n_{kin}/n_{0s}\to 0$.

where g_s remains the gyrocenter distribution evaluated at $\boldsymbol{R}$, which matters momentarily when the gyroaverage of the complete BGK model is determined. In what follows rather than a relaxation time τ_{rel} a collision rate $\nu = 1/\tau_{rel}$ will be used such that the BGK model takes on a form thats similar to Equation (14) for the actual Fokker-Planck collision operator in terms of collision frequencies.

2.5.2 Extension to interspecies collisions and gyroaveraging

The BGK operator as high-lighted only models the role of a self-collisions for each species (electrons-electron, ions-ions) but in a plasma there will also interspecies collisions between the electrons and ions. As the collision operator is additive due to the binary nature of the collision operator, the BGK model can be straightforwardly extended to include interspecies collisions for each species s as [117, 123]

$$C_{s,BGK} = C_{ss,BGK} + C_{s\tilde{s},BGK} \quad (\tilde{s} \neq s) \tag{42}$$

where in general $C_{ss',BGK}$ is given by

$$C_{ss',BGK} = -\nu_{ss'} \left(f_s - M_{ss'}[f_s, f_{s'}] \right) \tag{43}$$

where $\nu_{ss'}$ is the collision rate and the equivalent Maxwellian has become

$$M_{ss'}[f_s, f_{s'}] = n_{ss'}[f_s, f_{s'}] \left(\frac{m_s}{2\pi T_{ss'}[f_s, f_{s'}]} \right)^{3/2} \exp\left(-\frac{m_s}{2T_{ss'}[f_s, f_{s'}]} \left(\boldsymbol{v_s} - \boldsymbol{q_{ss'}}[\boldsymbol{f_s}, \boldsymbol{f_{s'}}] \right) \right). \tag{44}$$

Self-collisions are then described by the case $s' = s$ for which the double species label becomes redundant and $C_{ss,BGK}$ is given by Equation (38) and the equivalent Maxwellian M_{ss} reduces to Equation (23). For the interspecies case $M_{ss'}$ no longer describes a local thermal equilibrium of the species s itself, but rather it describes a local thermodynamic equilibrium distribution of only the subset of particles that have scattered with the "alien" species s' [123]. Because these scattered particles have exchanged energy and momentum with the particles from this "alien" species s' their statistical properties (i.e. moments of their distribution function) will now also contain information about the distribution f'_s, and consequently the velocity moments of the scattered particles will be in some "hybrid" state between the moments of f_s and $f_{s'}$.

The main problem with the interspecies BGK operator is the determination of these "hybrid" velocity moments since the extended BGK model of Equation (42) is no longer conservative for each species to model the effect of momentum and energy exchanges between the two species, but of course the combined momentum and energy of the two species has to be conserved since the collisions are elastic. The determination of the "hybrid" velocity moments is rather tedious and therefore deferred to Appendix G.1. This process involves postulating[32] that the "hybrid" moments can be decomposed into a linear combination of the known velocity moments of both species and proceeding to fit the expansion parameters to conservation of total energy/momentum and a relaxation problem expressing the tendency of the exchanges to over time establish a common equilibrium between the two species [124]. This exercise leaves some of the expansion parameters undetermined, but is generally valid for any arbitrary exchange problem as only basic physical laws for elastic collisions have been enforced [117]. To determine the remaining parameters it has been suggested by one of the originl authors to fit the BGK model to the

[32]This postulate can be justified based on the expressions fact that momentum exchange is linear process in the particle velocities and energy exchange is a quadratic process in the particle velocities, which can be split into a deterministic part given by the kinetic energy carried by the mean flow velocity and a thermal part related to the random motion of individual particles [123]. By exchanging momentum/energy (interspecies collisions) and reshuffling energy between its thermal and deterministic components (self-collisions) all possible elastic collision processes are then accounted for.

actual application of interest [123]. This is done in Appendix G.2 where the resulting momentum and energy exchange between electrons and ions from the BGK model is first fitted to the net exchange of energy and momentum from Coulomb collisions [3]. Lastly in Appendix G.3 all velocity moments are then linearised with the goal of linear stability analysis in mind, and the remaining BGK model is then expanded around a temperature ratio $\tau = T_i/T_e = 1$ to reflect the typical fusion reactor conditions of Figure 1b.

After a substantial effort the linearised BGK model for interspecies collisions for electrons and ions is then found to be

$$C_{ei,BGK} = -\nu_{ei} g_e \quad C_{ie,BGK} = -\nu_{ie} g_i$$

where the collision frequencies ν_{ei}, ν_{ie} correspond to the free model parameters $\nu_{ss'}$, which is a complete mirror of Equation (41) for the self-collisions and reflects the intuitive belief that the interspecies collisions should add to the relaxation of the kinetic response as they tend to steer the system to a combined equilibrium. This then gives the full BGK operator as will be used in Chapter 3 to analytically account for collisions as

$$C_{s,BGK} \approx -\nu_{ss} g_s - \nu_{ss'} g_s = -\nu_{s,eff} g_s \equiv C_{s,BGK}[g_s]. \tag{45}$$

Rather what is needed in the linearised GKE Equation (34) is not Equation (45) but its gyroaverage, which is straightforward to obtain as the collision operator no longer contains any derivatives that should be evaluated at constant particle position. The kinetic response g_s should however still be expanded from gyrocenter to particle position according to the recipe of Equation (33) resulting in

$$\langle \exp(i\boldsymbol{k}_\perp \cdot \boldsymbol{\rho_s}) C_{s,BGK}[\hat{g}_s \exp(-i\boldsymbol{k}_\perp \cdot \boldsymbol{\rho_s})] \rangle_{\boldsymbol{R}} = \langle -\nu_{s,eff} \hat{g}_s \rangle_{\boldsymbol{R}} = -\nu_{s,eff} \hat{g}_s \tag{46}$$

since the kinetic response is by definition independent of the gyrophase, and the exponential phase factor has been omitted.

3 Extended theory

The background theoretical framework of Chapter 2 will be employed to give an analytical description of TEMs in the presence of non-negligible collisionality. The main goal of this chapter will be to find the growth rate of TEMs and assess what influence the collision frequency has on it. As all plasma perturbations are taking to have the form of a normal-mode ansatz $\delta A(\boldsymbol{x}, t) = \delta A(\boldsymbol{x}) \exp(-i\omega t)$, by imposing that the frequency can be complex $\omega = \omega_R + i\gamma$ it follows that the imaginary part of the frequency results in exponential growth of the perturbations, where γ is its growth rate, whereas the real part ω_R will give the regular oscillation frequency [125].

First as a preliminary, in Section 3.1 the relevant parameter regime for TEMs is introduced and applied to the GKE Equation (34) to obtain solutions for the kinetic responses of ions and electrons, and the relevant concepts of bounce average and pitch-angle velocity coordinates are introduced which allow to distinguish trapped- from passing particles. With these preliminaries cleared, the paradigm and rationale for analysing the TEM perturbatively is introduced in Section 3.2, which is subsequently carried out in the remainder of this chapter. First in Section 3.3 the lowest solution for the plasma perturbation to the quasi-neutrality condition is calculated retaining all kinetic ion effects, and in Section 3.4 the perturbative response of trapped electrons to these plasma perturbations is considered. This is first evaluated in Section 3.4.1 for the limits of extremely weak and strong collisionality that are commonly considered in literature to simplify the trapped electron response by only accounting for the dominant dynamics. Then in Section 3.4.2 the perturbative approach is extended to arbitrary collisionality regimes by taking into account the proper velocity dependence of the involved frequencies, and it is shown that the obtained growth rates from this new approach match the common literature results by taking the appropriate limits. This perturbative approach can only be carried out completely analytically up to requiring the details of the magnetic geometry determining the shape of the magnetic wells and the magnetic drift of the trapped particles. The influence of differences in the magnetic geometry is explored in Section 3.5 by numerically solving for the perturbative growth rate of TEMs using the realistic magnetic fields of the DIII-D tokamak and the HSX/W7-X stellarators also considered for the simulations in Chapter 4. It will be shown that scaling laws for the growth rate with collision frequency can be determined from this numerical integration. At high collisionality these scaling laws show a universal damping behaviour in all geometries. At low collisionality differences between the geometries do emerge, where the collisions are found to exert a destabilising influence at low wavenumbers in the stellarator geometries, but unaffect the growth rate at in the tokamak. The exponents from these scaling laws are in good agreement with the considerations from the new method of Section 3.4.2.

3.1 Characteristion of TEMs in the gyrokinetic framework

3.1.1 TEM parameter regime

The gyrokinetic equation Equation (34) can describe any electrostatic perturbation of the plasma. As the influence of collisionality on specifically TEMs is of interest, it is sensible to look for solutions of Equation (34) that are in the appropriate parameter regime for TEMs. First the majority of electrostatic instabilities have a frequency and parallel wavenumber that satisfy $v_{Ti} \ll \frac{\omega}{k_\parallel} \ll v_{Te}$ such that Landau damping with either ions or electrons is avoided [93, 126]. This condition is immediately relevant for trapping as the typical bounce time of a trapped particle is given by [122]

$$\tau_{b,s} = \oint \frac{\mathrm{d}l}{\left|v_\parallel\right|} \sim \frac{1}{v_{Ts}} \oint \mathrm{d}l \sim \frac{L_\parallel}{v_{Ts}}$$

where the integration is over the full trapped particle orbit between the two bounce points, and $L_\parallel = 1/\left\|\boldsymbol{\nabla}_\parallel \ln B\right\|$ is the characteristic length of variations along the magnetic field. For

passing particles the transit time $\tau_{t,s}$ is of importance, which has a similar definition but with the integration over the connection length between regions of opposite magnetic curvature[33]. As passing particles have considerably larger parallel velocities, the transit time is typically much shorter than the bounce time. For tokamaks $\tau_{t,s}/\tau_{t,b} \sim \sqrt{a/R}$ where a, R are the minor and major radius of the torus [75, 128]. According to the scaling Equation (19) microinstabilities with perpendicular wavelengths comparable to the gyroradius $k_\perp \rho_s \sim \mathcal{O}(1)$ will have parallel wavelengths comparable to the macroscopic length of the system $k_\parallel L_\parallel \sim \mathcal{O}(1)$ such that the frequency ordering leads to

$$k_\parallel v_{Ti} \sim \omega_{bi}^T \ll \omega_{ti}^T \ll \omega \ll \omega_{be}^T \ll \omega_{te}^T \sim k_\parallel v_{Te} \tag{47}$$

where the bounce- and transit time respectively of a typical thermal particle have been introduced through $\omega_{bs,ts} = 2\pi/\tau_{bs,ts}$.

As a result of the frequency ordering Equation (47) trapped ion effects will be negligible as during a full period of the perturbations the ions will hardly move along the field at all, which makes passing and trapped ions virtually indistinguishable. By contrast trapped electrons will bounce many times during a period of the perturbation, making the instabilities sensitive to the fraction of trapped electrons.

There will be an especially strong coupling between the perturbations and the trapped electrons if their spatial structure has significant overlap with the trapped electron orbit [121, 129], which then identifies the TEM. This coupling requirement means that TEM cannot occur on the electron gyroradius scales as the there would be too little overlap with the trapped electron orbits as a result of the orbit precession from the non-vanishing magnetic drifts (see Figure 4), which places the relevant length scales[34] at $k_\perp \rho_i \sim \mathcal{O}(1)$.

3.1.2 Approximate solution to the GKE

The frequency ordering Equation (47) along with $\boldsymbol{\nabla}_\parallel \sim k_\parallel$ and the scalings Equation (19) means that the GKE takes a different form for ions and electrons. For ions the $v_\parallel \boldsymbol{\nabla}_\parallel \hat{g}_i$ term will be small compared with the other terms of Equation (34) such that it can be neglected. By using the simplified BGK operator Equation (45) to take into account collisions in an analytically tractable way, the GKE becomes a simple algebraic equation which is easily solved for the kinetic ion response

$$\hat{g}_i \approx \frac{e}{T_i} \frac{\left(\omega - \omega_{\star i}^T\right) F_{Mi}}{\omega - \omega_{di} + i\nu_{i,tot}} J_0(k_\perp \rho_i) \hat{\phi} \tag{48}$$

where the ion collision frequencies have been compressed as $\nu_{tot,i} = \nu_{ii} + \nu_{ie}$.

Meanwhile for the electrons the same $v_\parallel \boldsymbol{\nabla}_\parallel \hat{g}_e$ term will be much larger than the other terms of Equation (34) such that the GKE is unbalanced. This can be resolved by expanding the electron kinetic response $\hat{g}_e \approx \hat{g}_{e,0} + \hat{g}_{e,1}$ with $\hat{g}_{e,1}/\hat{g}_{e,0} \ll 1$ such that to leading order $\boldsymbol{\nabla}_\parallel \hat{g}_{e,0} = 0$ and to next order

$$v_\parallel \boldsymbol{\nabla}_\parallel \hat{g}_{e,1} - i\left(\omega - \omega_{de}\right) \hat{g}_{e,0} + \nu_{e,tot} \hat{g}_{e,0} = \frac{ie}{T_e} \left(\omega - \omega_{\star e}^T\right) F_{Me} \hat{\phi} J_0(k_\perp \rho_e). \tag{49}$$

[33] Formally this is defined as the distance along the field line between regions of "good" and "bad" curvature [92,127], which will be explained in Section 4.2. For tokamaks this ise an integration over a single poloidal turn [69], but for stellarators this will be an integration over a single field period of the discrete toroidal symmetry [43], as after that the magnetic field strength $B(l)$ will repeat itself and so will the parallel velocity $v(l)$.

[34] In the specific case of a tokamak, the frequency ordering Equation (47) together with $\omega \sim \omega_{\star e}$ leads to the requirement that the poloidal wavenumber must satisfy $k_\theta \rho_e \ll \sqrt{\epsilon} \ll 1$ [130] and $k_\theta \rho_{bi} \gg 1$ [131] where $\rho_{bi} = q\rho_i/\sqrt{\epsilon}$ is the width of a banana orbit. Both scalings indicate that $k_\perp \rho_i \sim \mathcal{O}(1)$.

the GKE is balanced again, where the BGK operator has also been used for the electrons. The remaining parallel dynamics can be dealt with by taking the bounce average of Equation (49), which is defined by

$$\overline{\cdots} = \frac{\oint (\cdots) \frac{\mathrm{d}l}{|v_\parallel|}}{\oint \frac{\mathrm{d}l}{|v_\parallel|}} \tag{50}$$

and is a essentially a time average measured along the particle orbit as it follows the field line. For passing particles this means averaging over the transit time, and the averaging of the $v_\parallel \boldsymbol{\nabla}_\parallel$ term is straightforward as the velocity along the field line does not change direction such that

$$\oint v_\parallel \boldsymbol{\nabla}_\parallel \hat{g}^p_{e,1} \frac{\mathrm{d}l}{|v_\parallel|} = \sigma \oint \boldsymbol{\nabla}_\parallel \hat{g}^p_{e,1} = 0$$

where $\sigma = v_\parallel / |v_\parallel| = \pm 1$ has been introduced which is constant along the full trajectory. Because the passing particles all return to the same position with the same velocity after traversing the field line, their distribution $\hat{g}^p_{e,1}$ is identical at the end points of integration which makes the integral vanish. For trapped particles, σ will change its sign during its bounce orbit as they traverse once the field line "forwards" in between the bounce points and once "backwards" to complete a full bounce orbit. Thus if $l_{1,2}$ denote the bounce points then the path of a trapped particle will be $l_1 \to l_2 \to l_1$, where in the first part $v_\parallel > 0$ and for the second part $v_\parallel < 0$, as illustrated in Figure 10 where this is contrasted against the situation for a passing particle discussed above.

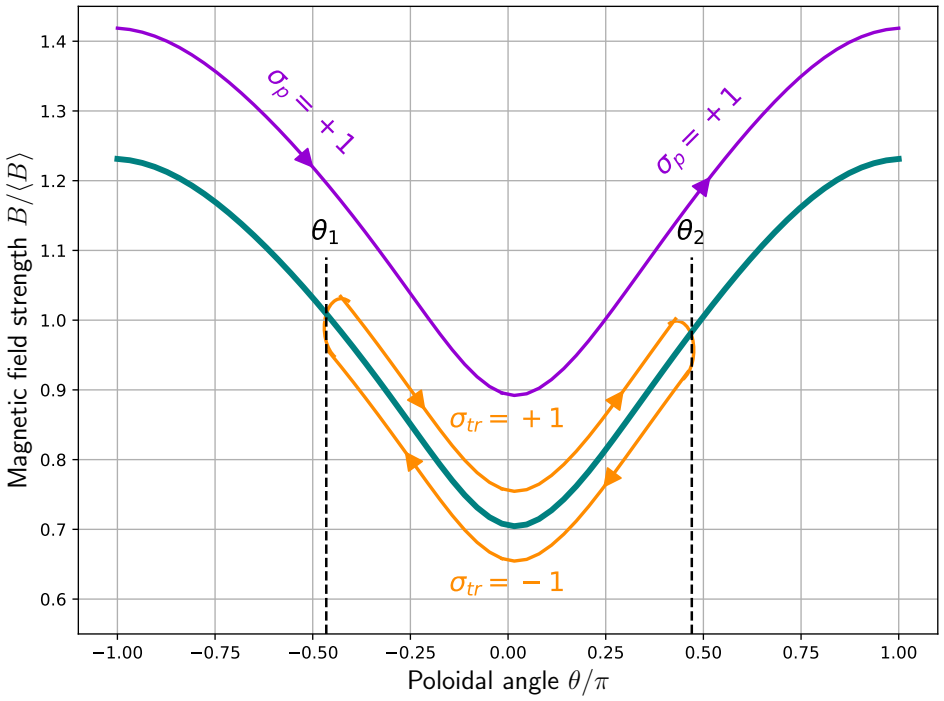

Figure 10: Situation sketch for the parallel velocity of a passing- (purple) and trapped particle (orange) used for the bounce averaging procedure of the parallel dyanmics term $v_\parallel \boldsymbol{\nabla}_\parallel \hat{g}_e$ in the GKE. The poloidal angle θ is used as a surrogate for the arc length l, based on their connection through Equation (M.3).

Consequently the field line integral can be split as

$$\oint v_\parallel \boldsymbol{\nabla}_\parallel \hat{g}^{tr}_{e,1} \frac{\mathrm{d}l}{|v_\parallel|} = \int_{l_1}^{l_2} \boldsymbol{\nabla}_\parallel \hat{g}^{tr}_{e,1}\big|_{\sigma=+1}\,\mathrm{d}l - \int_{l_2}^{l_1} \boldsymbol{\nabla}_\parallel \hat{g}^{tr}_{e,1}\big|_{\sigma=-1}\,\mathrm{d}l$$
$$= \left[\hat{g}^{tr}_e(l_2,\sigma=+1) - \hat{g}^{tr}_e(l_2,\sigma=-1)\right] + \left[\hat{g}^{tr}_e(l_1,\sigma=-1) - \hat{g}^{tr}_e(l_1,\sigma=+1)\right]$$

where it has been accounted for that the sign of σ affects both in which region of velocity space the kinetic response $\hat{g}^{tr}_{e,1}$ is evaluated and what the sign of the parallel gradient will be[35] and all terms involving the same bounce points have been been grouped together. Since the influx and outflux of trapped particles at each bounce point must balance since otherwise trapped particles could "leak out" from their magnetic well, both terms must vanish individually such that also for trapped particles the bounce average of the parallel dynamics will vanish. Consequently by bounce averaging Equation (49) also the electron GKE becomes a simple algebraic equation for the kinetic electron response

$$\hat{g_e} \approx \hat{g}_{e,0} = \frac{-e}{T_e} \frac{\left(\omega - \omega^T_{\star e}\right) F_{Me}}{\omega - \overline{\omega_{de}} + i\nu_{e,tot}} \overline{J_0(k_\perp \rho_e)\hat{\phi}} \tag{51}$$

where a quick inventorisation of variables shows that only $J_0, \hat{\phi}, \omega_{de}$ vary along the orbit of a particle. Although Equation (51) is valid for both passing and trapped electrons, it will typically vanish for passing electrons as they sample the full perturbation along the line such that $\overline{J_0(k_\perp \rho_e)\hat{\phi}} \approx 0$. Furthermore, as TEMs which are characterised by spatial scales of $k_\perp \rho_i \sim \mathcal{O}(1)$ the Bessel function may be approximated as $J_0(k_\perp \rho_e) \approx 1$ because of the large mass difference between electrons and ions.

3.1.3 Pitch-angle velocity coordinates

To obtain a consistent solution to the GKE, the approximate results for the kinetic responses Equations (48) and (51) will have to be substituted in the quasi-neutrality condition Equation (37). As Equation (51) vanishes for passing particles, only the region of velocity space corresponding to trapped particles will contribute to the integral over $\hat{g_e}$. The distinction between passing and trapped particles is best made by transforming to pitch-angle coordinates (v, λ, σ) defined by

$$v = \sqrt{v_\parallel^2 + v_\perp^2} \qquad v_\parallel = \sigma\sqrt{v^2 - v_\perp^2} = \sigma v\sqrt{1-\lambda B}$$
$$\lambda = \frac{\mu}{E} = \frac{v_\perp^2}{v^2 B} \qquad v_\perp^2 = v^2 - v_\parallel^2 = v^2 \lambda B$$

and $\sigma = v_\parallel / |v_\parallel|$. Using these new coordinates the velocity differential of cylindrical velocity coordinates $\mathrm{d}^3\boldsymbol{v} = \mathrm{d}\vartheta\, /2\, \mathrm{d}{v_\perp}^2\, \mathrm{d}v_\parallel$ is transformed with the Jacobian

$$\det J^{v_\parallel, v_\perp^2}_{v,\lambda} = \det \begin{bmatrix} \sigma\sqrt{1-\lambda B} & -\sigma\frac{vB}{2\sqrt{1-\lambda B}} \\ 2v\lambda B & v^2 B \end{bmatrix} = \frac{\sigma v^2 B}{\sqrt{1-\lambda B}}$$

such that $\mathrm{d}^3\boldsymbol{v} \to \sum_{\sigma=\pm 1} \frac{v^2 B}{2\sqrt{1-\lambda B}}\,\mathrm{d}v\,\mathrm{d}\lambda\,\mathrm{d}\vartheta$. The domain of velocity space $v_\parallel \in (-\infty, \infty), v_\perp \in (0,\infty), \vartheta \in [0, 2\pi)$ is then mapped to[36] $v \in [0,\infty), \lambda \in [0, 1/B), \vartheta \in [0, 2\pi)$ with $\sigma = \pm 1$ accounting for the different directions of $v_\parallel$.

[35] This is easiest to see using the gradient approximation $\boldsymbol{\nabla}_\parallel f \approx \frac{\Delta f}{\Delta l}$, where for $\sigma = +1$ the increment along the field line will be $\Delta l > 0$ but for $\sigma = -1$ the increment along the field line will be $\Delta l < 0$. Consequently in the limit of $|\Delta l| \to 0$ when the gradient approximation becomes exact, it follows that $\boldsymbol{\nabla}_\parallel f\big|_{\sigma=+1} = \frac{\partial f}{\partial l}$ but $\boldsymbol{\nabla}_\parallel f\big|_{\sigma=-1} = -\frac{\partial f}{\partial l}$.

[36] In practice the integral over the gyrophase ϑ will just give a 2π factor since the kinetic responses $\hat{g}_s$ are constructed to be gyrophase independent.

The distinction between passing and trapped particles is then mainly characterised by λ with small values corresponding to passing particles ($v_\perp^2/v_\parallel^2 \ll 1$) and large values corresponding to trapped particles ($\mu B \sim E$). However the introduction of finite collisionality results in another distinction between trapped and passed particles in velocity space. If a particle would be detrapped as a result of the accumulated effect of small changes to its pitch angle $v_\parallel/v_\perp$ before it completes many bounce orbits, then it cannot effectively be considered as trapped since it will manage to escape its magnetic well within the period of the perturbation and thus respond to the perturbations as if it were a passing particle as a result of the frequency ordering $\omega/\omega_{be}^T \ll 1$ [69, 83]. Therefore, as a practical limit a particle can only be considered as trapped if $\nu_s/\omega_{bs} \leq 1$ such that on average it will experience less than a single effective 90° collision per bounce orbit [121]. In term of pitch angle coordinates the bounce time is given by

$$\tau_b = \oint \frac{\mathrm{d}l}{|v_\parallel|} = \frac{1}{v} \oint \frac{\mathrm{d}l}{\sqrt{1-\lambda B}} \tag{52}$$

where v is constant along the field line because of energy conservation. Consequently the bounce frequency $\omega_b \sim 1/\tau_b \propto v$ increases linearly with particle speed while the collision frequencies Equation (16) all decrease with speed, such that the requirement[37] $\nu_s/\omega_{bs} \leq 1$ will set a lower limit to the speeds below which trapped particles can no longer be considered as trapped.

Finally, also because of energy conservation, the bounce averaging Equation (50) simplifies considerably when using pitch-angle coordinates

$$\overline{\cdots} = \frac{\oint (\cdots) \frac{\mathrm{d}l}{|v_\parallel|}}{\oint \frac{\mathrm{d}l}{|v_\parallel|}} = \frac{\oint (\cdots) \frac{\mathrm{d}l}{\sqrt{1-\lambda B(l)}}}{\oint \frac{\mathrm{d}l}{\sqrt{1-\lambda B(l)}}} \tag{53}$$

such that any quantity that depends on the distance along the field will be transformed to a quantity that depends on the pitch angle λ instead.

3.2 Perturbative approach to TEMs

If the approximate solutions for the ion and electron kinetic responses Equations (48) and (51) valid in the TEM regime are substituted in the quasi-neutrality equation condition Equation (37) it results in

$$(1+\tau)\hat{\phi} \approx \int \frac{\omega - \omega_{\star i}^T}{\omega - \omega_{di} + i\nu_{tot,i}} \frac{F_{Mi}}{n_0} J_0(k_\perp \rho_i)^2 \hat{\phi} \mathrm{d}^3 \boldsymbol{v_i} + \tau \int \frac{\omega - \omega_{\star e}^T}{\omega - \overline{\omega_{de}} + i\nu_{tot,e}} \frac{F_{Me}}{n_0} \overline{\hat{\phi}} \mathrm{d}^3 \boldsymbol{v_e} \tag{54}$$

where quasi-neutrality of the equilibrium $n_{i0} \approx n_{e0} = n_0$ and for the electrons $J_0(k_\perp \rho_e) \approx 1$ have been used, common prefactors have been cancelled, and the temperature ratio $\tau = T_{i0}/T_{e0}$ is introduced. Equation (54) takes the form of a dispersion relation $D(\omega, \boldsymbol{k}_\perp, \hat{\phi}) = 0$ that determines the allowed mode frequencies for a given spatial structure of the electrostatic perturbation[38].

The main difficulty in analytically solving Equation (54) is that the dispersion equation is non-local as a result of non-uniform magnetic field, which is a general property of instabilities in toroidal geometry [132]. In the specific case of TEMs this is due to populations of trapped electrons, which as a result of the frequency ordering Equation (47) are responsible for "communicating" information about the perturbation along the field line, while on the timescale of the

[37] The 90° scattering frequency introduced in Equation (17) is that of a typical particle with thermal speed. As the effort to decorrelate the initial momentum through small angle collisions will increase with the magnitude of the velocity, it logically follows that by letting $v_T \to v$ in Equation (16) one obtains the 90° scattering frequency for arbitrary particle speed.

[38] Recall that by using the WKB approximation Equation (28) for the electrostatic potential $\hat{\phi}$ account for the variation along the field lines and $\boldsymbol{k}_\perp$ serves as a proxy for the mode structure perpendicular to the field lines

oscillation period the ions remain stationary. Especially in stellarators where multiple magnetic wells of different depths exist along the field line, this complicates the analysis as these wells will be connected by the less deeply trapped particles that can escape the more shallow wells [93].

However, as the bounce average $\hat{\phi}$ will vanish for passing particles which sample the full perturbation along the field line, the integration over electron velocity space effectively only takes place over the trapped particle region. By means of a hand-waving argument this can be accounted for by integrating over all velocity space and correcting by the fraction of trapped particles $\int_{tr} \mathrm{d}^3\boldsymbol{v_e} \sim f_t \int \mathrm{d}^3\boldsymbol{v_e}$ [36] and consequently by symmetry of the kinetic responses the two terms on the right-hand side of Equation (54) scale as $\int \mathrm{d}^3\boldsymbol{v_e} / \int \mathrm{d}^3\boldsymbol{v_i} \sim f_t$. In tokamaks for example, the trapped particle fraction can be calculated analytically by assuming concentric flux surfaces as $f_t \approx \sqrt{2r/R}$ where r is the distance from the magnetic axis and R the major radius [133]. The trapped particle fraction can thus be at most $f_t \approx \sqrt{2a/R}$ where a is the minor radius, which is typically small and therefore the right-hand side of Equation (54) will be dominated by the ion response.

This would facilitate a perturbative treatment of the trapped electron term, where to lowest order the allowed mode is determined by the kinetic ions and adiabatic electrons, and to next order the interaction of the trapped electrons with the mode will result in a frequency shift $\delta\omega$. Mathematically this perturbative approach boils down to a Taylor expansion of the dispersion relation $D(\omega, \boldsymbol{k}_\perp, \hat{\phi}) = D_0(\omega, \boldsymbol{k}_\perp, \hat{\phi}) + D_1(\omega, \boldsymbol{k}_\perp, \hat{\phi})$ about a trapped particle fraction of zero

$$D_0(\omega_0, \hat{\phi}, \boldsymbol{k}_\perp) = 0 \qquad \left.\frac{\partial D_0(\omega, \hat{\phi}, \boldsymbol{k}_\perp)}{\partial \omega}\right|_{\omega_0} \delta\omega = D_1(\omega_0, \hat{\phi}, \boldsymbol{k}_\perp) \tag{55}$$

where the expansion is made around the frequency shift $\delta\omega$ which is directly proportional to the trapped particle fraction, ω_0 is the lowest order mode frequency and D_1 corresponds to the trapped electron term in Equation (54). This is the common approach in literature to treat TEMs gyrokinetically [83, 134], but often the leading order part is replaced by a cold-ion fluid model instead [84, 85, 120, 121, 126]. What all these approaches have in common is that they treat the trapped electron response only in extreme limits of weak/strong collisionality, which will be expanded upon in Section 3.4.2 by considering arbitrary collisionality. For the perturbative approach to be a valid treatment, it will have to be verified in retrospect that the trapped electrons dynamics are not dominant, i.e. the resulting frequency shift should remain small $\delta\omega/\omega_0 \ll 1$.

For the collision frequency, only the effect of interspecies collisions will be accounted for since the electron momentum can be scattered considerably by the transfer of a small fraction of the ion momentum because of the mass difference leading to strong (de)trapping. Meanwhile collisions among electrons would result in equal exchanges of momentum and as a consequence collisions between trapped/passing particles can swap their nature leading to no effective change in the trapped particle population. Therefore the *tot* subscript will be omitted for the remainder of this calculation.

3.3 Solution to the leading order dispersion relation

The leading order dispersion relation is obtained from Equation (54) by only retaining the adiabatic electron response, resulting in

$$D_0(\omega, \boldsymbol{k}_\perp, \hat{\phi}) = \left[1 + \tau - \int \frac{\omega - \omega^T_{\star i}}{\omega - \omega_{di} + i\nu_i} \frac{F_{Mi}}{n_0} J_0(k_\perp \rho_i)^2 \mathrm{d}^3\boldsymbol{v_i}\right] \hat{\phi}$$

where the kinetic ion response is brought to the other side and the electrostatic potential amplitude $\hat{\phi}$ is taken out of the integral since it only depends on the distance along the field line.

Consequently this means that the lowest order solution determined by $D_0(\omega_0, \hat{\phi}, \boldsymbol{k}_\perp) = 0$ either has the trivial root $\hat{\phi} = 0$ corresponding to no perturbations at all or a mode frequency ω_0 determined by the perpendicular mode structure through $k_\perp$ from the vanishing of the terms in square brackets. The integral over ion velocity can be simplified by using the order of magnitude estimate

$$\frac{\omega_{di}}{\omega} \sim \frac{k_\perp \delta v_{Ti}}{\omega} \sim \frac{k_\parallel v_{Ti}}{\omega} \sim \frac{\omega_{ti}}{\omega} \ll 1$$

which follows from $\omega_{di} = \boldsymbol{k}_\perp \cdot \boldsymbol{v_{ds}}$, Equation (27) for the drift velocity, the gyrokinetic ordering Equation (19) and the TEM frequency regime Equation (47). Furthermore, for the collision frequency a similar estimate for a typical thermal particle gives

$$\frac{\nu^{ie}(v_{Ti})}{\omega} = \frac{\nu^{ie}(v_{Ti})}{\nu^{ei}(v_{Te})} \frac{\nu^{ei}(v_{Te})}{\omega_{be}^T} \frac{\omega_{be}^T}{\omega_{bi}^T} \frac{\omega_{bi}^T}{\omega} \leq \sqrt{\frac{m_e}{m_i}} \tau^{-3/2} \frac{\omega_{bi}^T}{\omega} \ll 1$$

which follows from the trapping requirement for thermal particles $\nu^{ei}(v_{Te})/\omega_{be}^T \leq 1$, the parameter dependence of the collision frequencies Equations (17) and (18), considering a trapped ion and electron with a similar pitch-angle λ such that $\omega_{be}^T/\omega_{bi}^T \sim v_{Te}/v_{Ti}$ and the TEM frequency regime Equation (47) together with $\tau \approx 1$ for typical reactor conditions. Therefore the frequency denominator in the integrand can be safely expanded, such that the leading order frequency solution is determined by

$$1 + \tau \approx \int \left(1 - \frac{\omega_{\star i}^T}{\omega}\right) \left[1 + \frac{\omega_{di}}{\omega} - i\frac{\nu^{ie}}{\omega}\right] \left(\frac{m_i}{2\pi T_{i0}}\right)^{3/2} \exp\left(-\frac{m_i v_i^2}{2T_{i0}}\right) J_0\left(k_\perp \frac{v_{\perp,i}}{\Omega_i}\right)^2 \mathrm{d}^3\boldsymbol{v_i} \tag{56}$$

where the gyroradius is written out explicitly as a reminder of its velocity dependence for the integration, and Equation (23) has been substituted for the Maxwellian F_{Mi}. A final simplification concerns the magnetic drift velocity $\boldsymbol{v_{di}}$, which is determined by both the gradient in the magnetic field strength $\boldsymbol{\nabla} \ln B$ and the curvature vector $\boldsymbol{\kappa}$. The curvature vector can be written in terms of the plasma parameters as [46]

$$\boldsymbol{\kappa} = \boldsymbol{e_b} \cdot \boldsymbol{\nabla} \boldsymbol{e_b} = -\boldsymbol{e_b} \times (\boldsymbol{\nabla} \times \boldsymbol{e_b}) = \frac{\mu_0 \boldsymbol{\nabla} p}{B^2} + \frac{\boldsymbol{\nabla}_\perp B}{B} \tag{57}$$

by using Ampère's law ($\boldsymbol{\nabla} \times B = \mu_0 \boldsymbol{J}$) and the MHD force balance Equation (2), and where the perpendicular gradient is defined by $\boldsymbol{\nabla}_\perp = \boldsymbol{\nabla} - (\boldsymbol{e_b} \cdot \boldsymbol{\nabla})\, \boldsymbol{e_b}$. Aside from the gradient operator, the first term is essentially the normalised plasma pressure β which is at most a few percent due to macroscopic stability constraints [43], and will therefore be small. Physically this means that as a result of the relatively low charge particle density in the plasma compared to the current density in the external coils, the diamagnetic effect of the plasma is sufficiently weak that it does not significantly affect the magnetic geometry. Therefore the plasma medium has approximately the magnetic permeability of vacuum as far as the strong external magnetic field is considered, and within this "vacuum plasma" approximation, the diamagnetic response of the plasma can be neglected such that the curvature vector can be approximated as $\boldsymbol{\kappa} \approx \boldsymbol{\nabla}_\perp \ln B$. Consequently the magnetic drift frequency will be given by

$$\omega_{di} \approx \boldsymbol{k}_\perp \cdot \left(\frac{\boldsymbol{e_b}}{\Omega_i} \times \boldsymbol{\nabla}_\perp \ln B\right) \left[\frac{v_\perp^2}{2} + v_\parallel^2\right] \equiv \hat{\omega}_{di} \left[\frac{v_\perp^2}{2v_{Ti}^2} + \frac{v_\parallel^2}{v_{Ti}^2}\right] \tag{58}$$

where for notational convenience a characteristic drift frequency $\hat{\omega}_{di}$ normalised to the thermal velocity has been introduced.

For calculating the ion velocity integral it is most convenient to adopt cylindrical velocity coordinates $\mathrm{d}^3\boldsymbol{v} \to \mathrm{d}\vartheta\, v_\perp\, \mathrm{d}v_\perp\, \mathrm{d}v_\parallel$ as this best accounts for the dependence on the Bessel function and

drift frequency on the perpendicular/parallel velocity. Finally for the collision frequency, the deflection frequency ν_D^{ie} Equation (18) will be used which determines the remaining velocity dependence in the ion integral[39]. In Appendix I it is shown by using velocity coordinates normalised to the thermal speed, explicitly expanding each term in the product $\left(1-\frac{\omega_{\star i}^T}{\omega}\right)\left[1+\frac{\omega_{di}}{\omega}-i\frac{\nu^{ie}}{\omega}\right]$ that the dispersion relation becomes

$$\begin{aligned}1+\tau = \frac{\omega-\omega_{\star i}}{\omega}\left(S_1(k_\perp\rho_{Ti})+\frac{\hat{\omega}_{di}}{\omega}S_2(k_\perp\rho_{Ti})-i\frac{\tilde{\nu}^{ie}}{\omega}S_3(k_\perp\rho_{Ti})\right)\\ -\frac{\omega_{\star i}}{\omega}\eta_i\left(S_4(k_\perp\rho_{Ti})+\frac{\hat{\omega}_{di}}{\omega}S_5(k_\perp\rho_{Ti})-i\frac{\tilde{\nu}^{ie}}{\omega}S_6(k_\perp\rho_{Ti})\right)\end{aligned} \tag{59}$$

where $\tilde{\nu}^{ie}$ is the ion-electron collision frequency at thermal speed (defined similarly as $\hat{\omega}_{di}$ in Equation (58)) and $S_{\{1,6\}}$ denote the result of each separate velocity integral and are given by

$$\begin{aligned}S_1(x) &= \Gamma_0\left(\frac{x^2}{2}\right) & S_4(x) &= \frac{x^2}{2}\left(\Gamma_1\left(\frac{x^2}{2}\right)-\Gamma_0\left(\frac{x^2}{2}\right)\right)\\ S_2(x) &= \frac{x^2}{4}\Gamma_1\left(\frac{x^2}{2}\right)+\left(1-\frac{x^2}{4}\right)\Gamma_0\left(\frac{x^2}{2}\right) & S_5(x) &= \left(1-\frac{x^2}{2}\right)^2\Gamma_0\left(\frac{x^2}{2}\right)-\frac{x^2}{2}\left(\frac{x^2}{2}-\frac{3}{2}\right)\Gamma_1\left(\frac{x^2}{2}\right)\\ S_3(x) &= 2\times\,{}_2F_2\left[\begin{matrix}1/2 & 1/2\\ 1 & 3/2\end{matrix};-x^2\right] & S_6(x) &= \Gamma_0\left(\frac{x^2}{2}\right)-3\times\,{}_2F_2\left[\begin{matrix}1/2 & 1/2\\ 1 & 3/2\end{matrix};-x^2\right]\end{aligned}$$

where in literature it is custom to define the functions $\Gamma_n(\zeta) = I_n(\zeta)\exp(-\zeta)$ with I_n the nth order modified Bessel function, and ${}_pF_q$ denotes the more exotic generalised hypergeometric function of which e.g. the exponential and Bessel functions are special limiting cases $e^x = {}_0F_0\left[\,;x\right]$, $J_0(x) = {}_0F_1\left[\,;-x^2/4\right]$ [135]. These integrals are plotted in Figure 11, which shows that they are nicely behaved, typically peaking at zero argument (except for S_4) and asymptotically decaying to zero as $k_\perp\rho$ tends to infinity which reflects the limiting behaviour of the Bessel function in the original velocity integral.

By using quasi-neutrality the ion diamagnetic frequency can be rewritten as $\omega_{\star i} = -\tau\omega_{\star e}$ which will make Equation (59) more symmetric in terms of signs and temperature ratio

$$\begin{aligned}1+\tau = \left(1+\tau\frac{\omega_{\star e}}{\omega}\right)\left(S_1(k_\perp\rho_{Ti})+\frac{\hat{\omega}_{di}}{\omega}S_2(k_\perp\rho_{Ti})-i\frac{\tilde{\nu}^{ie}}{\omega}S_3(k_\perp\rho_{Ti})\right)\\ +\tau\frac{\omega_{\star e}}{\omega}\eta_i\left(S_4(k_\perp\rho_{Ti})+\frac{\hat{\omega}_{di}}{\omega}S_5(k_\perp\rho_{Ti})-i\frac{\tilde{\nu}^{ie}}{\omega}S_6(k_\perp\rho_{Ti})\right)\end{aligned}$$

which is a quadratic equation in the mode frequency ω, whose roots are straightforwardly obtained by multiplying both sides by $(\omega/\omega_{\star e})^2$ as

$$\begin{aligned}\frac{\omega}{\omega_{\star e}} &= \frac{\tau\left(S_1+\eta_iS_4\right)+\frac{\hat{\omega}_{di}}{\omega_{\star e}}S_2-i\frac{\tilde{\nu}^{ie}}{\omega_{\star e}}S_3}{2\left(1+\tau-S_1\right)}\\ &\pm\frac{\sqrt{\left[\tau\left(S_1+\eta_iS_4\right)+\frac{\hat{\omega}_{di}}{\omega_{\star e}}S_2-i\frac{\tilde{\nu}^{ie}}{\omega_{\star e}}S_3\right]^2}}{2\left(1+\tau-S_1\right)}\sqrt{1+\frac{4(1+\tau-S_1)\tau\left(\frac{\hat{\omega}_{di}}{\omega_{\star e}}\left[S_2+\eta_iS_5\right]-i\frac{\tilde{\nu}^{ie}}{\omega_{\star e}}\left[S_3+\eta_iS_6\right]\right)}{\left[\tau\left(S_1+\eta_iS_4\right)+\frac{\hat{\omega}_{di}}{\omega_{\star e}}S_2-i\frac{\tilde{\nu}^{ie}}{\omega_{\star e}}S_3\right]^2}}\end{aligned}$$

[39]The velocity dependence of the three fundamental processes Equation (18) shows that at low energies velocity deflection will be the dominant process, but for speeds $v \gtrsim v_{Ti}$ the effective friction on electrons is the most important collisional process. However, what matters for the density perturbation is the collective effect of all possible single particle collisions which are weighted by the speed distribution $\propto v^2\exp\left(-(v/v_T)^2\right)$ from which the low energy particles will have the largest contribution.

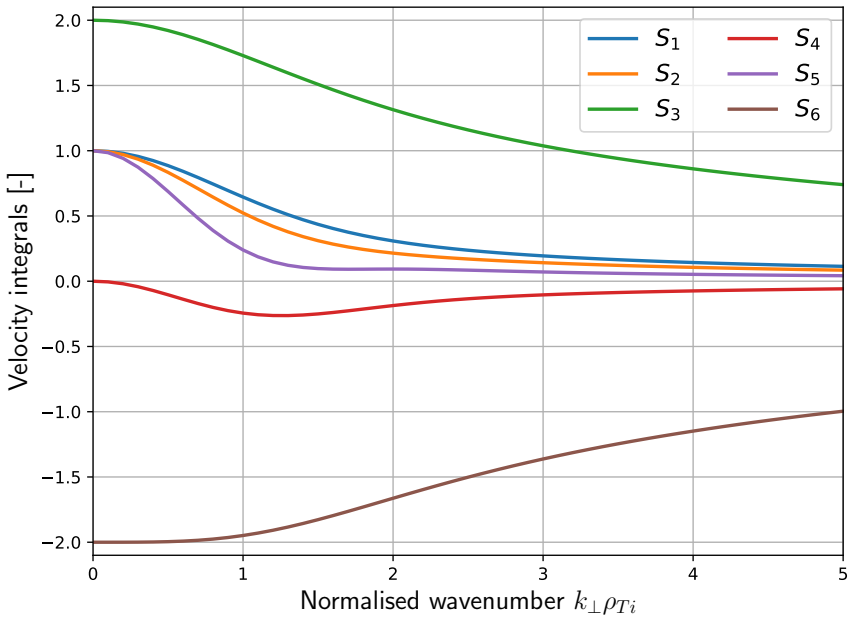

Figure 11: Visualisation of the dependence of the six stand-alone integrals that result from expanding the ion kinetic response for $\omega_{di}/\omega \sim \nu_i/\omega \ll 1$ giving respectively the lowest order contribution and influence of finite drift and collision frequency as a result of density gradient $(S_1, S_2, S_3))$ and temperature gradient (S_4, S_5, S_6) on perpendicular wavenumber of perturbations.

where the dependence of the integrals $S_{\{1,6\}}$ on $k_\perp \rho$ has been suppressed.

The main difficulty in getting a sensible solution for the mode frequency lies in the two square root terms because their argument is complex-valued. By writing a complex number very generally in terms of its phase and magnitude $\xi = |\xi| \exp(i\varphi)$, where the phase $\varphi \in [-\pi, \pi)$ uniquely determines where ξ lies in the complex plane. If this complex number is squared its phase will essentially be doubled $\xi^2 = |\xi|^2 \exp(2i\varphi)$, which has the potential to create a phase ambiguity as 2φ may exceed the domain of definition for the phase, such that a new phase $2\varphi' = 2\varphi \pm 2\pi n$ with $n \in \mathbb{Z}$ could equally describe its square $\xi^2 = |\xi|^2 \exp(2i\varphi')$ such that its square is not uniquely determined. This is troublesome as this means that $\sqrt{\xi^2} = \pm\xi$ depending on whether φ or φ' is used for the phase. This issue only arises if the initial phase of the complex number lies outside of $\varphi \in [-\pi/2, \pi/2)$ such that doubling the rotation of ξ in the complex plane doesn't bring its phase outside $[-\pi, \pi)$.

For the specific case at hand the complex number is $\xi = \tau\,(S_1 + \eta_i S_4) + \frac{\hat{\omega}_{di}}{\omega_{\star e}} S_2 - i\frac{\tilde{\nu}^{ie}}{\omega_{\star e}} S_3$. As the collision frequency is positive, the density gradient is typically radially inward ($\frac{\partial n}{\partial \psi} < 0$) and the electron charge is $q = -e$ it follows from Equation (30) that the electron diamagnetic frequency is positive $\omega_{\star e} > 0$, and $S_3 > 0$ for all wavenumbers (see Figure 11), it follows that ξ lies in the third or fourth quadrant of the complex plane. Consequently, this phase ambiguity will arise only if $\mathrm{Re}[\xi] = \tau\,(S_1 + \eta_i S_4) + \frac{\hat{\omega}_{di}}{\omega_{\star e}} S_2 < 0$ such that ξ is in the fourth quadrant. Focusing on the case where $\mathrm{Re}[\xi] > 0$ and $\sqrt{\xi^2}$ "behaves nicely" the two roots to the dispersion relation are obtained as

$$\frac{\omega}{\omega_{\star e}} = \begin{cases} \frac{\tau(S_1+\eta_i S_4)+\frac{\hat{\omega}_{di}}{\omega_{\star e}}S_2 - i\frac{\tilde{\nu}^{ie}}{\omega_{\star e}}S_3}{(1+\tau-S_1)} + \frac{\tau\left(\frac{\hat{\omega}_{di}}{\omega_{\star e}}[S_2+\eta_i S_5] - i\frac{\tilde{\nu}^{ie}}{\omega_{\star e}}[S_3+\eta_i S_6]\right)}{\tau(S_1+\eta_i S_4)+\frac{\hat{\omega}_{di}}{\omega_{\star e}}S_2 - i\frac{\tilde{\nu}^{ie}}{\omega_{\star e}}S_3} & + \text{ branch} \\ -\frac{\tau\left(\frac{\hat{\omega}_{di}}{\omega_{\star e}}[S_2+\eta_i S_5] - i\frac{\tilde{\nu}^{ie}}{\omega_{\star e}}[S_3+\eta_i S_6]\right)}{\tau(S_1+\eta_i S_4)+\frac{\hat{\omega}_{di}}{\omega_{\star e}}S_2 - i\frac{\tilde{\nu}^{ie}}{\omega_{\star e}}S_3} & - \text{ branch} \end{cases}$$

where the $\sqrt{1+\cdots}$ term has been expanded for $\hat{\omega}_{di}/\omega_{\star e} \sim \tilde{\nu}^{ie}/\omega_{\star e} \ll 1$. Of these two branches the latter contradicts the $\omega_{di}/\omega \sim \nu^{ie}/\omega \ll 1$ assumptions that were used to expand the frequency denominator in Equation (56) and thus gives an inconsistent solution which has to considered as an "unphysical branch". It is straightforward to show that if $\mathrm{Re}[\xi] < 0$ instead, the solutions for the $\pm$ branches simply switch, such that the physically relevant solution to the leading order dispersion relation Equation (54) follows as

$$\frac{\omega}{\omega_{\star e}} = \frac{\tau\left(S_1+\eta_i S_4\right)}{\left(1+\tau-S_1\right)} + \frac{\hat{\omega}_{di}}{\omega_{\star e}}\left[\frac{S_2}{1+\tau-S_1} + \frac{S_2+\eta_i S_5}{S_1+\eta_1 S_4}\right] - i\frac{\tilde{\nu}^{ie}}{\omega_{\star e}}\left[\frac{S_3}{1+\tau-S_1} + \frac{S_3+\eta_i S_6}{S_1+\eta_i S_4}\right] \tag{60}$$

which has been further linearised in $\hat{\omega}_{di}/\omega_{\star e} \sim \tilde{\nu}^{ie}/\omega_{\star e} \ll 1$.

Note that the derivation has been completely general aside from an assumption on the drift- and collision frequencies which follows from the frequency ordering Equation (47). For the scope of this thesis however, only density gradient driven TEMs are investigated, such that in the regime of interest the solution can be simplified by setting the temperature gradient to zero which amounts to $\eta_i = 0$, such that Equation (60) reduces to

$$\frac{\omega}{\omega_{\star e}} = \underbrace{\frac{\tau S_1}{\left(1+\tau-S_1\right)}}_{\approx\omega_0} + \frac{\hat{\omega}_{di}}{\omega_{\star e}}\frac{S_2\left(1+\tau\right)}{S_1\left(1+\tau-S_1\right)} - i\frac{\tilde{\nu}^{ie}}{\omega_{\star e}}\frac{S_3\left(1+\tau\right)}{S_1\left(1+\tau-S_1\right)}. \tag{61}$$

The first term in Equation (61) would be the lowest order solution to the dispersion relation ω_0 if the magnetic drift and collisions were neglected altogether and is purely real-valued, whereas the remaining two terms give a small shift in the real frequency and a small imaginary component that will damp the perturbations due to corrections the ion drift and collision frequency respectively. These three contributions are plotted versus $k_\perp \rho_{Ti}$ in Figure 12 for various temperature ratios τ to show the dispersive property of the mode frequency. It can be seen that the first term is rather insensitive to the temperature ratio and places the mode frequency $\omega/\omega_{\star e} \sim \mathcal{O}(0.1) - \mathcal{O}(1.0)$ which further validates the assumptions used to expand the frequency denominator in Equation (56). Furthermore in the long wavelength limit $k_\perp \rho_{Ti} \to 0$ this dominant contribution to the mode frequency is exactly the electron diamagnetic frequency $\omega_{\star e}$ independent of the temperature ratio. If the drifts and collisions were neglected, then only the adiabatic response of electrons to the perturbations and kinetic response of ions under influence of to the perturbed $\boldsymbol{E} \times \boldsymbol{B}$ drift are accounted for by the dispersion relation $D_0 = 0$. These are exactly same elements present in the simple fluid calculation of the basic drift wave from Appendix E which results in $\omega_{\star e}$ as the drift wave frequency. Since in the limit of $k_\perp \rho_{Ti} \to 0$ plasma fluid models correspond to velocity moments of the gyrokinetic equation [136], recovering this behaviour serves as a sanity check on the calculation. For completeness the dispersion of the general solution Equation (61) with finite temperature gradient are shown in Appendix J.

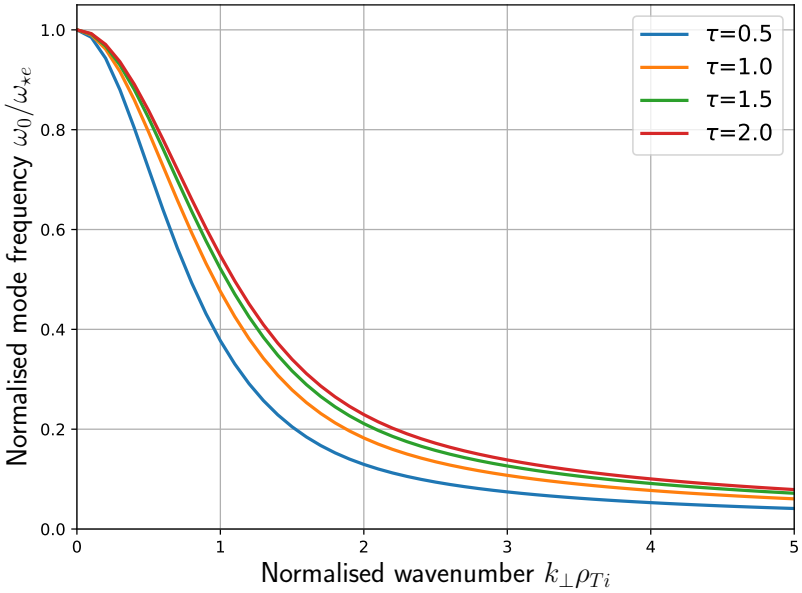

(a)

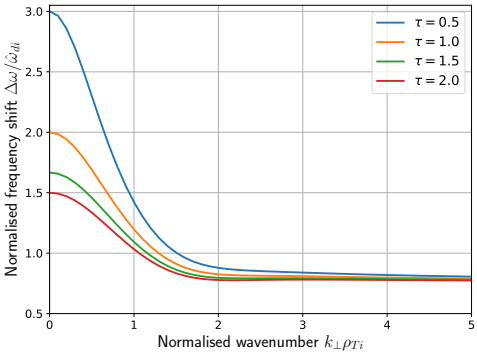

(b)

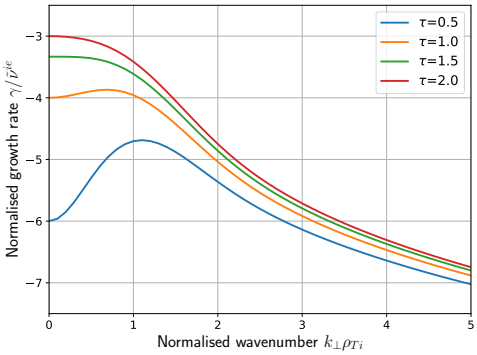

(c)

Figure 12: Contributions to the leading order dispersion relation $D_0(\omega, \boldsymbol{k}_\perp, \hat{\phi}) = 0$ without ion temperature gradients showing (a) the lowest order (real) frequency in absence of ion drift and collisions, (b) the shift in (real) frequency due to correction from ion drift, and (c) the growth rate due to correction from collisions for various temperature ratios $\tau = T_i/T_e$. Note that in (c) the growth rate is always negative corresponding to damping.

3.4 Perturbative solution to next order dispersion relation

With the leading order mode frequency determined by Equation (61), the shift in frequency $\delta\omega$ due to the kinetic response of trapped electrons can be calculated using the paradigm from Equation (55). For this calculation, only the dominant contribution to Equation (61) will be retained as ω_0. This is justified as the frequency shift due to ion drift is typically a much smaller effect than the variation of ω_0 with wavenumber [128], which is also an instance of a Finite Larmor Radius (FLR) effect. Furthermore the ion collisions provide only a very weak proportionality of the growth rate to $\tilde{\nu}^{ie}$ which is smaller by the mass ratio m_e/m_i compared to the typical electron frequency $\hat{\nu^{ei}}$, such that any instability drive by electron collisions will have a much larger effect on the actual growth rate.

With this limitation in mind, the leading order dispersion relation essentially reduces to

$$D_0(\omega, \hat{\phi}, \boldsymbol{k}_\perp) \approx \left(1 + \tau - \left(1 - \frac{\omega_{\star i}}{\omega}\right)\Gamma_0\left(\frac{(k_\perp\rho)^2}{2}\right)\right)\hat{\phi}$$

where the only surviving integral S_1 has been written out explicitly, such that to next order in the trapped electron fraction the dispersion relation becomes

$$\begin{aligned}\frac{\delta\omega}{\omega_0}\tau\frac{\omega_{\star e}}{\omega_0}\Gamma_0\hat{\phi} =& \tau\int_{tr}\frac{\omega_0 - \omega_{\star e}}{\omega_0 - \overline{\omega_{de}} + i\nu^{ei}}\frac{F_{Me}}{n_{e0}}\overline{\hat{\phi}}\mathrm{d}^3\boldsymbol{v_e} \\ =& \tau\left(\omega_0 - \omega_{\star e}\right)\sum_{\sigma=\pm}\int_0^\infty \mathrm{d}v_e\int_0^{1/B}\mathrm{d}\lambda\frac{\exp\left(-\frac{v_e^2}{v_{Te}^2}\right)\Big/\sqrt{\pi}^3 v_{Te}^3}{\omega_0 - \overline{\omega_{de}} + i\nu_e}\frac{\pi v^2 B}{\sqrt{1-\lambda B}}\overline{\hat{\phi}}\end{aligned} \tag{62}$$

where the dependence of Γ_0 on the wavenumber has been suppressed to keep the notation compact, and in the second step the Maxwellian was substituted and the pitch-angle coordinates discussed in Section 3.1.3 are used, but integration over λ, v still includes both passing- and trapped particles. To account only for the trapped particles for which $\overline{\hat{\phi}} \not\approx 0$, the integration limits have to be adapted. The proper limit on particle speeds is determined from the collisional cutoff to the trapped particle region of velocity space, which follows from the speed dependence of the 90° collision frequency (see Footnote 37) $\nu_e = \hat{\nu}^{ei}(v_{Te}/v_e)^3$ and bounce frequency $\omega_{be} = \omega_{be}^T v_e/v_{Te}$ Equation (52), resulting in[40]

$$v_{cut} = v_{Te}\sqrt[4]{\hat{\nu}^{ei}/\omega_{be}^T} \tag{63}$$

Meanwhile the proper limits on pitch-angle are determined by the deflection requirement $\lambda B = 1$, which has to met somewhere along the field line for a particle to be trapped. Consequently the trapped particle are characterised by pitch-angles $\lambda > 1/B_{max}$ with $B_{max} = \max\{B(l)\}$ being the global maximum field strength along the field line.

Unlike for D_0 it is not possible to solve Equation (62) directly for the frequency shift since it is non-local as a result of the bounce average. Furthermore as $\hat{\phi}$ is a Fourier coefficient it is in general a complex quantity such that the shift in real frequency $\mathrm{Re}[\delta\omega]$ and growth rate $\mathrm{Im}[\delta\omega]$ as a result of the trapped electrons are not easily extracted. The latter issue is alleviated by multiplying Equation (62) with $\hat{\phi}^*$ and integrating along the field line in so-called ballooning space[41] $\oint \mathrm{d}l\,/B$ resulting in

$$\frac{\delta\omega}{\omega_0}\frac{\omega_{\star e}}{\omega_0}\Gamma_0\oint\left|\hat{\phi}\right|^2\frac{\mathrm{d}l}{B} = \left(\omega_0 - \omega_{\star e}\right)\frac{2}{\sqrt{\pi}}\oint\mathrm{d}l\int_{x_{cut}}^\infty\mathrm{d}x\int_{1/B_{max}}^{1/B(l)}\mathrm{d}\lambda\,\frac{x^2\exp\left(-x^2\right)}{\omega_0 - \overline{\omega_{de}}(x,\lambda) + i\nu_e(x)}\frac{\overline{\hat{\phi}}(\lambda)\hat{\phi}^*(l)}{\sqrt{1-\lambda B(l)}}$$

[40] Here the distinction between $\hat{\nu}^{ei}$ and $\nu_{90^\circ}^{ab}$ according to Equation (17) has been dissolved, as this would merely result in a multiplicative correction of 0.93 to Equation (63).

[41] The appearance of the $1/B$ factor is a geometric effect resulting from the Clebsch representation of the magnetic field Equation (5), which makes the integration in ballooning-space actually equivalent to taking an average over the flux surface [46]. This is however beyond the scope of the thesis to discuss.

where the integration along the field line wraps around the torus until the field line "bites its own tail" again, normalised speed coordinates $x = v_e/v_{Te}$ have been used, the sum over σ simply gives a factor of two as there is no explicit dependence of the direction along which the field is traversed, and all functional dependencies have been made explicit. Aside from possibly the frequency shift $\delta\omega$ all quantities on the left-hand side are now real-valued such that the frequency shift and growth due to trapped electrons can directly be attributed to the real and imaginary parts of the integral over the trapped electron response on the right-hand side. Note that the integration order matters on the right-hand side, as the position along the field line determines the upper limit of admissible pitch-angles and in which magnetic well the bounce averages are appropriate to take. Exactly the same populations of trapped particles can be uniquely determined by reversing the order of integration [126, 137]

$$\oint \mathrm{d}l \int_{1/B_{max}}^{1/B(l)} \mathrm{d}\lambda \rightarrow \int_{1/B_{max}}^{1/B_{min}} \mathrm{d}\lambda \sum_{w(\lambda)} \int_{l_{1[w]}}^{l_{2[w]}} \mathrm{d}l \tag{64}$$

where $B_{min} = \min\{B(l)\}$ is the global minimum field strength along the field line. In Equation (64) the interval over λ covers all positions along the field line where trapped particles reside, and the different populations of trapped particles with a given pitch-angle λ' are now distinguished by their spatial separation among the different trapping wells, which are demarcated by the bounce points $l_{1[w]}, l_{2[w]}$ determined by the deflection condition $\lambda' B(l) = 1$. By this reversal of integration order, the position-dependent terms on the right-hand side naturally take the form seen in the bounce average as expressed in pitch-angle coordinates Equation (52) such that the solution to the perturbative frequency shift follows as[42]

$$\frac{\delta\omega}{\omega_0} = \frac{2}{\sqrt{\pi}} \frac{\omega_0 - \omega_{\star e}}{\Gamma_0} \frac{\omega_0}{\omega_{\star e}} \int_{1/B_{max}}^{1/B_{min}} \mathrm{d}\lambda \sum_{w(\lambda)} \int_{x_{cut}}^{\infty} \mathrm{d}x \, \frac{x^2 \exp\left(-x^2\right)}{\omega_0 - \overline{\omega_{de}} + i\nu_e} \left|\overline{\hat{\phi}}\right|^2 L_{eff[w]} \Big/ \oint \left|\hat{\phi}\right|^2 \frac{\mathrm{d}l}{B} \tag{65}$$

where the "effective well length" $L_{eff[w]} = \int_{l_{1[w]}}^{l_{2[w]}} \frac{\mathrm{d}l}{\sqrt{1-\lambda B(l)}}$ has been introduced[43]. As a result of the reversal of the integration order the shift in real frequency and growth rate due to trapped electrons are now easily linked to the real and imaginary parts of the integral over the normalised particle speeds as all other quantities are real-valued.

3.4.1 Standard literature results and collisionality regimes

Unlike for the ion case, the frequency denominator in Equation (65) cannot be expanded based on the frequency ordering for TEMs Equation (47). Rather, in the literature it is common to define different regimes of collisionality for which the integrand can be approximated by neglecting the appropriate terms [120, 128]. To now rigorously understand how the TEM is driven unstable by the magnetic drift as highlighted by the intuitive waveform model in Section 2.1.2, and see how collisions could destabilise the TEM, these common literature limits are first explored independently. Then their extension to arbitrary collisionality will be made, which presents the first original result from this thesis.

In the extreme limit of the strongly dissipative regime $\overline{\omega_{de}} < \omega \sim \omega_{\star e} < \nu^{ei} < \omega_{be}$ the collisional dynamics are the most dominant process and the speed integral in Equation (65) can be approximated by

[42] To be precise, all bounce averages should also have a well label w, this is however omitted for notational simplicity.

[43] In literature it is more common call this the "bounce time" $\tau_{b[w]}$ of the well [11, 92, 126, 137], but this is an ill-naming convention as it is dimensionally incorrect and the actual bounce time is given by $\tau_{b[w]} = L_{eff[w]}/v$ and thus depends on the energy of trapped particles.

$$\begin{aligned}\frac{\delta\omega}{\omega_0} \approx & \frac{2}{\sqrt{\pi}}\frac{\omega_0-\omega_{\star e}}{\Gamma_0}\frac{\omega_0}{\omega_{\star e}}\int_{1/B_{max}}^{1/B_{min}}\mathrm{d}\lambda\sum_{w(\lambda)}\int_{x_{cut}}^{\infty}\mathrm{d}x\,\frac{x^2\exp\left(-x^2\right)}{i\hat{\nu}^{ei}/x^3}\left|\overline{\hat{\phi}}\right|^2 L_{eff[w]}\Big/\oint\left|\hat{\phi}\right|^2\frac{\mathrm{d}l}{B} \\ = & \frac{i}{\sqrt{\pi}}\frac{\omega_0}{\hat{\nu}^{ei}}\frac{1-\frac{\omega_0}{\omega_{\star e}}}{\Gamma_0}\underbrace{\int_{x_{cut}^2}^{\infty}\mathrm{d}z\,z^2\exp(-z)}_{=\Gamma(3,x_{cut}^2)}\int_{1/B_{max}}^{1/B_{min}}\mathrm{d}\lambda\sum_{w(\lambda)}\left|\overline{\hat{\phi}}\right|^2 L_{eff[w]}\Big/\oint\left|\hat{\phi}\right|^2\frac{\mathrm{d}l}{B}\end{aligned} \tag{66}$$

where the electron-ion velocity deflection frequency ν_D^{ei} Equation (18) has been used for ν_e as the diffusion in the direction of the velocity causes (de)trapping, a change of variables $z = x^2$ has been made and $\Gamma(n,\xi)$ is the upper incomplete gamma function. Typically the velocity cut-off is taken to be very small (despite the limit of strong collisionality) such that $\Gamma(3, x_{cut}^2) \approx 2$, or even completely omitted from the analysis. The resulting frequency shift $\delta\omega$ is then purely imaginary and as the leading order solution $\omega_0/\omega_{\star e} \leq 1$ corresponds to a growth rate $\gamma/\omega_0 \propto \omega_0/\hat{\nu}^{ei} > 0$, indicating instability. Interestingly the growth rate decreases with collisionality, indicating that detrapping dominates over trapping and the collisions have a benign effect on the dissipative TEM instability.

The other extreme limit is the collisionsless regime $\nu_e < \overline{\omega_{de}} < \omega \sim \omega_{\star e} < \omega_{be}$ and the collisional dynamics can be neglected altogether and the speed integral is approximated by

$$\frac{\delta\omega}{\omega_0} = \frac{2}{\sqrt{\pi}}\frac{\omega_0-\omega_{\star e}}{\Gamma_0}\frac{\omega_0}{\omega_{\star e}}\int_{1/B_{max}}^{1/B_{min}}\mathrm{d}\lambda\sum_{w(\lambda)}\int_{0}^{\infty}\mathrm{d}x\,\frac{x^2\exp\left(-x^2\right)}{\omega_0-\overline{\omega_{de}}}\left|\overline{\hat{\phi}}\right|^2 L_{eff[w]}\Big/\oint\left|\hat{\phi}\right|^2\frac{\mathrm{d}l}{B}$$

where the speed cut-off x_{cut} is lifted as collisions have become irrelevant. At a first glance it seems like this would not lead to an instability as $\delta\omega$ will be purely real-valued, however this neglects the possibility of a resonance where $\omega_0 \approx \overline{\omega_{de}}$ which causes the kinetic electron response to diverge. As the bounce-averaged electron drift frequency is given by

$$\overline{\omega_{de}}(x,\lambda) \approx v^2\overline{\boldsymbol{k}_\perp\cdot\left(\frac{\boldsymbol{e_b}}{\Omega_s}\times\boldsymbol{\nabla}_\perp\ln B\left[1-\frac{\lambda B}{2}\right]\right)} \equiv x^2\overline{\omega_{de}^T}(\lambda) \tag{67}$$

where the "vacuum plasma" approximation $\boldsymbol{\kappa} \approx \boldsymbol{\nabla}_\perp \ln B$ is made, pitch-angle coordinates have been used and the bounce average drift frequency of a particle at thermal speed $\overline{\omega_{de}^T}$ has been introduced for convenient normalisation, such a resonance will occur for trapped particles which have the correct resonant speed

$$x_{res} = \sqrt{\frac{\omega_0}{\overline{\omega_{de}^T}}} \tag{68}$$

provided that $\overline{\omega_{de}^T}$ and ω_0 have the same sign. If this satisfied there will always be a population of trapped electrons that are resonant since there is no speed cut-off in the absence of collisions.

To investigate whether such a resonance could lead to an instability the mode frequency is given a small imaginary part $\omega_0 \to \omega_0 + i\delta\gamma$ to lift the resonance, and after calculating the integral the speed the limit for marginal stability $\delta\gamma \downarrow 0$ is taken to see if the imaginary part of the resulting frequency shift also consistently vanishes. In Appendix K it has shown that this reduces to an instance of the Sothotski-Plemelj theorem along the real-line [138]

$$\lim_{\gamma\downarrow 0}\int_0^\infty \mathrm{d}x\,\frac{x^2\exp\left(-x^2\right)}{\omega_0-\overline{\omega_{de}}+i\delta\gamma} = \mathcal{P}\left\{\int_0^\infty \mathrm{d}x\,\frac{x^2\exp\left(-x^2\right)}{\omega_0-\overline{\omega_{de}^T}}\right\} - i\frac{\pi}{\overline{\omega_{de}^T}}\int_0^\infty \mathrm{d}x\,x^2\exp\left(-x^2\right)\delta(x^2-x_{res}^2) \tag{69}$$

where $\mathcal{P}$ denotes the Cauchy Principle Value and the Dirac-Delta takes care of whether the resonance can occur or not. Substituting Equation (69) result back in Equation (65) then gives the resulting growth rate as a result of drift resonances with trapped electrons

$$\frac{\gamma}{\omega_0} = \sqrt{\pi}\frac{\left(1-\frac{\omega_0}{\omega_{\star e}}\right)}{\Gamma_0}\int_{1/B_{min}}^{1/B_{max}} \mathrm{d}\lambda \sum_{w(\lambda)} \left(\frac{\omega_0}{\overline{\omega_{de}^T(\lambda)}}\right)^{3/2} \exp\left(-\frac{\omega_0}{\overline{\omega_{de}^T(\lambda)}}\right)\left|\overline{\hat{\phi}}\right|^2 L_{eff,w} \Big/ \oint \left|\hat{\phi}\right|^2 \frac{\mathrm{d}l}{B} \quad (70)$$

which is positive and such that resonances with the precession frequency of trappped particles provide the collisionless TEM instability mechanism, as first pointed out by Adam et al [134].

In Equation (70) it has tacitly been assumed that such a resonance does exist, which requires ω_{de} to have the same sign as ω_0 such that the resonance speed Equation (68) $x_{res} \in \mathbb{R}$. As the leading order mode frequency Equation (61) is always in the electron diamagnetic direction this will be satisfied whenever $\omega_{\star e}\overline{\omega_{de}} > 0$. As the precession frequency is due to the particle drifts in the inhomogeneous magnetic field the magnetic geometry essentially completely determines the stability properties of the plasma against collisionless TEMs. By decomposing the wavevector in Clebsch coordinates as $\boldsymbol{k}_\perp = k_\psi \boldsymbol{\nabla}\psi + k_\alpha \boldsymbol{\nabla}\alpha$ the precession frequency can be rewritten as [126]

$$\overline{\omega_{de}} = \overline{\boldsymbol{k}_\perp \cdot \boldsymbol{v_{de}}} = k_\psi \overline{\boldsymbol{v_{de}} \cdot \boldsymbol{\nabla}\psi} + k_\alpha \overline{\boldsymbol{v_{de}} \cdot \boldsymbol{\nabla}\alpha} = \frac{1}{e\tau_{be}}\left(\frac{\partial \mathcal{J}}{\partial \psi}k_\alpha - \frac{\partial \mathcal{J}}{\partial \alpha}k_\psi\right) \quad (71)$$

where Equation (8) was used for the bounce-averaged guiding centre drifts. With this representation of the bounce average drift, the stability criterion can be assessed by

$$\omega_{\star e}\overline{\omega_{de}} = \frac{T_e}{e^2\tau_{be}}\frac{\mathrm{d}\ln n_e}{\mathrm{d}\psi}\left(\frac{\partial \mathcal{J}}{\partial \alpha}k_\psi k_\alpha - k_\alpha^2 \frac{\partial \mathcal{J}}{\partial \psi}\right).$$

In general the density gradient will be negative as a result of centrally peaked profiles such that the sign of the terms in brackets determines whether a resonance can occur. In the special case of an omnigeneous magnetic field in which the average radial drift $\overline{\boldsymbol{v_{ds}} \cdot \boldsymbol{\nabla}\psi} = 0 = \frac{\partial \mathcal{J}}{\partial \alpha}$ vanishes (like in tokamaks and optimised stellarators), whether or not a resonance will occur is completely determined by the "profile" of the second adiabatic invariant $\mathcal{J}$. In a max-$\mathcal{J}$ configuration where $\mathcal{J}$ peaks at the plasma centre and $\frac{\partial J}{\partial \psi} < 0$ everywhere, the signs of the frequencies will thus be reversed $\omega_{\star e}\overline{\omega_{de}} < 0$ such that a resonance cannot occur, making them stable against TEMs as first pointed out by Proll et al [95]. Tokamaks in contrast are neither maximum-$\mathcal{J}$ nor minimum-$\mathcal{J}$ such that there will be always be some population of trapped particles for which $\omega_{\star e}\overline{\omega_{de}} > 0$ and TEMs are expected to be unstable, explaining why TEMs are observed to be one of the root causes for the observed transport in present day experiments, as highlighted in Section 1.1.

3.4.2 Going beyond literature: the domain splitting approach

Although insightful to the different TEM instability mechanisms, these literature results consider only the asymptotic limits where either the collision frequency or the precession frequency resonance dominates in the denominator of Equation (65). It is unsure if and how these results can be extrapolated, as Equation (70) predicts the growth rate a finite growth rate at low collisionality whereas Equation (66) predicts the growth rate to diverge as the collisionality is decreased, and these branches should continuously match in some intermediate collisionality regime. A remedy to this issue comes from the realisation that these literature regimes neglect the fact that both frequencies have a qualitatively opposite dependence on the (normalised) particle speed $\nu_e \propto 1/x^3$, $\overline{\omega_{de}} \propto x^2$. Consequently even at extremely low collisionality there will be fraction of low energy particles with a high collision frequency that exceeds their precession frequency, and vice versa for high collisionality. Therefore these regimes are not applicable over

the full speed integral even though they are applied as such in literature. What will determine the dominant driving mechanism for a given particle energy is whether $\overline{\omega_{de}}/\omega_0$ or ν_e/ω_0 is largest, which using Equations (67) and (68) can be written as

$$\frac{\overline{\omega_{de}}}{\omega_0} = \left(\frac{x}{x_{res}}\right)^2 \qquad \frac{\nu_e}{\omega_0} = \left(\frac{x_\nu}{x}\right)^3$$

where another characteristic collision speed has been introduced as

$$x_\nu = \sqrt[3]{\frac{\hat{\nu}^{ei}}{\omega_0}} \tag{72}$$

by means of an analogy with the resonant speed x_{res} such that these parameters give the particle energies at which the precession and collision frequency are comparable in magnitude to the leading order mode frequency ω_0. Based on these parameters a critical speed x_{crit} can be defined at which the magnitude of the collision and precession frequency are equal $\nu_e(x_{crit}) = |\overline{\omega_{de}}|$ and the dominant driving mechanism will shift from dissipative to collisionless

$$x_{crit} = \sqrt[5]{\frac{\hat{\nu}^{ei}}{\left|\overline{\omega_{de}^T}\right|}} = |x_\nu|^{3/5}|x_{res}|^{2/5} \tag{73}$$

where the absolute value takes care of any possible signs in the frequencies[44] such that $x_{crit} \in \mathbb{R}^+$. Consequently as a first crude approximation the integral over particle speeds could be split into a purely dissipative ($x < x_{crit}$) and purely collisionless ($x > x_{crit}$) domain. To a lesser degree of approximation, rather than completely neglecting the other driving mechanism in each domain it could be included as a small correction such that

$$\frac{1}{\omega_0 - \overline{\omega_{de}}(x) + i\nu_e(x)} \approx \begin{cases} \dfrac{1}{\omega_0 + i\nu_e(x)}\left(1 + \dfrac{\overline{\omega_{de}}(x)}{\omega_0 + i\nu_e(x)}\right) & x < x_{crit} \\ \dfrac{1}{\omega_0 - \overline{\omega_{de}}(x)}\left(1 - \dfrac{i\nu_e(x)}{\omega_0 - \overline{\omega_{de}}(x)}\right) & x > x_{crit} \end{cases} . \tag{74}$$

In Appendix L it is shown that near the critical speed, where the approximation is most likely to break down, Equation (74) is in fact a decent approximation provided that the critical speed does not coincide with the resonance speed. In terms of this domain splitting approximation the frequency shift due to trapped electrons is given as

$$\begin{aligned} \frac{\delta\omega}{\omega_0} =& \frac{2}{\sqrt{\pi}} \frac{\left(\frac{\omega_0}{\omega_{\star e}} - 1\right)}{\Gamma_0} \int_{1/B_{max}}^{1/B_{min}} \mathrm{d}\lambda \sum_{w(\lambda)} \left[\int_{x_\nu^{3/4}\sqrt[4]{\frac{\omega_0}{\omega_{be}^T(\lambda)}}}^{x_{crit}(\lambda)} \mathrm{d}x \, \frac{x^2 \exp\left(-x^2\right)}{1 + i\left(\frac{x_\nu}{x}\right)^3} + \cdots \right. \\ &+ \frac{1}{x_{res}^2(\lambda)} \int_{x_\nu^{3/4}\sqrt[4]{\frac{\omega_0}{\omega_{be}^T(\lambda)}}}^{x_{crit}(\lambda)} \mathrm{d}x \, \frac{x^4 \exp\left(-x^2\right)}{\left(1 + i\left(\frac{x_\nu}{x}\right)^3\right)^2} + \int_{x_{crit}(\lambda)}^{\infty} \frac{x^2 \exp\left(-x^2\right)}{1 - \left(\frac{x}{x_{res}(\lambda)}\right)^2} + \cdots \\ &\left. -ix_\nu^3 \int_{x_{crit}(\lambda)}^{\infty} \frac{\exp\left(-x^2\right)}{x\left(1 - \left(\frac{x}{x_{res}(\lambda)}\right)^2\right)^2} \right] \left|\overline{\hat{\phi}}(\lambda)\right|^2 L_{eff[w]}(\lambda) \Big/ \oint \left|\hat{\phi}(l)\right|^2 \frac{\mathrm{d}l}{B} \end{aligned} \tag{75}$$

where the speed-cut off Equation (63) has been rewritten in terms of x_ν and ω_0 has been taken out of the denominators in all integrals which naturally makes the different speed parameters x_{res}, x_ν

[44] Although the collision frequency $\hat{\nu}^{ei}$ is certainly positive, the lowest order mode frequency ω_0 which enters the definition of x_ν will in general not always positive since $\omega_0 \sim \omega_{\star e} \propto -\frac{\mathrm{d}\ln n_e}{\mathrm{d}\psi}$. Consequently if the density profile would not be peaked at the centre the diamagnetic drift frequency could be negative.

appear. The real power of this novel approach is twofold; first by recalling the dependence of the critical speed on x_{res}, x_ν (Equation (73)) and letting $x_{res} \to \infty$ and $x_\nu \gg 1$ only the first term remains and Equation (75) reduces to the result in the strongly dissipative regime Equation (66), while letting $x_\nu \to 0$ only the third term remains and Equation (75) reduces to the result for the collisionless regime Equation (70). Thus Equation (75) can be reduced to the "classic" results from literature. But second and foremost, Equation (75) provides predictive capability for the growth rate of TEMs. If the critical speed x_{crit} would exceed the resonance speed x_{res} then the resonance with the precession frequency would be avoided, and in absence of a resonance it is expected that the growth rates would be strongly quenched. Because of the dependence of x_{crit} on x_ν Equation (73) this sets a threshold collision frequency

$$x_{crit} > |x_{res}| \Rightarrow |x_\nu| > |x_{res}| \Rightarrow \hat{\nu}^{ei} > |\omega_0| \left| \frac{\omega_0}{\overline{\omega_{de}^T}(\lambda)} \right|^{3/2} \tag{76}$$

above which collisions are capable to filter out the resonance. In Appendix L this prediction of the threshold collision frequency is tested by numerically integrating the full speed integral from Equation (65) $\int_{x_{cut}}^{\infty} \mathrm{d}x \, \frac{x^2 \exp(-x^2)}{\omega_0 - \overline{\omega_{de}} + i\nu_e}$ for a wide range of x_ν, x_{res} parameters to get an "exact" answer without invoking the domain splitting approximation. There it is shown that the threshold frequency prediction is perfectly reproduced by the reduction in magnitude of this integral in the resonant case $x_{res} \in \mathbb{R}$ whenever $|x_\nu|$ exceeds $|x_{res}|$. But it is also found that when $|x_\nu| < |x_{res}|$ the collisions could add to the resonant instability drive or (as expected) that collisions form the destabilisation mechanism when the resonance is not possible $x_{res} \in \mathbb{C}$. This is investigated in more detail below, when the role of geometry is taking into account.

3.5 Realistic investigation of geometric effects

Although the results obtained by the domain splitting approach Section 3.4.2 provide a nice first qualitative insight about when and how collisions will affect the growth rate of TEMs, the threshold collision frequency Equation (76) is not the most useful metric because the criterion depends on the bounce frequency which depends on the pitch-angle and even more strongly on the magnetic geometry. Thus each population of trapped particles along the field line will have their own threshold collision frequency, whereas the collision frequency itself is constant along the field line due to its dependence on the plasma profiles Equation (17). As it is the combined effect of all trapped particles that results in instability, it is therefore imperative to take into account the integration over pitch-angle to determine the actual growth rate of TEMs. Furthermore, even if there were a unique threshold collision frequency for all trapped particles, it would depend on the perpendicular wavelength $k_\perp$ of the perturbations through ω_0, and even if this effect were negligible for the integration over trapped particle, the total frequency total frequency shift $\delta\omega/\omega_0$ would still be dispersive through the integral prefactor in Equation (65). This dispersive

Therefore to investigate the influence of collisionality on the growth rate Equation (65) has to be evaluated numerically, which has the benefit that actual realistic magnetic geometries can be used to identify the populations of trapped particles and assess whether the influence of collisions is universal or differs between magnetic configurations. It is particularly interesting to see if collisions could spoil the stability properties of max-$\mathcal{J}$ configurations. For the numerical integration a code which has been recently used to find the Available Energy of trapped particles [50] involving the same integration over energies and pitch-angle has been retrofitted to use the actual integrand of Equation (65). To account for realistic geometries, the Geometric Interface for Stellarators and Tokamaks (GIST) code is used to generate all geometric information about the magnetic field from a calculated magnetic equilibrium configuration [139]. To facilitate a potential comparison with the numerical simulations that follow in Chapter 4 for simulations,

the same geometries of the DIII-D tokamak and HSX/W7-X stellarators are considered for the numerical integration, which are highlighted in Figure 13. The differences between these geometries are striking, with the axisymmetry and conventional torus shape of DIII-D made very apparent in Figure 13a. This in contrast to the twisting shape of the flux surface in seen in the stellarator configurations. The most apparent features of HSX are the helically shaped contours of the magnetic field and four-fold discrete toroidal symmetry resulting in the square-like top view as seen in Figure 13b. Meanwhile the most noticeable aspects of W7-X are the nearly poloidally closed contours of the magnetic which indicate the configuration approximates quasi-isodynamicity [46,140], and the five-fold discrete toroidal symmetry resulting in a pentagon-like top view of W7-X seen in Figure 13c.

For this comparison between theory and simulation some differences have to be taken into account. In simulations what is set is the binormal wavenumber k_y, which is related to k_α with a dimensional prefactor to have the proper dimension of a inverse meters rather than the perpendicular wavenumber $k_\perp$. These wavenumbers are related through [16]

$$k_\perp = \sqrt{g^{xx}k_x^2 + 2g^{xy}k_xk_y + g^{yy}k_y^2} \tag{77}$$

where g^{ij} are elements of the metric tensor for the coordinate system used in simulations (more about that in Chapter 4) and k_x is the radial wavenumber similarly related to k_ψ with a dimensional prefactor. Consequently the perpendicular wavenumber varies with distance along the field line for a given set of k_x, k_y. Therefore to bridge the gap to theory where ω_0 has been considered as constant in deriving Equation (65), the weighted average of the wavenumber $\langle k_\perp \rangle$ along the field line is considered according to the method from [143,144]

$$\left\langle k_\perp^2 \right\rangle = \frac{\int k_\perp^2 \left|\hat{\phi}\right|^2 \frac{\mathrm{d}l}{B}}{\int \left|\hat{\phi}\right|^2 \frac{\mathrm{d}l}{B}}. \tag{78}$$

To further accommodate normalisation for numerical implementation[45] all frequencies in Equation (65) are normalised by the diamagnetic frequency $\omega_{\star e}$ such that the numerical integration friendly form of Equation (65) is

$$\frac{\delta\omega}{\langle\omega_0\rangle} = \frac{2}{\sqrt{\pi}} \frac{\left\langle \frac{\omega_0}{\omega_{\star e}} \right\rangle - 1}{\langle \Gamma_0 \rangle} \left\langle \frac{\omega_0}{\omega_{\star e}} \right\rangle \int_{1/B_{max}}^{1/B_{min}} \mathrm{d}\lambda \sum_{w(\lambda)} \int_{x_{cut}}^{\infty} \mathrm{d}x \, \frac{x^2 \exp\left(-x^2\right)}{\left\langle \frac{\omega_0}{\omega_{\star e}} \right\rangle - \frac{\overline{\omega_{de}}}{\omega_{\star e}} + i\frac{\nu_e}{\omega_{\star e}}} \left|\overline{\hat{\phi}}\right|^2 L_{eff[w]} \Big/ \oint \left|\hat{\phi}\right|^2 \frac{\mathrm{d}l}{B} \tag{79}$$

where the short-hand notation $\langle F \rangle = F(\langle k_\perp \rangle)$ for any function of the perpendicular wavenumber is introduced.

Two additional simplifications are made for the numerical integration. First, as the most unstable modes are typically the most radially extended ones which can feed from the full density gradient in the plasma [96], the radial wavenumber is set to $k_x = 0 (= k_\psi)$. This approximation does somewhat blur the line between omnigeneous and non-omnigeneous magnetic fields as it makes the radial drifts disappear from the precession frequency Equation (71). Second, the electrostatic potential is approximated to be a "flute-mode" $\hat{\phi}(l) \approx \hat{\phi}_0$ which is constant along the field line. This approximation is definitely more severe and not very realistic, however it is a common approximation made in literature to get semi-analytical results which for tokamaks at least gives results that are within a factor of 2 of using more realistic mode structure [83,134,145,146].

[45] Technically speaking such normalisation is not strictly required, as Equation (65) is already inherently dimensionless. Nevertheless normalisation remains a good practice and it is even necessary to respect the inherent normalisations from GIST/GENE in order to "feed" the geometric information into the integrals.

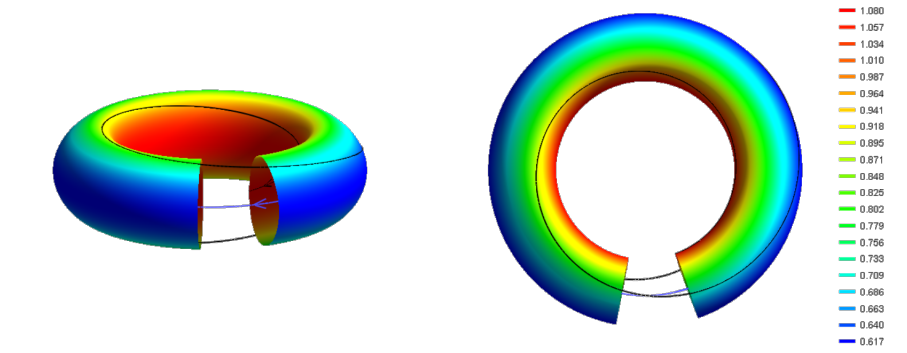

(a)

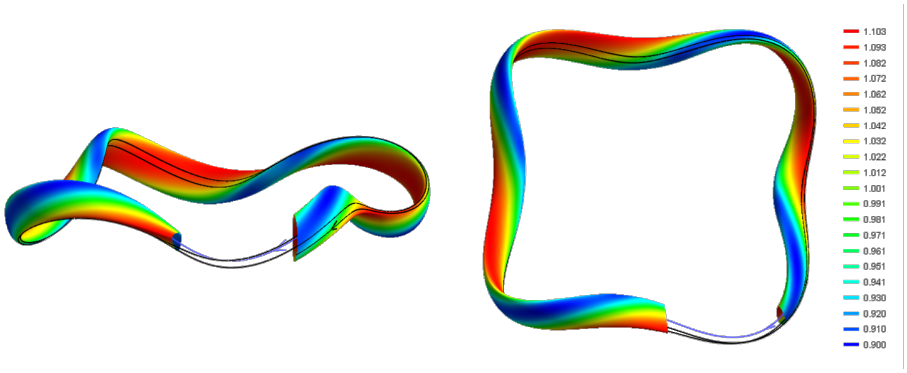

(b)

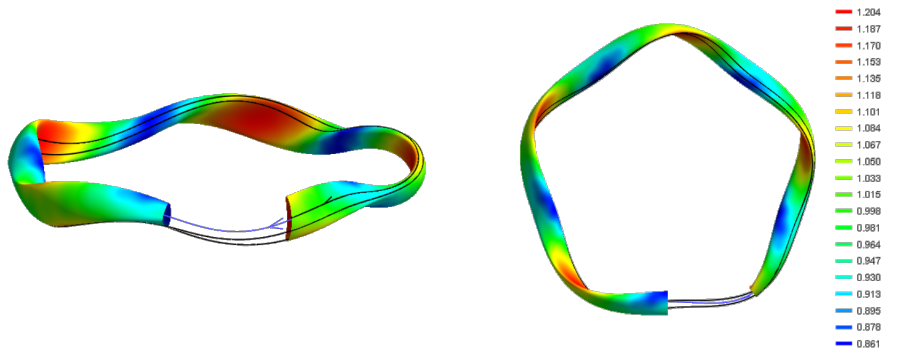

(c)

Figure 13: Magnetic geometries used for the perturbative calculation showing both a side- and top view of what the flux surfaces look like for (a) DIII-D,(b) HSX, and (c) W7-X respectively. The contours give the magnetic field strength B normalised to its average on the flux surface, while the blue/black lines correspond to the to the magnetic axis and a magnetic field spanning two poloidal turns on the flux surface respectively. These magnetic equilibria are the result of a reconstruction from experimental measurements using the EFIT code [141] in case of DIII-D and full 3D equilibrium calculation using the VMEC code [142] for HSX and W7-X.

i

Nevertheless invoking the "flute-mode" approximation allows to emphasise any inherent differences between the magnetic geometries as result of the distribution of the trapped particles among the different magnetic wells and the possibility of a resonance as a result of the profile of the second adiabatic invariant $\mathcal{J}$. Furthermore as the leading order dispersion relation $D_0(\omega, \boldsymbol{k}_\perp, \hat{\phi}) = 0$ is solved by Equation (60) regardless of the mode structure along the field line, any arbitrary choice of $\hat{\phi}(l)$ would provide a consistent solution to the perturbative paradigm of Equation (55).

With these approximations in mind Equation (79) is solved numerically by scanning over the normalised wavenumber $k_y\rho_{ci}$, where the gyroradius at ion sound speed ρ_{ci} is used as to have the same normalisation as the GENE code[46] to facilitate comparison with the simulation results from Chapter 4. The collision frequency is also scanned over in the normalised form of $\nu^{ei}/\omega_{\star e}^{\text{phys}}$, where $\omega_{\star e}^{\text{phys}} = T_e/(eB_0 a\rho_{ci})$, with B_0 denoting the magnetic field strength on the magnetic axis. This choice of normalisation of the collision frequency removes any inherent scale factor related to the turbulence[47] as $\omega_{\star e}^{\text{phys}}$ corresponds to the electron diamagnetic frequency at a wavenumber and density gradient of $k_y\rho_{ci} = a/L_n = 1$. Details about the normalisation process of Equation (79) can be found in Appendix M.2.

The results for the frequency shift $\delta\omega/\langle\omega_0\rangle$ as a function of binormal wavenumber and collision frequency for the three geometries are in shown in Figure 14. Regardless of the value of the collision frequency or geometry, it can be seen that the relative perturbation $\delta\omega/\langle\omega_0\rangle$ increases along with the poloidal wavenumber. This is a consequence of the fact that the perpendicular wavenumber $k_\perp$ is directly proportional to the poloidal wavenumber k_y according to Equation (78), and the leading order solution for ω_0 Equation (61) decreases with wavenumber. Consequently at large $k_y\rho_{ci}$ the perturbative approach will not provide a valid solution to the original quasi-neutrality condition Equation (54). Nevertheless, even if the perturbative approach cannot yield a quantitatively valid answer, it can still at least qualitatively describe what the influence of collisions on the growth rate $\gamma = \text{Im}[\delta\omega/\langle\omega_0\rangle]$ of TEM will be since $D_1(\omega, \boldsymbol{k}_\perp, \hat{\phi})$ (see right-hand side of Equation (62)) contains all of the trapped electron dynamics which are responsible for driving the instability. A universal observation from Figure 14 is that regardless of the geometry and collisionality there is always instability $\gamma > 0$, so the collisions do not lead to absolute damping ($\gamma < 0$) of the perturbations. More interestingly are the differences between geometries. It can be seen that in stellarator geometry the real frequency shift is larger than in the tokamak case. In contrast the instability is much worse in tokamaks, where the growth rates are larger and also become significant at lower wavelenghts. The most interesting difference is the apparent lack of destabilisation as a result of collisionality in DIII-D, which appears in both stellarator. This feature is most prominent in W7-X however where the growth rates at low collisionality are much lower which can be attributed to the favourable max-$\mathcal{J}$ property of the magnetic configuration.

[46] This results in an additional translation factor of $v_{Ti}/c_{s,i} = \sqrt{2\tau}$ between the normalised binormal wavenumber to the normalised perpendicular wavenumber $k_\perp\rho_{Ti}$ appearing in theory besides Equation (78).

[47] If this normalisation were not done but the collision frequency was simply varied as $\nu^{ei}/\omega_{\star e}$ then the actual physical collision frequency ν^{ei} would increase as k_y is varied which would complicate the interpretation of the results.

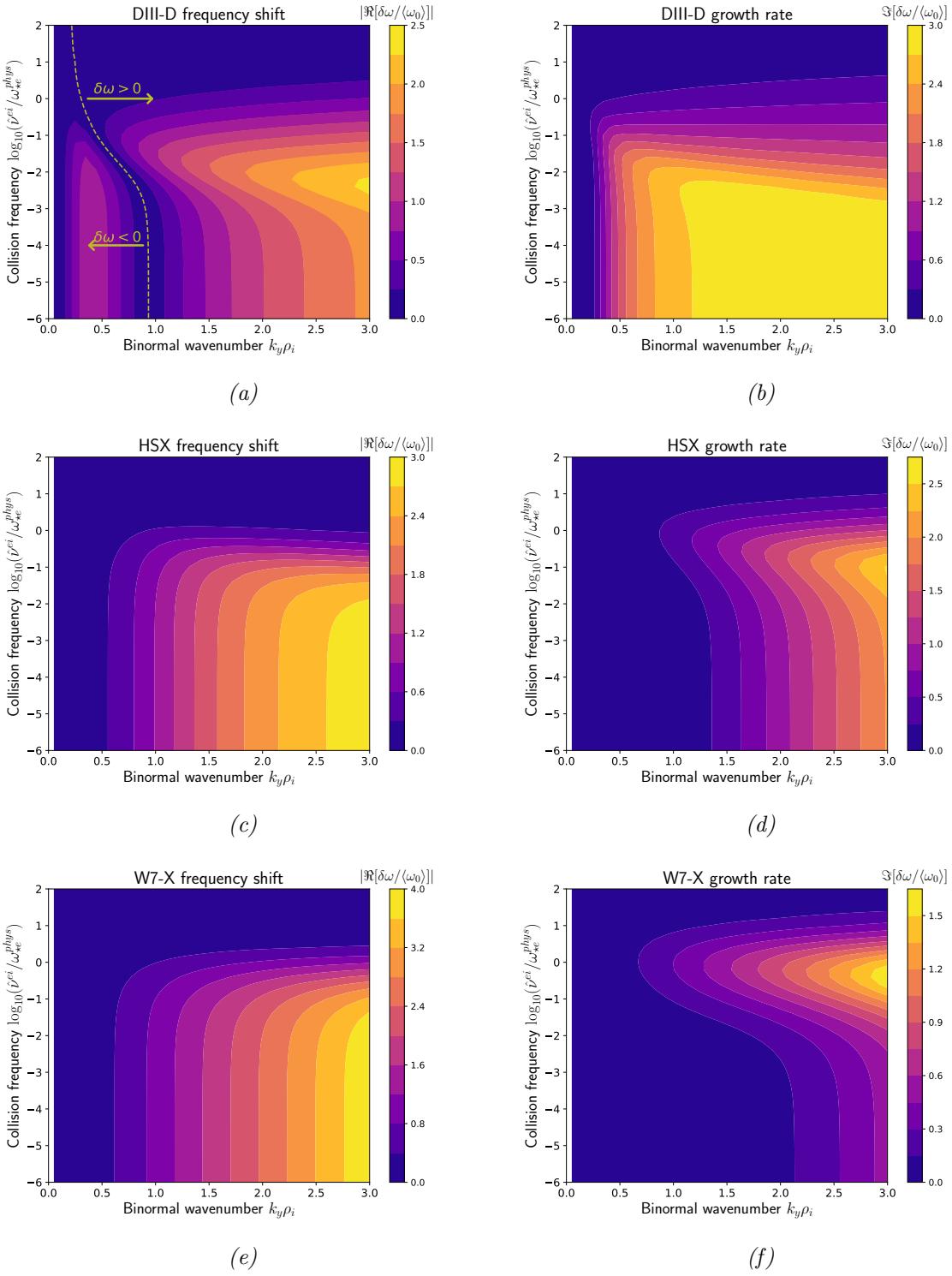

Figure 14: Results for the full perturbative frequency shift $\delta\omega/\langle\omega_0\rangle$ for different magnetic geometries, showing (a) real- and (b) imaginary parts in DIII-D, (c) real- and (d) imaginary parts in HSX, and (e) real- and (f) imaginary parts in W7-X. Note that the coloirbar has been adapted such that in all plots bright colours indicate a large perturbation and dark colours indicate small perturbation, and the collision frequency is plotted logarithmically whereas the wavenumber is plotted linearly. In case of DIII-D the real frequency shift is both negative and positive as indicated in (a), whereas for HSX and W7-X the real frequency shift is negative over the full parameter range.

Continuing with the analysis of the growth rates, the shape of the contours seem to suggest that the growth is rather insensitive to the collision frequency in the low collisionality regime, then starts to increase in an intermediate collisionality regime, until it makes a turnover and decreases again at high collisionality regime. To further investigate this behaviour and see if there might be a universal scaling between the growth rate and collision frequency in the different geometries, for several fixed wavenumbers the logarithm of the growth rate is traced over with collisionality. Additionally this allows to zoom in on what happens in the low k_y region of the contours where the growth rates are so small they are indistinguishable from zero. This is shown in Figure 15, where indeed the curves reveal differences between low and high k_y.

To investigate how the growth rate scales with the collision frequency, the slopes of the lines are estimated in different collisionality regimes by the differences between their ends points, which results in power-law scalings. The general trend of all lines, however, is that after a turnover regime at intermediate collisionality where the curves bulge, all curves are decaying with collision frequency at high collisionality. This turnover regime corresponds to the observation in Appendix L that for a collision parameter below threshold ($x_\nu < x_{res}$) the collisions add to the instability drive from resonance by increasing the imaginary part of the speed integral. To check whether this decay is universal, the slopes of the curves after turnover are averaged[48] to give a power-law $\gamma \propto \left(\hat{\nu}^{ei}\right)^{-(0.8\text{-}0.9)}$ at high collisionality, which is nearly the same for all devices. Perhaps surprisingly the exponent of the power law is not -1 as would be expected from Equation (66). Initially this was believed to be caused by the non-negligible speed cut-off x_{cut} at such high collisionalities for which the upper incomplete gamma function in Equation (66) deviates considerably from 2.0, however a separate calculation with this cut-off suppressed showed only marginal differences in the exponent. Rather it was found that the influence of the averaging window for the slope influenced the exponent more significantly. A scaling closer to -1 could perhaps be achieved by extending the numerical integration to significantly higher collisionalities to increase the averaging window, but this was not pursued.

In contrast at low collisionality before the curves turn over, the slopes are either virtually flat or clearly positive over a few orders of magnitude of collisionality depending whether the wavenumber $k_y\rho_{ci}$ is low or high. For each geometry, a separate power-law is determined by averaging over the slopes of the near-flat curves and the positively sloping curves. For DIII-D all curves are considered to be flat, whereas for HSX and W7-X all but the curves for lowest two and three wavenumbers respectively are considered flat. For the flat regime[49] this again leads to a common scaling law $\gamma \propto \left(\hat{\nu}^{ei}\right)^{-(0.02\text{-}0.04)}$ showing a negligible dependence on collisionality and indicating that the instability is driven by a resonance.

Lastly, for the positively sloping regime, an exception is made for DIII-D where the growth rate of the lowest wavenumber $k_y\rho_i = 0.25$ the only which is destabilised by collisions. Therefore the slope from this curve is taken into account for comparison with the slopes in HSX/W7-X. Two different power-laws are found[50], with the growth rate in DIII-D scaling as $\left(\hat{\nu}^{ei}\right)^{0.17}$ whereas in HSX and W7-X it scales as $\left(\hat{\nu}^{ei}\right)^{0.79\text{-}0.81}$. This is difference is fully explainable by the fact that the $k_y\rho_i = 0.25$ curve in DIII-D is in the turnover process from collisionless to

[48] For this averaging procedure the slope of all curves are averaged over the window of the last decade and a half of the collision frequency, i.e. $\log_{10}(\hat{\nu}^{ei}/\omega_{\star e}^{\text{phys}}) \in [0.5, 2.0]$

[49] For this averaging procedure different windows of the collision frequency are used for the different curves to respect their turn-over regions. For DIII-D the slope of all flat curves is determined on the interval $\log_{10}(\hat{\nu}^{ei}/\omega_{\star e}^{\text{phys}}) \in [-6, -2]$. For HSX the intervals that have been used are $[-6, -2], [-6, -2.5]$ and $[-6, -3.5]$ for wavenumbers $k_y\rho_i > 1.5, ky\rho_i = 1.03, k_y\rho_i = 0.74$ respectively. For W7-X the interval $[-6, -3]$ is used for $k_y\rho_i > 1.5$ and $[-6, -4.5]$ for $k_y\rho_i = 1.03$.

[50] In DIII-D the $k_y\rho_i = 0.25$ slope is determined in the range $[-3.5, -1.5]$ and no averaging has taken place as there is only a single wavenumber. For HSX the $k_y\rho_i = 0.25$ slope is determined on $[-6, -1.5]$ while the $k_y\rho_i = 0.54$ slope is determined on $[-5.5, -1.0]$. Lastly for W7-X the slopes of the $k_y\rho_i = 0.25, 0.54$ curves is determined on $[-6, -1.5]$ while the slope of the $k_y\rho_i = 0.74$ curve is determined on the interval $[-5.5, -1.5]$.

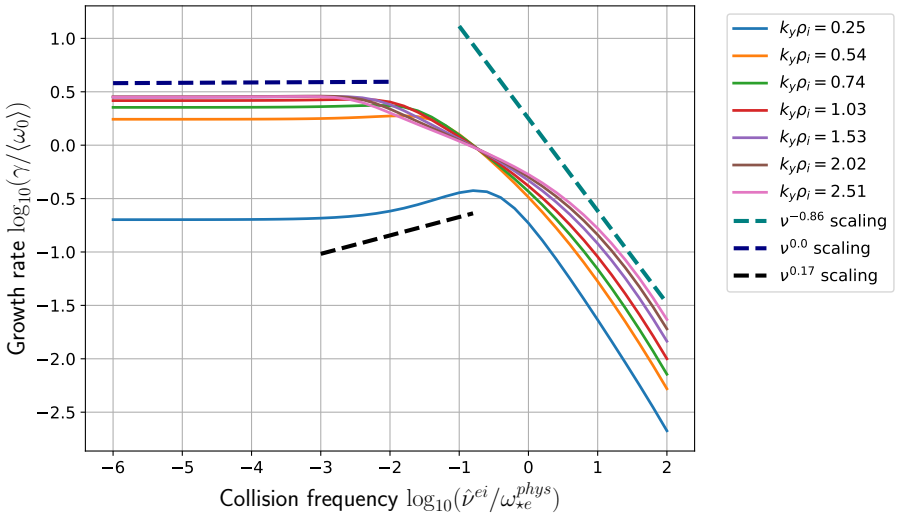

(a)

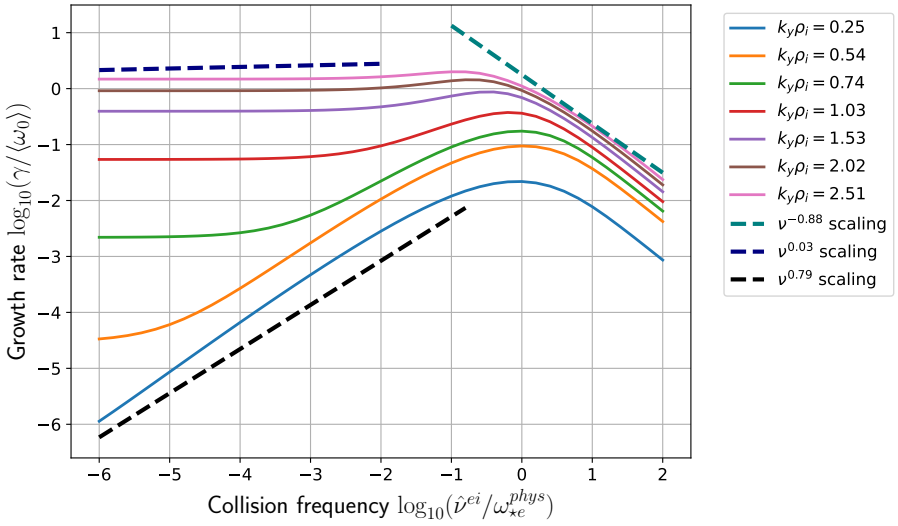

(b)

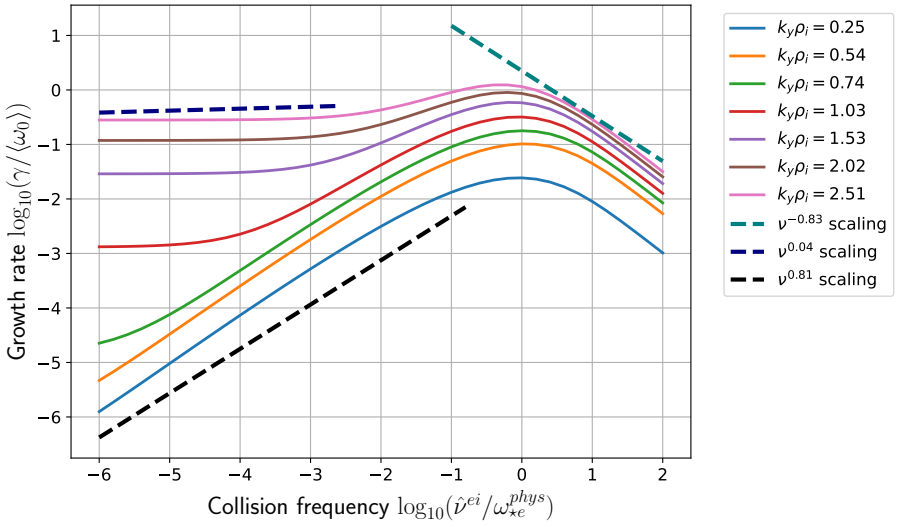

(c)

Figure 15: Growth rate vs collision frequency on a double logarithmic scale for binormal wavenumbers $k_y\rho_i = [0.25, 0.54, 0.74, 1.03, 1.53, 2.02, 2.51]$ for (a) DIII-D, (b) HSX and (c) W7-X. The power law scalings are obtained by estimating the slope of the straightlines by the end-points of the different collisionality regimes.

dissipative dynamics, whereas the selected low $k_y\rho_i$ stellarator curves maintain their slope at low collisionality. This indicates that as $\hat{\nu}^{ei} \to 0$ the growth rate would vanish as well and there would be no collisionless TEM at these low wavenumbers. This is further supported by the fact that the exponent of 0.8 is close to a linear scaling of the growth rate with the collision frequency, which would correspond to the expected growth rate resulting from the expansion of the $1/(\omega_0 - \overline{\omega_{de}}(x) + i\nu_e)$ denominator above the critical speed Equation (74) occurring in the domain-splitting approximation of Section 3.4.2 in case that the resonance is not possible. Based on the fact that the precession frequency Equation (71) increases with k_y, whereas the lowest order mode frequency decreases with k_y, it would indeed be expected that at the low wavenumbers, where this scaling is found, the resonant drive would be an inefficient instability mechanism as only very few high energetic particles will have the correct resonant speed.

4 Simulation results

In Chapter 3 the gyrokinetic framework developed in Chapter 2 was investigated analytically to investigate how TEMs are influenced by collisions, but to keep things tractable quite some assumptions and approximations were made along the way. These place constraints on the instabilities which can accurately be described by this theory, and furthermore the method is limited to providing predictions for the growth rate whereas the spatial structure of perturbations along the field line remains unknown.

These restrictions will be lifted in this chapter which presents the simulations results obtained with the GENE code, which numerically employs the same gyrokinetic framework. Firstly, a quick overview of the working mechanism and most important normalisations of the GENE code is given in Section 4.1 to make the reader familiar with the numerics. Then in Section 4.2 a set of "base-case" simulations is presented in the absence of collisions which form a reference for comparing with the collisional simulations, and the methods of mode identification are introduced. Lastly, the results for the collisional simulations are presented in Section 4.3, where the emphasis will be on the observed differences witch respect to the "base-case". Ultimately, these simulation results can then serve as a test for the obtained growth rates from the perturbative approach, which will be the topic of Chapter 5.

4.1 Introduction to the GENE code

The GENE (Gyrokinetic Electromagnetic Numerical Experiment) code is developed by Jenko et al [17], and numerically solves the GKE (Equation (25)). GENE can solve the gyrokinetic equation either linearly or non-linearly by switching off/on the advective $\boldsymbol{E}\times\boldsymbol{B}$ non-linearity, and has been extensively benchmarked against other gyrokinetic codes in both cases [75,90,102,147,148]. Furthermore, GENE can simulate an arbitrary number of kinetic plasma species, take into collisions and general electromagnetic fluctuations in the plasma. In this thesis however, GENE will only be used to solve the linear gyrokinetic equation for a two species plasma consisting of deuterium ions and electrons using the exact[51] mass ratio $m_e/m_i = 2.7244 \times 10^{-4}$, while suppressing electromagnetic fluctuations to remain within the electrostatic approximation. Only the supplementary option to include a collision operator will be used. Additionally. the Geometric Interface for Stellarators and Tokamaks (GIST) code [139] is used to create the necessary geometrical input data which allows GENE to take into account realistic magnetic geometries, as opposed to using simplified analytical magnetic equilibria like the $s-\alpha$ model[52] which can result in significant discrepancies [148]. Most importantly, GENE is highly parallelisable achieving close to 90% parallisation efficiencies [151] and is thus suitable to be used on high performance computers. To this end GENE will be run on the MARCONI cluster which is part of an EUROfusion workpackage [152]. Especially for stellarators, such a parallelisation is imperative as the geometric complexity of stellarators results in a significant increase of the computational costs compared with tokamaks [153].

Different versions of GENE exist depending on the complexity of the simulation domain [154]. For the work in this thesis the local version of GENE is used, which solves the gyrokinetic equation in so-called *flux-tube* geometry. This geometry exploits the $k_\parallel/k_\perp \ll 1$ spatial anisotropy of the fluctuations by coiling a box of several gyroradii wide (since $k_\perp\rho \sim \mathcal{O}(1)$) around a single magnetic field line which is traced for one or several poloidal turns, allowing to solve for the evo-

[51] In literature sometimes simulations are also performed with a "heavy electron" model using a mass ratio of $m_e/m_i \sim \mathcal{O}(1e-3)$ is considered to reduce the computational effort by allowing for larger timesteps and spatial resolutions [15, 75, 102, 149]

[52] This is the most simplified model for a tokamak equilibrium with a sheared magnetic field, whose flux surfaces are concentric circles displaced from the magnetic axis due to the so-called Shafranov shift as a result of the plasma diamagnetic effect [150].

lution of turbulence using a minimal simulation volume [68]. Because the perpendicular extends of the simulation volume are small compared with equilibrium scales, within a flux-tube the turbulence can be considered to be locally driven, i.e. the instability mechanism is completely determined by the local value of the pressure profile and its gradients, magnetic field strength and shear, etc. at the position of the magnetic field line and variations of these variables in the perpendicular direction are not taken into account [153, 155]. The Clebsch representation of the magnetic field Equation (5) naturally gives (ψ, α) as the choices for the perpendicular coordinates, which are conveniently rescaled to have the proper physical dimension of meters by

$$x = \frac{\psi - \psi_0}{B_0 r_0} \quad y = r_0 \left(\alpha - \alpha_0\right).$$

Here r_0 is the radial distance from magnetic axis, B_0 is the magnetic field strength on axis, and ψ_0, α_0 are the Clebsch coordinates for the central magnetic field which is traced in the flux tube and thus only described by the z coordinate, which is taken to be the poloidal angle θ. One subtlety hidden in the flux-tube geometry is that the coordinates are curvilinear and non-orthogonal, and as a consequence the rectangular computational domain (x, y, z) actually corresponds to a sheared and curved physical volume inside the torus [16, 68, 156], which is illustrated in Figure 16. For more details on the flux-tube geometry, see Appendix N.

GENE is a so-called Eulerian code, which means that the gyrokinetic equation is solved on a fixed 5D phase-space grid [157]. For the flux-tube geometry, the three spatial coordinates are x, y, z as described above, with the location of the origin corresponding to the point along the field line where the central magnetic field is closest to the outer radius of the torus. Meanwhile the two velocity space coordinates used by GENE are the parallel velocity and magnetic moment $v_\parallel, \mu$. The main assumption for the flux-tube approach is that the perpendicular extent of the simulation volume is larger than the correlation length of the fluctuations, such that the turbulence inside the box is statistically independent to the turbulence outside the box [68, 153].

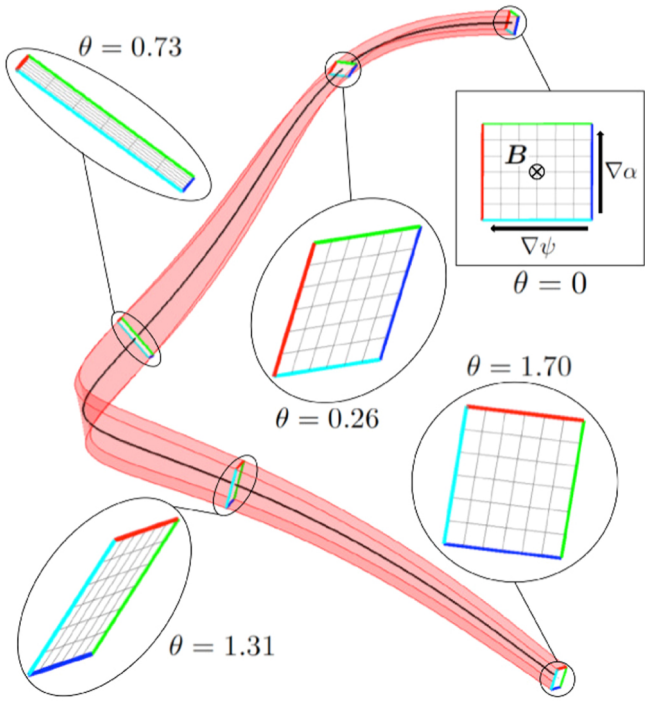

Figure 16: Visualisation of the physical 3D volume that is spun by a flux-tube in the W7-X stellarator. Indicated in black is the central field line along which the tube is expanded in α, ψ directions. Note how the cross-section of the flux tube is sheared through space as a result of the geometry and how the box follows the curvature of the central field line. Adapted from [153].

As furthermore only the fluctuations themselves vary in the perpendicular direction, a pseudo-spectral approach using Fourier modes for the (x, y) directions is used, such that derivatives are handled analytically as $\frac{\partial}{\partial\{x,y\}} \rightarrow ik_{x,y}$ [16]. The discretisation in the perpendicular directions is then achieved through a truncation for the number of wavenumbers. The remaining coordinates are discretised on numerical grids, and the derivatives are taken using finite differences. This introduces coupling between subset of grid points and could cause unphysical grid-scale oscillations in the results, which is compensated for by introducing artificial hyperdiffusion[53] [158]. This hyperdiffusion is only necessary in the $z, v_\parallel$ directions, as derivatives in the magnetic moment only enter through the collision operator, which is already diffusive by nature as a result of its Fokker-Planck form Equation (11) and thus provides a source of dissipation at small scales [16]. Finally, the GKE is then evolved in time using a Runge-Kutta scheme with adaptive timestepping, and the dynamics of the collision operator are separated from the remainder of the kinetic equation for an optimal number of evaluations per timestep depending on the collision frequency [157].

Lastly, as GENE solves the GKE numerically, all variables have to be suitably normalised to be dimensionless. The full steps in the normalisation process of GENE can be found in Appendix M.1. Of most importance for the work of this thesis is the normalisation of the spatial and temporal scales. The equilibrium length scales such as the curvature and driving gradients are normalised to the minor radius a of the torus[54] whereas the fluctuation length scales are normalised to the ion gyroradius at sound speed $\rho_s = c_s/\Omega_i$. Combining these previous two normalisations, then gives a natural unit for normalising the timescales to a/c_s. As a consequence of these normalisations wavenumbers are in units of inverse gyroradii and the frequency/growth rates are in units of c_s/a. Also of particular interest for the work of this thesis is the normalisation of the collision frequency. In GENE the normalised collision frequency as used by the code input is given by [157]

$$\tilde{\nu_c} = 2.303\,08 \times 10^{-5} \frac{n_{\text{ref}}[10^{19}\text{m}^{-3}]a[\text{m}]}{T^2_{\text{ref}}[\text{keV}]} \ln\Lambda \tag{80}$$

where the reference (electron) density and temperature refer to the pressure profile at the central field line of the flux-tube and have been expressed in the convenient units of 10^{19}m^{-3} and keV similar to the Coulomb logarithm in Equation (13). Furthermore the minor radius has been expressed in the unit of m which results in the numerical value of the prefactor. This normalised collision frequency is related to the characteristic ion-electron collision frequency of Equation (17) by

$$\hat{\nu}^{ei} = 4\frac{n_i}{n_{\text{ref}}}\sqrt{\frac{m_i}{m_e}}\tilde{\nu_c}\frac{c_s}{a} \approx 171\sqrt{A}\tilde{\nu_c}\frac{c_s}{a} \tag{81}$$

where in the last step quasi-neutrality was used, and the mass number A of the ion species is introduced to use the ion-electron mass ratio.

4.2 Collisionless base case simulations

4.2.1 Overview of geometries and simulation parameters

The GENE simulations are performed for three different magnetic geometries; the DIII-D tokamak, the HSX stellarator and the W7-X stellarator. To focus on the differences between the

[53] The hyperdiffusion coefficient is implemented as an additional derivative $D = -i^n\epsilon_\xi \left(\frac{\Delta\xi}{2}\right)^n \frac{\mathrm{d}^n}{\mathrm{d}\xi^n}$, where ϵ_ξ can be used to set the strength of the hyperdiffusion, the order of the derivative is typically $n = 4$, ξ is any variable for which hyperdiffusion is desired and $\Delta\xi$ is the grid resolution in that variable. Because of the combination $(\Delta\xi\frac{\partial}{\partial\xi})^n$ the hyperdiffusion only has a significant dissipative effect at the smallest scales which are comparable to the grid resolution while leaving large scale structures comparable to full grid sizes intact.

[54] In typical tokamak literature it is however more common to use the major radius R of the torus for normalisation of the equilibrium length scales.

magnetic field in the geometries, they are made as similar as possible by choosing the flux-tube to span a single poloidal turn and lie on the flux surface[55] characterised by a total enclosed flux of $s = \psi/\psi_a = 0.5$ where ψ_a is the enclosed toroidal flux at the plasma edge. As the flux increases with distance from the magnetic axis as $\psi \propto r^2$, this corresponds to a flux surface at a radius of $r/a \approx 0.71$. For consistency with neglecting electromagnetic fluctuations the input magnetic fields correspond to equilibria at $\beta = 0$. The only differences between the geometries is then the structure of the magnetic field, which determines the magnetic wells through B as well as the particle drifts through its gradients.

The differences between flux surfaces of the configurations have already been highlighted in Figure 13, which have been chosen at the corresponding radial position of $r/a = 0.71$ at which the flux-tube simulations are performed. The variation of the magnetic field strength and its curvature within the flux-tube generated on this surface are shown in Figure 17, where the curvature vector $\boldsymbol{\kappa}$ is represented by its so-called "normal component" as this curvature component is associated with MHD instabilities of the plasma, with negative values corresponding to "bad curvature" regions [3,12,46]. In the low β approximation this component roughly correspond to the radial derivative of the magnetic field strength, such that negative values correspond to radially outward drifts. Notice how there is an overlap between these regions of bad curvature and the magnetic wells in DIII-D and HSX, whereas this is partially avoided in W7-X, particularly at the outboard side.

For the simulation parameters, a seemingly artificial case with only density gradients is considered. This is done to create an idealised limit where other instabilities driven by the temperature gradient can be ruled out, and the TEM can be isolated as much as possible [137]. In literature it is quite common to consider such idealised scenarios to study particular gyrokinetic instabilities [149]. ITG modes are typically simulated using only isothermal adiabatic electrons ($\eta_e = 0$) and having an ion temperature gradient much larger than density gradient $\eta_i \ll 1$ [71,73,79,127,147,160] whereas ETG modes are typically simulated in the opposite limit [17,74,102,161]. Although an electron temperature gradient could also drive TEMs, including a finite η_e in the simulations would result in a mixed TEM/ETG spectrum [75]. Similarly if an ion temperature gradient would be included a mixed TEM/ITG spectrum would ensue if the electrons are not treated adiabatically [68,76,143,149,149,162]. As the main goal of the thesis is to assess the role of the collisionality on TEMs, the normalised density gradient is fixed to the value $a/L_n = 3.0$ for all simulations, which is a typical value considered in gyrokinetic simulations of stellarators [11,137]. Furthermore as the most transport relevant instabilities which significantly affect the confinement time occur at long wavelengths w.r.t. the ion gyroradius, simulations are performed for wavenumbers up to $k_y\rho_s = 2$ as in [76,95,163], which is in between extrema found in literature of only simulating extremely long wavelengths $k_y\rho \leq 1$ [75,77,143,164] and taking into account extremely small wavenelgths $k_y\rho \geq 5$ [19,95,165]. Each simulation set for a value of the collision frequency then consists of a scan over the binormal wavenumber $k_y\rho_s$ ranging from 0.1-2.0 with a stepsize of 0.1. Lastly the temperature ratio is fixed $\tau = 1.0$ for all simulations, which is a decent approximation for actual experimental conditions of DIII-D [166–168] and W7-X [55,169,170] but not in HSX where the confinement time is too short for ions and electrons to exchange sufficient energy such that ions remain "cold" at several tens of eV while the electrons are heated to about a keV [171–173]. Accounting for different temperature ratios would complicate the comparison between the geometries and thus the simulations for HSX will be somewhat artifical but the simulations could nevertheless still be insightful to assess how turbulence in an HSX-like reactor would behave.

[55] As the three devices, however, have different major radii R_0, these surfaces do correspond to distinct aspect ratios r/R_0.

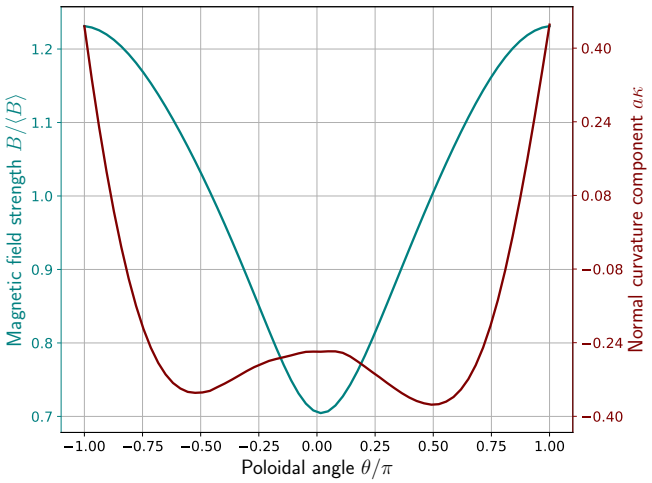

(a)

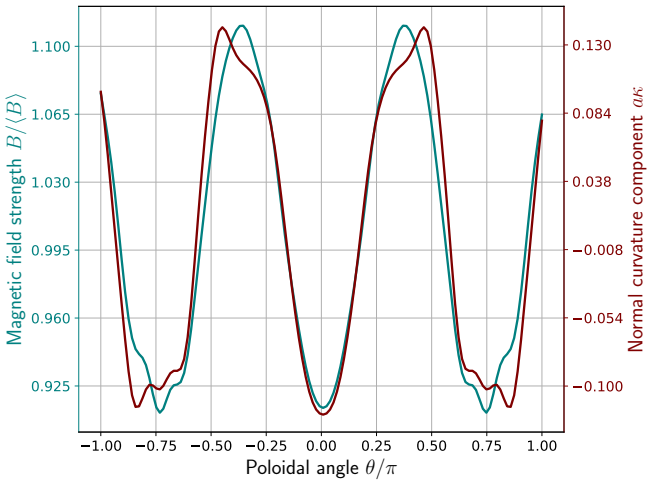

(b)

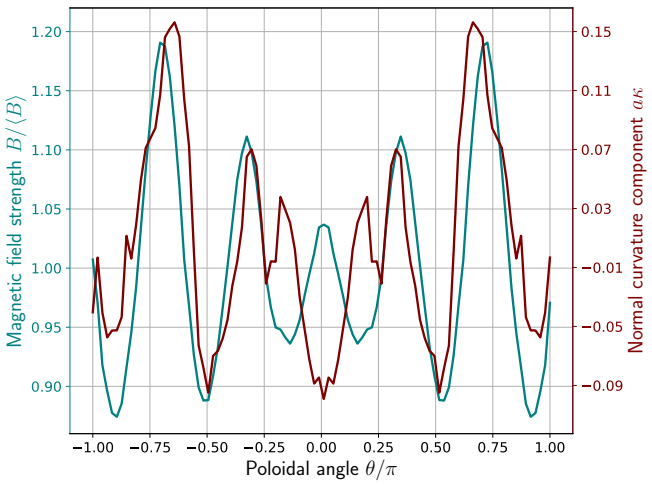

(c)

Figure 17: Plots of magnetic field strength and normal component of the curvature vector within the flux-tube geometry used as simulation input for (a) DIII-D, (b) HSX, and (c) W7-X respectively. The variation of all geometric quantities related to the magnetic field (like B and κ) within the flux-tube are the generated output from the GIST code [159], which uses the EFIT/VMEC equilibrium data from Figure 13 as input.

4.2.2 Convergence test and base-case results

As the simulations are performed using finite resolutions it is important to assess whether the results are actually physical or a numerical effect of the discretisation. Nevertheless for computational costs it is desirable to use as low as possible resolutions, leading to trade-off. For an optimal compromise in this trade-off convergence tests are first performed in the grid resolutions to assess that the results are fairly insensitive to the chosen resolutions. For linear simulations the number of Fourier modes in the y direction is fixed to one, and the number of grid points in the parallel direction $nz0$ is determined by the resolution used to generate the geometric information using the GIST code. For TEMs it has empirically been found that a resolution of 16 grid points along the field line per magnetic is sufficient to resolve the TEM [96], such that the chosen resolutions of $nz0 = 64, 128, 96$ for DIII-D, HSX, W7-X respectively are ample for the simulations of interest.

This leaves three resolutions to be set: $nkx0, nv0, nw0$ corresponding to the number of Fourier modes in the x direction[56], and the number of grid points in the $v_\parallel, \mu$ directions respectively. To find a balance in the required resolutions, simulations are first performed with a low resolution set of $nkx0 = 11, nv0 = 24, nw0 = 8$ and then subsequently doubled, tripled, quadrupled, etc.. After each consecutive run the results for the growth rate and real frequency are compared and if the descrepancy is less than 5% while the spectral distribution in k_x has remained identical the result is considered as converged. As the resolution increases are rather course by changing both spatial and velocity resolutions simultaneously, next a hybrid convergence test between the previous and new resolution is done where only $nkx0$ or $nv0, nw0$ are increased to see if additional spatial or velocity resolution is required for convergence and find a more minimal set of resolutions. Lastly, the value of the hyperdiffusivity ϵ_z (see Footnote 53 for notation) is adjusted from its (relatively high) default value of 2.0 to roughly the maximum linear growth rate found in the scan over wavenumbers according to [157, 158] and a last check is done to see whether the results are insensitive to the decrease in hyperdiffusion. The hyperdiffusion in velocity space is kept to its default value of 0.2.

The resulting resolution sets from this convergence test are shown in Table 1, where it can be seen that stellarator geometries are much more computationally demanding requiring higher resolutions. The only exception where convergence could be not reached, not even by increasing the initial resolution sixfold were the smallest two wavenumbers in HSX $k_y\rho_s = 0.1, 0.2$. A similar issue has previously been observed in non-linear simulations of HSX, where a longer flux tube spanning multiple poloidal turns was required to reach convergence in the heat flux at low wavenumbers, which is believed to be caused by the low magnetic shear of the device [174]. As only a single poloidal turn flux-tube was available, these wavenumbers are subsequently omitted from the analysis and all future simulations including collisions. The corresponding result for the converged growth rate and real frequency obtained with these resolutions is shown in Figure 18, which will be analysed in the next section.

[56] As a consequence of the double Fourier transform and the relation between Fourier coefficients $\hat{\phi}_{k_x,k_y} = \hat{\phi}^*_{-k_x,k_y}$, $\hat{\phi}_{k_x,k_y} = \hat{\phi}^*_{k_x,-k_y}$ for real valued quantities such as all physical observables, working with positive and negative wavenumbers in the x and y directions is redundant since $\hat{\phi}_{-k_x,-k_y} = \hat{\phi}_{k_x,k_y}$. Therefore as the order of Fourier transforms taken by GENE is first in the y, x directions, the number of Fourier modes in the x direction and the number of radial grid points (as would be needed to compute fluxes) in the x direction are identical $nkx0 = nx0$. Meanwhile the number of grid points in the y direction is $ny0 = 2nky0$ as negative wavenumbers ky are retained (although the "physical" y grid is never explicitly needed).

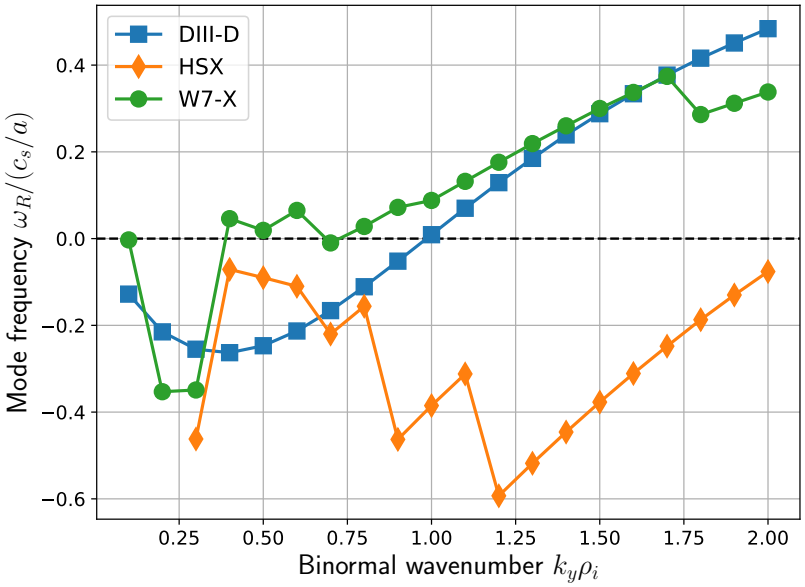

(a)

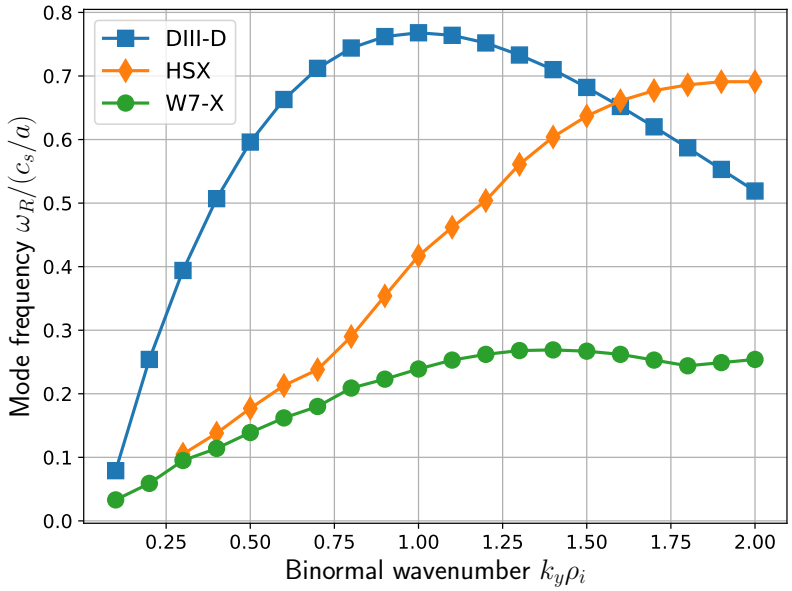

(b)

Figure 18: Converged results for (a) the real frequency and (b) the growth rate for the different geometries which form the reference base-case for comparison against the collisional simulations of Section 4.3. The dotted black line in (a) corresponds the transition between modes traversing in the ion- and electron diamagnetic directions.

	nkx0	nz0	nv0	nw0	ϵ_z
DIII-D	21	64	48	16	0.75
HSX	43	128	120	40	0.70
W7-X	33	96	96	32	0.25

Table 1: Minimal resolution sets of each geometry for which convergence in the complex mode frequency and spectral distribution of the perturbations was reached for the collisionless base-case simulations.

4.2.3 Mode identification

An important question is of course *what* has been simulated by GENE. To identify which type of instability (often called a linear (eigen)mode of the linearised GKE) the results correspond to three methods will be used. First of all the sign of the real frequency ω_R can be used as a signature for the type of instability, where in particular for TEM the mode is expected to traverse in the electron diamagnetic direction $\omega_{\star e}$. As a result of the GENE normalisations to ion scales a positive frequency corresponds to a mode traversing in the ion diamagnetic direction. Furthermore discrete jumps in the real frequency as the wavenumber is varied are indicative for a change in instability type corresponding to another branch of the dispersion relation which has become more unstable [125, 164, 175]. As a second tool the cross-phases between the different fluctuations can be used to asses the type of instability, as according to the waveform model for the instabilities discussed in Section 2.1 the electrostatic potential perturbation will be typically $\pi/2$ out of phase with the perturbation of the driving factor for instability. In GENE the fluctuations in the temperature are also treated anisotropically and split in a $\delta T_\parallel, \delta T_\perp$ where the parallel temperature fluctuation is defined as $\delta T_\parallel \equiv \int m v_\parallel^2 \delta f \mathrm{d}^3\boldsymbol{v}$ and idem for the perpendicular temperature (with a factor of 1/2) [157]. As passing particles are characterised by their large parallel velocity the $\delta T_\parallel$ fluctuations can be taken as a proxy for the passing particle response while $\delta T_\perp$ can be taken as a proxy for the trapped particle response [143]. Lastly the spatial mode structure along the field line is a third method for mode identification, since TEMs are expected to peak in magnetic wells where the trapped particle reside. In contrast, although it is not discussed in this thesis, the passing particle instability of the ITG is characterised by peaking of the mode structure in bad curvature regions rather than magnetic wells [95, 127]. These methods will now be applied to the results of Figure 18.

4.2.3.1 DIII-D

Starting with the simplest case of the DIII-D tokamak, it can be seen from Figure 18 that for wavenumbers $k_y\rho_s \leq 1$ the mode is traversing in the direction of $\omega_{\star e}$, and then switches to the ion direction for larger wavenumbers. This switch however occurs very gradually as opposed to changes in ω_R in the stellarators, indicating that this is not a change to a different instability type. Interestingly enough the growth rate γ peaks at $k_y\rho_s = 1$ where the transition occurs. These are all the properties of the so-called "ubiquitous mode" (UM) from Coppi et al [175], which is the short wavelength extension of the classical TEM corresponding to the large $k_y\rho$ limit of the same branch of the dispersion relation as the TEM [69, 164], thus explaining the smoothness in ω_R curve. Rather than being a kinetic instability, the instability is more fluid-like and is no longer driven by a resonance with the electron drift but a combination of ion/electron drifts such that the mode still relies on the existence of trapped electrons, but is less tied to the magnetic wells and is more localised to the regions of bad curvature [19]. The growth rate of this fluid-like instability is, however, much larger than the resonant growth rate of classical TEM at the same wavenumber such that the UM becomes the dominant instability mechanism, which peaks when the competing mechanisms of electron/ion drift cancel at zero real frequency [175]. A look at the mode structures along the field line in Figure 19a reveals that at low $k_y\rho$ the mode

is peaked at $\theta = 0$ at the depth of the magnetic well as expected for a classical TEM, but as the wavenumber increases and the mode has transitioned to UM regime the mode structure is more flattened out and extends more towards higher field regions to maximise the ion drive from the unfavourable curvature regions.

Taking a look at the cross-phases in Figure 19b it can be seen that at low $k_y\rho$ the instability is driven by a combination of $\delta T_{\perp,e}$ and δn fluctuations as expected for TEMs. Oddly enough the $\delta T_{\perp,e}$ crossphase becomes negative indicating stabilisation already at $k_y\rho = 0.8$ before the transition to UM occurs, and there is no similar instability driving factor characterised by positive cross-phase occuring for the ions after the transition to UM. The only match between the cross-phases and the UM transition is that this occurs when the cross-phase with the density fluctuation is exactly $+\pi/2$ where the maximum instability drive is expected as the $\boldsymbol{E} \times \boldsymbol{B}$ will purely enhance the density perturbations as seen in the basic drift-wave models from Section 2.1. The cross-phase with the density perturbations alone can in fact completely explain the growth rate growth rate spectrum from Figure 18, initially increasing up to $k_y\rho = 0.1$ as the cross-phases approaches $\varphi \to +\pi/2$ and then decreasing again as the cross-phase passes $+\pi/2$ and continues to rise resulting in a more out of phase $\boldsymbol{E} \times \boldsymbol{B}$ fluctuations again.

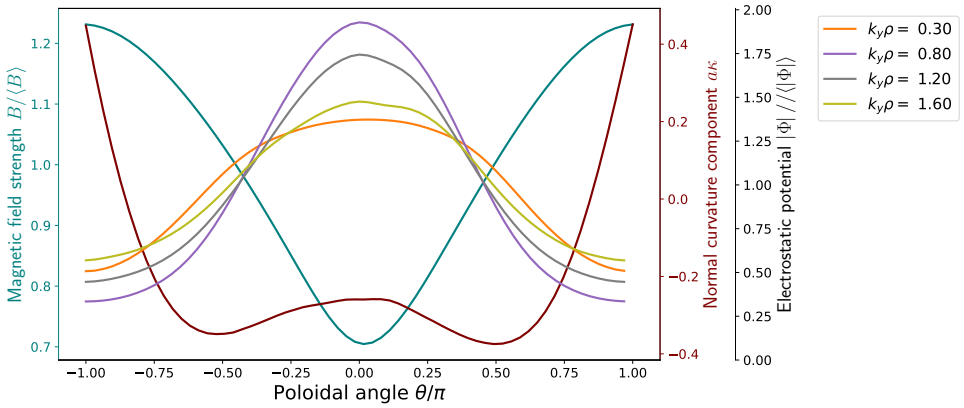

(a)

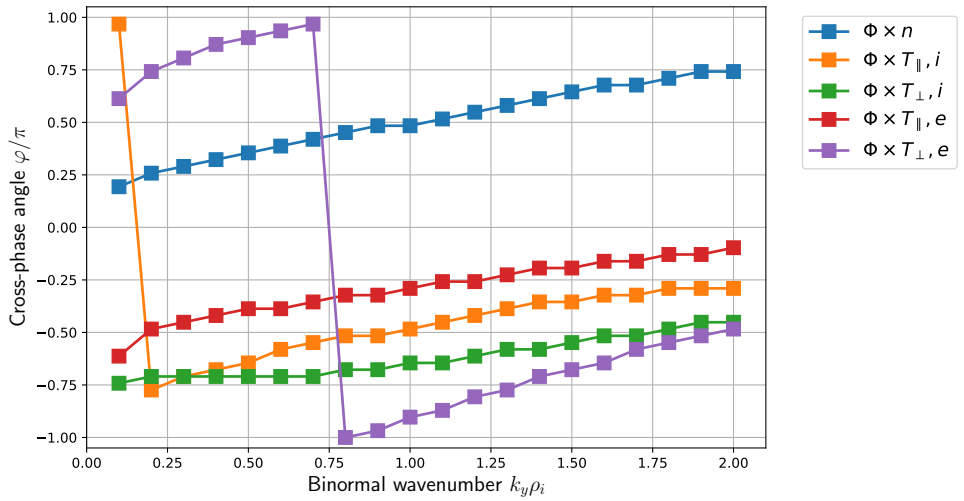

(b)

Figure 19: Analysis of the base-case results for DIII-D showing (a) the shape of the mode structure in the flux tube for some selected wavenumbers compared with the shape of the magnetic field and curvature and (b) the cross-phases between the different perturbations, as obtained from a weighted average over the mode structure of the electrostatic potential.

4.2.3.2 HSX

Moving on to the analysis of HSX, the spectrum of the real frequency shows that the instability is always propagating in the electron diamagnetic direction $\omega_{\star e}$, but several transitions to a different branch of eigenmode occur. As the magnetic field in HSX is not a max-$\mathcal{J}$ configuration, these modes are expected to be TEMs. In contrast to DIII-D however, there is no emergence of the UM and the growth rate does therefore not peak but there is a clear transition around $k_y\rho \sim 0.8$ where the modes becomes increasingly unstable with wavenumber. In this case mode identification is most easily performed by looking at the mode structure along the field line in Figure 20a, which shows strong correlation between significant changes in mode structure and the different branches in the spectrum for ω_R. Except for the mode at the lowest wavenumber $k_y\rho = 0.3$ all mode structures are clear TEMs and only differ in which of the magnetic wells they peak, with a general trend that as $k_y\rho$ increases the instability becomes more and more tokamak-like peaking only at the central magnetic well at the outboard side where there is the most overlap between bad curvature and well sturcture, which are slightly shifted toward the inboard side ($\theta = \pm\pi$), which also explains the "kink" in the growth rate curve near $k_y\rho \approx 0.7$ where the transition occurs between mode peaking at the in- and outboard sides of the torus.

Returning to the exception at $k_y\rho = 0.3$, the mode does not seem to favour peaking at the magnetic wells or bad curvature regions, and is hardly localised anywhere in the geometry almost satisfying $\Phi/\langle\Phi\rangle \approx 1$ where $\langle\Phi\rangle$ is the average electrostatic potential along the entire field line. This mode is in fact the so-called "Universal Instability" (UI) which is a general electrostatic plasma instability corresponding to another unstable variant the basic drift wave that relies only on the existence of a density gradient and is therefore unaffected by trapping effects, which is traditionally studied in slab geometry [165, 176]. The UI is also found to exist in toroidal geometry, as inferred from tokamak simulations, with typical characteristics besides its unlocalised mode structure that it occurs at low wavenumbers and low magnetic shear, propagates in the electron diamagnetic direction, and is driven by parallel Landau resonances of passing particles [163]. The existence of the UI in stellarator geometries have only recently been established in gyrokinetic simulations [177], where they are more strongly anticipated to occur than in tokamaks as a consequence of the much lower magnetic shear typical for stellarators [43].

Taking a look at the cross-phases in Figure 20b the UI can indeed by clearly distinguished from the TEMs by a much weaker coupling to the $\delta T_{\perp,e}$ fluctuations although there does not seem to be a destabilising interaction with the $\delta T_{\parallel}$ fluctuations of either species as expected for the Landau resonances. Furthermore at $k_y\rho = 0.3$ the cross-phases would predict a negligibly small growth rate compared with $k_y\rho = 0.4$ even though this is not observed in the actual spectrum of Figure 18.

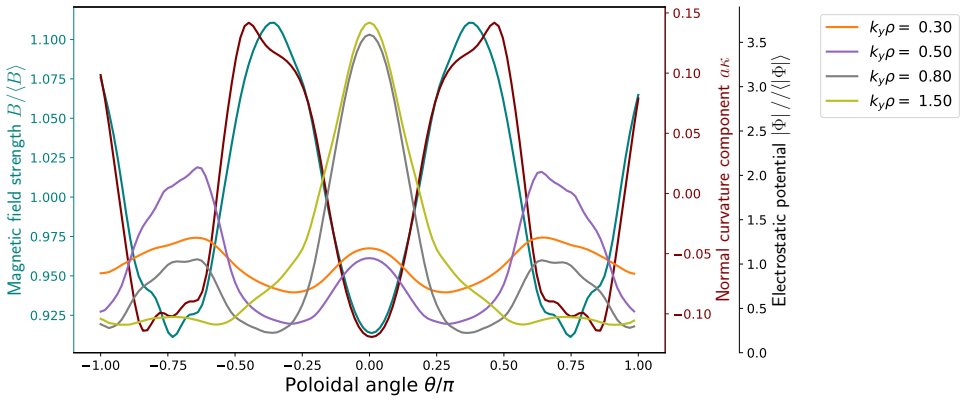

(a)

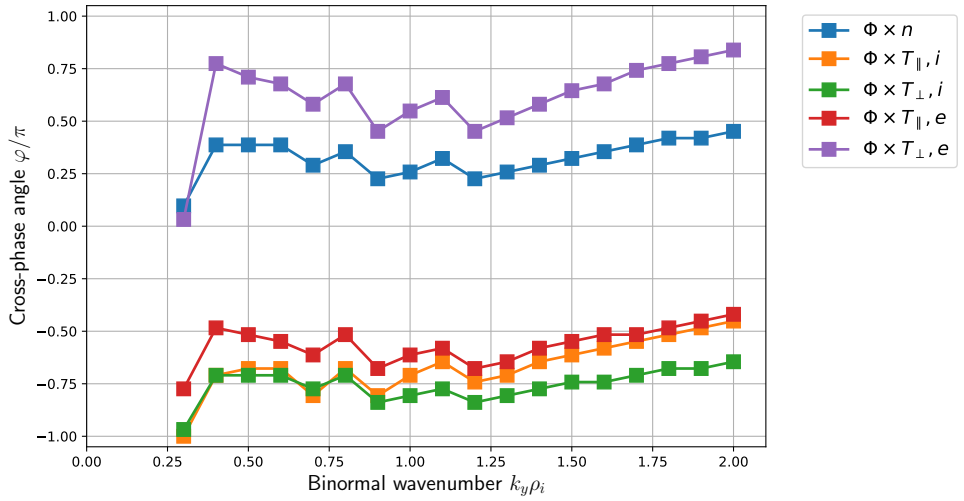

(b)

Figure 20: Analysis of the base-case results for HSX showing (a) the shape of the mode structure in the flux tube for some selected wavenumbers compared with the shape of the magnetic field and curvature and (b) the cross-phases between the different perturbations, as obtained from a weighted average over the mode structure of the electrostatic potential.

4.2.3.3 W7-X

Lastly the modes in W7-X are investigated, which is expected to be stable against classical TEMs as the magnetic configuration results in the max-$\mathcal{J}$ property. From the spectrum of the real frequency it can be seen that modes propagating in the electron diamagnetic direction are only found for $k_y\rho < 0.4$ with the remainder of the modes traversing in the $\omega_{\star i}$ direction, identifying only a few candidates for potential classical TEMs. The modes in the ion branch of the spectrum is the so-called ion-driven trapped electron mode (iTEM) identified by Plunk et al as the extension of the UM to stellarator geometry [93], and is characteristed by a non-resonant destablisation from ion drift which requires the interaction of the fluctuations with the trapped electrons to change the propagation direction of the unstable drift wave. Just like with the UM it can indeed be seen that the ω_R passes through zero at $k_y\rho = 0.1, 0.7$.

Taking a look at some of the mode structures in Figure 21a it can be seen that with the exception of the $k_y\rho = 0.3$ mode which clearly propagates in the electron diamagnetic direction all other modes show a clear TEM structure and the different branches in ω_R can again be associated with the mode structure peaking in a different magnetic well like in HSX. The major differences is however that these iTEMs cannot peak at the outboard side because of the mismatch between bad curvature and magnetic well at $\theta = 0$, explaining the much lower growth rates of the instability. The only exception is the $k_y\rho = 0.3$ mode which is insensitive to the magnetic geometry and together with its propagation direction in the electron diamagnetic direction is a typical UI. Typically the UI would be overshadowed by the TEM as a result from the much stronger resonant instability drive by trapped electrons, and is therefore expected to emerge only in more peculiar magnetic configurations like in W7-X where such a resonant drive is rendered impossible [132].

Taking a look at the cross-phases in Figure 21b the UI can clearly be identified by sharp drops in the cross-phases $\delta T_\perp$ of both species, although striklingly it is the $\delta T_{\parallel,i}$ fluctuation which has an a positive cross-phase as opposed to the $\delta T_{\parallel,e}$ fluctuation based on the fact that the UI is characterised by a resonance with passing electrons [132, 165]. The cross-phases also provide some insight to the mode at $k_y\rho = 0.2$ (not shown in Figure 21a, but discussed in more detail in Section 4.3) which also propagates in the electron diamagnetic direction, but has a hybrid mode structure in between TEM- and UI-like. This is reflected by the cross-phases, where the δn cross-phase is seen to drop similar to the $k_y\rho = 0.3$ mode in both HSX and W7-X which have clear UI-like mode structure, but the $\delta T_{\perp,e}$ cross phase remains similar to those of iTEM modes at larger wavenumbers, indicating some competition with instability drive from trapped electrons.

Also interestingly the $\delta T_{\perp,e}$ cross-phase does not change sign near the transition to iTEM as observed before in the tomakak case for the UM. However, similar to the tokamak case of Figure 19b there does not seem to be a change to the stability properties of the cross-phase from the $\delta T_{\perp,i}$ fluctuations as expected, and the zero crossings of the real frequency seems to be completely linked to the density fluctuations cross-phase being $+\pi/2$.

4.3 Collisional simulations

4.3.1 Changes to the code and realistic collisionality regimes

In order to perform collisional simulations, a collision operator has to be specified for the GENE code to use. Since the collisions are expected to mainly influence the TEM through collisional (de)trapping, only the pitch-angle scattering part of the collision operator is accounted for, which is a common choice for collisional simulations in literature [18, 74, 75, 77], which at least for the case of electron-ion collisions accurately decribes the full Coulomb collision operator to lowest order in the mass ratio [20, 70]. This means that in the code the "test" part of the collision

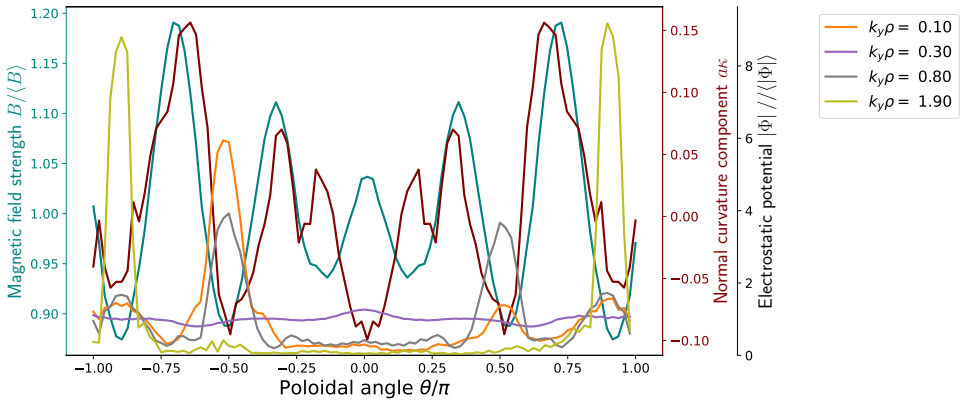

(a)

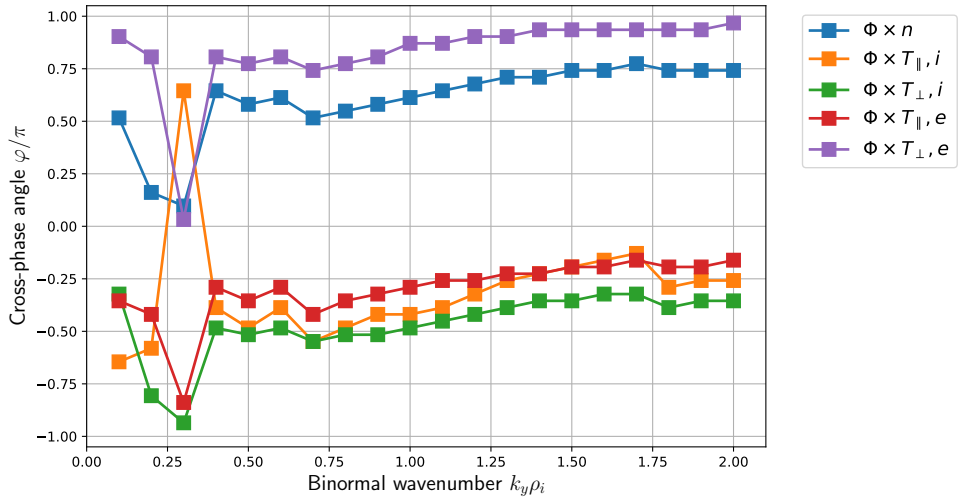

(b)

Figure 21: Analysis of the base-case results for W7-X showing (a) the shape of the mode structure in the flux tube for some selected wavenumbers compared with the shape of the magnetic field and curvature and (b) the cross-phases between the different perturbations, as obtained from a weighted average over the mode structure of the electrostatic potential.

operator (see Section 2.3) is modelled as [86, 106]

$$\langle C_{ss'}(g_s, F_{Ms'}\rangle_{\boldsymbol{R}} = \nu_D^{ss'} \langle \mathcal{L}(g_s)\rangle_{\boldsymbol{R}} = \frac{\nu_D^{ss'}}{2}\left[\frac{\partial}{\partial\xi}\left(1-\xi^2\right)\frac{\partial}{\partial\xi} - \left(1+\xi^2\right)\frac{v^2}{v_{Ts}^2}k_\perp\rho_{Ts}\right] g_s$$

where $\xi = v_\parallel/v$ is a proper dimensionless pitch-angle variable, $\mathcal{L}$ the Lorentz scattering operator as given by Equation (15), and the gyroaveraging procedure does not affect the diffusion in pitch angle but results in a FLR correction for the perpendicular velocity diffusion term (as alluded to in Section 2.5). For the "field" part of the collision operator a conservative model operator which ensures that particles, momentum and energy remain conserved, as a direct evaluation of the Rosenbluth potentials Equation (12) it typically believed to be too computationally intensive [87, 88, 90, 178], although state-of-the-art is now moving towards exact treatment of the field particle operator [89, 91].

A second concern is the input values of the collision frequency parameter $\tilde{\nu}_c$ which can essentially be set to arbitrary values. To prevent simulating unrealistically low or high collisionality, the experimental profile data for density and temperature shown in Figure 22 are used as a reference guide for realistic ranges of the collision frequency parameters, where the dashed

line corresponds to the radial position of the flux-tube used in the simulations. Using Equation (81) the collision frequencies in Figure 22 correspond to GENE collision frequency ranges of[57] $\log_{10}(\tilde{\nu_c}) \simeq [-3.5, -2.5], [-5.0, -2.5], [-3.5, -1.0]$ for DIII-D, HSX and W7-X respectively indicating that there is fairly little overlap between the devices for assessing the influence of collisionality. Furthermore, the collision frequency range for the reactor regime parameters from Figure 1a spans $[-5, -3.5]$ showing a clear mismatch between present day experiments and future reactor conditions. To properly assess the influence of collisionality on the instabilities and facilitate a comparison with the perturbative theory calculation of Section 3.5, the collision frequency will have to be varied through several orders of magnitude. Therefore using the realistic ranges above as a guide the collision frequency parameter is varied between $\log_{10}(\tilde{\nu_c}) = [-6.0, -1.0]$ with a stepsize of 1.0, thus spanning the full plasma conditions from deep core to edge regions in any realistic device.

4.3.2 Simulation results

For the results that follow below, only the frequency spectrum and mode structure are discussed and used to assess the influence of collisions on the instability since the cross-phase diagnostic did not prove to be extremely reliable tool in the base-case scenario. For completeness, the changes in the cross-phase with collisionality are presented in Appendix O, where in general the influence of collisions on the cross-phase is negligible, leading in general to a reduction of the cross-phase angle with the δn perturbation across all devices and a sudden switch of cross-phase sign of the $\delta T_\perp$ perturbations as collisionality is increased in HSX and W7-X only.

4.3.2.1 DIII-D

In the case of DIII-D, simulations at the highest collision frequency $\tilde{\nu_c} = 0.1$ proved not to be feasible as the numerical methods were unstable resulting, in large spectral pile-up of the perturbations at the largest radial wavenumbers $|k_x|$ for all k_y in the scan. This could not be cured by increasing the resolutions or hyperdiffusion further such that only the results up to $\tilde{\nu_c} = 0.01$ are retained. At the second highest collision frequency a similar spectral pile-up also occurred but only at the two largest wavenumbers $k_y\rho = 1.9, 2.0$, as shown in Figure 23, which are therefore omitted from the analysis.

The results for the frequency and growth rate for the numerically stable simulations are shown in Figure 24, from which it can be seen there is a general downwards and smooth trend in both ω_R, γ as the collision frequency is increased, with exception of the highest collision frequency of $\tilde{\nu} = 0.01$. A separate run at double the resolutions has been performed to assess that this is not a numerical effect which matched within 10% showing that the results are indeed converged. Regarding the $\tilde{\nu} = 0.1$ simulation as a separate case, there is a slight shift of the zero-crossing of the real frequency to higher wavenumbers and an even weaker shift in the peak of the growth rate to smaller wavenumbers, which is line with the theory predictions of the Ubiquitous Mode [175]. As the collision frequency is increased the TEM structure becomes slightly less peaked and starts to "leak out" of the magnetic well explaining the reduction in growth rates as shown in Figures 25a and 25b. At the higher wavenumbers where the base-case result changes to an Ubiquitous Mode the collisions gradually make the mode structure more curvature driven as shown in Figures 25c and 25d, which is expected as the trapped electron instability mechanism will be reduced by the decreasing fraction of effectively trapped electrons and provides less competition to the ion curvature drive mechanism. Furthermore the reduction in the trapped electron fraction also explains the decrease in the growth rate at the high wavenumber part of the spectrum. The mode structures from Figure 25 also explain why the frequency spectrum

[57] The maximum collision frequency is determined at $r/a = 0.95$ as at the edge of the plasma the density and temperature drop too rapidly for the collision frequency to vary smoothly.

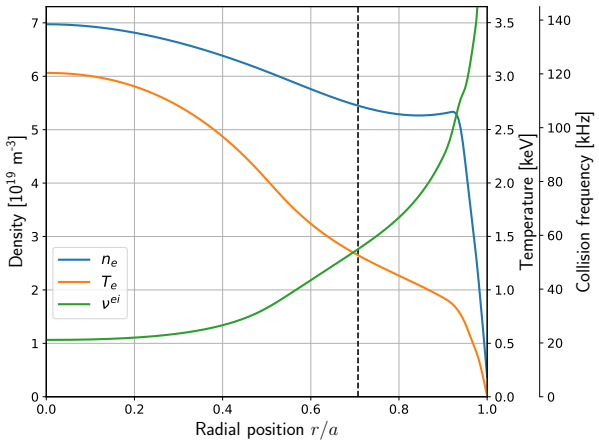

(a)

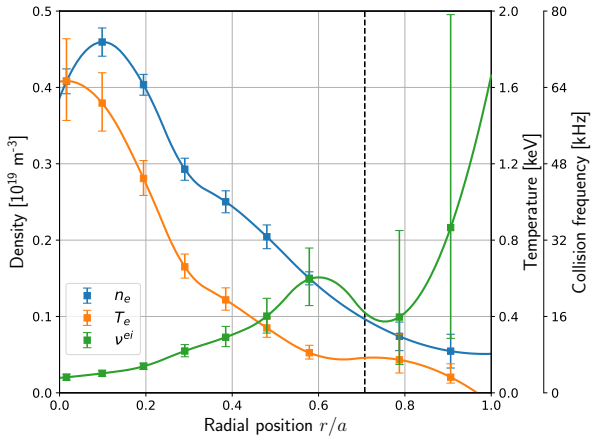

(b)

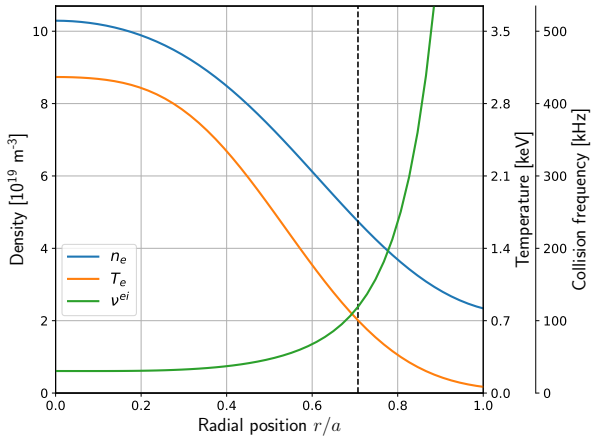

(c)

Figure 22: Experimental density- and temperature profiles for (a) DIII-D [168], (b) HSX [172] and (c) W7-X [170] and the corresponding profile of the 90° scattering frequency calculated from Equation (17). The dashed vertical line corresponds to the radial position of the flux-tube used for the simulations and is included as a reference. The data from (a),(c) corresponds to fits to experimental measurements while (b) corresponds to raw data supplemented with interpolating splines of second order. All data is reproduced with the permission from respective authors.

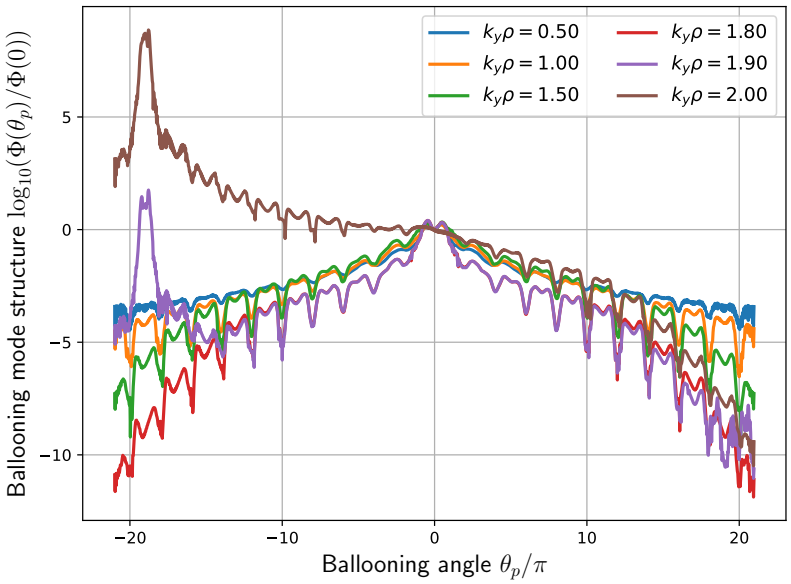

Figure 23: Ballooning representation of the electrostatic potential perturbation for several values of the binormal wavenumber from the $\tilde{\nu_c} = 0.01$ simulations, showing the spectral pile-up for $k_y\rho = 1.9, 2.0$ near $\theta_p = -20$. This ballooning representation of the perturbations is closely related to their representation in Fourier modes, and the ballooning angle θ_p is closely related to the radial wavenumber k_x [156], such that $\Phi(\theta_p)$ can be interpreted as a spectral-intensity-like quantity. This ballooning representation is however beyond the scope of the thesis to discuss (see e.g. Footnote 69 and the references therein).

for $\tilde{\nu} = 0.01$ stands out, as it corresponds to a different type of instability which is strongly curvature driven, and also explains the emergence of a new branch at $k_y\rho = 1.60$ where the mode structure mirrors its asymmetry w.r.t. $\theta = 0$.

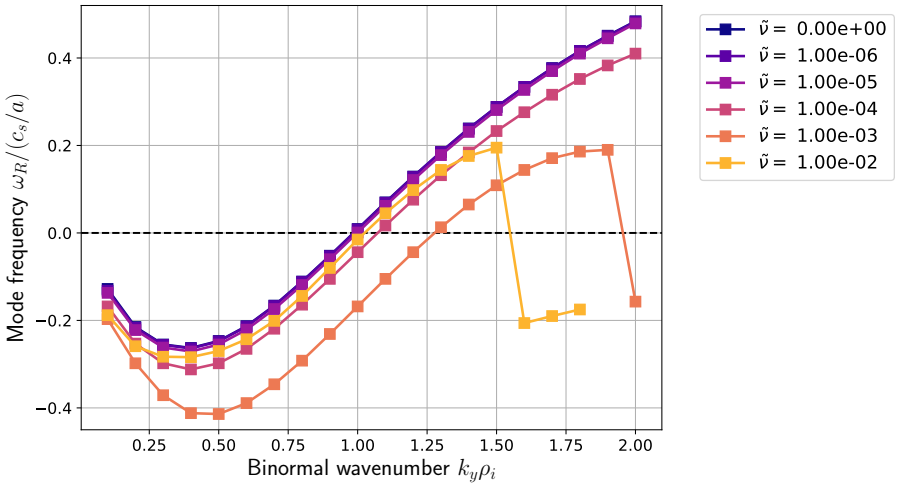

(a)

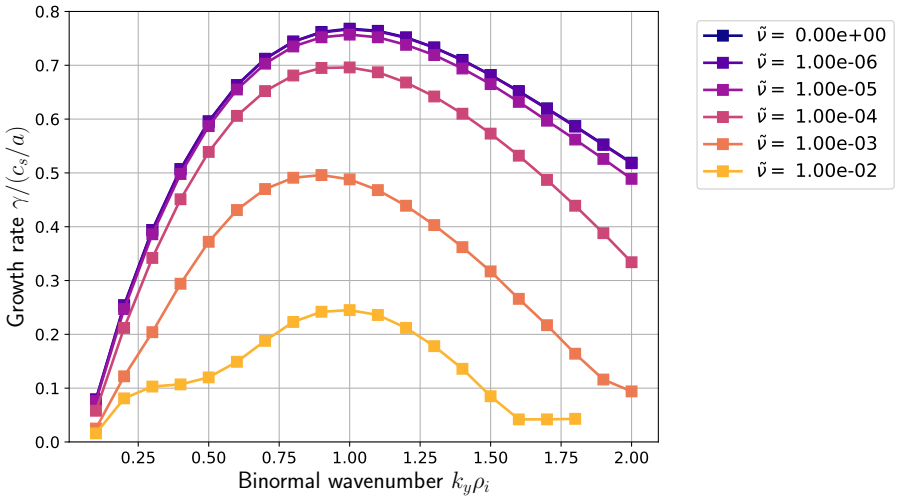

(b)

Figure 24: Dependence of (a) the real frequency and (b) the growth rate of the instabilities in DIII-D on the collision frequency, where the lines are colour coded such that dark hues correspond to a low collisionality and light hues correspond to a high collisionality. The dotted black line in (a) corresponds the transition between modes traversing in the ion- and electron diamagnetic directions.

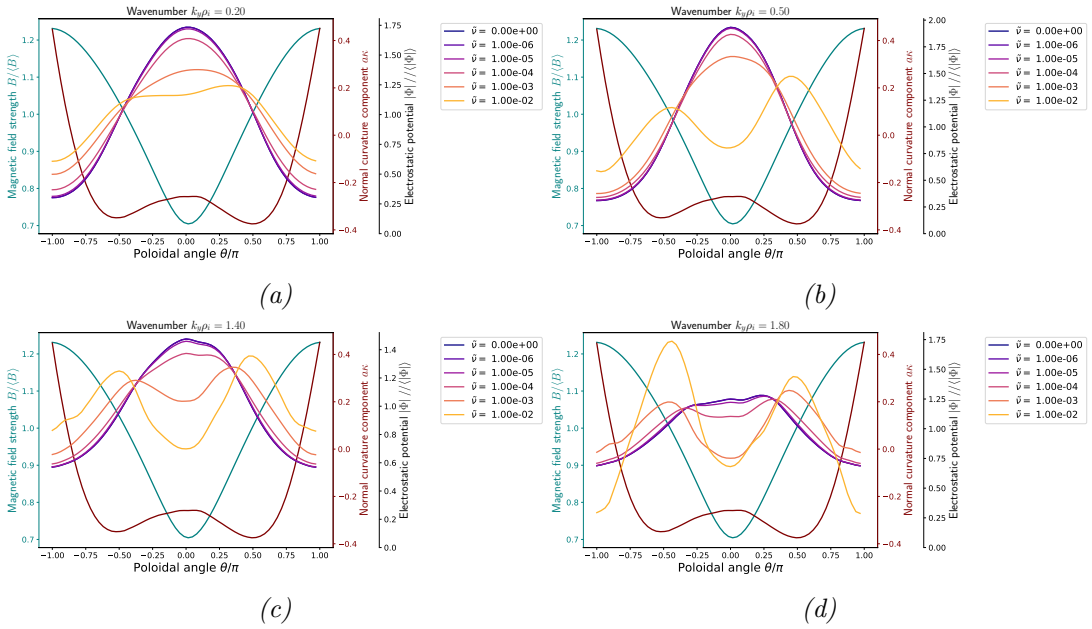

Figure 25: Changes to the shape of the mode structure of the electrostatic potential along the field line with collisionality for (a) $k_y\rho = 0.20$, (b) $k_y\rho = 0.50$, (c) $k_y\rho = 1.40$, (d) $k_y\rho = 1.80$, where the lines are colour coded such that dark hues correspond to a low collisionality and light hues correspond to a high collisionality. The cases of (a) and (b) correspond to the TEM regime of the base-case whereas the cases (c) and (d) correspond to the UM regime of the base-case.

4.3.2.2 HSX

For the collisional simulations in HSX and W7-X all results were healthy and no data had to be disregarded. Starting with HSX, the results for the frequency and growth rate are shown in Figure 26. In contrast to the DIII-D results the growth spectrum does not monotonically decrease with increasing collisionality at all wavenumbers. Although this collisional stabilisation is present at high $k_y\rho$, there seems to be some destablisation as a result of collisions at low $k_y\rho$. From the spectrum of ω_R it can be seen that the collisions have a significant influence on the transitions to different branches of the dispersion relation. This is most easily seen for the transition to the the high wavenumber branch, which occurs for $k_y\rho = 1.20$ in the collisionless case but already happens at $k_y\rho = 0.70$ for the highest collisionalities. More interestingly, however, is the behaviour at low wavenumber where in the base-case the UI and transitions between different TEMs are observed. The addition of collisions is seen to completely change the observed branches at low $k_y\rho$, indicating the emergence of a different type of mode compared to the base-case.

These potential changes in the mode type could explain the observed the destabilisation if the new mode changes from trapped- to passing particle drive. The changes in the mode structure for a few cases of interest are shown in Figure 27 where strikingly it can be seen that at low $k_y\rho < 0.4$ increasing collisionality promotes a change of the mode character from TEM-like to more UI-like (see Figure 27a). This confirms the suspicion about the destablisation effect at $k_y\rho < 0.4$, as apparently the UI becomes more unstable than the TEM with increased collisionality. However, as both the wavenumber and collisionality are increased a gradual transition back to TEM occurs (see Figures 27b and 27c). The destabilisation in the range of $0.4 < k_y\rho < 1.0$, where the collisional simulations transition back to TEM, can be explained from the fact that the new modes are more strongly peaked at the outboard side with more overlap between unfavourable curvature and the magnetic well (most clearly illustrated by Figure 27c). In contrast at high $k_y\rho$, when the collisionless mode from the base-case also is also located at the outboard side, the mode peaking decreases with collisionality as seen in Figure 27d, explaining why the collisional γ curves cross those of the base-case and stabilisation with collisionality is observed again.

A last feature of interest is that the at the largest collisionality $\tilde{\nu_c} = 0.1$ the propagation frequency of the mode changes to the ion diamagnetic direction and the growth rate starts to plummet more strongly for $k_y\rho \gtrsim 1.70$. This is explained by the mode structure at higher wavenumbers which reveals that the two "bumps" seen near $\theta = \pm 0.3$ in Figure 27d which are not present at the lower collisionalities have grown into small sidebands to the central peak, such that there is a small contribution from the favourable curvature region $\kappa > 0$.

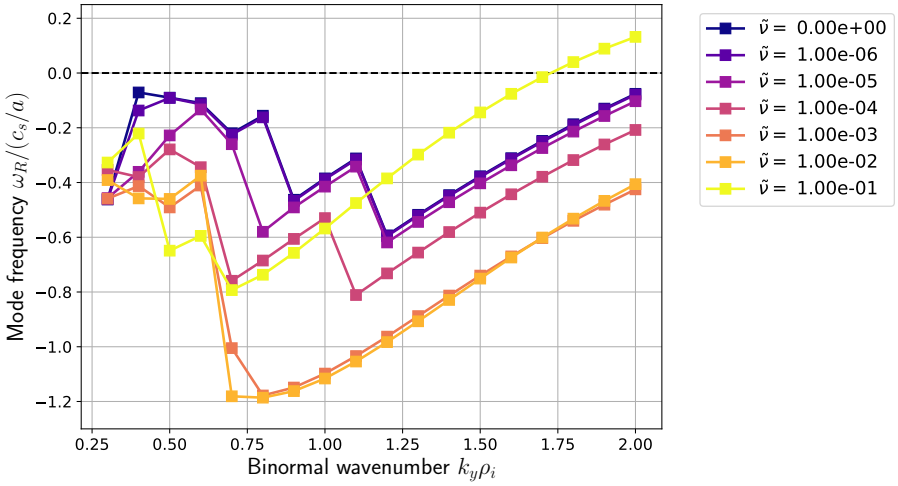

(a)

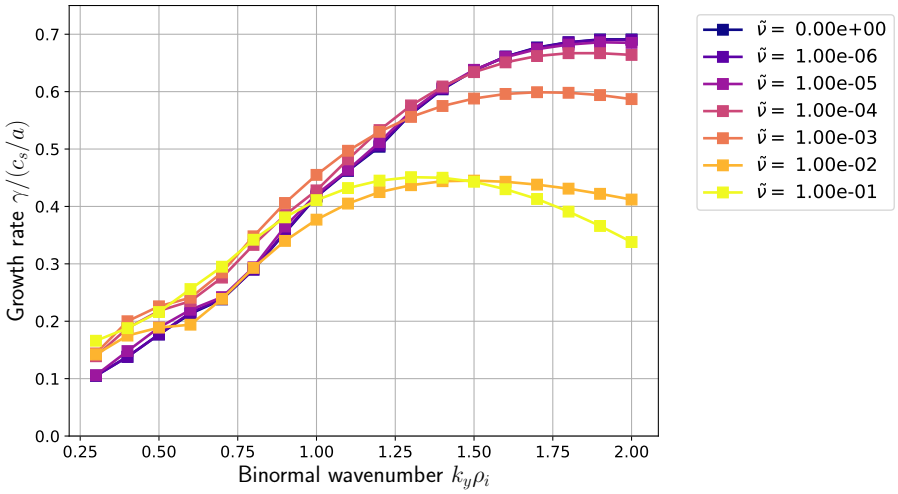

(b)

Figure 26: Dependence of (a) the real frequency and (b) the growth rate of the instabilities in HSX on the collision frequency, where the lines are colour coded such that dark hues correspond to a low collisionality and light hues correspond to a high collisionality. The dotted black line in (a) corresponds the transition between modes traversing in the ion- and electron diamagnetic directions.

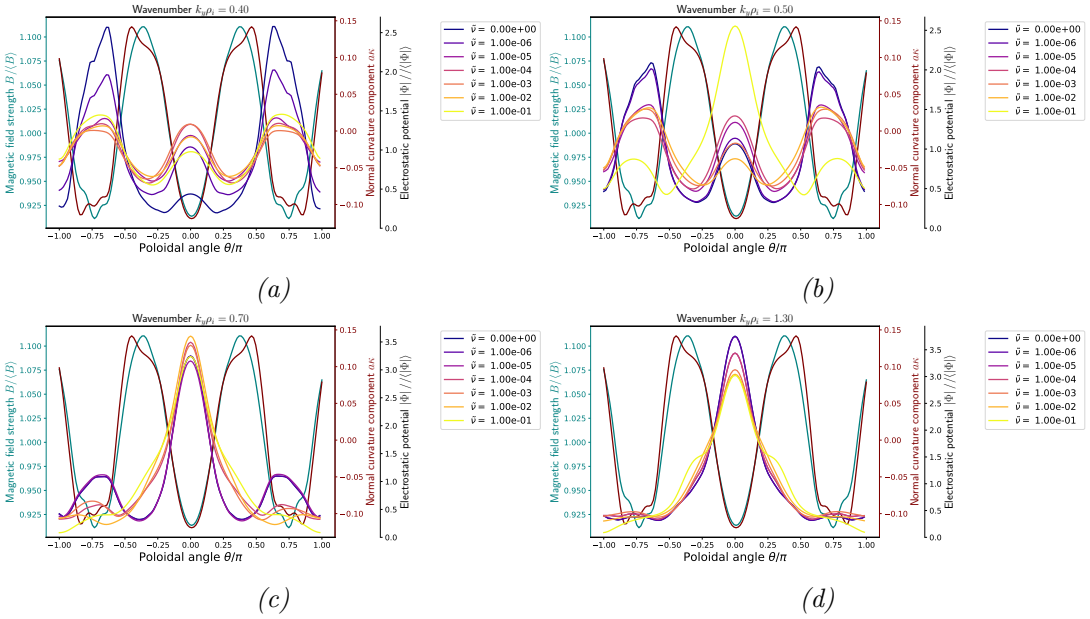

Figure 27: Changes to the shape of the mode structure of the electrostatic potential along the field line with collisionality for (a) $k_y\rho = 0.40$, (b) $k_y\rho = 0.50$, (c) $k_y\rho = 0.70$, (d) $k_y\rho = 1.20$, where the lines are colour coded such that dark hues correspond to a low collisionality and light hues correspond to a high collisionality. The transitions to different branches of the dispersion relation caused by the collisions are clearly identified by the different shape of the mode structure.

4.3.2.3 W7-X

Lastly the simulation results for the mode frequency and growth rate for W7-X are shown in Figure 28. Similarly as in HSX the growth rate spectra reveals that at low $k_y\rho$ the collisions have a destabilising influence whereas at high $k_y\rho$ the collisions are stabilising. Much more interestingly the spectrum of the real frequency reveals that collisions are capable of exciting instabilities propagating in the electron diamagnetic direction $\omega_{\star e}$ where previously iTEMs were found. This hints at the possibility of collisions driving the classical TEM, which is expected to be absent due to maximum-$\mathcal{J}$ property of the magnetic configuration, unstable. However, these modes could equally be the UI which are also characterised by a negative frequency ω_R, so a more elaborate investigation of the mode structure is required is warranted.

The changes to the mode structure for a handful of interesting wavenumbers are shown in Figure 29. From Figure 29a it can be seen that at $k_y\rho = 0.2$, where in the base-case the mode structure is some hybrid form between UI and (i)TEM, the collisions are able to "wash-out" the remaining TEM feature and result in a pure UI mode. Furthermore the base-case UI at $k_y\rho = 0.3$ is unaffected by collisions and remains an UI at all collisionalities, indicating that increasing collisionality favours the UI at low wavenumber as also observed in HSX. Meanwhile at intermediate wavenumbers $k_y\rho$ (and at $k_y\rho = 0.1$) where the base-case mode is an iTEM, the collisional modes largely have an UI character which is not strongly influenced by the geometry and even peaks in region of local magnetic maxima (as seen in Figures 29b to 29d). Unlike at low $k_y\rho$ the mode structure does not immediately change towards UI at the slightest collisionality but occurs only above $\tilde{\nu}_c = 1 \times 10^{-4}$, which is consistent with theory calculations of UI predicting that collisions initially stabilise the UI but above a certain collisionality start increasing the growth rates [179].

Notable exceptions to this transition to UI however can be found at the $\tilde{\nu_c} = 1 \times 10^{-4}$ mode in Figure 29c and $\tilde{\nu_c} = 1 \times 10^{-4}, 1 \times 10^{-3}$ modes in Figure 29d which show signs of peaking at the magnetic wells near $\theta = \pm\pi/2$. Since the propagation frequency ω_R in these cases is in the electron diamagnetic direction these could be TEMs, however, the peaking of the mode structure is not as strongly pronounced as for the iTEM case. Looking at the mode structure for higher wavenumbers provides some insight in the character of these modes as the solution for $\tilde{\nu_c} = 1 \times 10^{-3}$ is already in its last branch of ω_R, whereas the solution for $\tilde{\nu_c} = 1 \times 10^{-4}$ still undergoes a change to a branch propagating in the ion diamagnetic direction at slightly higher wavenumbers. From Figures 29e and 29f it can be seen that the $\tilde{\nu_c} = 1 \times 10^{-4}$ mode solution is peaked more strongly at the same $\theta = \pm\pi/2$ wells after transitioning to the iTEM branch whereas the $\tilde{\nu_c} = 1 \times 10^{-3}$ mode solution doesn't change. Since the solution for $\tilde{\nu_c} = 1 \times 10^{-3}$ is less strongly localised to the well and shows a local increase in its amplitude at $\theta = 0.0$ this mode is most likely a hybrid case of UI-TEM where the trapped electrons provide some additional destabilisation. In contrast, the $\tilde{\nu_c} = 1 \times 10^{-4}$ mode solution has its amplitude more evidently localised to the well at $\theta = \pm\pi/2$ and this localisation is further strengthened after transitioning to iTEM, indicating that this was indeed likely a classical TEM emerging as a result of collisions spoiling the favourable bounce average drift of the max-$\mathcal{J}$ configuration. More striking in Figures 29e and 29f is however the mode structure at the highest collisionality $\tilde{\nu_c} = 0.1$ which starts to favour the outboard side of the torus ($|\theta| < \pi/2$ although still with little regard to either curvature of the magnetic wells, such that this mysterious mode is neither UI nor TEM like.

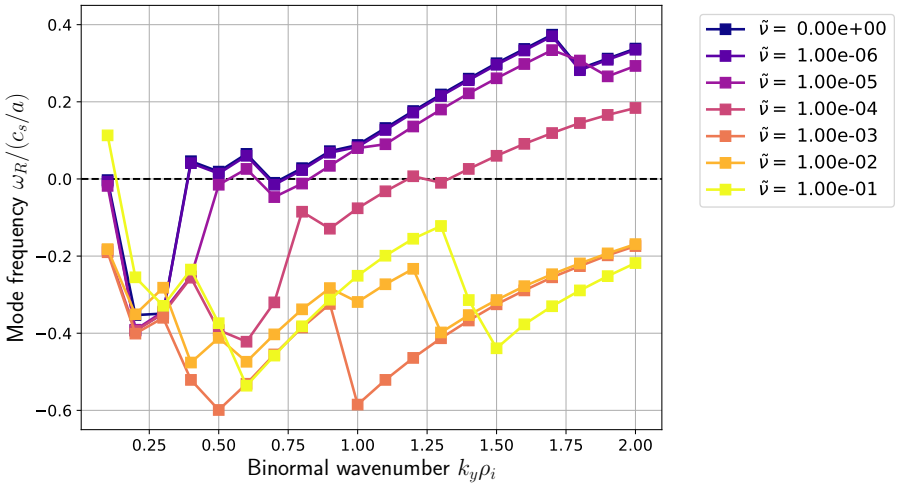

(a)

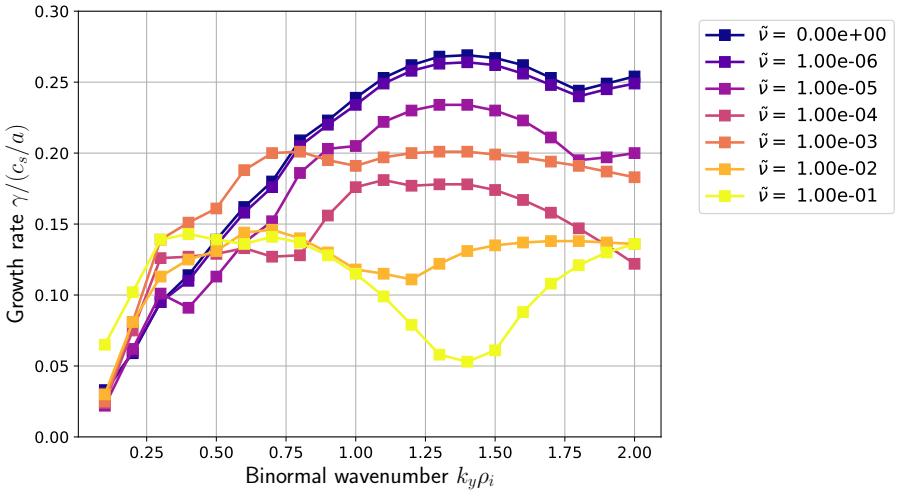

(b)

Figure 28: Dependence of (a) the real frequency and (b) the growth rate of the instabilities in W7-X on the collision frequency, where the lines are colour coded such that dark hues correspond to a low collisionality and light hues correspond to a high collisionality. The dotted black line in (a) corresponds the transition between modes traversing in the ion- and electron diamagnetic directions.

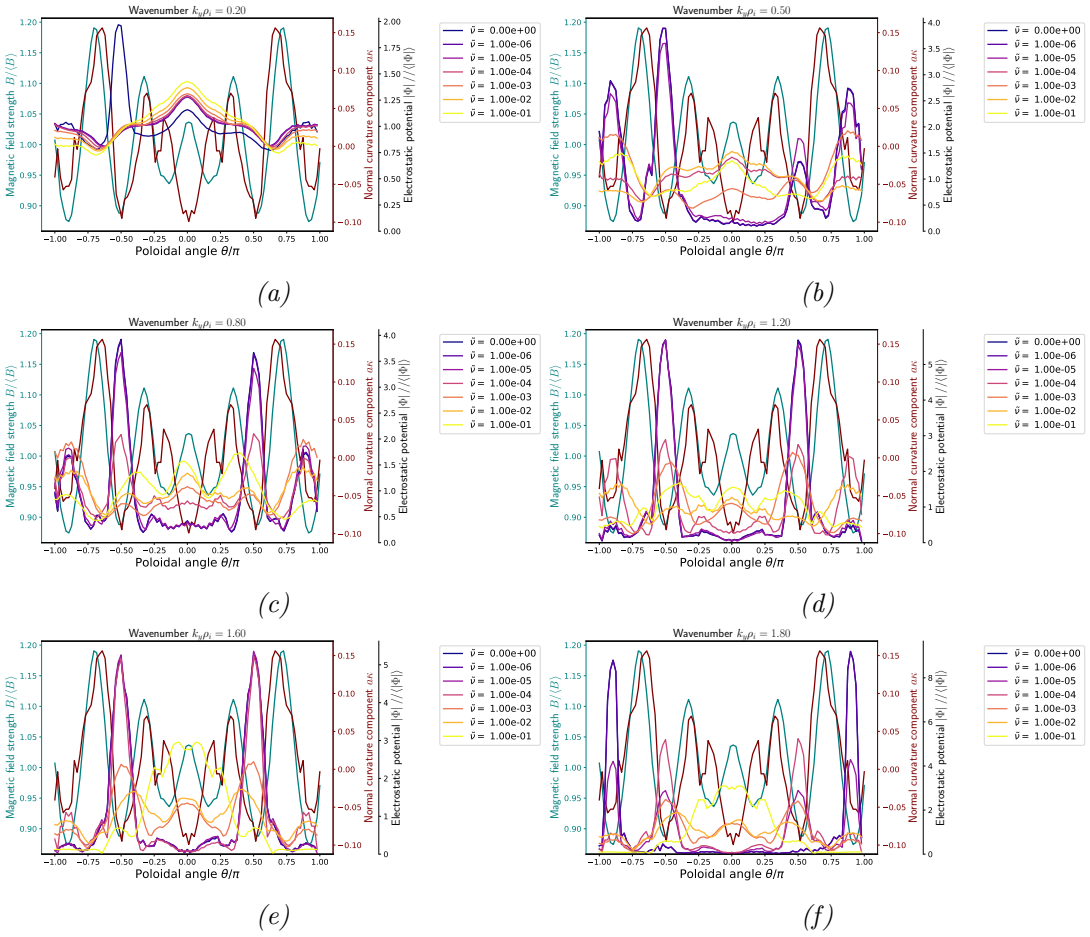

Figure 29: Changes to the shape of the mode structure of the electrostatic potential along the field line with collisionality for (a) $k_y\rho = 0.40$, (b) $k_y\rho = 0.50$, (c) $k_y\rho = 0.70$, (d) $k_y\rho = 1.20$, where the lines are colour coded such that dark hues correspond to a low collisionality and light hues correspond to a high collisionality. The transitions to different branches of the dispersion relation caused by the collisions are clearly identified by the different shape of the mode structure.

5 Comparison between theory and simulation

The effect of finite collisionality on the stability TEMs has been independently investigated using analytical theory by means of a perturbative approach in Chapter 3 and simulations by a gyrokinetic code in Chapter 4. Both methods have given result for the growth rate and have considered the same set of magnetic geometries. Before moving on to wrap up the thesis, it would be proper to ask whether there is agreement between the results from these methods. This is first assessed on a qualitative level in Section 5.1, and then as an ultimate test on a quantitative level in Section 5.2

5.1 Qualitative comparison of growth rates

The qualitative comparison is straightforward as it can be performed visually by comparing the trends of the growth rate from the perturbative approach Figure 15 with those from simulations Figures 24, 26 and 28, which is further facilitated by the scaling laws. The perturbative calculation predicts that at extremely low collisionality DIII-D is most unstable, followed by HSX which has low growth rates at low wavenumbers but becomes more unstable as $k_y\rho$ increases until the growth rates are comparable to DIII-D, and lastly that the growth rates in W7-X remain small for all wavenumbers which is in decent agreement with the base case simulation results of Figure 18. From the scaling laws of Figure 15a it is found that at initially at low collisionality the growth rates in DIII-D are unaffected by collisionality, but start to decrease at high collisionality which is confirmed by the collisional simulation results of Figure 24. Meanwhile the scaling laws for HSX Figure 15b predict that the high wavenumber modes are largely unaffected by collisions until the dissipative effect of collisions is strong enough to decrease the growth rate, while at lower wavenumbers the growth rates increase with collisionality, as is also in line with the collisional simulation results of Figure 26. For W7-X the scaling laws of Figure 15c predict that the modes below $k_y\rho = 1.0$ are destablised by collisions up to a maximum value after which the growth rates decrease again but remain larger than their collisionless counterpart. In contrast the growth rate of the modes above $k_y\rho = 1.0$ are initially not affected by collisions at low collisionality, then somewhat destabilised at intermediate collisionality but eventually get stabilised by strong dissipation at high collisionality. These observations are mostly in agreement with the collisional simulation results of Figure 28, except for the high wavenumbers at intermediate collisionality. Thus it be ascertained that there is least a decent qualitative agreement between the trends in growth rates from both methods. This raises the question if, besides just qualitative agreement, there is also quantitative agreement between the calculations, which could make the perturbative approach whose calculations are relatively cheap enough to be performed on a home computer system an attractive alternative to the gyrokinetic simulations which require super computers.

5.2 Quantitative comparison of growth rates

To facilitate a quantitative comparison between these methods, however, the different normalisations which are used have to be matched to reach a common basis of reference. The collision frequency is most easily matched by translating the GENE values to the physical collision frequency $\hat{\nu}^{ei}$ to get a handful of discrete points along the logarithmic $\hat{\nu^{ei}}/\omega_{\star e}^{\text{phys}}$ axis used in the perturbative calculation. Comparing the growth rates is a little more intricate, as the GENE results use a fixed reference normalisation of c_s/a and stay within the same $\mathcal{O}(0.1-1.0)$ range, whereas the perturbative results are normalised to $\langle\omega_0\rangle$ which changes with wavenumber and span a handful of order of magnitudes. A comparison of the relative changes in the growth rate, which would be attractive to consider since it is normalisation independent, is thus not feasible as these diverge for the perturbative calculation. Therefore the absolute change of the growth rates expressed in the fixed GENE units of c_s/a are compared instead, which also removes the

hidden dependence of the perturbative growth rates on $k_y\rho$. The translation factors for converting between these normalisations are given in Appendix M.3, and the resulting comparison of growth rates is presented in Figure 30.

It can be seen that the quantitative comparison between the solutions is rather poor, which is somewhat to be expected given the numerous approximations that went into simplified perturbative calculation. Especially the fundamental approximation that the shift in frequency is small $\delta\omega/\omega_0 \ll 1$ which justifies the use of the perturbative approach is quickly violated as already clear from Figure 14 where both the real and imaginary part of the frequency shift are of $\mathcal{O}(1)$ in a large part of parameter space. What determines the validity of the perturbative approach is that the total frequency shift in both real and imaginary should be small, for which the absolute value $|\delta\omega|$ can be taken as a decent proxy. In Appendix P it is shown that that the magnitude of the frequency shift typically only stays below the 30% mark at low wavenumber ($k_y\rho < 0.1$ for DIII-D and $k_y\rho < 0.5$ for HSX/W7-X) or at very high collisionality $\log_{10}(\hat{\nu}^{ei}/\omega_{\star e}^{\mathrm{phys}}) > 0.5$. Furthermore the perturbative calculation inconsistently assumes the instability is an TEM with a constant amplitude of the electrostatic potential along the field line, whereas the GENE simulations much more realistically result in a TEM mode structure which peaks in the magnetic wells and allows for transitions to different modes like the UI and UM, whose instability mechanism cannot be described by trapped electron drift resonances and collisional (de)trapping at all in case of UI or only partially in case of UM. Another potential source for discrepancy is that the GENE simulations take into account the velocity space details of the realistic Fokker-Planck collision operator, whereas the perturbative approach uses the simplified BGK operator.

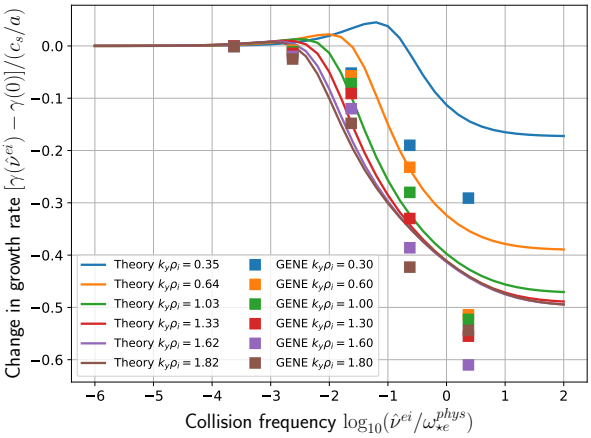

(a)

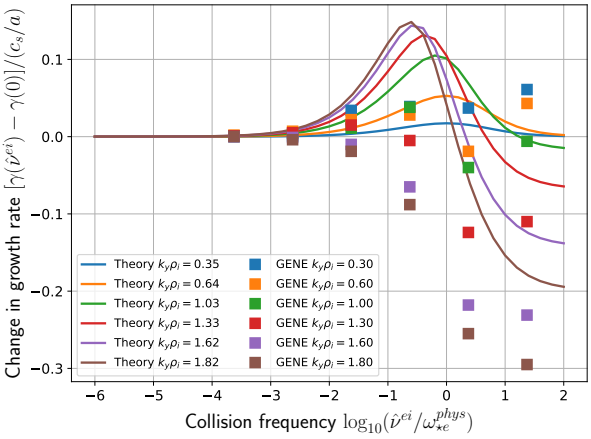

(b)

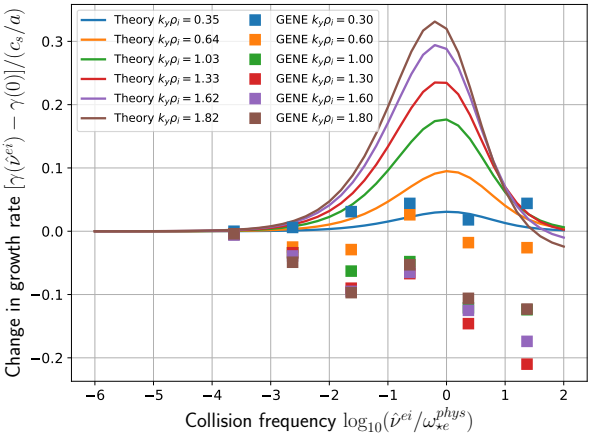

(c)

Figure 30: Comparison for the change in growth rate w.r.t. collisionless situation between the perturbative calculation and GENE simulations for (a) DIII-D, (b) HSX and (c) W7-X. For the perturbative calculation the wavenumbers which are the closest match to the wavenumbers used in the GENE simulations have been selected for the comparison.

6 Conclusion and outlook

In this thesis the influence of collisionality on TEMs is investigated in both tokamak and stellarator geometries using both analytical theory and numerical simulations. A concise overview of the main results is presented in Section 6.1, after which the limitations on the present research and ideas for future research are discussed in Section 6.2.

6.1 Summary of results

In summary, this thesis set out to assess what influence of collisions may have on onset of the TEMs instability which is the dominant source of turbulent electron transport in present day experiments [7, 94]. This is investigated through both analytical theoretically and numerical simulations.

For the theory part an approximate perturbative calculation of the trapped electron response has been formulated which extends the existing literature results applicable only in extreme limits of collision frequency to an arbitrary collisionality regime and predicts that above a certain limit TEMs would be stabilised by collisions as the drift resonance is avoided regardless of geometry. Additionally the calculations predicts differences between geometries, with DIII-D experiencing pure stabilisation but HSX and W7-X experiencing destabilisation at low wavenumbers and stabilisation at high wavenumbers.

From the simulations it is found that the dominant instability in DIII-D are TEMs which are strictly stabilised by collisions. In HSX the growth rates around found to increase at low wavenumbers and intermediate wavenumbers, which is mostly due to a transition of the mode to a more dangerous TEM peaking at the outboard side. At high wavenumbers, however, the amplitude of this mode is quenched w.r.t. its collisionless counterpart such that growth rates decrease with collisionality similar to DIII-D. Most interesting are the W7-X results, where the collisionless resonant TEMs are prohibited by the max-$\mathcal{J}$ property of the magnetic field and an iTEM occurs instead. For W7-X the collisions seem to excite a transition towards the UI, which is practically insensitive to the existence of trapped particles or the details of the magnetic geometry. An exception however seems to occur at $0.8 < k_y\rho < 1.20$ where for a collisionality of $\tilde{\nu_c} = 1 \times 10^{-4}$ a mode with TEM like signatures occurs, however, with the limited and unreliable available data on the cross-phases it is not possible to determine that this mode is indeed strictly driven by the trapped electrons and does not correspond to a collisional iTEM variant whose real frequency is shifted downwards to the electron diamagnetic direction.

Although there is decent qualitative agreement between both methods, they have a poor quantitative match which can be attributed to the many approximations and simplifications made to keep the theory analytically tractable, whereas the simulations are completely general and can be performed up to an arbitrary level of desired detail. Note that the simulations presented in this thesis constitute the first (to the best of the author's knowledge) collision frequency scan for electrostatic growth rates in W7-X, with previous collisional simulations consisting of a driving gradient scan at a fixed value of $\tilde{\nu_c} = 0.057$ which reflects plasma conditions at the edge rather than the core where transport is more dangerous.

6.2 Outlook

The work in this thesis indicates that the main role of collisions on the TEM is to quench its growth rates, as intuitively would be expected based on the reduction of the effective fraction of trapped particles, a feature both present in simulations and theory. Of particular interest was whether collisions could result in the emergence of TEMs in W7-X which is stable against collisionless TEMs, but collisions could spoil the favourable average electron precession drift as a result of momentum decorrelation along the trajectory of trapped particles which "resets" the

memory of the magnetic geometry that electrons build up over their orbit. The perturbative calculation indeed predicts increasing (but still small) growth rates whereas the simulations show that the main role of collisions is to facilitate a transition towards the Universal Instability which is caused by passing particles instead. Such mode transitions occur as a consequence of the disparate influence collisions have on the different instabilities and are much more prominent in stellarators than tokamaks, where as a result of the more complex 3D magnetic geometry typically a significant number of plasma instabilities can exist compared with the handful of instabilities found in tokamaks [16, 144].

Limitations on parameter regime

In the work quite some level of simplification has been introduced for both the theory and simulations which allowed to zoom in on TEMs. Most severe is the limitation to density gradient drive only, which is a poor reflection of the realistic plasma profiles of Figures 1a and 22, especially for tokamaks where the temperature profile is significantly steeper than the density profile. However given the discussion of subdominant instabilities above, this simplification is necessary as the inclusion of temperature gradients could make the simulations prone towards the ITG/ETG instability making it difficult to asses how collisions influence TEMs. In view of the max-$\mathcal{J}$ stability criterion for TEM however the electron temperature gradient is relevant, as detailed analysis of the energy exchange between electrons and the perturbed electric field shows that above a gradient length ratio of $\eta_e = 2/3$ the trapped electrons could provide energy to the instability and contribute to the growth rate [95, 126]. However, in the limit of the iTEM which has been observed in the simulations the electrons have been shown to exert a stabilising influence for any $\eta_e > 0$ (correponding to usual peaked n, T profiles) [93]. Additionally the role of magnetic fluctuations has been neglected by invoking the electrostatic approximation, which is justified by the fact that typical fluctuation levels satisfy $e\delta\phi/T_e \gg \|\delta \boldsymbol{B}_\perp\|/B_0 \gg \left|\delta B_\parallel\right|/B_0$ such that magnetic instabilities are subdominant at low β [109]. Furthermore the growth rates of collisionless TEMs are known to be insensitive to β unlike the ITG instability which undergoes stabilisation with increasing pressure gradient [156], and since the collision operator has no reference to the magnetic field it may be postulated that this does not change for collisional TEMs. The growth rate of magnetic fluctuations however increases with β such they may become the dominant instability at a β of a few % [125]. This is however a relevant regime for stellarators which can operate at much higher β than tokamaks which are pressure limited by the onset of MHD instabilities [43, 44]. However gyrokinetic flux-tube simulations at finite β are difficult to perform since the magnetic geometry has to be consistently changed with β to account for the influence of the plasma diamagnetic effect on the magnetic equilibrium [180].

Compatibility of flux-tube approach with non-axisymmmetric geometries

Another intricacy involved in the simulation is the use of flux-tube concept for stellarators. As a result of the axisymmetry of tokamaks a single flux-tube spanning a single poloidal turn is sufficient to sample the full geometry as all field lines on a flux surface are equivalent and the geometry repeats itself after a poloidal turn [16]. This is not true in stellarators where each field line on a flux surface corresponds to slightly different flux-tube which result in different growth rates and fluxes corresponding to the same flux surface and some suitable averaging over flux-tubes would be required [43, 139]. With how costly stellarator simulations are this is not feasible and it is therefore common practice to simulate only the most unstable flux-tube [95, 155] as done in this thesis. Additionally the boundary condition used assumes periodicity in the turbulence structure between the end-points of the flux-tube (see Appendix N) which is not true in stellarators. However a detailed investigation by Martin et al implementing more "stellarator friendly" boundary conditions show that the linear results are rather insensitive to the choice of boundary condition provided that the flux-tube spans at least a full poloidal turn, although

non-linear simulations could benefit from lower resolution requirements [153].

Inconclusive evidence for absolute stability of W7-X against collisional TEMs

A major limitation of the simulation results is that only the most unstable eigenmode is found as a result of the explicit time integration of the GKE, such that any initialised perturbation which can excite all instabilities will ultimately be dominated by the solution with the largest growth rate leading to convergence of the results. No insight about stable or subdominant[58] perturbations can be gained, such that it cannot be said that W7-X is absolutely stable to TEMs even in face of collisions. For mainly illustrative purposes and as a brief preliminary exploration, GENE has also been run with an eigenvalue setting[59] to find some of the subdominant modes in W7-X. This has been done for $k_y\rho = 0.50$ in the collisionless case and with a collision frequency of $\tilde{\nu}_c = 1 \times 10^{-5}$ and 1×10^{-3}, resulting in the frequency spectra of Figure 31. This shows that in the collisionless case the instabilities concentrate in the iTEM region with positive ω_R as expected from the max-$\mathcal{J}$ propery of the configuration, but as the collision frequency is increased the spectrum gradually shifts towards negative values of ω_R indicating that TEMs could exist as a subdominant instability next to the UI. This does provide some additional support that the mode found at $0.8 < k_y\rho < 1.20$ for $\tilde{\nu_c} = 1 \times 10^{-4}$ could plausibly be a TEM. A thorough confirmation, however, would require additional simulations dedicated to this parameter region with a finer stepsize in the collision frequency and the implementation of additional diagnostics which can separate the contributions from trapped and passing particles to the instability drive as opposed to the poor proxy indicators of the $\delta T_\parallel, \delta T_\perp$ fluctuation cross-phase available for present simulations. Furthermore future simulations might also investigate the effect of including energy scattering in the collision operator, which have been shown to provide additional stabilisation to TEMs in tokamak [76].

Improvements of the perturbative approach

Some comments with regard to the theoretical work in this thesis are also due. The results presented in Chapter 3 concern a perturbative approach of the trapped electron response with quite some approximations. The discrepancy with the numerical simulations is quite large and several reasons for this have been highlighted in Chapter 5. Future work could improve the discrepancy between these two methods by two reasonable paths. First the simulations could repeated with a BGK operator at the same collision frequencies to assess whether the abstraction of the full kinetic details of the Fokker-Planck collision operator Equation (11) has a significant results on the growth rates, and if so compare with the perturbative calculation again. A more computationally friendly approach for improvement would be to lift the very unrealistic flute mode approximation for the electrostatic potential $\hat{\phi}(l) \approx \hat{\phi}_0$ used for the perturbative calculation to highlight the differences in geometry. The mode structure solutions from GENE show that TEMs are characterised by an elecrostatic potential profile which peaks in regions of low magnetic fields and bad curvature. Therefore as a significant improvement the GENE results

[58] These are perturbations with a positive growth rate which are smaller than the growth rate of the dominant instability, which will eventually "fade out" from the simulations as a result of floating point number truncation.

[59] For the initial value setting, the GKE is explicitly evolved by means of direct time integration which can be used to solve the GKE both linearly and non-linearly. As far as the linear physics is concerned, the gyrokinetic equation can be cast in the form $\frac{\partial g}{\partial t} = L[g]$ where L is a linear operator which can be represented as a matrix, such that by assuming Fourier modes with a time dependence of $\exp(i\omega t)$ the linearised GKE takes the form of an eigenvalue problem whose eigenvalues correspond to the complex mode frequencies and whose eigenveigenvectors correspond to to the spatial structure of the perturbations, such that the linearised GKE can also be solved as an eigenvalue problem [181]. A direct solution to the eigenvalue problem would require the construction and inversion of the linear operator matrix which is extremely computationally extensive, and rather GENE uses an iterative method based on trial functions for the perturbations such that only matrix-vector products have to be computed and as a result a subset of eigenvalues is computed instead of the full spectrum, which has the advantage that one can zoom in on the region of interest of eigenvalues corresponding to a positive growth rate [16].

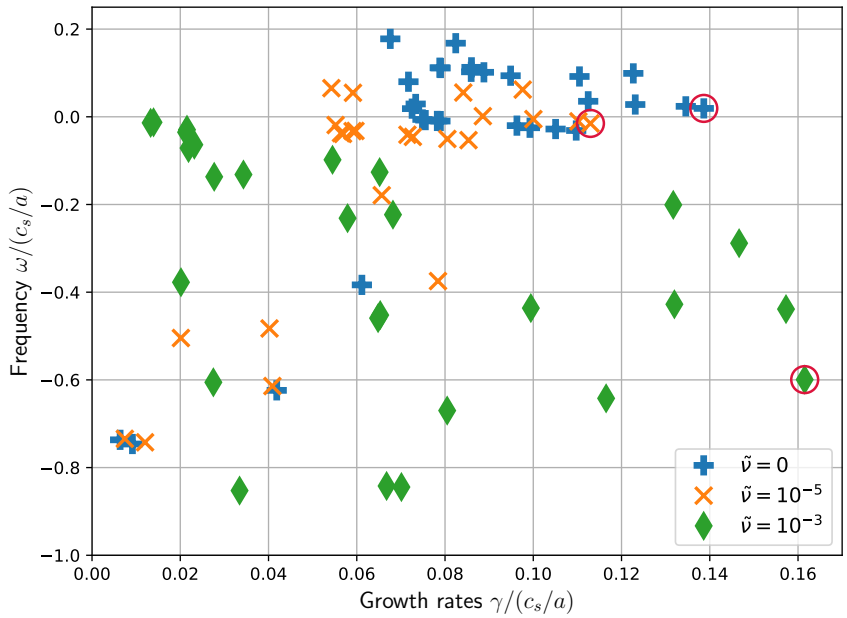

Figure 31: Eigenvalue spectrum of the 25 most unstable eigenmodes of the linearised GKE at binormal wavenumber $k_y\rho = 0.50$ for W7-X in the collisionless case, and two collisional cases corresponding to low and intermediate values of $\tilde{\nu}_c$ considered for the simulations of Chapter 4. The red encircled eigenvalues correspond to the most unstable eigenvalue at each value of $\tilde{\nu}_c$ and coincides with the results of Figure 28.

for the mode structure could be used as an additional input for the perturbative calculation, which affects both the electron response and field line normalising integral in Equation (79) as well as the average value of the perpendicular wavenumber Equation (77) used in the lowest order solution $\langle\omega_0\rangle$. This would however mean that costly gyrokinetic simulations have to be run on a super computer to generate input for a relatively cheap calculation which can be performed on a personal computer, which defeats the purpose of using analytical theory to make predictions about turbulence. As a hybrid option, a "proxy function" for the mode structure $\hat{\phi}(l)$ depending only on the fixed geometry input (B, κ) could be used to empirically account for the peaking of the mode in magnetic wells and bad curvature regions, which currently being investigated as an option for developing a proxy of the critical gradients below which the linear instabilities do not occur [182, 183].

Alternative theoretical approaches

However the largest restriction on the analytical approach is without a doubt the fact that the trapped electron response is accounted for perturbatively, while being the most important instability drive for TEMs. Indeed the resulting frequency shift $\delta\omega$ far exceeds the leading order frequency ω_0 accounting only for adiabatic electrons and kinetic ions. Nevertheless the perturbative approach takes into account the full kinetic details of the electrons, which is significantly more accurate than $i\delta$ models from early literature which take into account the non-adiabatic nature of electrons in an ad-hoc way as $\frac{\delta n}{n_0} = \frac{e\phi}{T_e}\exp(-i\delta)$ where $\delta > 0$ accounts for the phase delay between electron density- and potential fluctuations [85, 184–186]. Here δ is used as a proxy for any effect which prevents the electrons from establishing equilibrium along the field line such as collisions, trapping or drift-resonances [69, 187, 188]. In Appendix E.2 it is shown

that including the non-adiabaticity of electrons in this way to basic drift wave model leads to an instability whose growth rate depends on δ.

Two alternative analytical methods for finding the TEM growth rate were considered which treat the trapped electron response on equal footing with the remainder of the GKE. First a thermodynamic description of plasma turbulence was considered based on the free energy budget of the perturbations. This free energy consists of an entropy-like term which measures the energy stored in the perturbation of the distribution function and an internal energy term which measures the kinetic energy of the perturbed $\boldsymbol{E} \times \boldsymbol{B}$ drift [189–191], and for plasma turbulence takes on a similar role as the kinetic energy does in fluid turbulence [8,192]. What is special about the free energy is conserved by the $\boldsymbol{E} \times \boldsymbol{B}$ non-linearity such that it can be used to to analyse plasma turbulence in both linear and non-linear phases [191,193–195]. The work done on free energy can be found in Appendix Q which first extends the derivation of the evolution equation for the free energy using the conventions of reference [111] to an non-uniform plasma in an inhomogeneous magnetic field, and then applies the resulting equation to the approximate solutions for the ion and electron kinetic response derived in Section 3.1 which describe the linear TEM eigenmode to determine how the collisions influence the sign of the growth rate. However this strategy resulted in a paradox-esque situation where the sign of the growth rate can only be determined if the growth rate is a priori known. As a second alternative, the use of a variational approach was considered. Variational approaches are extremely powerful and ubiquitous in physics spanning classical mechanics [196], general relativity [197] and quantum mechanics [198]. Within fusion, the variational principle is the working principle of the VMEC code used to calculate 3D magnetic equilibria [142, 199] and stellarator coil optimisation [200]. The variational approach has also been applied to gyrokinetics in the past, with the focus on finding the mode frequency at the limit of marginal stability in absence of collisions [126, 182], and in the non-resonant fluid limit also to find the growth rate [175,201]. Some preliminary work on an attempt to extent the validity of the variational approach to find the gyrokinetic growth rates can be found in Appendix R, which is complicated by the inclusion of both growth rate and collisions which require a complex variant of the "classical" real variational principle [202]. This creates a problem, where the resulting Euler-Lagrange equations are not guaranteed to be consistent with the original quasi-neutrality condition they attempt to solve, which is a known issue in variational formulation of dissipative quantum mechanics [203]. This matter has not been succesfully resolved during the course of this thesis and might be considered for continuation in future work.

Bridging linear stability analysis to turbulent transport

Finally to make the circle complete with Chapter 1, the need for investigating the role of collisions was motivated based on Equation (1) which necessitates a sufficiently large density, temperature and energy confinement time for fusion to be viable as an energy source, the latter of which is limited by the turbulent transport. The turbulent transport fluxes are due to advection of the fluctuating particle density and energy by the equally fluctuating $\boldsymbol{E} \times \boldsymbol{B}$ drift and is therefore non-linear in the perturbations [71, 72, 75], such that the transport fluxes are not properly resolved by the simulations. The relation between linear instabilities and the turbulent transport is non-trivial as typically the modes with largest growth do not correspond to the modes which contain the most transport [204]. In terms of Fourier modes the $\boldsymbol{E} \times \boldsymbol{B}$ drift can be expressed as a convolution [191]

$$(\boldsymbol{v}_{\boldsymbol{E}} \cdot \boldsymbol{\nabla} g_s)_{\boldsymbol{k}_\perp} = -\frac{1}{B^2} \sum_{\boldsymbol{k}'_\perp} \boldsymbol{B} \cdot \left(\boldsymbol{k}'_\perp \times \left[\boldsymbol{k}_\perp - \boldsymbol{k}'_\perp\right]\right) J_0(k'_\perp \rho_s) \hat{\phi}_{\boldsymbol{k}'_\perp} \hat{g}_{s,\boldsymbol{k}_\perp - \boldsymbol{k}'_\perp}$$

which is responsible for "shuffling" energy between modes at different spatial scales [192], resulting in the eventual saturation of turbulence by drawing energy away from the growing modes at

a similar rate as the energy injection by the linear driving term [16, 68, 74]. Plasma turbulence however belongs to so-called "weak turbulence" which means that growth rates of instabilities are sufficiently small such that properties of linear instabilities can fully develop before they will interact non-linearly [128, 205]. This leads to the development of so-called mixing-length estimates for the diffusion coefficients $D \sim \gamma/k_\perp^2$ which allow to estimate transport fluxes based on linear properties by quasi-linear models as [144, 206]

$$\{\Gamma, Q\} \propto \{\boldsymbol{\nabla} n, \boldsymbol{\nabla} T\} \times \sum_{\boldsymbol{k}} \frac{\gamma_{\boldsymbol{k}}}{\langle k_\perp^2 \rangle} \tag{82}$$

where $\langle k_\perp \rangle$ is the weighted average of the perpendicular wavenumber over the mode structure $\hat{\phi}$ and $\gamma_{\boldsymbol{k}}$ is the growth rate at the wavenumber $\boldsymbol{k}$, which gives the best method for determining the turbulent transport with the available data of linear simulations. Such quasi-linear estimates however ultimately fail to predict the actual saturated levels of turbulence and thus do not accurately describe the absolute levels of transport [164]. Nevertheless, a quasi-linear model can always be matched to a particular non-linear simulation to give the correct level of transport, and then be used to "extrapolate" the fluxes using only linear data from simulations with new parameters [18, 207, 208]. In the past, however, poor matches between changes to the quasi-linear estimates and non-linear simulations of heat and particle fluxes with collisionality have have been observed [73, 75]. By supplementing the simple quasi-linear model of Equation (82) with additional physics-based weighting terms, it has in general been found that quasi-linear estimates better approximate the heat- and particle fluxes from simulations over an extended parameter regime [144, 209–211].

The eventual failure of quasi-linear models when the physicals parameters are changed significantly during the "extroplation" can be attributed to the complexity of the non-linear interactions which is typically not accounted for. The non-linear evolution of turbulence is described by a phase where energy injection from the most unstable instability into another mode can create a secondary instability, and if this secondary instability results in a density gradient which is aligned with the equilibrium gradients, the initial driving factor is enhanced and may feed novel energy into previously unstable or subdominant modes resulting in tertiary instability etc. [212]. As it is the intricate balance between this cycle of energy injection and redistribution to other modes which determines the saturated steady-state, non-linear simulations are ultimately required in the future to determine whether collisions not only reduce TEM growth rates but also TEM associated transport in DIII-D and HSX, and whether W7-X remains non-linearly stable against TEMs and to find out how severe the transport associated by the UI.

References

[1] Hannah Ritchie and Max Roser. *Our World in Data:* Energy. https://ourworldindata.org/energy, 2020. Accessed on 2021-09-27. (Cited on page 1.)

[2] Samer Fawzy, Ahmed I. Osman, John Doran, and David W. Rooney. Strategies for mitigation of climate change: a review. *Environmental Chemistry Letters 2020 18:6*, 18(6):2069–2094, jul 2020. (Cited on page 1.)

[3] Jeffrey P. Freidberg. *Plasma physics and fusion energy.* Cambridge University Press, may 2007. (Cited on pages 1, 2, 3, 6, 7, 17, 18, 26, 31, 59, 122, 130, 134, and 137.)

[4] John David Jackson. *Classical electrodynamics.* John Wiley & Sons, 1999. (Cited on page 1.)

[5] John Wesson, D.J. Campbell, J.W. Connor, R.D. Gill, J. Hugill, C.N. Lashmore-Davies, G.M. McCracken, H.R. Wilson, A.E. Costley, B. Lloyd, D.F. Start, R.J. Hastie, G.F. Matthews, B.J.D. Tubbing, A. Herrmann, J.J. O'Rourke, and D.J. Ward. *Tokamaks.* Oxfor University Press, fourth edition, 2004. (Cited on pages 1, 2, 3, 5, 8, 13, 16, 108, and 122.)

[6] John A. Krommes. The gyrokinetic description of microturbulence in magnetized plasmas. *Annual Review of Fluid Mechanics*, 44:175–201, 2012. (Cited on pages 2, 10, 20, 21, and 121.)

[7] X. Garbet, Y. Idomura, L. Villard, and T. H. Watanabe. Gyrokinetic simulations of turbulent transport. *Nuclear Fusion*, 50(4), 2010. (Cited on pages iii, 2, 9, 10, 11, 20, 23, 27, and 83.)

[8] A A Schekochihin, S C Cowley, W Dorland, G W Hammett, G G Howes, G G Plunk, E Quataert, and T Tatsuno. Gyrokinetic turbulence: a nonlinear route to dissipation through phase space. *Plasma Physics and Controlled Fusion*, 50(12):124024, nov 2008. (Cited on pages 2, 10, 16, 87, 162, and 167.)

[9] J. W. Connor and H. R. Wilson. Survey of theories of anomalous transport. *Plasma Physics and Controlled Fusion*, 36(5):719, may 1994. (Cited on page 2.)

[10] Ulrich Stroth. A comparative study of transport in stellarators and tokamaks. *Plasma Physics and Controlled Fusion*, 40(1):9, jan 1998. (Cited on page 2.)

[11] J A Alcusón, P Xanthopoulos, G G Plunk, P Helander, F Wilms, Y Turkin, A von Stechow, and O Grulke. Suppression of electrostatic micro-instabilities in maximum-J stellarators. *Plasma Physics and Controlled Fusion*, 62(3):035005, jan 2020. (Cited on pages 2, 11, 12, 44, and 59.)

[12] D.A. Baker, T.K. Fowler, H.P. Furth, R.F. Post, W.E. Quinn, M.N. Rosenbluth, P.H. Rutherford, J.L. Shohet, and Edward Teller. *Fusion Volume 1 : Magnetic confinement Part A.* Academic Press, 1981. (Cited on pages 2, 4, 7, 8, 13, 59, and 122.)

[13] M. Siccinio, J. P. Graves, R. Kembleton, H. Lux, F. Maviglia, A. W. Morris, J. Morris, and H. Zohm. Development of the plasma scenario for EU-DEMO: Status and plans. *Fusion Engineering and Design*, 176:113047, mar 2022. (Cited on pages iii and 3.)

[14] M. Siccinio, W. Biel, M. Cavedon, E. Fable, G. Federici, F. Janky, H. Lux, F. Maviglia, J. Morris, F. Palermo, O. Sauter, F. Subba, and H. Zohm. DEMO physics challenges beyond ITER. *Fusion Engineering and Design*, 156:111603, jul 2020. (Cited on pages iii and 3.)

[15] Tobias Görler. *MULTISCALE EFFECTS IN PLASMA MICROTURBULENCE*. PhD thesis, Unversität Ulm, 2009. (Cited on pages 2 and 56.)

[16] Florian Merz. *GYROKINETIC SIMULATION OF MULTIMODE PLASMA TURBULENCE*. PhD thesis, Westfälischen Wilhelms-Universität Münster, 2008. (Cited on pages 2, 11, 49, 57, 58, 84, 85, 88, 147, 154, and 156.)

[17] F. Jenko, W. Dorland, M. Kotschenreuther, and B. N. Rogers. Electron temperature gradient driven turbulence. *Physics of Plasmas*, 7(5):1904, apr 2000. (Cited on pages 2, 12, 16, 56, and 59.)

[18] C. Angioni, A. G. Peeters, F. Jenko, and T. Dannert. Collisionality dependence of density peaking in quasilinear gyrokinetic calculations. *Physics of Plasmas*, 12(11):112310, nov 2005. (Cited on pages 2, 67, and 88.)

[19] Yong Shen, J. Q. Dong, J. Li, M. K. Han, J. Q. Li, A. P. Sun, and H. P. Qu. Properties of ubiquitous modes in tokamak plasmas. *Nuclear Fusion*, 59(10):106011, aug 2019. (Cited on pages 2, 16, 59, and 63.)

[20] P. Helander and D.J. Sigmar. *Collisional Transport in Magnetized Plasmas*. Cambridge University Press, 2002. (Cited on pages 2, 10, 16, 17, 67, and 106.)

[21] J. G. Cordey, K. Thomsen, A. Chudnovskiy, O. J.W.F. Kardaun, T. Takizuka, J. A. Snipes, M. Greenwald, L. Sugiyama, F. Ryter, A. Kus, J. Stober, J. C. Deboo, C. C. Petty, G. Bracco, M. Romanelli, Z. Cui, Y. Liu, D. C. McDonald, A. Meakins, Y. Miura, K. Shinohara, K. Tsuzuki, Y. Kamada, H. Urano, M. Valovic, R. Akers, C. Brickley, A. Sykes, M. J. Walsh, S. M. Kaye, C. Bush, D. Hogewei, Y. Martin, A. Cote, G. Pacher, J. Ongena, F. Imbeaux, G. T. Hoang, S. Lebedev, and V. Leonov. Scaling of the energy confinement time with β and collisionality approaching ITER conditions. *Nuclear Fusion*, 45(9):1078, aug 2005. (Cited on page 3.)

[22] D. C. McDonald, J. G. Cordey, C. C. Petty, M. Beurskens, R. Budny, I. Coffey, M. De Baar, C. Giroud, E. Joffrin, P. Lomas, A. Meigs, J. Ongena, G. Saibene, R. Sartori, and I. Voitsekhovitch. The beta scaling of energy confinement in ELMy H-modes in JET. *Plasma Physics and Controlled Fusion*, 46(5A):A215, apr 2004. (Cited on page 3.)

[23] H. Yamada, J. H. Harris, A. Dinklage, E. Ascasibar, F. Sano, S. Okamura, J. Talmadge, U. Stroth, A. Kus, S. Murakami, M. Yokoyama, C. D. Beidler, V. Tribaldos, K. Y. Watanabe, and Y. Suzuki. Characterization of energy confinement in net-current free plasmas using the extended International Stellarator Database. *Nuclear Fusion*, 45(12):1684, nov 2005. (Cited on page 3.)

[24] E O Kiselev, M I Patrov, G S Kurskiev, N N Bakharev, V K Gusev, A Yu Telnova, N A Khromov, I V Miroshnikov, Yu V Petrov, N V Sakharov, V B Minaev, A D Sladkomedova, P B Shchegolev, V V Solokha, V A Tokarev, and S Yu Tolstyakov. Thermal energy confinement time scaling with Ip and BT in the Globus-M H-mode. In *45TH EPS CONFERENCE ON PLASMA PHYSICS*, 2018. (Cited on page 3.)

[25] Arthur Stanley Eddington. *The internal constitution of the stars*. Cambridge University Press, 1988. (Cited on page 3.)

[26] Friedrich-Karl Thielemann, Jordi Isern, Albino Perego, Peter Von Ballmoos, Andrei Bykov, Roger Chevalier, John Raymond, Maurizio Falanga, Rudolf Von Steiger, F.-K Thielemann, J Isern, Isern@ice Cat, A Perego, P Von Ballmoos, and Omp Eu. Nucleosynthesis in Supernovae. *Space Science Reviews 2018 214:3*, 214(3):1–62, mar 2018. (Cited on page 3.)

[27] Richard A Dunlap. *An introduction to the physics of nuclei and particles*. Thomson/Brooks-Cole, 2003. (Cited on page 3.)

[28] M L E Oliphant, P H Arteck, Lord Rutherford, By M L E O, and Messel Research Fellow. Transmutation effects observed with heavy hydrogen. *Proceedings of the Royal Society of London. Series A, Containing Papers of a Mathematical and Physical Character*, 144(853):692–703, may 1934. (Cited on page 3.)

[29] Arnab Rai Choudhuri. *Astrophysics for Physicists*. Cambridge University Press, 2010. (Cited on page 3.)

[30] Robert Goldston and Paul Rutherford. *Introduction to Plasma Physics*. CRC Press, 1995. (Cited on pages 4, 7, 13, 17, and 108.)

[31] Yevgen Kazakov, Dirk Van Eester, and Jef Ongena. Plasma heating in present-day and future fusion machines. *12th Carolus Magnus Summer School on Plasma and Fusion Energy Physics*, 2015. (Cited on page 4.)

[32] Jaume Masoliver and Ana Ros. Integrability and chaos: the classical uncertainty. *European Journal of Physics*, 32(2):431, jan 2011. (Cited on page 4.)

[33] V.P. Smirnov. Tokamak foundation in USSR/Russia 1950–1990. *Nuclear Fusion*, 50(1):014003, dec 2009. (Cited on page 4.)

[34] Marco Ariola and Alfredo Pironti. *Magnetic Control of Tokamak Plasmas*. Advances in Industrial Control. Springer International Publishing, Cham, second edition edition, 2016. (Cited on page 5.)

[35] Egbert Westerhof. Non-inductive current drive. *Fusion Science and Technology*, 61(2T):312–319, 2012. (Cited on page 5.)

[36] Josefine Proll. *TRAPPED-PARTICLE INSTABILITIES IN QUASI-ISODYNAMIC STELLARATORS*. PhD thesis, University of Greifswald, Greifswald, 2013. (Cited on pages iii, 5, 8, 15, 37, and 140.)

[37] Lyman Jr. Spitzer. The Stellarator Concept. *The Physics of Fluids*, 1(253), 1958. (Cited on page 5.)

[38] Allen H. Boozer. What is a stellarator? *Physics of Plasmas*, 5(5):1647, apr 1998. (Cited on pages 5 and 6.)

[39] R. L. Dewar and S. R. Hudson. Stellarator symmetry. *Physica D: Nonlinear Phenomena*, 112(1-2):275–280, jan 1998. (Cited on page 5.)

[40] P. Xanthopoulos, H. E. Mynick, P. Helander, Y. Turkin, G. G. Plunk, F. Jenko, T. Görler, D. Told, T. Bird, and J. H.E. Proll. Controlling turbulence in present and future stellarators. *Physical Review Letters*, 113(15):155001, oct 2014. (Cited on page 6.)

[41] E. G. Highcock, A. A. Schekochihin, S. C. Cowley, M. Barnes, F. I. Parra, C. M. Roach, and W. Dorland. Zero-Turbulence Manifold in a Toroidal Plasma. *Physical Review Letters*, 109(26):265001, dec 2012. (Cited on page 6.)

[42] Josefine H E Proll, Pavlos Xanthopoulos, Harry Mynick, and Sam A Lazerson. Progress in Turbulence Optimization Research for Stellarator Plasmas. In *The 35th Annual Meeting of the Society for Plasma and Nuclear Fusion Proceedings*, 2018. (Cited on page 6.)

[43] P Helander, C D Beidler, T M Bird, M Drevlak, Y Feng, R Hatzky, F Jenko, R Kleiber, J H E Proll, Yu Turkin, and P Xanthopoulos. Stellarator and tokamak plasmas: a compar-

ison. *Plasma Physics and Controlled Fusion*, 54(12):124009, nov 2012. (Cited on pages 6, 8, 33, 38, 65, 84, 130, and 174.)

[44] Yuhong Xu. A general comparison between tokamak and stellarator plasmas. *Matter and Radiation at Extremes*, 1(4):192–200, jul 2016. (Cited on pages 6 and 84.)

[45] Allen H. Boozer. Plasma equilibrium with rational magnetic surfaces. *The Physics of Fluids*, 24(11):1999, jun 1981. (Cited on pages 6 and 153.)

[46] Per Helander. Theory of plasma confinement in non-axisymmetric magnetic fields. *Reports on Progress in Physics*, 77(8), 2014. (Cited on pages 6, 7, 8, 38, 43, 49, 59, and 148.)

[47] William Denis D'haeseleer, William Nicholas Guy Hitchon, James D. Callen, and J. Leon Shohet. *Flux Coordinates and Magnetic Field Structure*. Springer Berlin Heidelberg, 1 edition, 1991. (Cited on pages 6 and 153.)

[48] T. G. Northrop. Adiabatic theory of charged particle motion. In Billy M. McCormac, editor, *Radiation Trapped in the Earth's Magnetic Field*, pages 26–44, Dordrecht, 1966. Springer Netherlands. (Cited on pages 7 and 8.)

[49] Jonathan Clifford Zahn. *Relation between the magnetic moments associated with the first and third adiabatic invariants*. PhD thesis, Rice University, 1988. (Cited on page 8.)

[50] R.J.J. Mackenbach, J.H.E. Proll, and P. Helander. Available Energy of Trapped Electrons and Its Relation to Turbulent Transport. *Physical Review Letters*, 128(17):175001, apr 2022. (Cited on pages 8 and 48.)

[51] N. J. Lopes Cardozo, A. G. G. Lange, and G. J. Kramer. Fusion: Expensive and Taking Forever? *Journal of Fusion Energy 2015 35:1*, 35(1):94–101, sep 2015. (Cited on page 9.)

[52] Mitsuru Kikuchi. The large tokamak JT-60: a history of the fight to achieve the Japanese fusion research mission. *The European Physical Journal H 2018 43:4*, 43(4):551–577, nov 2018. (Cited on page 10.)

[53] EAST Team. China's Experimental Advanced Superconducting Tokamak sets new world record. *iEnergy*, 1(1):3–3, mar 2022. (Cited on page 10.)

[54] Joelle Mailloux. Overview of JET results for optimising ITER operation. *Nuclear Fusion*, jan 2022. (Cited on page 10.)

[55] R. C. Wolf, A. Alonso, S. Äkäslompolo, J. Baldzuhn, M. Beurskens, C. D. Beidler, C. Biedermann, H. S. Bosch, S. Bozhenkov, R. Brakel, H. Braune, S. Brezinsek, K. J. Brunner, H. Damm, A. DInklage, P. Drewelow, F. Effenberg, Y. Feng, O. Ford, G. Fuchert, Y. Gao, J. Geiger, O. Grulke, N. Harder, D. Hartmann, P. Helander, B. Heinemann, M. Hirsch, U. Höfel, C. Hopf, K. Ida, M. Isobe, M. W. Jakubowski, Y. O. Kazakov, C. Killer, T. Klinger, J. Knauer, R. König, M. Krychowiak, A. Langenberg, H. P. Laqua, S. Lazerson, P. McNeely, S. Marsen, N. Marushchenko, R. Nocentini, K. Ogawa, G. Orozco, M. Osakabe, M. Otte, N. Pablant, E. Pasch, A. Pavone, M. Porkolab, A. Puig Sitjes, K. Rahbarnia, R. Riedl, N. Rust, E. Scott, J. Schilling, R. Schroeder, T. Stange, A. Von Stechow, E. Strumberger, T. Sunn Pedersen, J. Svensson, H. Thomson, Y. Turkin, L. Vano, T. Wauters, G. Wurden, M. Yoshinuma, M. Zanini, D. Zhang, and Wendelstein 7-X team. Performance of Wendelstein 7-X stellarator plasmas during the first divertor operation phase. *Physics of Plasmas*, 26(8):082504, aug 2019. (Cited on pages 10 and 59.)

[56] Marek Rubel. Fusion Neutrons: Tritium Breeding and Impact on Wall Materials and Components of Diagnostic Systems. *Journal of Fusion Energy 2018 38:3*, 38(3):315–329, sep 2018. (Cited on page 10.)

[57] M. Turnyanskiy, R. Neu, R. Albanese, R. Ambrosino, C. Bachmann, S. Brezinsek, T. Donne, T. Eich, G. Falchetto, G. Federici, D. Kalupin, X. Litaudon, M. L. Mayoral, D. C. McDonald, H. Reimerdes, F. Romanelli, R. Wenninger, and J. H. You. European roadmap to the realization of fusion energy: Mission for solution on heat-exhaust systems. *Fusion Engineering and Design*, 96-97:361–364, oct 2015. (Cited on page 10.)

[58] P.T. Lang, A. Loarte, G. Saibene, L.R. Baylor, M. Becoulet, M. Cavinato, S. Clement-Lorenzo, E. Daly, T.E. Evans, M.E. Fenstermacher, Y. Gribov, L.D. Horton, C. Lowry, Y. Martin, O. Neubauer, N. Oyama, M.J. Schaffer, D. Stork, W. Suttrop, P. Thomas, M. Tran, H.R. Wilson, A. Kavin, and O. Schmitz. ELM control strategies and tools: status and potential for ITER. *Nuclear Fusion*, 53(4):043004, mar 2013. (Cited on page 10.)

[59] A W Leonard. Plasma detachment in divertor tokamaks. *Plasma Physics and Controlled Fusion*, 60(4):044001, feb 2018. (Cited on page 10.)

[60] Shanliang Zheng and Thomas N. Todd. Study of impacts on tritium breeding ratio of a fusion DEMO reactor. *Fusion Engineering and Design*, 98-99:1915–1918, oct 2015. (Cited on page 10.)

[61] Richard J. Pearson, Armando B. Antoniazzi, and William J. Nuttall. Tritium supply and use: a key issue for the development of nuclear fusion energy. *Fusion Engineering and Design*, 136:1140–1148, nov 2018. (Cited on page 10.)

[62] H Arnichand, J Citrin, S Hacquin, R Sabot, A Krämer-Flecken, X Garbet, C Bourdelle, C Bottereau, F Clairet, J C Giacalone, Z O Guimarães-Filho, R Guirlet, G Hornung, A Lebschy, P Lotte, P Maget, A Medvedeva, D Molina, V Nikolaeva, D Prisiazhniuk, the Tore Supra, and the ASDEX Upgrade Teams. Identification of trapped electron modes in frequency fluctuation spectra. *Plasma Physics and Controlled Fusion*, 58(1):014037, nov 2015. (Cited on page 10.)

[63] D.L. Brower, W.A. Peebles, and N.C. Luhmann. The spectrum, spatial distribution and scaling of microturbulence in the TEXT tokamak. *Nuclear Fusion*, 27(12):2055, dec 1987. (Cited on page 10.)

[64] D. Guo, L. Nie, R. Ke, M. Xu, Z.H. Wang, T. Long, Y.F. Wu, B.D. Yuan, S.B. Gong, H. Liu, and HL-2A Team. Experimental study of cross phase influence on Reynolds stress in the HL-2A tokamak. *Nuclear Fusion*, 58(2):026015, dec 2017. (Cited on page 10.)

[65] N. Fedorczak, J. P. Gunn, Ph Ghendrih, G. Ciraolo, H. Bufferand, L. Isoardi, P. Tamain, and P. Monier-Garbet. Experimental investigation on the poloidal extent of the turbulent radial flux in tokamak scrape-off layer. *Journal of Nuclear Materials*, 415(1):S467–S470, aug 2011. (Cited on page 10.)

[66] S.J. Zweben and R.W. Gould. Structure of edge-plasma turbulence in the Caltech tokamak. *Nuclear Fusion*, 25(2):171, feb 1985. (Cited on page 10.)

[67] Gregory G. Howes, Steven C. Cowley, William Dorland, Gregory W. Hammett, Eliot Quataert, and Alexander A. Schekochihin. Astrophysical Gyrokinetics: Basic Equations and Linear Theory. *The Astrophysical Journal*, 651(1):590–614, nov 2006. (Cited on pages 10, 22, 27, 117, 162, and 168.)

[68] Michael Alan Beer. *GYROFLUID MODELS OF TURBULENT TRANSPORT IN TOKAMAKS*. PhD thesis, Princeton University, jan 1995. (Cited on pages 10, 57, 59, 88, and 153.)

[69] W. M. Tang. Microinstability theory in tokamaks. *Nuclear Fusion*, 18(8):1089, aug 1978. (Cited on pages 10, 33, 36, 63, 86, and 116.)

[70] F. L. Hinton and R. D. Hazeltine. Theory of plasma transport in toroidal confinement systems. *Reviews of Modern Physics*, 48(2):239, apr 1976. (Cited on pages 10, 17, 18, and 67.)

[71] G. L. Falchetto and M. Ottaviani. Effect of Collisional Zonal-Flow Damping on Flux-Driven Turbulent Transport. *Physical Review Letters*, 92(2):025002, jan 2004. (Cited on pages 10, 59, and 87.)

[72] W. W. Lee and W. M. Tang. Gyrokinetic particle simulation of ion temperature gradient drift instabilities. *The Physics of Fluids*, 31(3):612, sep 1988. (Cited on pages 10 and 87.)

[73] Z. Lin, T. S. Hahm, W. W. Lee, W. M. Tang, and P. H. Diamond. Effects of Collisional Zonal Flow Damping on Turbulent Transport. *Physical Review Letters*, 83(18):3645, nov 1999. (Cited on pages 10, 59, and 88.)

[74] G J Colyer, A A Schekochihin, F I Parra, C M Roach, M A Barnes, Y-c Ghim, and W Dorland. Collisionality scaling of the electron heat flux in ETG turbulence. *Plasma Physics and Controlled Fusion*, 59(5):055002, mar 2017. (Cited on pages 10, 16, 59, 67, and 88.)

[75] T Vernay, S Brunner, L Villard, B F McMillan, S Jolliet, A Bottino, T Görler, and F Jenko. Global gyrokinetic simulations of TEM microturbulence. *Plasma Physics and Controlled Fusion*, 55(7):074016, jul 2013. (Cited on pages 10, 33, 56, 59, 67, 87, and 88.)

[76] P. Manas, Y. Camenen, S. Benkadda, W. A. Hornsby, and A. G. Peeters. Enhanced stabilisation of trapped electron modes by collisional energy scattering in tokamaks. *Physics of Plasmas*, 22(6):062302, jun 2015. (Cited on pages 10, 59, 85, 140, and 172.)

[77] C. Zhao, T. Zhang, and Y. Xiao. Gyrokinetic simulation of dissipative trapped electron mode in tokamak edge. *Physics of Plasmas*, 24(5):052509, may 2017. (Cited on pages 10, 59, and 67.)

[78] P. Helander. Microstability of Magnetically Confined Electron-Positron Plasmas. *Physical Review Letters*, 113(13):135003, sep 2014. (Cited on page 10.)

[79] K Kauffmann, R Kleiber, R Hatzky, and M Borchardt. Global linear gyrokinetic simulations for LHD including collisions. *Journal of Physics: Conference Series*, 260(1):012014, nov 2010. (Cited on pages 11 and 59.)

[80] Liu Chen, P.N. Guzdar, J.Y. Hsu, P.K. Kaw, C. Oberman, and R. White. Theory of dissipative drift instabilities in sheared magnetic fields. *Nuclear Fusion*, 19(3):373, mar 1979. (Cited on page 11.)

[81] P. N. Guzdar, Liu Chen, P. K. Kaw, and C. Oberman. Effect of Magnetic Shear on Dissipative Drift-Wave Instabilities. *Physical Review Letters*, 40(24):1566, jun 1978. (Cited on page 11.)

[82] L. Chen, M.S. Chance, and C.Z. Cheng. Absolute dissipative drift-wave instabilities in tokamaks. *Nuclear Fusion*, 20(7):901, jul 1980. (Cited on page 11.)

[83] J. W. Connor, R. J. Hastie, and P. Helander. Stability of the trapped electron mode in steep density and temperature gradients. *Plasma Physics and Controlled Fusion*, 48(6):885, may 2006. (Cited on pages 11, 36, 37, 49, and 140.)

[84] T. Rafiq and C. C. Hegna. Dissipative trapped-electron instability in quasihelically symmetric stellarators. *Physics of Plasmas*, 13(6):062501, jun 2006. (Cited on pages 11, 28, and 37.)

[85] A. Kendl and H. Wobig. Geometric effects on drift wave stability in advanced stellarators. *Physics of Plasmas*, 6(12):4714, nov 1999. (Cited on pages 11, 28, 37, and 86.)

[86] I. G. Abel, M. Barnes, S. C. Cowley, W. Dorland, and A. A. Schekochihin. Linearized model Fokker–Planck collision operators for gyrokinetic simulations. I. Theory. *Physics of Plasmas*, 15(12):122509, dec 2008. (Cited on pages 11, 22, 25, 27, and 68.)

[87] M. Barnes, I. G. Abel, W. Dorland, D. R. Ernst, G. W. Hammett, P. Ricci, B. N. Rogers, A. A. Schekochihin, and T. Tatsuno. Linearized model Fokker–Planck collision operators for gyrokinetic simulations. II. Numerical implementation and tests. *Physics of Plasmas*, 16(7):072107, jul 2009. (Cited on pages 11, 68, and 167.)

[88] H. Sugama, T.-H. Watanabe, and M. Nunami. Linearized model collision operators for multiple ion species plasmas and gyrokinetic entropy balance equations. *Physics of Plasmas*, 16(11):112503, nov 2009. (Cited on pages 11, 22, 68, and 167.)

[89] Qingjiang Pan, Darin R. Ernst, and Paul Crandall. First implementation of gyrokinetic exact linearized Landau collision operator and comparison with models. *Physics of Plasmas*, 27(4):042307, apr 2020. (Cited on pages 11, 22, 68, and 167.)

[90] P. Crandall, D. Jarema, H. Doerk, Q. Pan, G. Merlo, T. Görler, A. Bañón Navarro, D. Told, M. Maurer, and F. Jenko. Multi-species collisions for delta-f gyrokinetic simulations: Implementation and verification with GENE. *Computer Physics Communications*, 255:107360, oct 2020. (Cited on pages 11, 22, 56, 68, and 167.)

[91] B.J. Frei, J. Ball, A.C.D. Hoffmann, R. Jorge, P. Ricci, and L. Stenger. Development of advanced linearized gyrokinetic collision operators using a moment approach. *Journal of Plasma Physics*, 87(5):905870501, oct 2021. (Cited on pages 11, 25, and 68.)

[92] P Helander, T Bird, F Jenko, R Kleiber, G G Plunk, J H E Proll, J Riemann, and P Xanthopoulos. Advances in stellarator gyrokinetics. *Nuclear Fusion*, 55(5):053030, apr 2015. (Cited on pages 11, 33, and 44.)

[93] G. G. Plunk, J. W. Connor, and P. Helander. Collisionless microinstabilities in stellarators. Part 4. The ion-driven trapped-electron mode. *Journal of Plasma Physics*, 83(4), aug 2017. (Cited on pages 11, 32, 37, 67, 84, and 174.)

[94] D. R. Ernst, J. Lang, W. M. Nevins, M. Hoffman, Y. Chen, W. Dorland, and S. Parker. Role of zonal flows in trapped electron mode turbulence through nonlinear gyrokinetic particle and continuum simulationa). *Physics of Plasmas*, 16(5):055906, may 2009. (Cited on pages 11 and 83.)

[95] J. H.E. Proll, P. Helander, J. W. Connor, and G. G. Plunk. Resilience of Quasi-Isodynamic Stellarators against Trapped-Particle Instabilities. *Physical Review Letters*, 108(24):245002, jun 2012. (Cited on pages 11, 46, 59, 63, 84, and 169.)

[96] J. H.E. Proll, P. Xanthopoulos, and P. Helander. Collisionless microinstabilities in stellarators. II. Numerical simulations. *Physics of Plasmas*, 20(12):122506, dec 2013. (Cited on pages 11, 49, 61, and 140.)

[97] F. Simon B. Anderson, Abdulgader F. Almagri, David T. Anderson, Peter G. Matthews, Joseph N. Talmadge, and J. Leon Shohet. The Helically Symmetric Experiment, (HSX) Goals, Design and Status. *https://doi.org/10.13182/FST95-A11947086*, 27(3T):273–277, apr 1995. (Cited on page 12.)

[98] Craig Beidler, Guenter Grieger, Franz Herrnegger, Ewald Harmeyer, Johann Kisslinger, Wolf Lotz, Henning Maassberg, Peter Merkel, Juergen Nuehrenberg, Fritz Rau, Joerg Sapper, Francesco Sardei, Ruben Scardovelli, Arnulf Schlueter, and Horst Wobig. Physics and

Engineering Design for Wendelstein VII-X. *http://dx.doi.org/10.13182/FST90-A29178*, 17(1):148–168, 1990. (Cited on page 12.)

[99] J L Luxon. A design retrospective of the DIII-D tokamak. *Nuclear Fusion*, 42(5):614, may 2002. (Cited on page 12.)

[100] M. Fivaz, S. Brunner, G. De Ridder, O. Sauter, T. M. Tran, J. Vaclavik, L. Villard, and K. Appert. Finite element approach to global gyrokinetic Particle-In-Cell simulations using magnetic coordinates. *Computer Physics Communications*, 111(1-3):27–47, jun 1998. (Cited on page 16.)

[101] W. Dorland and G. W. Hammett. Gyrofluid turbulence models with kinetic effects. *Physics of Fluids B: Plasma Physics*, 5(3):812, jun 1998. (Cited on page 16.)

[102] W. M. Nevins, J. Candy, S. Cowley, T. Dannert, A. Dimits, W. Dorland, C. Estrada-Mila, G. W. Hammett, F. Jenko, M. J. Pueschel, and D. E. Shumaker. Characterizing electron temperature gradient turbulence via numerical simulation. *Physics of Plasmas*, 13(12):122306, dec 2006. (Cited on pages 16, 56, and 59.)

[103] R.L. Liboff. *Kinetic Theory: Classical, Quantum and Relativistic Descriptions*. Springer-Verlag, third edit edition, 2003. (Cited on page 16.)

[104] Gérard Belmont, Laurence Rezeau, Caterina Riconda, and Arnaud Zaslavsky. Kinetic Theory of Plasma. *Introduction to Plasma Physics*, pages 57–74, jan 2019. (Cited on pages 17 and 28.)

[105] Marshall N. Rosenbluth, William M. MacDonald, and David L. Judd. Fokker-Planck Equation for an Inverse-Square Force. *Physical Review*, 107(1):1, jul 1957. (Cited on pages 17 and 110.)

[106] B. Li and D. R. Ernst. Gyrokinetic Fokker-Planck Collision Operator. *Physical Review Letters*, 106(19):195002, may 2011. (Cited on pages 18 and 68.)

[107] Alain J. Brizard. A guiding-center Fokker–Planck collision operator for nonuniform magnetic fields. *Physics of Plasmas*, 11(9):4429, aug 2004. (Cited on pages 18 and 25.)

[108] R. John Taylor. *Classical Mechanics* . Univerity Science Books, 2005. (Cited on pages 20 and 163.)

[109] A. J. Brizard and T. S. Hahm. Foundations of nonlinear gyrokinetic theory. *Reviews of Modern Physics*, 79(2):421, apr 2007. (Cited on pages 21, 25, 27, 84, and 162.)

[110] Daniel H. E. Dubin, John A. Krommes, C. Oberman, and W. W. Lee. Nonlinear gyrokinetic equations. *The Physics of Fluids*, 26(12):3524, jun 1983. (Cited on page 21.)

[111] A. A. Schekochihin, S. C. Cowley, W. Dorland, G. W. Hammett, G. G. Howes, E. Quataert, and T. Tatsuno. ASTROPHYSICAL GYROKINETICS: KINETIC AND FLUID TURBULENT CASCADES IN MAGNETIZED WEAKLY COLLISIONAL PLASMAS. *The Astrophysical Journal Supplement Series*, 182(1):310, may 2009. (Cited on pages 22, 27, 87, 116, 162, 166, and 169.)

[112] P. H. Rutherford and E. A. Frieman. Drift Instabilities in General Magnetic Field Configurations. *The Physics of Fluids*, 11(3):569, aug 1968. (Cited on pages 23 and 116.)

[113] W. J. Miloch, S. V. Vladimirov, and V. V. Yaroshenko. Complex wakes behind objects in multispecies plasmas. *Europhysics Letters*, 101(1):15001, jan 2013. (Cited on page 26.)

[114] S. P. Hirshman and D. J. Sigmar. Approximate Fokker-Planck collision operator for transport theory applications. *Physics of Fluids*, 19(10):1532–1540, aug 1976. (Cited on pages 27 and 116.)

[115] W.M. Tang, C.S. Liu, M.N. Rosenbluth, P.J. Catto, and J.D. Callen. Finite-beta and resonant-electron effects on trapped-electron instabilities. *Nuclear Fusion*, 16(2):191, apr 1976. (Cited on pages 27 and 29.)

[116] P. L. Bhatnagar, E. P. Gross, and M. Krook. A Model for Collision Processes in Gases. I. Small Amplitude Processes in Charged and Neutral One-Component Systems. *Physical Review*, 94(3):511, may 1954. (Cited on pages 27 and 28.)

[117] E. P. Gross and M. Krook. Model for Collision Processes in Gases: Small-Amplitude Oscillations of Charged Two-Component Systems. *Physical Review*, 102(3):593, may 1956. (Cited on pages 28, 30, and 125.)

[118] S. Livi and E. Marsch. Comparison of the Bhatnagar-Gross-Krook approximation with the exact Coulomb collision operator. *Physical Review A*, 34(1):533, jul 1986. (Cited on page 28.)

[119] Stephen J. Bradshaw and John Raymond. Collisional and radiative processes in optically thin plasmas. *Space Science Reviews*, 178(2-4):271–306, oct 2013. (Cited on page 28.)

[120] F. Y. Gang, P. H. Diamond, and M. N. Rosenbluth. A kinetic theory of trapped-electron-driven drift wave turbulence in a sheared magnetic field. *Physics of Fluids B: Plasma Physics*, 3(1):68, jun 1991. (Cited on pages 28, 37, and 44.)

[121] N. Dominguez, B. A. Carreras, V. E. Lynch, and P. H. Diamond. Dissipative trapped electron modes in l=2 torsatrons. *Physics of Fluids B: Plasma Physics*, 4(9):2894, sep 1992. (Cited on pages 28, 33, 36, and 37.)

[122] G. Rewoldt, W. M. Tang, and E. A. Frieman. Two-dimensional spatial structure of the dissipative trapped-electron mode. *The Physics of Fluids*, 20(3):402, aug 1977. (Cited on pages 28 and 32.)

[123] P. L. Bhatnagar. On the BGK Collision Model for a Two-Component Assembly. *Zeitschrift für Astrophysik*, 54:234, 1962. (Cited on pages 30, 31, 125, and 130.)

[124] John M. Greene. Improved Bhatnagar-Gross-Krook model of electron-ion collisions. *The Physics of Fluids*, 16(11):2022, jul 1973. (Cited on pages 30 and 126.)

[125] G. G. Plunk and Per Helander. Energetic bounds on gyrokinetic instabilities. Part II. Modes of optimal growth. jan 2022. (Cited on pages 32, 63, 84, and 169.)

[126] P Helander, J H E Proll, and G G Plunk. Collisionless microinstabilities in stellarators. I. Analytical theory of trapped-particle modes. *Phys. Plasmas*, 20:122505, 2013. (Cited on pages 32, 37, 44, 46, 84, 87, 169, and 177.)

[127] G. G. Plunk, P. Helander, P. Xanthopoulos, and J. W. Connor. Collisionless microinstabilities in stellarators. III. The ion-temperature-gradient mode. *Physics of Plasmas*, 21(3):032112, mar 2014. (Cited on pages 33, 59, and 63.)

[128] T. S. Hahm and W. M. Tang. Weak turbulence theory of collisionless trapped electron driven drift instability in tokamaks. *Physics of Fluids B: Plasma Physics*, 3(4):989, jun 1991. (Cited on pages 33, 43, 44, and 88.)

[129] G. Depret, X. Garbet, P. Bertrand, and A. Ghizzo. Trapped-ion driven turbulence in tokamak plasmas. *Plasma Physics and Controlled Fusion*, 42(9):949, sep 2000. (Cited on page 33.)

[130] H. Biglari, P. H. Diamond, and P. W. Terry. Theory of trapped-ion-temperature-gradient-driven turbulence and transport in low-collisionality plasmas. *The Physics of Fluids*, 31(9):2644, jun 1998. (Cited on page 33.)

[131] H. Biglari, P. H. Diamond, and M. N. Rosenbluth. Toroidal ion-pressure-gradient-driven drift instabilities and transport revisited. *Physics of Fluids B: Plasma Physics*, 1(1):109, jun 1998. (Cited on page 33.)

[132] P. Helander and G. G. Plunk. The universal instability in general geometry. *Physics of Plasmas*, 22(9):090706, sep 2015. (Cited on pages 36, 67, and 118.)

[133] Y. R. Lin-Liu and R. L. Miller. Upper and lower bounds of the effective trapped particle fraction in general tokamak equilibria. *Physics of Plasmas*, 2(5):1666, jun 1995. (Cited on page 37.)

[134] J. C. Adam, W. M. Tang, and P. H. Rutherford. Destabilization of the trapped-electron mode by magnetic curvature drift resonances. *The Physics of Fluids*, 19(4):561, aug 1976. (Cited on pages 37, 46, and 49.)

[135] Alexander. O. Gogolin, Elena G. Tsitsishvili, and Andreas Komnik. Hypergeometric Series with Applications. In *Lectures on Complex Integration*, pages 63–111. Springer, Cham, 2014. (Cited on page 39.)

[136] A. I. Smolyakov and X. Garbet. Drift kinetic equation in the moving reference frame and reduced magnetohydrodynamic equations. *Physics of Plasmas*, 17(4):042105, apr 2010. (Cited on page 41.)

[137] J.H.E. Proll, G.G. Plunk, B.J. Faber, T. Görler, P. Helander, I.J. McKinney, M.J. Pueschel, H.M. Smith, and P. Xanthopoulos. Turbulence mitigation in maximum-J stellarators with electron-density gradient. *Journal of Plasma Physics*, 88(1):905880112, feb 2022. (Cited on pages 44 and 59.)

[138] F. D. (Fedor Dmitrievich) Gakhov. *Boundary Value Problems*. Pergamon Press, 1966. (Cited on page 45.)

[139] P. Xanthopoulos, W. A. Cooper, F. Jenko, Yu Turkin, A. Runov, and J. Geiger. A geometry interface for gyrokinetic microturbulence investigations in toroidal configurations. *Physics of Plasmas*, 16(8):082303, aug 2009. (Cited on pages 48, 56, 84, and 153.)

[140] A. Dinklage, C. D. Beidler, P. Helander, G. Fuchert, H. Maaßberg, K. Rahbarnia, T. Sunn Pedersen, Y. Turkin, R. C. Wolf, T. Andreeva, S. Bozhenkov, B. Buttenschön, Y. Feng, J. Geiger, M. Hirsch, U. Höfel, M. Jakubowski, T. Klinger, J. Knauer, A. Langenberg, H. P. Laqua, N. Marushchenko, A. Mollén, U. Neuner, H. Niemann, E. Pasch, L. Rudischhauser, H. M. Smith, T. Stange, G. Weir, T. Windisch, D. Zhang, and Wendelstein 7-X team. Magnetic configuration effects on the Wendelstein 7-X stellarator. *Nature Physics 2018 14:8*, 14(8):855–860, may 2018. (Cited on page 49.)

[141] LL Lao, H St JOHN, RD Stambaugh, Ag Kellman, and W Pfeiffer. Reconstruction of current profile parameters and plasma shapes in tokamaks. *Nuclear Fusion*, 25(11):1611, nov 1985. (Cited on pages iv and 50.)

[142] S. P. Hirshman, W. I. van RIJ, and P. Merkel. Three-dimensional free boundary calculations using a spectral Green's function method. *Computer Physics Communications*, 43(1):143–155, dec 1986. (Cited on pages iv, 50, and 87.)

[143] Tilman Dannert and Frank Jenko. Gyrokinetic simulation of collisionless trapped-electron mode turbulence. *Physics of Plasmas*, 12(7):072309, jul 2005. (Cited on pages 49, 59, and 63.)

[144] M. J. Pueschel, B. J. Faber, J. Citrin, C. C. Hegna, P. W. Terry, and D. R. Hatch. Stellarator Turbulence: Subdominant Eigenmodes and Quasilinear Modeling. *Physical Review Letters*, 116(8):085001, feb 2016. (Cited on pages 49, 84, and 88.)

[145] M. Tagger, G. Laval, and R. Pellat. Trapped ion mode driven by ion magnetic drift resonance in a fat torus. *Nuclear Fusion*, 17(1):109, feb 1977. (Cited on page 49.)

[146] F. Romanelli and S. Briguglio. Toroidal semicollisional microinstabilities and anomalous electron and ion transport. *Physics of Fluids B: Plasma Physics*, 2(4):754, jun 1998. (Cited on page 49.)

[147] G. L. Falchetto, B. D. Scott, P. Angelino, A. Bottino, T. Dannert, V. Grandgirard, S. Janhunen, F. Jenko, S. Jolliet, A. Kendl, B. F. McMillan, V. Naulin, A. H. Nielsen, M. Ottaviani, A. G. Peeters, M. J. Pueschel, D. Reiser, T. T. Ribeiro, and M. Romanelli. The European turbulence code benchmarking effort: turbulence driven by thermal gradients in magnetically confined plasmas. *Plasma Physics and Controlled Fusion*, 50(12):124015, nov 2008. (Cited on pages 56 and 59.)

[148] X. Lapillonne, S. Brunner, T. Dannert, S. Jolliet, A. Marinoni, L. Villard, T. Görler, F. Jenko, and F. Merz. Clarifications to the limitations of the s-α equilibrium model for gyrokinetic computations of turbulence. *Physics of Plasmas*, 16(3):032308, mar 2009. (Cited on page 56.)

[149] F Merz and F Jenko. Nonlinear interplay of TEM and ITG turbulence and its effect on transport. *Nuclear Fusion*, 50(5):054005, apr 2010. (Cited on pages 56 and 59.)

[150] H. J. De Blank. Plasma Equilibrium in Tokamaks. *https://doi.org/10.13182/FST12-A13495*, 61(2 T):89–95, 2017. (Cited on page 56.)

[151] Alberto Bottino, Frank Jenko, Hermann Lederer, Reinhard Tisma, and Roman Hatzky. Application Enabling in DEISA: Petascaling of Plasma Turbulence Codes. Application Enabling in DEISA: Petascaling of Plasma Turbulence Codes Application Enabling in DEISA: Petascaling of Plasma Turbulence Codes. In *Parallel Computing: Architectures, Algorithms and Applications*, volume 38, pages 713–720. IOS Press, 2007. (Cited on page 56.)

[152] F. Iannone, G. Bracco, C. Cavazzoni, R. Coelho, D. Coster, O. Hoenen, A. Maslennikov, S. Migliori, M. Owsiak, A. Quintiliani, B. Palak, V. Pais, F. Robin, E. Rossi, and I. Voitsekhovitch. MARCONI-FUSION: The new high performance computing facility for European nuclear fusion modelling. *Fusion Engineering and Design*, 129:354–358, apr 2018. (Cited on page 56.)

[153] M. F. Martin, M. Landreman, P. Xanthopoulos, N. R. Mandell, and W. Dorland. The parallel boundary condition for turbulence simulations in low magnetic shear devices. *Plasma Physics and Controlled Fusion*, 60(9):095008, jul 2018. (Cited on pages iv, 56, 57, 85, and 154.)

[154] T. Görler, X. Lapillonne, S. Brunner, T. Dannert, F. Jenko, F. Merz, and D. Told. The global version of the gyrokinetic turbulence code GENE. *Journal of Computational Physics*, 230(18):7053–7071, aug 2011. (Cited on pages 56 and 153.)

[155] E. Sánchez, J. M. García-Regana, A. Banón Navarro, J. H.E. Proll, C. Mora Moreno, A. González-Jerez, I. Calvo, R. Kleiber, J. Riemann, J. Smoniewski, M. Barnes, and F. I. Parra. Gyrokinetic simulations in stellarators using different computational domains. *Nuclear Fusion*, 61(11):116074, oct 2021. (Cited on pages 57 and 84.)

[156] M.J. Pueschel. *Electromagnetic Effects in Gyrokinetic Simulations of Plasma Turbulence*. PhD thesis, University of Münster, 2009. (Cited on pages v, 57, 71, and 84.)

[157] GENE development team. *The Gyrokinetic Plasma Turbulence Code GENE: User Manual*, June 2020. (Cited on pages 57, 58, 61, 63, and 148.)

[158] M. J. Pueschel, T. Dannert, and F. Jenko. On the role of numerical dissipation in gyrokinetic Vlasov simulations of plasma microturbulence. *Computer Physics Communications*, 181(8):1428–1437, aug 2010. (Cited on pages 58, 61, and 147.)

[159] P. Xanthopoulos and F. Jenko. Clebsch-type coordinates for nonlinear gyrokinetics in generic toroidal configurations. *Physics of Plasmas*, 13(9):092301, sep 2006. (Cited on pages iv, 60, and 151.)

[160] A. M. Dimits, G. Bateman, M. A. Beer, B. I. Cohen, W. Dorland, G. W. Hammett, C. Kim, J. E. Kinsey, M. Kotschenreuther, A. H. Kritz, L. L. Lao, J. Mandrekas, W. M. Nevins, S. E. Parker, A. J. Redd, D. E. Shumaker, R. Sydora, and J. Weiland. Comparisons and physics basis of tokamak transport models and turbulence simulations. *Physics of Plasmas*, 7(3):969, feb 2000. (Cited on page 59.)

[161] Y. Idomura, S. Tokuda, and Y. Kishimoto. Global profile effects and structure formations in toroidal electron temperature gradient driven turbulence. *Nuclear Fusion*, 45(12):1571, nov 2005. (Cited on page 59.)

[162] P. Xanthopoulos and F. Jenko. Gyrokinetic analysis of linear microinstabilities for the stellarator Wendelstein 7-X. *Physics of Plasmas*, 14(4):042501, apr 2007. (Cited on pages 59 and 147.)

[163] J. Chowdhury, R. Ganesh, S. Brunner, J. Vaclavik, and L. Villard. Toroidal universal drift instability: A global gyrokinetic study. *Physics of Plasmas*, 17(10):102105, oct 2010. (Cited on pages 59 and 65.)

[164] G. Rewoldt and W. M. Tang. Toroidal microinstability studies of high-temperature tokamaks. *Physics of Fluids B: Plasma Physics*, 2(2):318, jun 1998. (Cited on pages 59, 63, and 88.)

[165] Matt Landreman, Thomas M. Antonsen, and William Dorland. Universal instability for wavelengths below the ion Larmor scale. *Physical Review Letters*, 114(9):095003, mar 2015. (Cited on pages 59, 65, and 67.)

[166] L. Bardóczi, T. L. Rhodes, A. Bañón Navarro, C. Sung, T. A. Carter, R. J. La Haye, G. R. McKee, C. C. Petty, C. Chrystal, and F. Jenko. Multi-field/-scale interactions of turbulence with neoclassical tearing mode magnetic islands in the DIII-D tokamak. *Physics of Plasmas*, 24(5):056106, may 2017. (Cited on page 59.)

[167] M. E. Austin, A. Marinoni, M. L. Walker, M. W. Brookman, J. S. Degrassie, A. W. Hyatt, G. R. McKee, C. C. Petty, T. L. Rhodes, S. P. Smith, C. Sung, K. E. Thome, and A. D. Turnbull. Achievement of Reactor-Relevant Performance in Negative Triangularity Shape in the DIII-D Tokamak. *Physical Review Letters*, 122(11):115001, mar 2019. (Cited on page 59.)

[168] B. A. Grierson, G. M. Staebler, W. M. Solomon, G. R. McKee, C. Holland, M. Austin, A. Marinoni, L. Schmitz, R. I. Pinsker, and Diii D. Team. Multi-scale transport in the DIII-D ITER baseline scenario with direct electron heating and projection to ITER. *Physics of Plasmas*, 25(2):022509, feb 2018. (Cited on pages v, 59, and 70.)

[169] N. Pablant, A. Langenberg, A. Alonso, J. Baldzuhn, C. D. Beidler, S. Bozhenkov, R. Burhenn, K. J. Brunner, A. Dinklage, G. Fuchert, O. Ford, D. A. Gates, J. Geiger, M. Hirsch, U. Höfel, Ye O. Kazakov, J. Knauer, M. Krychowiak, H. Laqua, M. Landreman, S. Lazerson, H. Maaßberg, O. Marchuck, A. Mollen, E. Pasch, A. Pavone, S. Satake,

T. Schröder, H. M. Smith, J. Svensson, P. Traverso, Y. Turkin, J. L. Velasco, A. Von Stechow, F. Warmer, G. Weir, R. C. Wolf, D. Zhang, and Wendelstein 7-X team. Investigation of the neoclassical ambipolar electric field in ion-root plasmas on W7-X. *Nuclear Fusion*, 60(3):036021, feb 2020. (Cited on page 59.)

[170] C. D. Beidler, H. M. Smith, A. Alonso, T. Andreeva, J. Baldzuhn, M. N.A. Beurskens, M. Borchardt, S. A. Bozhenkov, K. J. Brunner, H. Damm, M. Drevlak, O. P. Ford, G. Fuchert, J. Geiger, P. Helander, U. Hergenhahnw, M. Hirsch, U. Höfel, Ye O. Kazakov, R. Kleiber, M. Krychowiak, S. Kwak, A. Langenberg, H. P. Laqua, U. Neuner, N. A. Pablant, E. Pasch, A. Pavone, T. S. Pedersen, K. Rahbarnia, J. Schilling, E. R. Scott, T. Stange, J. Svensson, H. Thomsen, Y. Turkin, F. Warmer, R. C. Wolf, and Zhang. Demonstration of reduced neoclassical energy transport in Wendelstein 7-X. *Nature 2021 596:7871*, 596(7871):221–226, aug 2021. (Cited on pages v, 59, and 70.)

[171] J. C. Schmitt, J. N. Talmadge, and D. T. Anderson. Measurement of a helical Pfirsch–Schlüter current with reduced magnitude in HSX. *Nuclear Fusion*, 53(8):082001, jul 2013. (Cited on page 59.)

[172] J. C. Schmitt, J. N. Talmadge, D. T. Anderson, and J. D. Hanson. Modeling, measurement, and 3-D equilibrium reconstruction of the bootstrap current in the Helically Symmetric Experiment. *Physics of Plasmas*, 21(9):092518, sep 2014. (Cited on pages v, 59, and 70.)

[173] S. T.A. Kumar, J. N. Talmadge, T. J. Dobbins, F. S.B. Anderson, K. M. Likin, and D. T. Anderson. Determination of radial electric field from Pfirsch–Schlüter flows in the HSX stellarator. *Nuclear Fusion*, 57(3):036030, feb 2017. (Cited on page 59.)

[174] B. J. Faber, M. J. Pueschel, P. W. Terry, C. C. Hegna, and J. E. Roman. Stellarator microinstabilities and turbulence at low magnetic shear. *Journal of Plasma Physics*, 84(5), oct 2018. (Cited on page 61.)

[175] B. Coppi and F. Pegoraro. Theory of the ubiquitous mode. *Nuclear Fusion*, 17(5):969, oct 1977. (Cited on pages 63, 69, and 87.)

[176] Matt Landreman, Gabriel G. Plunk, and William Dorland. Generalized universal instability: transient linear amplification and subcritical turbulence. *Journal of Plasma Physics*, 81(5):905810501, oct 2015. (Cited on page 65.)

[177] P. Costello, J.H.E. Proll, and G.G. Plunk. The universal instability in optimised stellarators. In preparation for publication, 2022. (Cited on page 65.)

[178] Y. Idomura, H. Urano, N. Aiba, and S. Tokuda. Study of ion turbulent transport and profile formations using global gyrokinetic full-f Vlasov simulation. *Nuclear Fusion*, 49(6):065029, may 2009. (Cited on page 68.)

[179] Dilip K. Bhadra. "Universal" Drift Instability in a Collisional Plasma. *The Physics of Fluids*, 14(5):977, aug 1971. (Cited on page 77.)

[180] K. Aleynikova, A. Zocco, P. Xanthopoulos, P. Helander, and C. Nührenberg. Kinetic ballooning modes in tokamaks and stellarators. *Journal of Plasma Physics*, 84(6), dec 2018. (Cited on page 84.)

[181] Mike Kotschenreuther, G. Rewoldt, and W. M. Tang. Comparison of initial value and eigenvalue codes for kinetic toroidal plasma instabilities. *Computer Physics Communications*, 88(2-3):128–140, aug 1995. (Cited on page 85.)

[182] Paul Mulholland. Optimising for the delayed onset of trapped-electron modes in stellarator geometry. Master's thesis, Utrecht University, 2021. (Cited on pages 86, 87, and 177.)

[183] J. H.E. Proll, H. E. Mynick, P. Xanthopoulos, S. A. Lazerson, and B. J. Faber. TEM turbulence optimisation in stellarators. In *42nd European Physical Society Conference on Plasma Physics*, volume 58, page 014006. IOP Publishing, oct 2015. (Cited on page 86.)

[184] Wendell Horton, R. Estes, H. Kwak, and Duk In Choi. Toroidal mode coupling effects on drift wave stability. *The Physics of Fluids*, 21(8):1366, aug 1978. (Cited on page 86.)

[185] M. Nadeem, T. Rafiq, and M. Persson. Local magnetic shear and drift waves in stellarators. *Physics of Plasmas*, 8(10):4375, sep 2001. (Cited on page 86.)

[186] R. E. Waltz and A. H. Boozer. Local shear in general magnetic stellarator geometry. *Physics of Fluids B: Plasma Physics*, 5(7):2201, jun 1993. (Cited on page 86.)

[187] M. Persson, J. L. V. Lewandowski, and H. Nordman. Drift waves in helical symmetry. *Physics of Plasmas*, 3(10):3720, jun 1996. (Cited on page 86.)

[188] R. A. Koch and Wendell Horton. Effects of electron angle scattering in plasma waves. *The Physics of Fluids*, 18(7):861, sep 1975. (Cited on page 86.)

[189] J. Candy and R. E. Waltz. Velocity-space resolution, entropy production, and upwind dissipation in Eulerian gyrokinetic simulations. *Physics of Plasmas*, 13(3):032310, mar 2006. (Cited on pages 87 and 162.)

[190] B. Scott. Derivation via free energy conservation constraints of gyrofluid equations with finite-gyroradius electromagnetic nonlinearities. *Physics of Plasmas*, 17(10):102306, oct 2010. (Cited on pages 87, 162, and 167.)

[191] P. Helander and G. G. Plunk. Upper Bounds on Gyrokinetic Instabilities in Magnetized Plasmas. *Physical Review Letters*, 127(15):155001, oct 2021. (Cited on pages 87, 162, 163, 167, and 169.)

[192] S. S. Cerri, A. Bañón Navarro, F. Jenko, and D. Told. Collision-dependent power law scalings in two dimensional gyrokinetic turbulence. *Physics of Plasmas*, 21(8):082305, aug 2014. (Cited on pages 87 and 162.)

[193] A. Bañón Navarro, P. Morel, M. Albrecht-Marc, D. Carati, F. Merz, T. Görler, and F. Jenko. Free energy cascade in gyrokinetic turbulence. *Physical Review Letters*, 106(5):055001, jan 2011. (Cited on pages 87, 162, and 163.)

[194] A. Bañón Navarro, P. Morel, M. Albrecht-Marc, D. Carati, F. Merz, T. Görler, and F. Jenko. Free energy balance in gyrokinetic turbulence. *Physics of Plasmas*, 18(9):092303, sep 2011. (Cited on pages 87, 162, and 169.)

[195] P. Helander and G. G. Plunk. Energetic bounds on gyrokinetic instabilities. Part 1. Fundamentals. *Journal of Plasma Physics*, 88(2):905880207, dec 2022. (Cited on pages 87, 162, 163, 164, and 169.)

[196] Cornelius Lanczos. *The variational principles of mechanics*. Dover Publications, fourth edition edition, 1986. (Cited on page 87.)

[197] M. P. Hobson, G. P. Efstathiou, and A. N. Lasenby. *General Relativity: An Introduction for Physicists*. Cambridge University Press, Cambridge, 2006. (Cited on page 87.)

[198] Ángel S. Sanz and Salvador Miret-Artés. *A Trajectory Description of Quantum Processes. I. Fundamentals*. Lecture Notes in Physics. Springer Berlin Heidelberg, Berlin, Heidelberg, 1 edition, 2012. (Cited on pages 87 and 175.)

[199] S. P. Hirshman and J. C. Whitson. Steepest-descent moment method for three-dimensional magnetohydrodynamic equilibria. *The Physics of Fluids*, 26(12):3553, jun 1983. (Cited on page 87.)

[200] S. A. Henneberg, S. R. Hudson, D. Pfefferlé, and P. Helander. Combined plasma–coil optimization algorithms. *Journal of Plasma Physics*, 87(2):905870226, 2021. (Cited on page 87.)

[201] Ksenia Aleynikova and Alessandro Zocco. Quantitative study of kinetic ballooning mode theory in simple geometry. *Physics of Plasmas*, 24(9):092106, aug 2017. (Cited on pages 87 and 177.)

[202] Michel Gondran and Rita Hoblos Saade. Complex Calculus of Variations. *IFAC Proceedings Volumes*, 34(13):727–730, aug 2001. (Cited on pages 87 and 175.)

[203] Heinz Jürgen Wagner. Schrödinger quantization and variational principles in dissipative quantum theory. *Zeitschrift für Physik B Condensed Matter 1994 95:2*, 95(2):261–273, jun 1994. (Cited on pages 87, 175, and 177.)

[204] John A. Krommes. A tutorial introduction to the statistical theory of turbulent plasmas, a half-century after Kadomtsev's Plasma Turbulence and the resonance-broadening theory of Dupree and Weinstock. *Journal of Plasma Physics*, 81(6), sep 2015. (Cited on page 87.)

[205] Patrick H. Diamond, Sanae I. Itoh, and Kimitaka Itoh. Modern plasma physics: Physical kinetics of turbulent plasmas. *Modern Plasma Physics: Physical Kinetics of Turbulent Plasmas*, 9780521869201:1–417, jan 2010. (Cited on page 88.)

[206] A. Bader, B. J. Faber, J. C. Schmitt, D. T. Anderson, M. Drevlak, J. M. Duff, H. Frerichs, C. C. Hegna, T. G. Kruger, M. Landreman, I. J. McKinney, L. Singh, J. M. Schroeder, P. W. Terry, and A. S. Ware. Advancing the physics basis for quasi-helically symmetric stellarators. *Journal of Plasma Physics*, 86(5), 2020. (Cited on page 88.)

[207] F Jenko, T Dannert, and C Angioni. Heat and particle transport in a tokamak: advances in nonlinear gyrokinetics. *Plasma Physics and Controlled Fusion*, 47(12B):B195, nov 2005. (Cited on page 88.)

[208] C. Bourdelle, J. Citrin, B. Baiocchi, A. Casati, P. Cottier, X. Garbet, and F. Imbeaux. Core turbulent transport in tokamak plasmas: bridging theory and experiment with QuaLiKiz. *Plasma Physics and Controlled Fusion*, 58(1):014036, nov 2015. (Cited on page 88.)

[209] J. Citrin, C. Bourdelle, P. Cottier, D. F. Escande, Ö D. Gürcan, D. R. Hatch, G. M.D. Hogeweij, F. Jenko, and M. J. Pueschel. Quasilinear transport modelling at low magnetic shear. *Physics of Plasmas*, 19(6):062305, jun 2012. (Cited on page 88.)

[210] G. G. Whelan, M. J. Pueschel, P. W. Terry, J. Citrin, I. J. McKinney, W. Guttenfelder, and H. Doerk. Saturation and nonlinear electromagnetic stabilization of ITG turbulence. *Physics of Plasmas*, 26(8):082302, aug 2019. (Cited on page 88.)

[211] T. Xie, M. J. Pueschel, and D. R. Hatch. Quasilinear modeling of heat flux from microtearing turbulence. *Physics of Plasmas*, 27(8):082306, aug 2020. (Cited on page 88.)

[212] M. J. Pueschel, T. Görler, F. Jenko, D. R. Hatch, and A. J. Cianciara. On secondary and tertiary instability in electromagnetic plasma microturbulence. *Physics of Plasmas*, 20(10):102308, oct 2013. (Cited on page 88.)

[213] S. Chandrasekhar. Dynamical Friction. I. General Considerations: the Coefficient of Dynamical Friction. *ApJ*, 97:255, mar 1943. (Cited on page 113.)

[214] E. A. Frieman and Liu Chen. Nonlinear gyrokinetic equations for low-frequency electromagnetic waves in general plasma equilibria. *The Physics of Fluids*, 25(3):502, jun 1982. (Cited on page 116.)

[215] W. M. Tang, J. W. Connor, and R. J. Hastie. Kinetic-ballooning-mode theory in general geometry. *Nuclear Fusion*, 20(11):1439, nov 1980. (Cited on page 118.)

[216] J. W. Connor, R. J. Hastie, and J. B. Taylor. High mode number stability of an axisymmetric toroidal plasma. *Proceedings of the Royal Society of London. A. Mathematical and Physical Sciences*, 365(1720):1–17, feb 1979. (Cited on page 118.)

[217] J. W. Connor and J. B. Taylor. Ballooning modes or Fourier modes in a toroidal plasma? *The Physics of Fluids*, 30(10):3180, jun 1987. (Cited on page 118.)

[218] Michael A. Lieberman and Allan J. Lichtenberg. *Principles of Plasma Discharges and Materials Processing*. John Wiley & Sons, Inc., Hoboken, NJ, USA, apr 2005. (Cited on page 122.)

[219] H. Reimerdes, T. C. Hender, S. A. Sabbagh, J. M. Bialek, M. S. Chu, A. M. Garofalo, M. P. Gryaznevich, D. F. Howell, G. L. Jackson, R. J. La Haye, Y. Q. Liu, J. E. Menard, G. A. Navratil, M. Okabayashi, S. D. Pinches, A. C. Sontag, E. J. Strait, W. Zhu, M. Bigi, M. De Baar, P. De Vries, D. A. Gates, P. Gohil, R. J. Groebner, D. Mueller, R. Raman, J. T. Scoville, W. M. Solomon, DIII-D team, JET team, and NSTX team. Cross-machine comparison of resonant field amplification and resistive wall mode stabilization by plasma rotation. *Physics of Plasmas*, 13(5):056107, may 2006. (Cited on page 130.)

[220] C. Angioni, A. G. Peeters, X. Garbet, A. Manini, and F. Ryter. Density response to central electron heating: theoretical investigations and experimental observations in ASDEX Upgrade. *Nuclear Fusion*, 44(8):827, jun 2004. (Cited on page 140.)

[221] Howard Haber. The Sokhotski-Plemelj Formula. `http://scipp.ucsc.edu/~haber/ph215/Plemelj18.pdf`, 2018. Part of lectures notes for Physics 215 at University of California Santa Cruz. Accessed on 2021-09-19. (Cited on page 140.)

[222] Serge Lang. *Undergraduate Analysis*. Undergraduate Texts in Mathematics. Springer New York, New York, NY, 2 edition, 1997. (Cited on page 143.)

[223] Frans T.M. Nieuwstadt, Bendiks J. Boersma, and Jerry Westerweel. *Turbulence: Introduction to theory and applications of turbulent flows*. Springer International Publishing, jul 2016. (Cited on page 162.)

[224] David Chandler. *Introduction to modern statistical mechanics*. Oxford University Press, 1987. (Cited on page 163.)

[225] I M Gelfand and S V Fomin. *Calculus of Variations (Dover Books on Mathematics)*. Dover Publications, oct 2000. (Cited on page 173.)

[226] Katsuhisa Ohta. Time-dependent variational principle with constraints. *Chemical Physics Letters*, 329(3-4):248–254, oct 2000. (Cited on pages 175 and 176.)

A Instability mechanism of the ITG mode

To investigate the effects of a temperature gradient on the potential instability of a microperturbation, consider again the situation of the drift wave, but with a background temperature gradient $\boldsymbol{\nabla} T$ instead of a density gradient. To account for the inhomogeneous magnetic field, the ions are given a drift velocity which depends on the temperature, which is taken to be in the y direction, but the electrons are taken to respond adiabatically.

A wave-like plasma perturbation δx of guiding centers will now not cause a density perturbation, but a temperature perturbation as particles are effectively displaced towards a region of different background temperature. By analogy with the drift wave case of Section 2.1.1 this temperature perturbation is $\delta T = -\delta x(y) \frac{\mathrm{d}T_0}{\mathrm{d}x}$. Since the electrons are taken to respond adiabatically, they will quickly equilibrate these temperature differences along the field line, which leaves the displaced ions at their original temperature. If the drift velocity would be constant then the ion drift would not lead to an accumulation of charge since the background density is taken to be uniform. If however the drift velocity depends on the temperature (as is the case for the magnetic drift), then there will be an imbalance between the in- and out fluxes of ions, as shown in Figure A.1a.

The resulting charge density is easiest calculated from charge conservation $\frac{\partial \rho}{\partial t} + \boldsymbol{\nabla} \cdot \boldsymbol{J} = 0$, taking $\boldsymbol{J} = +en_0 v_{di}(T(x,y))\boldsymbol{e_y}$ for the ion current, resulting in

$$\frac{\partial \rho}{\partial t} = -en_0 \frac{\mathrm{d}v_{di}}{\mathrm{d}T} \frac{\partial T}{\partial y} \approx +en_0 \frac{\mathrm{d}v_{di}}{\mathrm{d}T} \frac{\mathrm{d}T_0}{\mathrm{d}x} \frac{\mathrm{d}\delta x(y)}{\mathrm{d}y}.$$

If a small time increment δt is considered in which the temperature perturbation can be considered constant[60] it follows analogolously to the trapped particle case of Section 2.1.2 that the potential perturbation will be $\pi/2$ out of phase with the temperature perturbation, which results in an $\boldsymbol{E} \times \boldsymbol{B}$ drift $\boldsymbol{E} \times \boldsymbol{B} \propto -\frac{\mathrm{d}^2 \delta x(y)}{\mathrm{d}y^2} \boldsymbol{e_x}$ in phase with the initial guiding center perturbation $\delta x(y)$), thus enhancing its amplitude as shown in Figure A.1b. As the ion magnetic drift depends on the ion temperature, and the amplitude of the temperature perturbation is directly proportional to the (ion) temperature gradient, this instability is called the ion temperature gradient mode.

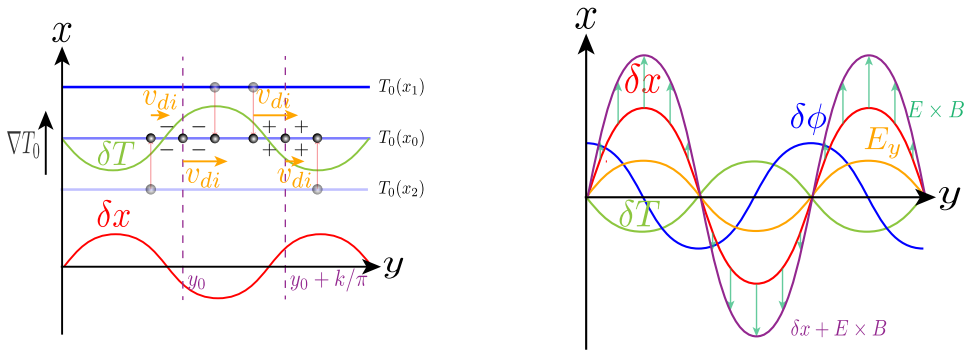

(a) *(b)*

Figure A.1: Schematic mechanism of the ion temperature gradient mode showing (a) how the temperature dependent magnetic drift results in charge density and (b) the waveforms of all perturbed quantities along with the effect of the $\boldsymbol{E} \times \boldsymbol{B}$ drift on the initial displacement.

[60] Even if this assumption is not made, the electrostatic potential $\phi \propto \rho$ will still have the waveform as $\frac{\mathrm{d}\delta x(y)}{\mathrm{d}y}$ since a time integration of $\delta x(y,t) = A(t)\sin(ky)$ only affects the amplitude, i.e. be $+\pi/2$ out of phase with the initial temperature perturbation which will result in the same conclusion.

B Details of the derivation for the collision operator

In the derivations that follow, the theory presented in Chapter 3 of [20] is closely followed.

B.1 Derivation of Fokker-Planck equation for the collision operator

The net effect of all binary Coulomb collisions with particles of species b on the distribution of species a will be statistical, as for each collision pair the relative velocity u will be randomly picked from the two distribution functions. If $P_{ab}(\boldsymbol{v}, \boldsymbol{\Delta v})$ is the probability that a collision with a particle of species b changes the velocity of a particle of species a to $\boldsymbol{v} \to \boldsymbol{v} + \boldsymbol{\Delta v}$ within an interaction time Δt then the distribution function will evolve as

$$f_a(\boldsymbol{x} + \boldsymbol{v}\Delta t, \boldsymbol{v}, t + \Delta t) = \int f_a(\boldsymbol{x}, \boldsymbol{v} - \boldsymbol{\Delta v}, t) P_{ab}(\boldsymbol{v} - \boldsymbol{\Delta v}, \boldsymbol{\Delta v}) \mathrm{d}^3\boldsymbol{\Delta v}$$

where $\boldsymbol{x} + \boldsymbol{v}\Delta t$ in the argument of the distribution function accounts for streaming of the trajectories, $f_a \times P_{ab}$ gives the density of particles that will have their velocity changed from $\boldsymbol{v} - \boldsymbol{\Delta v} \to \boldsymbol{v}$ and a trace over all possible velocity changes is performed. As the main effect of Coulomb collisions up to lowest are small angle deflections, it follows that $\|\boldsymbol{\Delta v}\| / \langle \|\boldsymbol{v}\| \rangle \sim \|\boldsymbol{\Delta v}\| / v_{Ta} \ll 1$ such that a Taylor expansion of the integrand is justified

$$\begin{aligned} f_a(\boldsymbol{x} + \boldsymbol{v}\Delta t, \boldsymbol{v}, t + \Delta t) \approx \int f_a(\boldsymbol{x}, \boldsymbol{v}, t) P_{ab}(\boldsymbol{v}, \boldsymbol{\Delta v}) \mathrm{d}^3\boldsymbol{\Delta v} - \int \boldsymbol{\Delta v} \cdot \boldsymbol{\nabla}_v [f_a(\boldsymbol{x}, \boldsymbol{v}, t) P_{ab}(\boldsymbol{v}, \boldsymbol{\Delta v})] \mathrm{d}^3\boldsymbol{\Delta v} \\ + \frac{1}{2} \int \boldsymbol{\Delta v}^\top \cdot \left(\boldsymbol{\nabla}_v \boldsymbol{\nabla}_v^\top \left[f_a(\boldsymbol{x}, \boldsymbol{v}, t) P_{ab}(\boldsymbol{v}, \boldsymbol{\Delta v}) \right] \right) \cdot \boldsymbol{\Delta v} \mathrm{d}^3\boldsymbol{\Delta v} + \mathcal{O}(\boldsymbol{\Delta v}^3) \end{aligned}$$

where $\boldsymbol{\nabla}_v$ is the gradient operator w.r.t. velocity coordinates, $\top$ denotes the transpose and $\boldsymbol{\nabla}_v \boldsymbol{\nabla}_v^\top$ represents the Hessian operator. Since P_{ab} is a proper probability it satisfies $\int P_{ab} \mathrm{d}^3\boldsymbol{\Delta v} = 1$ and since the velocity changes $\boldsymbol{\Delta v}$ are per definition random, the Taylor expansion can be written more elegantly in component form as

$$f_a(\boldsymbol{x} + \boldsymbol{v}\Delta t, \boldsymbol{v}, t + \Delta t) - f_a(\boldsymbol{x}, \boldsymbol{v}, t) \approx -\frac{\partial}{\partial v_k} \left[f_a(\boldsymbol{x}, \boldsymbol{v}, t) \langle \Delta v_k \rangle^{ab} \right] + \frac{1}{2} \frac{\partial^2}{\partial v_k \partial v_l} \left[f_a(\boldsymbol{x}, \boldsymbol{v}, t) \langle \Delta v_k \Delta v_l \rangle^{ab} \right]$$

where the order of integration over $\boldsymbol{\Delta v}$ and derivative w.r.t. $\boldsymbol{v}$ have been interchanged, the Einstein summation convention has been implied and $\langle \cdots \rangle^{ab} = \int (\cdots) P_{ab} \mathrm{d}^3\boldsymbol{\Delta v}$ encapsulates the net statistical effect of the collisions. Dividing both sides by Δt and taking the limit of $\Delta t \to 0$ the LHS simply becomes a partial derivative w.r.t. time as a result of collisions and the RHS is aptly called the collision operator

$$\left(\frac{\partial f_a}{\partial t} \right)_{col} \equiv C_{ab} = \lim_{\Delta t \to 0} -\frac{\partial}{\partial v_k} \left[f_a(\boldsymbol{x}, \boldsymbol{v}, t) \left\langle \frac{\Delta v_k}{\Delta t} \right\rangle^{ab} \right] + \frac{\partial^2}{\partial v_k \partial v_l} \left[f_a(\boldsymbol{x}, \boldsymbol{v}, t) \left\langle \frac{\Delta v_k \Delta v_l}{2\Delta t} \right\rangle^{ab} \right]. \tag{B.1}$$

Since in the limit of $\delta t \to 0$ the streaming of the distribution function vanishes, this means that the collision operator of Equation (B.1) describes collisions locally at fixed position $\boldsymbol{x}$ and thus does not introduce spatial correlations between the distribution function f_a at different positions. This feature makes the collision operator problem tractable. On the RHS of Equation (B.1) the first term describes a net drag force on the distribution function and the second term describes a diffusive effect, and hence the collision operator has the form of Fokker-Planck equation (up to the order of neglected terms).

B.2 Calculation of the statistical effect

For a binary Coulomb interaction, the Lagrangian $\mathcal{L}$ can be mapped to that of the motion of an effective particle with the reduced mass $m_\star$ moving in a static Coulomb field[61] with an additional

[61] This field is static in the sense that mathematically it appears to originate from a virtual particle at the origin that is unaffected by the motion of the effective particle of reduced mass $m_\star$ around it.

constant related to the kinetic energy from the motion of the centre of mass

$$\mathcal{L} = \frac{m_a + m_b}{2}\dot{\boldsymbol{R}}^2 + \frac{1}{2}m_\star \dot{\boldsymbol{r}}^2 - \frac{q_a q_b}{4\pi\epsilon_0 \|\boldsymbol{r}\|}$$

where $\boldsymbol{R} = (m_a\boldsymbol{x_a} + m_b\boldsymbol{x_b})/(m_a + m_b)$ is the centre of mass, $m_\star = m_a m_b/(m_a + m_b)$, $\boldsymbol{r} = \boldsymbol{x_a} - \boldsymbol{x_b}$ is the particle separation, a, b refer to the species, ϵ_0 is the vacuum permittivity and m, q denote the mass and charge respectively. If species b is taken as the "target" particle, then the velocity of an incident "test" particle undergoes the small changes[62]

$$\begin{aligned}
\Delta v_x &\approx -\left(1 + \frac{m_a}{m_b}\right)\left(\frac{q_a q_b}{2\pi\epsilon_0 m_a}\right)^2 \frac{1}{2r^2u^3} \\
\Delta v_y &\approx \frac{q_a q_b}{2\pi\epsilon_0 m_a}\frac{\cos\phi}{ur} \\
\Delta v_z &\approx \frac{q_a q_b}{2\pi\epsilon_0 m_a}\frac{\sin\phi}{ur}
\end{aligned} \tag{B.2}$$

where the initial relative velocity $\boldsymbol{u} = \dot{\boldsymbol{r}} = \boldsymbol{v_a} - \boldsymbol{v_b}$ is aligned with the x direction of a coordinate system before the collision event, and ϕ denotes the deflection angle in the yz plane.

Several factors introduce a statistical effect of such collisions; the distribution of target particles f_b will results in different relative velocities with the test particle, the spatial distribution of both particles gives different interparticle distances $r = \|\boldsymbol{r}\|$, and the perpendicular deflection angle ϕ is arbitrary. Therefore the net statistical effect of collisions involves an average of the test particle velocity changes Equation (B.2) over the quasi-phase volume $\mathrm{d}^6\Omega$ spun by the velocities of species b and the spatial volume occupied by the effective particle of the reduced mass moving in the static Coulomb field. As the relative distance r effectively takes on the role of an impact parameter and the effective particle moves with a velocity u, the volume spun by this effective particle as it moves during the interaction is $dV = r\,\mathrm{d}r\,\mathrm{d}\phi\,u\Delta t$, resulting in a net statistical effect of

$$\langle\cdots\rangle^{ab} = \int(\cdots) \times f_b(\boldsymbol{x_b}, \boldsymbol{v_b}, t) r u(\boldsymbol{v_a}, \boldsymbol{v_b})\Delta t \mathrm{d}^3\boldsymbol{v_b}\,\mathrm{d}r\,\mathrm{d}\phi\,.$$

where f_b is the distribution function of target particles of species b and the dependencies on the other integration variables has been made explicit for transparency. Substituting Equation (B.2) gives

$$\begin{aligned}
\left\langle\frac{\Delta v_x}{\Delta t}\right\rangle^{ab} &= -\frac{1}{2}\left(1 + \frac{m_a}{m_b}\right)\left(\frac{q_a q_b}{2\pi\epsilon_0 m_a}\right)^2 \int\frac{\mathrm{d}r}{r}\int_0^{2\pi}\mathrm{d}\phi\int\frac{1}{u^2}f_b\mathrm{d}^3\boldsymbol{v_b} \\
\left\langle\frac{\Delta v_y}{\Delta t}\right\rangle^{ab} &= \left(\frac{q_a q_b}{2\pi\epsilon_0 m_a}\right)\int\mathrm{d}r\int_0^{2\pi}\sin\phi\,\mathrm{d}\phi\int f_b\mathrm{d}^3\boldsymbol{v_b} = 0 \\
\left\langle\frac{\Delta v_z}{\Delta t}\right\rangle^{ab} &= \left(\frac{q_a q_b}{2\pi\epsilon_0 m_a}\right)\int\mathrm{d}r\int_0^{2\pi}\cos\phi\,\mathrm{d}\phi\int f_b\mathrm{d}^3\boldsymbol{v_b} = 0
\end{aligned}$$

where the y, z components vanish physically as a result of symmetry in the deflection process as each ϕ is equally likely. The issue lies in evaluating the integral over impact parameters r for the x component as it is divergent for small lower bounds and large upper bounds. These bounds are fortunately naturally constraint; as a result of the Debye shielding the Coulomb fields of a target particle will approximately vanish beyond the Debye length λ_D and in case of repulsive

[62] These correspond to lowest order expansions of $\cos\alpha_\star - 1 \approx \alpha_\star^2/2$ and $\sin\alpha_\star \approx \alpha_\star$ in the deflection angle $\alpha_\star = q_a q_b/(2\pi\epsilon_0 r m_\star u^2)$ of the relative velocity from the x-axis. Note that $\alpha_\star$ is roughly the ratio of the potential energy to kinetic energy of a pair interaction such that $\alpha_\star \ll 1$ is consistent with the weak coupling approximation in Section 2.2.

interactions there is a distance of closest approach r_{ca} set by energy conservation. In case of an attractive interaction energy conservation does not place a lower bound on the integral, but the validity of the approximation of small deflections does as for small r the interaction will be strong enough to cause significant deviation of the test particle trajectory. Taking $r_{min} = r_{ca}$ in those cases as well yields the Coulomb logarithm[63] $\ln\Lambda = \int_{r_{ca}}^{\lambda_D} \mathrm{d}r\,/r$ such that

$$\begin{aligned}\left\langle \frac{\Delta v_x}{\Delta t} \right\rangle^{ab} &= -\frac{L^{ab}}{4\pi}\left(1+\frac{m_a}{m_b}\right)\int \frac{1}{u^2} f_b \mathrm{d}^3\boldsymbol{v_b} \\ \left\langle \frac{\Delta v_y}{\Delta t} \right\rangle^{ab} &= \left\langle \frac{\Delta v_z}{\Delta t} \right\rangle^{ab} = 0\end{aligned} \tag{B.3}$$

where $L^{ab} = (q_a q_b/m_a\epsilon_0)^2 \ln\Lambda$ is a measure of the interaction strength between species a and b. The Coulomb logarithm is closely related to the number of charged particles within the Debye sphere and is thus typically $\ln\Lambda \gg 1$ for most plasmas of interest [30]. Equivalently the unique quadratic terms in Equation (B.1) evaluate to

$$\begin{aligned}\left\langle \frac{\Delta v_x^2}{2\Delta t} \right\rangle^{ab} &= \frac{\pi}{8}\left(1+\frac{m_a}{m_b}\right)^2\left(\frac{q_a q_b}{2\pi\epsilon_0 m_a}\right)^4 \int \frac{\mathrm{d}r}{r^3}\int \frac{1}{u^5} f_b \mathrm{d}^3\boldsymbol{v_b} \\ \left\langle \frac{\Delta v_y^2}{2\Delta t} \right\rangle^{ab} &= \left\langle \frac{\Delta v_z^2}{2\Delta t} \right\rangle^{ab} = \frac{L^{ab}}{8\pi}\int \frac{1}{u} f_b \mathrm{d}^3\boldsymbol{v_b} \\ \left\langle \frac{\Delta v_x \Delta v_y}{2\Delta t} \right\rangle^{ab} &= \left\langle \frac{\Delta v_y \Delta v_z}{2\Delta t} \right\rangle^{ab} = \left\langle \frac{\Delta v_x \Delta v_z}{2\Delta t} \right\rangle^{ab} = 0\end{aligned} \tag{B.4}$$

where all cross-terms vanish again due to symmetry considerations, and the squared terms in the y and z directions are equal as a result of the rotational invariance in the yz plane. The $\left\langle \frac{\Delta v_x^2}{2\Delta t} \right\rangle$ term no longer contains a diverging integral, however its relative magnitude w.r.t. the perpendicular terms can be estimated by taking the same $[r_{ca}, \lambda_D]$ integration boundaries for which the dominant small angle deflections occur, taking a typical effective particle where $r_{ca} \sim q_a q_b/(4\pi\epsilon_0 m_\star v_{T_\star}^2)$ with the thermal velocity $v_{T_\star}$ a measure of the average relative velocity u, and taking $r_{ca} \ll \lambda_D$ since the Coulomb logarithm $\ln\Lambda \gg 1$, such that

$$\frac{\left\langle \Delta v_x^2/2\Delta t \right\rangle^{ab}}{\left\langle \Delta v_y^2/2\Delta t \right\rangle^{ab}} \sim \frac{1}{\ln\Lambda}\underbrace{\frac{v_{T_\star}^4 \int \frac{1}{u^5} f_b \mathrm{d}^3\boldsymbol{v_b}}{\int \frac{1}{u} f_b \mathrm{d}^3\boldsymbol{v_b}}}_{\mathcal{O}(1)}.$$

Thus as $\ln\Lambda \gg 1$ for any plasma, the contribution from $\left\langle \Delta v_x^2/2\Delta t \right\rangle^{ab}$ to the diffusion terms is negligible, especially so for fusion plasmas. The disappearance of the divergent integral over impact parameters also justifies cutting off the Taylor series at second order, as the next order correction would result in $\left\langle \frac{\Delta v_k \Delta v_l \Delta v_m}{6\Delta t} \right\rangle$ terms in Equation (B.1) which would in turn be $1/\ln\Lambda$ smaller than the diffusive terms.

The above calculation was done under the assumption that the initial relative velocity is aligned with the x direction of a collision coordinate system. As this coordinate system is unique for

[63] The lower bound has been based on classical principle of energy conservation. However quantum effects also pose a lower bound, as the particles involved in the collision effectively become indistinguishable if they approach each other within the thermal de Broglie wavelength λ_T. The correct lower bound for the integral should thus be $\min r_{ca}, \lambda_T$ [5]. As this correction is typically important for electrons, it resolves the ambiguity of the lower bound for the attractive interactions.

each collision, the results should be mapped to an arbitrary "laboratory" coordinate system which is identical for all particles. This mapping proceeds then as follows for the linear term

$$\begin{aligned}\left\langle \frac{\Delta v_k}{\Delta t} \right\rangle^{ab} &= \left\langle \frac{\boldsymbol{e_k} \cdot \boldsymbol{\Delta v}}{\Delta t} \right\rangle^{ab} = \left\langle \frac{\boldsymbol{e_k} \cdot (\boldsymbol{e_x}\Delta v_x + \boldsymbol{e_y}\Delta v_y + \boldsymbol{e_z}\Delta v_z)}{\Delta t} \right\rangle^{ab} \\ &= \left\langle \frac{\boldsymbol{e_k} \cdot \boldsymbol{e_x}\Delta v_x}{\Delta t} \right\rangle^{ab} = -\frac{L^{ab}}{4\pi}\left(1 + \frac{m_a}{m_b}\right) \int \frac{u_k}{u^3} f_b \mathrm{d}^3\boldsymbol{v_b}\end{aligned} \tag{B.5}$$

where Equation (B.3) was used in the second step and in the last step it was used that the aligned collision coordinate system is characterised by $\boldsymbol{e_x} = \boldsymbol{u}/u$. With a bit more effort the quadratic term is similarly mapped as

$$\begin{aligned}\left\langle \frac{\Delta v_k \Delta v_l}{2\Delta t} \right\rangle^{ab} &= \left\langle \frac{\boldsymbol{e_k} \cdot (\boldsymbol{e_x}\Delta v_x + \boldsymbol{e_y}\Delta v_y + \boldsymbol{e_z}\Delta v_z)\, \boldsymbol{e_l} \cdot (\boldsymbol{e_x}\Delta v_x + \boldsymbol{e_y}\Delta v_y + \boldsymbol{e_z}\Delta v_z)}{2\Delta t} \right\rangle^{ab} \\ &\approx \left\langle \frac{(\boldsymbol{e_k} \cdot \boldsymbol{e_y})(\boldsymbol{e_l} \cdot \boldsymbol{e_y})\Delta v_y^2 + (\boldsymbol{e_k} \cdot \boldsymbol{e_z})(\boldsymbol{e_l} \cdot \boldsymbol{e_z})\Delta v_z^2}{2\Delta t} \right\rangle^{ab} \\ &= \left\langle \frac{\big(\boldsymbol{e_k} \cdot \boldsymbol{e_l} - (\boldsymbol{e_k} \cdot \boldsymbol{e_x})(\boldsymbol{e_l} \cdot \boldsymbol{e_x})\big)\Delta v_y^2}{2\Delta t} \right\rangle^{ab} = \frac{L^{ab}}{8\pi} \int U_{kl} f_b \mathrm{d}^3\boldsymbol{v_b}\end{aligned} \tag{B.6}$$

where Equation (B.4) was used, the Δv_x^2 term was neglected in the second step, $\boldsymbol{e_x} = \boldsymbol{u}/u$ was again used in the last step and the tensor

$$U_{kl} = \frac{u^2\delta_{kl} - u_k u_l}{u^3} \tag{B.7}$$

has been introduced, with δ_{kl} denoting the Kronecker delta.

B.3 Rosenbluth and Landau forms of the collision operator

From Equations (B.5) and (B.6) it follows that the net statistical effect of collisions is determined by integrals over the relative velocity and the distribution function of target particles (aside from a multiplicative constant). These integrals can be written compactly in terms of so-called Rosenbluth potentials

$$\begin{aligned}\varphi_b(\boldsymbol{v}) &= -\frac{1}{4\pi} \int \frac{1}{u(\boldsymbol{v}, \boldsymbol{v'})} f_b(\boldsymbol{v'}) \mathrm{d}^3\boldsymbol{v'} \\ \psi_b(\boldsymbol{v}) &= -\frac{1}{8\pi} \int u(\boldsymbol{v}, \boldsymbol{v'}) f_b(\boldsymbol{v'}) \mathrm{d}^3\boldsymbol{v'}\end{aligned} \tag{B.8}$$

where for future notational convenience primed velocities refer to the velocities of species b and unprimed velocities refer to species a. Since the relative speed is $u = \sqrt{\sum_j (v_j - v'_j)^2}$ it follows by changing the order of integration over primed velocities and derivation w.r.t. unprimed velocities that Equation (B.5) can be written as

$$\left\langle \frac{\Delta v_k}{\Delta t} \right\rangle^{ab} = -L^{ab}\left(1 + \frac{m_a}{m_b}\right) \frac{\partial \varphi_b}{\partial v_k} \tag{B.9}$$

and that Equation (B.6) can be written as

$$\left\langle \frac{\Delta v_k \Delta v_l}{2\Delta t} \right\rangle^{ab} = -L^{ab} \frac{\partial^2 \psi_b}{\partial v_k \partial v_l}. \tag{B.10}$$

The physical meaning of the Rosenbluth potentials follows by an analogy with electrostatics, where the Poisson equation $\nabla^2\Phi = -\rho/\epsilon_0$ leads to an electrostatic potential $\Phi(\boldsymbol{x}) = \frac{1}{4\pi\epsilon_0}\int\frac{\rho(\boldsymbol{x'})}{\|\boldsymbol{x}-\boldsymbol{x'}\|}\mathrm{d}^3\boldsymbol{x'}$, therefore comparison with Equation (B.8) gives that the first Rosenbluth potential is the solution to the Poisson equation

$$\nabla^2_{\boldsymbol{v}}\varphi_b = f_b \tag{B.11}$$

where the derivatives are not taken w.r.t. spatial but velocity coordinates, i.e. $\nabla^2_{\boldsymbol{v}} = \sum_j \frac{\partial^2}{\partial v_j^2}$. Thus the target particle distribution f_b acts as a source for φ_b, hence the name potential. Meanwhile the Laplacian of the second Rosenbluth potential gives

$$\begin{aligned}\nabla^2_v\psi_b &= \sum_j -\frac{1}{8\pi}\int\frac{\partial^2 u}{\partial v_j^2}f_b(\boldsymbol{v'})\mathrm{d}^3\boldsymbol{v'} = \sum_j -\frac{1}{8\pi}\int U_{jj}f_b\mathrm{d}^3\boldsymbol{v'}\\ &= -\frac{1}{8\pi}\sum_j\int\frac{u^2-u_j^2}{u^3}f_b\mathrm{d}^3\boldsymbol{v'} = -\frac{1}{4\pi}\int\frac{1}{u}f_b\mathrm{d}^3\boldsymbol{v'} = \varphi_b\end{aligned} \tag{B.12}$$

such that φ_b in turn acts as a source term for ψ_b, and the two potentials are consequently related such that the effective drag force and diffusion force on the test particle distribution are not independent.

In terms of the Rosenbluth potentials the Fokker-Planck equation for the collision operator Equation (B.1) becomes

$$\begin{aligned}C_{ab}(f_a,f_b) =& L^{ab}\frac{\partial}{\partial v_k}\left[(1+\frac{m_a}{m_b})\frac{\partial\varphi_b}{\partial v_k}f_a - \frac{\partial}{\partial v_l}\left(\frac{\partial^2\psi_b}{\partial v_k\partial v_l}f_a\right)\right]\\ =& L^{ab}\frac{\partial}{\partial v_k}\left[(1+\frac{m_a}{m_b})\frac{\partial\varphi_b}{\partial v_k}f_a - \frac{\partial}{\partial v_k}\underbrace{\left(\sum_l\frac{\partial^2\psi_b}{\partial v_l^2}\right)}_{=\nabla^2_{\boldsymbol{v}}\psi_b}f_a - \frac{\partial^2\psi_b}{\partial v_k\partial v_l}\frac{\partial f_a}{\partial v_l}\right]\\ =& L^{ab}\frac{\partial}{\partial v_k}\left[\frac{m_a}{m_b}\frac{\partial\varphi_b}{\partial v_k}f_a - \frac{\partial^2\psi_b}{\partial v_k\partial v_l}\frac{\partial f_a}{\partial v_l}\right]\end{aligned} \tag{B.13}$$

where summation over repeated indices have been suppressed for notational convenience unless this would lead to confusion or explicitly needed. This is the form of the collision operator for a general inverse-square force first derived by Rosenbluth et al [105].

The issue of Coulomb collisions has historically first been investigated by Landau who derived a more symmetric expression of the collision operator, which is more transparent in its dependence on f_b. Landau's form of the collision operator can be obtained from Equation (B.13) by substituting the derivatives of the Rosenbluth potentials. The tensor U_{kl} Equation (B.7) has the property that its divergence

$$\sum_l\frac{\partial U_{kl}}{\partial v_l} = -\frac{2u_k}{u^3} = -\sum_l\frac{\partial U_{kl}}{\partial v_l'}$$

such that $\frac{\partial\varphi_b}{\partial v_k}$ can be rewritten as

$$\begin{aligned}\frac{\partial\varphi_b}{\partial v_k} =& \frac{1}{4\pi}\int\frac{u_k}{u^3}f_b(\boldsymbol{v'})\mathrm{d}^3\boldsymbol{v'} = \frac{1}{8\pi}\int\sum_l\frac{\partial U_{kl}}{\partial v_l'}f_b(\boldsymbol{v'})\mathrm{d}^3\boldsymbol{v'}\\ =& \frac{1}{8\pi}\int\sum_l\left(\frac{\partial}{\partial v_l'}\left[U_{kl}f_b(\boldsymbol{v'})\right] - U_{kl}\frac{\partial f_b(\boldsymbol{v'})}{\partial v_l'}\right)\mathrm{d}^3\boldsymbol{v'} = -\frac{1}{8\pi}\sum_l\int U_{kl}\frac{\partial f_b(\boldsymbol{v'})}{\partial v_l'}\mathrm{d}^3\boldsymbol{v'}\end{aligned}$$

where the first term to the integral vanishes as it yields a boundary term and a proper distribution function obeys $f \to 0$ as $\|\boldsymbol{v}\| \to \infty$. Using this expression for $\frac{\partial \varphi_b}{\partial v_k}$ and the regular expression for $\frac{\partial^2 \psi_b}{\partial v_k \partial v_l}$ such that the tensor U_{kl} is a common prefactor to both terms in Equation (B.13), the collision operator is written as

$$C_{ab}(f_a, f_b) = \frac{L^{ab} m_a}{8\pi} \frac{\partial}{\partial v_k} \int U_{kl} \left(\frac{f_b(\boldsymbol{v'})}{m_a} \frac{\partial f_a(\boldsymbol{v})}{\partial v_l} - \frac{f_a(\boldsymbol{v})}{m_b} \frac{\partial f_b(\boldsymbol{v'})}{\partial v'_l} \right) \mathrm{d}^3 \boldsymbol{v'} \tag{B.14}$$

which is the symmetric version of the collision operator obtained by Landau.

B.4 Collision with a Maxwellian distribution

A case of interest that is still analytically tractable is the collision operator for test particles with an arbitrary distribution function f_a with target particles from a Maxwellian distribution f_{Mb}. In that case the Rosenbluth form of the collision operator Equation (B.13) simplifies significantly. Because the Maxwellian distribution is isotropic the Rosenbluth potentials Equation (B.8) will inherit this property and thus depend only on the speed of the test particle $v = \|\boldsymbol{v}\|$. Consequently the velocity derivatives of the Rosenbluth potentials in Equation (B.13) are determined by

$$\begin{aligned} \frac{\partial \varphi_b}{\partial v_k} =& \varphi'_b \frac{\partial v}{\partial v_k} = \varphi'_b \frac{v_k}{v} \\ \frac{\partial^2 \psi_b}{\partial v_k \partial v_l} =& \frac{\partial}{\partial v_k} \left(\psi'_b \frac{\partial v}{\partial v_l} \right) = \psi''_b \frac{v_l v_k}{v^2} + \psi'_b W_{kl} \end{aligned} \tag{B.15}$$

where a prime denotes the derivative w.r.t. to v and the tensor W_{kl}

$$W_{kl} = \frac{\partial^2 v}{\partial v_l \partial v_k} = \frac{v^2 \delta_{kl} - v_k v_l}{v^3}$$

is the test particle velocity equivalent to the tensor U_{kl} for the relative velocity. Consequently by analogy W_{kl} will have the same relations to v as U_{kl} has to u, repeated below for convenience

$$\sum_k W_{kk} = \frac{2}{v}, \quad \sum_l \frac{\partial W_{kl}}{\partial v_l} = -\frac{2 v_k}{v^3}, \quad \sum_l W_{kl} v_l = 0.$$

Substituting Equation (B.15) for the Rosenbluth potentials gives the collision operator as

$$\begin{aligned} C_{ab}(f_a, f_{Mb}) =& L^{ab} \frac{\partial}{\partial v_k} \left[\frac{m_a}{m_b} \varphi'_b \frac{v_k}{v} f_a - \frac{\partial f_a}{\partial v_l} W_{kl} \psi'_b - \psi''_b \frac{v_l v_k}{v^2} \frac{\partial f_a}{\partial v_l} \right] \\ =& - L^{ab} \frac{\partial}{\partial v_k} \left(W_{kl} \frac{\partial f_a}{\partial v_l} \psi'_b \right) + L^{ab} \frac{\partial}{\partial v_k} \left\{ v_k \left[\frac{m_a}{m_b} \varphi'_b \frac{f_a}{v} - \psi''_b \frac{1}{v} \frac{\partial f_a}{\partial v} \right] \right\} \end{aligned} \tag{B.16}$$

where in the second step the terms explicitly containing v_k were split and the chain rule was used to write $\frac{\partial f_a}{\partial v} = \frac{\partial f_a}{\partial v_l} \frac{\partial v_l}{\partial v}$. The term in curly brackets of Equation (B.16) takes on the form of a divergence in velocity coordinates which is most conveniently expressed in spherical velocity coordinates (v, θ, ϕ) since the term in square brackets depends only on v, simplifying the divergence to a single term

$$\boldsymbol{\nabla}_v \cdot (\boldsymbol{v} A(v)) = \frac{1}{v^2} \frac{\partial}{\partial v} \left(v^3 A(v) \right). \tag{B.17}$$

The first term in Equation (B.16) in round brackets can be expanded by the product rule as

$$\frac{\partial}{\partial v_k} \left(W_{kl} \frac{\partial f_a}{\partial v_l} \psi'_b \right) = \frac{\partial}{\partial v_k} \left(W_{kl} \frac{\partial f_a}{\partial v_l} \right) \psi'_b + W_{kl} \frac{\partial f_a}{\partial v_l} \psi''_b \frac{\partial v}{\partial v_k} = \frac{\partial}{\partial v_k} \left(W_{kl} \frac{\partial f_a}{\partial v_l} \right) \psi'_b$$

where the last term vanishes due to $\sum_k W_{kl} v_k = 0$. The surviving term can also be conveniently expressed in terms of vector operators in an orthogonal velocity coordinate system by explicitly writing out the tensor contraction

$$\sum_k \frac{\partial}{\partial v_k} \sum_l \left(\frac{v^2 \delta_{kl} - v_k v_l}{v^3} \frac{\partial f_a}{\partial v_l} \right) = \underbrace{\sum_k \frac{\partial}{\partial v_k} \left(\frac{1}{v} \frac{\partial f_a}{\partial v_k} \right)}_{\boldsymbol{\nabla}_v \cdot \left(\frac{1}{v} \boldsymbol{\nabla}_v f_a \right)} - \underbrace{\sum_k \frac{\partial}{\partial v_k} \left(\frac{v_k}{v^3} \underbrace{\sum_l v_l \frac{\partial f_a}{\partial v_l}}_{\boldsymbol{v} \cdot \nabla_v f_a} \right)}_{\boldsymbol{\nabla}_v \cdot \left(\frac{\boldsymbol{v}}{v^3} (\boldsymbol{v} \cdot \boldsymbol{\nabla}_v) f_a \right)}$$

Using the expression of divergence and gradient in a spherical coordinate system gives

$$\frac{\partial}{\partial v_k} \left(W_{kl} \frac{\partial f_a}{\partial v_l} \right) = \frac{1}{v^3} \left(\frac{1}{\sin\theta} \frac{\partial}{\partial \theta} \left(\sin\theta \frac{\partial f_a}{\partial \theta} \right) + \frac{1}{\sin^2\theta} \frac{\partial^2 f_a}{\partial \varphi^2} \right) = \frac{2}{v^3} \mathcal{L}\{f_a\} \tag{B.18}$$

where $\mathcal{L}\{\cdots\}$ is the called the Lorentz scattering operator.

In Equation (B.18) a factor of two has been introduced when introducing the Loretnz scattering operator, which is a convenient normalisation inspired the physical processes in play. According to Equations (B.9) and (B.10) the derivatives of the Rosenbluth potentials are related to the (generally anisotropic) drag and diffusion coefficients of a test particle. If for simplicity one considers a coordinate system where the initial velocity is aligned with the x direction, that is $\boldsymbol{v} = v_\parallel \boldsymbol{e_x}$ it follows from Equation (B.15) that the drag vector and diffusion tensor are given in a Cartesian coordinate system as

$$\left\langle \frac{\Delta v_k}{\Delta t} \right\rangle^{ab} = - L^{ab} (1 + \frac{m_a}{m_b}) \varphi_b' \begin{pmatrix} 1 \\ 0 \\ 0 \end{pmatrix}$$

$$\left\langle \frac{\Delta v_k \Delta v_l}{2\Delta t} \right\rangle^{ab} = - L^{ab} \begin{pmatrix} \psi_b'' & 0 & 0 \\ 0 & \psi_b'/v & 0 \\ 0 & 0 & \psi_b'/v \end{pmatrix}$$

As typically drag is associated with momentum losses of the test particle due to collisions this motivates the introduction of the slowing down frequency ν_s^{ab} such that $\left\langle \frac{\Delta v_k}{\Delta t} \right\rangle^{ab} = -\boldsymbol{v} \nu_s^{ab}$ it follows by comparison that this frequency is given by

$$\nu_s^{ab} = L^{ab} \left(1 + \frac{m_a}{m_b} \right) \frac{\varphi_b'}{v}. \tag{B.19}$$

Similarly the velocity diffusion is associated with energy gain and losses of the test particle due to collisions such that the diffusion tensor can be written as $\left\langle \frac{\Delta v_k \Delta v_l}{2\Delta t} \right\rangle^{ab} = \frac{v^2}{2} \nu_{kl}$ where ν_{kl} is a collision frequency tensor accounting for the generally anisotropic rates of energy exchange. By comparison with the example above it follows that there are essentially two energy exchange rates since the two perpendicular directions are equivalent, which identifies the two unique frequencies of the collision frequency tensor ν_{kl} as

$$\nu_\parallel^{ab} = \frac{2 L^{ab}}{v^2} \psi_b'' \tag{B.20}$$

$$\nu_D^{ab} = \frac{2 L^{ab}}{v^3} \psi_b' \tag{B.21}$$

giving respectfully the rate of parallel diffusion and perpendicular diffusion.

Then finally using Equations (B.17) and (B.18) to simplify Equation (B.16) gives the collision operator in terms of these three fundamental test particle collision frequencies as

$$C_{ab}(f_a, f_{Mb}) = \nu_D^{ab}\mathcal{L}\{f_a\} + \frac{1}{v^2}\frac{\partial}{\partial v}\left[v^3\left(\frac{m_a}{m_a+m_b}\nu_s^{ab}f_a + \frac{1}{2}\nu_\parallel v\frac{\partial f_a}{\partial v}\right)\right]. \tag{B.22}$$

Note that the Lorentz-operator as defined by Equation (B.18) describes diffusion on a v =constant surface as it only changes the directional distribution of test particle velocities such that the first term of Equation (B.22) is energy conserving and will drive isotropisation of the test particle distribution f_a. This part of the collision operator describes pitch-angle scattering as it effectively changes the ratio of perpendicular to parallel velocity. The remaining two terms give the net effect of energy scattering as a result from competition between drag and diffusion forces on the test particles since they involve changes in v.

All that is left to do is an explicit calculation of the derivatives of the Rosenbluth potentials to determine the test particle collision frequencies of Equations (B.19) to (B.21). This is done easiest from the Laplacian interpretation of these potentials Equations (B.11) and (B.12). For a Maxwellian target particle distribution Equation (B.11) becomes

$$\nabla_v^2\varphi_b = \frac{1}{v^2}\frac{\mathrm{d}}{\mathrm{d}v}\left(v^2\frac{\mathrm{d}\varphi_b}{\mathrm{d}v}\right) = f_{Mb}(v) = n_b\left(\frac{1}{\sqrt{\pi}v_{Tb}}\right)^3\exp\left(-\frac{v^2}{v_{Tb}^2}\right)$$

where isotropy allows the conversion of partial derivatives to full derivatives and the thermal velocity $v_{Tb} = \sqrt{2T_b/m_b}$ has been used. Integrating Equation (B.11) once over the velocity domain $[0, v]$ will give the required derivative φ_b' for the slowing down frequency Equation (B.19), where the integration is easiest performed in terms of the normalised velocity $y = \tilde{v}/v_{Tb}$

$$\begin{aligned}\varphi_b' =& \frac{n_b}{\pi^{3/2}v^2}\int_0^{x_b} y^2\exp\left(-y^2\right)\mathrm{d}y = \frac{n_b}{4\pi v^2}\left[\frac{1}{\sqrt{\pi}}\int_0^{x_b}\frac{\mathrm{d}^2\exp\left(-y^2\right)}{\mathrm{d}y^2}\,\mathrm{d}y + \frac{2}{\sqrt{\pi}}\int_0^{x_b}\exp\left(-y^2\right)\mathrm{d}y\right]\\ =& \frac{n_b}{4\pi v^2}\left(\phi(x_b) - x_b\phi'(x_b)\right) = \frac{n_b}{2\pi v_{Tb}^2}G(x_b)\end{aligned} \tag{B.23}$$

where $\tilde{v}$ is introduced as integration variable for book keeping purposes and $x_b = v/v_{Tb}$ is a convenient normalised velocity. The first integral was evaluated using the fundamental theorem of calculus, the second integral is the definition of the error function $\phi(x) = 2/\sqrt{\pi}\int_0^x \exp\left(-\xi^2\right)\mathrm{d}\xi$, and the Chandrasekhar function[64] $G(x)$ is introduced in the last step defined by

$$G(x) = \frac{\phi(x) - x\phi'(x)}{2x^2}. \tag{B.24}$$

By similar means the required derivative of ψ_b for the deflection frequency Equation (B.21) can be obtained from Equation (B.12), if Equation (B.23) is first integrated once more to obtain $\varphi_b(v)$. This involves the integral of the Chandrasekhar function, which can be obtained using integration by parts as

$$\int_0^x G(\xi)\,\mathrm{d}\xi = \int_0^x\frac{\phi(\xi) - \xi\phi'(\xi)}{2\xi^2}\,\mathrm{d}\xi = -\frac{1}{2\xi}\left(\phi(\xi) - \xi\phi'(\xi)\right)\Big|_0^x - \frac{1}{2}\int_0^x\phi''(\xi)\,\mathrm{d}\xi = -\frac{\phi(x)}{2x}.$$

Then the isotropy requirement reduces Equation (B.12) to

$$\nabla_v^2\psi_b = \frac{1}{v^2}\frac{\mathrm{d}}{\mathrm{d}v}\left(v^2\frac{\mathrm{d}\psi_b}{\mathrm{d}v}\right) = \varphi_b = \frac{n_b}{2\pi v_{Tb}}\int_0^{x_b}G(y)\,\mathrm{d}y = -\frac{n_b}{4\pi v}\phi(x_b)$$

[64]Note that multiple definitions of the Chandrasekhar function exist in literature, most dealing with astrophysical radiation topics. In the literature on collisions $G(x)$ is called the Chandrasehkar function because it is related to his other work on the friction coefficient due to gravity for celestial bodies moving through background matter, which involves a similar integral over a Maxwellian distribution [213].

where $v = v_{Tb}x_b$ was used in the last step to favour the reintroduction of a velocity factor as the Laplacian depends explicitly on v. The derivative ψ_b' then follows by integrating over the domain $[0, v]$ one last time

$$\begin{aligned}\psi_b' =& -\frac{n_b v_{Tb}^2}{4\pi v^2}\int_0^{x_b}\phi(y)y\,\mathrm{d}y = -\frac{n_b v_{Tb}^2}{4\pi v^2}\left(\frac{1}{2}y^2\phi(y)\Big|_0^{x_b} - \int_0^{x_b}\underbrace{\phi'(y)\frac{y^2}{2}}_{=\frac{1}{\sqrt{\pi}}y^2\exp(-y^2)}\,\mathrm{d}y\right)\\ =& -\frac{n_b v_{Tb}^2}{4\pi v^2}\left(\frac{1}{2}x_b^2\phi(x_b) - \frac{1}{2}G(x_b)x_b^2\right) = -\frac{n_b}{8\pi}\left(\phi(x_b) - G(x_b)\right)\end{aligned} \tag{B.25}$$

where integration by parts was used on the second step, in the third step the remaining integral was solved by noting that it is identical to the integral in Equation (B.23), and $x_b = v/v_{Tb}$ was used for cancellation. As a final ingredient for the second derivative ψ_b'' is required for the parallel diffusion frequency Equation (B.20) which is obtained straightforwardly by taking the derivative of Equation (B.25)

$$\psi_b'' = -\frac{n_b}{8\pi v_{Tb}}\left(\phi'(x_b) + \frac{\phi''(x_b)}{2x_b} + \frac{2G(x_b)}{x_b}\right) = -\frac{n_b}{4\pi}\frac{G(x_b)}{v} \tag{B.26}$$

where the derivative of Equation (B.24) has been explicitly expanded using the quotient rule, and the derivatives of the error function cancel since $\phi''(x) = -4x/\sqrt{\pi}\exp\left(-x^2\right) = -2x\phi'(x)$.

Now the test particle collision frequencies of Equations (B.19) to (B.21) are readily evaluated by substituting Equations (B.23), (B.25) and (B.26) for the derivatives of the Rosenbluth potentials as

$$\begin{aligned}\nu_s^{ab} =& \hat{\nu}^{ab}\left(1 + \frac{m_b}{m_a}\right)\frac{T_a}{T_b}\frac{2G(x_b)}{x_a}\\ \nu_\parallel^{ab} =& \hat{\nu}^{ab}\frac{2G(x_b)}{x_a^3}\\ \nu_D^{ab} =& \hat{\nu}^{ab}\frac{\phi(x_b) - G(x_b)}{x_a^3}\end{aligned} \tag{B.27}$$

where $x_a = v/v_{Ta}$ is a second normalised velocity variable and the common prefactor $\hat{\nu}^{ab}$ sets a basic test particle collision frequency scale determined solely by the plasma parameters of the colliding species

$$\hat{\nu}^{ab} = \frac{2L^{ab}n_b}{8\pi v_{Ta}^3} = \frac{n_b}{4\pi v_{Ta}^3}\left(\frac{q_a q_b}{\epsilon_0 m_a}\right)^2\ln\Lambda$$

which is closely related to the typical momentum loss frequency $\bar{\nu}^{ab}$ associated with complete momentum decorrelation[65] by the numerical prefactor $\hat{\nu}^{ab} = \bar{\nu}^{ab}3\sqrt{\pi}/4$.

B.5 A rigorous proof that the equilibrium distribution is Maxwellian

As a bonus, by substituting the result for the test particle collision frequencies Equation (B.27) back in the result for the collision operator with a Maxwellian Equation (B.22), it can rigorously be proven that the Maxwellian distribution is the equilibrium solution with vanishing self-collisions, that is $C_{aa}(f_a^{eq}, f_{Ma}) = 0$ if $f_a^{eq} = f_{Ma}$. Demanding that both terms in Equation (B.22) vanish independently, $\mathcal{L}\{f_a^{eq}\} = 0$ requires f_a^{eq} to be isotropic in velocity space such

[65] In other words cumulative small angle deflections leading up to a net 90° scattering of the initial velocity.

that $f_a^{eq}(\boldsymbol{v}) = f_a^{eq}(v)$ only. In order for the second term to vanish as well, the distribution function should obey

$$\frac{\mathrm{d}}{\mathrm{d}v}\left(v^3\nu_s^{aa}(v)f_a^{eq} + v^4\nu_\parallel^{aa}(v)\frac{\mathrm{d}f_a^{eq}}{\mathrm{d}v}\right) = 0$$

where $b \to a$ was substituted and the partial derivatives have been replaced by total derivatives. Demanding that the resulting integration constant is zero, it follows that the equilibrium distribution obeys the differential equation

$$\frac{1}{f_a^{eq}}\frac{\mathrm{d}f_a^{eq}}{\mathrm{d}v} = -\frac{\nu_s^{aa}(v)}{\nu_\parallel^{aa}(v)v} = -\frac{2v}{v_{Ta}^2}$$

where Equation (B.27) was substituted for the collision frequencies. Integrating w.r.t. velocity gives

$$\ln\left(\frac{f_a^{eq}(v)}{f_a^{eq}(0)}\right) = -\frac{v^2}{v_{Ta}^2}$$

ergo if $f_a^{eq}(v)$ is properly normalised such that $\int f_a^{eq}(v)\mathrm{d}^3\boldsymbol{v} = n_a$ it follows that f_a^{eq} will be the Maxwellian distribution function. It should be noted that this is the centralised Maxwellian without an average flow $\boldsymbol{q} = \int f_M \boldsymbol{v}\mathrm{d}^3\boldsymbol{v}/\int f_M \mathrm{d}^3\boldsymbol{v}$, however from the formulation of the collision operator either in terms of Rosenbluth potentials Equation (B.13) or the Landau form Equation (B.14) it follows that C_{ab} is Gallilean invariant as the velocity $\boldsymbol{v}$ only enters as a derivative or as the relative velocity. Thus one can always transform to a co-moving frame $\boldsymbol{v} \to \boldsymbol{v} - \boldsymbol{q}$ where this average flow would vanish, without affecting the collision operator and thus obtaining a centralised Maxwellian as equilibrium solution in the co-moving frame. Conversely, the Gallilean invariance means that in a "lab" frame the equilibrium distribution will then be a shifted Maxwellian.

C Intermediate steps in the derivation of the gyrokinetic equation

C.1 Order of magnitude estimates

For a general order of magnitude estimate of the different terms in Equation (22) the derivatives of the distribution function will be estimated by considering the scale over which the distribution function will vary significantly. For perturbations with frequency ω this means $\frac{\partial f_s}{\partial t} \sim \omega f_s$, while the restriction that the distribution be 2π periodic in the gyrophase gives $\frac{\partial f_s}{\partial \vartheta} \sim f_s/\pi$. As the average energy of particles in the plasma is the thermal energy, a significant variation in the distribution will occur only if the energy changes by an amount similar to the average such that $\frac{\partial f_s}{\partial E} \sim f_s/T_s$. Lastly, the convective derivative $\dot{\boldsymbol{R}} \cdot \boldsymbol{\nabla}_{\boldsymbol{R}} f_s$ can be estimated by recalling that the isobars are flux surfaces, so the density (to which f_s is proportional) will vary significantly over the distance L_n only perpendicular to the field. Consequently, it are the cross field drifts that matter for the convective derivative which are also small compared to the thermal velocity such that $\dot{\boldsymbol{R}} \cdot \boldsymbol{\nabla}_{\boldsymbol{R}} f_s \sim f_s \delta v_{Ts}/L_n$. Plugging in these order of magnitude estimates and dividing by Ω_s gives

$$\underbrace{\frac{\omega}{\Omega_s}}_{\delta} f_s + \underbrace{\delta\frac{v_{Ts}}{L_n\Omega_s}}_{\delta^2} f_s + \underbrace{\frac{\omega}{\Omega_s}\frac{q_s\phi}{T_s}}_{\delta^2} f_s + \underbrace{\frac{1}{\pi}}_{\approx 0.3} f_s = \underbrace{\frac{C_s(f_s)}{\Omega_s}}_{\delta f_s}.$$

where the scalings Equation (19) have been used on the left-hand side, and on the right-hand side the collision frequency has been estimated as $\nu \sim \omega$ in line with the scope of the project to consider the influence of a non-negligible collisionality. Thus $\frac{\partial f_s}{\partial \vartheta}$ is unbalanced, such that to lowest order the distribution function has to be independent on the gyrophase.

C.2 The equilibrium solution

This invites an expansion of the distribution function as $f_s = f_{0s} + \delta f$ where the next order correction δf is due to turbulence, and may contain a dependence on the gyrophase. The lowest order solution is then obtained by considering the turbulence-free equilibrium situation where $\phi = 0$

$$\frac{\partial f_{0s}}{\partial t} + \dot{\boldsymbol{R}}\Big|_{\phi=0} \cdot \boldsymbol{\nabla}_{\boldsymbol{R}} f_{0s} = C_s(f_{0s}) \tag{C.1}$$

where the same order of magnitude estimate gives $\frac{\partial f_{0s}}{\partial t} \approx C_s(f_{0s}, f_{0s})$. The evolution of the equilibrium is very slow compared to the gyrokinetic timescales and formally occurs on a time $\tau_{eq} \sim \mathcal{O}(1/\delta^2\omega)$ [111]. Consequently the equilibrium can be taken as frozen and is then solved by $C_s(f_{0s}) \approx 0$, which in Appendix B.5 is shown to be solved by the Maxwellian distribution function

$$F_{Ms} = n_{0s}(\psi)\left(\frac{m_s}{2\pi T_{0s}(\psi,t)}\right)^{3/2} \exp\left(-\frac{m_s v^2}{2T_{0s}(\psi,t)}\right) \tag{C.2}$$

where the density is stationary, but the temperature is allowed to have a weak time dependence occurring on τ_{eq} to allow for the equilibration process between ion- and electron temperatures[66]. Still in the turbulence free situation, there will be a next order correction to F_{Ms} due to role of the guiding center drifts in Equation (C.1) which is purely due to the magnetic geometry and is the source of neoclassical transport [69]. As this correction will add to the total fluctuation level, which is typically dominated by the turbulent part, and a description of neoclassical transport is beyond the scope of this thesis it will be omitted.

C.3 Perturbation of the distribution function

To next order in the distribution function δf is determined by including the role of turbulence, which has two effects[67]. First the particles will gain potential energy next to kinetic energy such that the Maxwellian changes as

$$F_{Ms} = n_s\left(\frac{m_s}{2\pi T_{0s}}\right)^{3/2} \exp\left(-\frac{mv^2/2 + q_s\phi}{T_{0s}}\right) = F_{M0s}\exp\left(-\frac{q_s\phi}{T_{0s}}\right) \approx F_{M0s}\left(1 - \frac{q_s\phi}{T_{0s}}\right)$$

where functional dependencies are suppressed, F_{M0s} denotes the unperturbed equilibrium Maxwellian given by Equation (C.2), and the scaling Equation (20) was used in the last step. This additional correction to the distribution function is the usual Boltzmann factor which accounts for the shielding of electric fields due to fast motion of particles along the field line. From now one, whenever the terms Maxwellian and equilibrium distribution are used they will refer F_{M0s} exclusively and the zero subscript will be omitted. Secondly, there will also be a kinetic response g_s to the perturbed field which is largely due to the slow magnetic drifts of the guiding centers and the additional $\boldsymbol{E} \times \boldsymbol{B}$ that arises from the perturbed electric field. Consequently the total perturbed distribution will be $\delta f_s = g_s - \frac{q_s\phi}{T_s} F_{Ms}$.

Substitution this decomposition back into the kinetic equation Equation (22) yields

$$\frac{\partial F_{Ms}}{\partial t} + \frac{\partial g_s}{\partial t} + \dot{\boldsymbol{R}} \cdot \boldsymbol{\nabla}_{\boldsymbol{R}}(F_{Ms} + g_s) + q_s \left.\frac{\partial \phi}{\partial t}\right|_{\boldsymbol{x}} \left(\frac{\partial F_{Ms}}{\partial E} + \frac{\partial g_s}{\partial E}\right) + \Omega_s \frac{\partial g_s}{\partial \vartheta} = C_s(F_{Ms} + g_s) \tag{C.3}$$

[66] Formally $C_s(f_{0s}) = 0$ requires both the collision operator for self interactions C_{ss} and the collision operator for exchange interactions $C_{ss'}$ to vanish, and the proof in Appendix B.5 only concerns the solution for $C_{ss} = 0$. Nevertheless using the Landau form of the collision operator Equation (B.14) it can be shown that $C_{ss'} \propto -(T_{s0} - T_{s'0})$ if a Maxwellian Equation (C.2) distribution is used for both species [114].

[67] Note that these are very handwaving arguments to introduce the adiabatic and kinetic responses that constitute δf, nevertheless they make for the physically correct picture that would otherwise require arduous amount of algebra to derive, which is not the goal of this chapter meant to sketch the essential theoretical elements that will be used later. For the formal derivation the interested reader is referred to [112] for the linear- and [214] non-linear case.

where the adiabatic response drops out since it is not of kinetic nature[68]. A similar order of magnitude estimate of these different terms can be made, where the short scale nature of the turbulence has to be taken into account such that g_s varies on the gyroradius scale which makes the relative contribution of the two convective terms

$$\frac{\dot{\boldsymbol{R}} \cdot \boldsymbol{\nabla}_{\boldsymbol{R}} g_s}{\dot{\boldsymbol{R}} \cdot \boldsymbol{\nabla}_{\boldsymbol{R}} F_{Ms}} \sim \frac{\delta v_{Ts} g_s / \rho_s}{\delta v_{Ts} F_{Ms} / L_n} \sim 1$$

and meanwhile the typical average particle energies will be influenced by the presence of the $\boldsymbol{E} \times \boldsymbol{B}$ drift, such that the new typical energy

$$\frac{1}{2} m_s \left(v_{Ts}^2 + v_E^2 \right) \sim T_{0s}(1 + \delta^2) \approx T_s$$

where the scaling Equation (19) has been used, is not significantly affected such that the relative weight of the two energy terms is

$$\frac{\frac{\partial g_s}{\partial E}}{\frac{\partial F_{Ms}}{\partial E}} \sim \frac{g_s / T_{0s}}{F_{Ms/T_{0s}}} \sim \delta$$

which reveals that that again the $\Omega_s \frac{\partial g_s}{\partial \vartheta}$ term containing the fast dynamics is unbalanced and must vanish. Consequently the kinetic response can also be expanded as $g_s \approx g_{0s} + g_{1s}$ where the leading order part is gyrophase independent and by construction $g_{1s}/g_{0s} \sim \delta$.

For the collision operator, the bilinearity property of Equation (11) in the distribution functions f_a, f_b can be used to expand the collision operator as

$$C_s(F_{Ms} + g_s) = C_s(F_{Ms}, F_{Ms}) + C_s(g_s, F_{Ms}) + C_s(F_{Ms}, g_s) + C_s(g_s, g_s)$$

where the first part contains the equilibrium contribution, the second and third part are linear in the perturbation and the last part is non-linear in the perturbations.

Subtracting the equilibrium contribution Equation (C.1) from Equation (C.3) and retaining only the leading order contribution in δ to each term gives

$$\frac{\partial g_{0s}}{\partial t} + \left(\dot{\boldsymbol{R}} - \dot{\boldsymbol{R}}\Big|_{\phi=0} \right) \cdot \boldsymbol{\nabla}_{\boldsymbol{R}} F_{Ms} + \dot{\boldsymbol{R}} \cdot \boldsymbol{\nabla}_{\boldsymbol{R}} g_{0s} + q_s \left. \frac{\partial \phi}{\partial t} \right|_{\boldsymbol{x}} \frac{\partial F_{Ms}}{\partial E} + \Omega_s \frac{\partial g_{1s}}{\partial \vartheta} = C_s(F_{Ms}, g_{0s}) + C_s(g_{0s}, F_{Ms}).$$

The remaining convective derivative of the equilibrium can be simplified by realising that the equilibrium gradient is still only perpendicular to the field lines, and the presence of the fluctuating electric field results in an additional $\boldsymbol{E} \times \boldsymbol{B}$ drift of the guiding center, such that $\dot{\boldsymbol{R}} - \dot{\boldsymbol{R}}_{\phi=0} = \boldsymbol{E} \times \boldsymbol{B}/B^2$ (this can be made rigorous using the expression for $\left\langle \dot{\boldsymbol{R}} \right\rangle_{\boldsymbol{R}}$ in Appendix D).

The only dependence on the fast gyrophase dynamics is now in $\frac{\partial g_{1s}}{\partial \vartheta}$, the particle position $\boldsymbol{x}$ and the guiding center drift $\dot{\boldsymbol{R}}$. Because the timescale of the perturbations satisfies $\omega/\Omega_s \sim \delta$, these fast dynamics cannot influence the instability properties such as the phase difference between density and potential fluctuations, and can be removed by applying an average over the gyration

$$\langle \cdots \rangle_{\boldsymbol{R}} \equiv \frac{1}{2\pi} \oint \cdots \mathrm{d}\vartheta$$

[68] Although it is true the adiabatic response is essentially a fluid-like response mechanism, it is not true that a brute force substitution of δf into Equation (22) makes all terms involving the adiabatic response vanish. This is however a consequence of the handwaving way with which the adiabatic response has been introduced, as an actual direct approach requires a transformation of derivatives at constant particle position to constant guiding center position, but results in the same equation for g_s [67].

where the guiding center $\boldsymbol{R}$ is kept fixed during the integration so only the direction of the gyroradius vector $\boldsymbol{\rho}$ varies due to gyration. Applying this transform then gives

$$\frac{\partial g_{0s}}{\partial t} + \left\langle \frac{\boldsymbol{E}\times\boldsymbol{B}}{B^2} \right\rangle_{\boldsymbol{R}} \cdot \boldsymbol{\nabla}_{\boldsymbol{R}} F_{Ms} + \left\langle \dot{\boldsymbol{R}} \right\rangle_{\boldsymbol{R}} \cdot \boldsymbol{\nabla}_{\boldsymbol{R}} g_{0s} + q_s \left\langle \left.\frac{\partial \phi}{\partial t}\right|_{\boldsymbol{x}} \right\rangle_{\boldsymbol{R}} \frac{\partial F_{Ms}}{\partial E} = \left\langle C^L(g_s) \right\rangle_{\boldsymbol{R}}$$

where the linear part of the collision operator has been collapsed into $C^L(g_s)$ and the gyrophase dependent part of g_{1s} drops out due to periodicity in ϑ, such that a distinction between g_{0s} and g_{1s} is no longer required and consequently omitted.

C.4 Gyroaveraging procedure of the perturbations

Using Equation (28) to characterise the electrostatic potential perturbation its spatial variation then follows as

$$\boldsymbol{\nabla}\phi = \phi(\boldsymbol{x},t)\left(\underbrace{\boldsymbol{\nabla}\ln\hat{\phi}}_{\mathcal{O}(1/L_n)} + i \underbrace{\frac{\boldsymbol{\nabla}S(\boldsymbol{x})}{\delta}}_{\mathcal{O}(1/\delta L_n)\sim\mathcal{O}(1/\rho)} \right) \approx i\frac{\boldsymbol{\nabla}S(\boldsymbol{x})}{\delta}\phi(\boldsymbol{x},t). \tag{C.4}$$

If one interprets $\boldsymbol{\nabla}S(\boldsymbol{x})/\delta$ as a wavevector $\boldsymbol{k}$, then Equation (C.4) is the familiar result as if ϕ were expanded as a Fourier series in space, with $\hat{\phi}$ being the corresponding Fourier coefficient. The scaling $k_\parallel/k_\perp \sim \delta$ Equation (19) implies that the wavevector can be approximated[69] by its perpendicular component $\boldsymbol{k}_\perp \approx \boldsymbol{\nabla}S/\delta$. Using Equation (C.4) the gyroaverage of the $\boldsymbol{E}\times\boldsymbol{B}$ drift can be calculated as

$$\begin{aligned}
\langle \boldsymbol{\nabla}\boldsymbol{\phi} \rangle_{\boldsymbol{R}} =& \exp(-i\omega t)\left\langle i\boldsymbol{k}_\perp \hat{\phi}(\boldsymbol{R}+\boldsymbol{\rho_s}) \exp\left(i(\frac{S(\boldsymbol{R}+\boldsymbol{\rho_s})}{\delta}) \right) \right\rangle_{\boldsymbol{R}} \\
\approx& \exp(-i\omega t)\left\langle i\boldsymbol{k}_\perp \left[\hat{\phi}(\boldsymbol{R}) + \boldsymbol{\rho_s}\cdot\boldsymbol{\nabla}\hat{\phi}\right] \exp\left(i(\frac{S(\boldsymbol{R})}{\delta} + \boldsymbol{\rho_s}\cdot\boldsymbol{k}_\perp) \right) \right\rangle_{\boldsymbol{R}} \\
\approx& \hat{\phi}(\boldsymbol{R}) \exp\left(i(\frac{S(\boldsymbol{R})}{\delta} - \omega t) \right) \langle i\boldsymbol{k}_\perp \exp(i\boldsymbol{k}_\perp\cdot\boldsymbol{\rho_s}) \rangle_{\boldsymbol{R}}
\end{aligned}$$

where the gradient must be evaluated at the particle position $\boldsymbol{x} = \boldsymbol{R}+\boldsymbol{\rho}$ as this determines the local electric field that a particle experiences, and this has subsequently been expanded around $\boldsymbol{R}$ in the second step. In the final step the scalings $k_\perp\rho_s \sim \mathcal{O}(1)$ and $\rho/L_n \sim \delta$ from Equation (19) have been used to neglect the variation of $\hat{\phi}$ on the gyroradius scale. The gyroaverage of the phase factor can be calculated by realising that at the guiding center $\boldsymbol{k}_\perp$ is fixed and $\boldsymbol{\rho}$ only changes direction during gyration such that

$$\langle \exp(i\boldsymbol{k}_\perp\cdot\boldsymbol{\rho_s}) \rangle_{\boldsymbol{R}} = \frac{1}{2\pi}\int_0^{2\pi} \exp(ik_\perp\rho\sin(\vartheta))\,\mathrm{d}\vartheta = J_0(k_\perp\rho_s) \tag{C.5}$$

where J_0 is the Bessel function of zeroth order. Consequently the gyroaveraged electric field is

$$\langle \boldsymbol{E} \rangle_{\boldsymbol{R}} = -\langle \boldsymbol{\nabla}\phi \rangle_{\boldsymbol{R}} \approx \underbrace{-i\boldsymbol{k}_\perp\phi(\boldsymbol{R},t)}_{=\boldsymbol{E}(\boldsymbol{R},t)} J_0(k_\perp\rho_s)$$

Completely analogous to the gyroaverage of the gradient, it can be straightforwardly shown that

$$\left\langle \left.\frac{\partial\phi}{\partial t}\right|_{\boldsymbol{x}} \right\rangle_{\boldsymbol{R}} = -i\omega\phi(\boldsymbol{R},t)J_0(k_\perp\rho_s).$$

[69] This leads to some subtlety on flux surfaces where the rotational transform is non-rational and a single field line essentially traces out the complete flux surface, which creates an inconsistency as $k_\parallel \approx \mathbf{0}$ implies that $S(\boldsymbol{x})$ must be constant on the full flux surface and consequently also $\boldsymbol{k}_\perp = 0$. This issue is remedied by the so-called ballooning transform [215, 216], which forms an equivalent description to Fourier modes for drift-waves in a torus [132, 217]. This is however beyond the scope of the present thesis to discuss.

by first evaluating the derivative and then performing the expansion from particle position to guiding center position in the exponential phase-factor.

Substituting these results into Equation (25) and collecting all terms involving g_s on the left-hand side gives

$$\frac{\partial g_s}{\partial t} + \left(v_\parallel \boldsymbol{e_b} + \boldsymbol{v_E} + \boldsymbol{v_{ds}}\right) \cdot \boldsymbol{\nabla_R} g_s - \left\langle C_s^L(g_s) \right\rangle_{\boldsymbol{R}} = -i\omega J_0 \phi(\boldsymbol{R}, t) \frac{q_s \phi(\boldsymbol{R}, t)}{T_{0s}} F_{Ms} - \boldsymbol{v_E} \cdot \boldsymbol{\nabla_R} F_{Ms} \tag{C.6}$$

where the derivative of the Maxwellian w.r.t. energy follows straightforward as $\frac{\partial F_{Ms}}{\partial E} = -F_{Ms}/T_s$ from Equation (23).

Because density and temperature are flux functions, the convective derivative[70] of F_{Ms} follows as

$$\begin{aligned} -\boldsymbol{v_E} \cdot \boldsymbol{\nabla_R} F_{Ms} =& i\phi(\boldsymbol{R}, t) J_0 \frac{\boldsymbol{k}_\perp \times \boldsymbol{e_b}}{B} \cdot \boldsymbol{\nabla}\psi \frac{\partial F_{Ms}}{\partial \psi} \\ =& i J_0 \frac{q_s \phi(\boldsymbol{R}, t)}{T_{0s}} \omega_{\star s}^T F_{Ms} \end{aligned}$$

where Equation (23) and Equation (27) have been used for the definitions of $F_{Ms}, \boldsymbol{v_E}$, and the frequency $\omega_{\star s}^T$ is defined by

$$\begin{aligned} \omega_{\star s}^T =& \omega_{\star s} \left(1 + \eta_s \left[\frac{E}{T_s} - \frac{3}{2}\right]\right) \\ \omega_{\star s} =& \frac{T_s}{q_s} \frac{(\boldsymbol{k}_\perp \times \boldsymbol{e_b}) \cdot \boldsymbol{\nabla}\psi}{B} \frac{\mathrm{d} \ln n_s}{\mathrm{d}\psi}. \\ \eta_s =& \frac{\mathrm{d} \ln T_s}{\mathrm{d}\psi} \Big/ \frac{\mathrm{d} \ln n_s}{\mathrm{d}\psi} \end{aligned}$$

The physical interpretation of these frequencies and the Bessel function is provided in the main text in Section 2.3.

Similar to the derivatives of the electrostatic potential ϕ, the derivatives of the kinetic response g_s appearing on the right-hand side of Equation (29) are easy to evaluate using its WKB expansion Equation (31) as

$$\begin{aligned} \frac{\partial g_s}{\partial t} =& -i\omega g_s(\boldsymbol{R}) \\ \boldsymbol{\nabla_R} g_s =& g_s(\boldsymbol{R}, t) \left(\underbrace{\boldsymbol{\nabla} \ln \hat{g_s}}_{\mathcal{O}(1/L_n)} + i \underbrace{\frac{\boldsymbol{\nabla} S(\boldsymbol{R})}{\delta}}_{\mathcal{O}(1/\delta L_n) \sim \mathcal{O}(1/\rho)} \right) \approx i \frac{\boldsymbol{\nabla} S(\boldsymbol{x})}{\delta} g_s(\boldsymbol{R}, t). \end{aligned}$$

D Derivation of the gyroaveraged guiding center velocity

Starting from the definition of the guiding center $\boldsymbol{R}$ from Equation (21) the guiding center velocity is found by expanding the derivative

$$\frac{\mathrm{d}\boldsymbol{R}}{\mathrm{d}t} = \underbrace{\boldsymbol{v}}_{i} - \underbrace{\frac{\dot{\boldsymbol{e_b}} \times \boldsymbol{v}}{\Omega}}_{ii} - \underbrace{\frac{\boldsymbol{e_b} \times \dot{\boldsymbol{v}}}{\Omega}}_{iii} + \underbrace{\frac{\boldsymbol{e_b} \times \boldsymbol{v}}{\Omega^2} \dot{\Omega}}_{iv} \tag{D.1}$$

[70] The distinction between particle and guiding center position does not matter for this derivative as the pressure varies on the macroscopic length scales $L_n = \|-\boldsymbol{\nabla} \ln n\|^{-1}$ and $L_T = \|-\boldsymbol{\nabla} \ln T\|^{-1}$ which are comparable to the plasma radius see Figure 1b.

where $\boldsymbol{v} = \dot{\boldsymbol{r}}$ is used and the dot denotes derivative w.r.t. time. The gyro-average $\langle \cdots \rangle_{\boldsymbol{R}} = \frac{1}{2\pi} \oint \cdots \mathrm{d}\vartheta$ of Equation (D.1) is best evaluated term by term. Term i is straightforward to average using the velocity decomposition $\boldsymbol{v} = v_\parallel \boldsymbol{e_b} + \boldsymbol{v}_\perp$, where $\boldsymbol{v}_\perp$ constitutes the gyromotion, giving

$$\langle \boldsymbol{v} \rangle_{\boldsymbol{R}} = \langle v_\parallel \boldsymbol{e_b} \rangle_{\boldsymbol{R}} + \langle \boldsymbol{v}_\perp \rangle_{\boldsymbol{R}} = v_\parallel \boldsymbol{e_b}(\boldsymbol{R}) + \boldsymbol{0} \tag{D.2}$$

as the parallel velocity remains constant during gyroaveraging, but the direction of the perpendicular velocity oscillates poloidally.

Term *iii* is simplified by substitution Newton's equation of motion for a charged particle in an electromagnetic field

$$\begin{aligned} \left\langle \frac{\boldsymbol{e_b} \times \dot{\boldsymbol{v}}}{\Omega} \right\rangle_{\boldsymbol{R}} &= \left\langle \frac{\boldsymbol{e_b}}{\Omega} \times \frac{q}{m} (\boldsymbol{E} + \boldsymbol{v} \times \boldsymbol{B}) \right\rangle_{\boldsymbol{R}} \\ &= \left\langle \frac{\boldsymbol{e_b} \times \boldsymbol{E}}{B} \right\rangle_{\boldsymbol{R}} + \langle \boldsymbol{e_b} \times (\boldsymbol{v} \times \boldsymbol{e_b}) \rangle_{\boldsymbol{R}} \end{aligned}$$

where the definition of the gyrofrequency $\Omega = \frac{qB}{m}$ and magnetic field $\boldsymbol{B} = B\boldsymbol{e_b}$ were used in the last step. For the electrostatic perturbations under consideration the electric field can be written as the gradient of the electrostatic potential $\boldsymbol{E} = -\boldsymbol{\nabla}\phi$, and the magnetic force term can be simplified using the vector triple product relation $\boldsymbol{a} \times (\boldsymbol{b} \times \boldsymbol{c}) = (\boldsymbol{a} \cdot \boldsymbol{c})\, \boldsymbol{b} - (\boldsymbol{a} \cdot \boldsymbol{b})\, \boldsymbol{c}$, resulting in

$$\left\langle \frac{\boldsymbol{e_b} \times \dot{\boldsymbol{v}}}{\Omega} \right\rangle_{\boldsymbol{R}} = -\left\langle \frac{\boldsymbol{e_b} \times \boldsymbol{\nabla}\phi}{B} \right\rangle_{\boldsymbol{R}} + \langle \boldsymbol{v}_\perp \rangle_{\boldsymbol{R}} = -\frac{\boldsymbol{e_b}(\boldsymbol{R})}{B(\boldsymbol{R})} \times \langle \boldsymbol{\nabla}\phi \rangle_{\boldsymbol{R}} + \boldsymbol{0}. \tag{D.3}$$

Terms *ii* and *iv* deal with the time derivative of the magnetic field direction and strength respectively. Since the perturbations under consideration are electrostatic, they do not alter the equilibrium magnetic field which is static as a result from quasi-neutrality ($\frac{\partial \boldsymbol{B}}{\partial t} = 0$). Therefore the only change in time a particle experiences from the magnetic is due its own motion through the non-uniform magnetic field, i.e. the time derivative is just the convective derivative $\frac{\mathrm{d}}{\mathrm{d}t} \to (\boldsymbol{v} \cdot \boldsymbol{\nabla})$.

Term *ii* can be solved by realising that the direction of $\dot{\boldsymbol{e_b}}$ is constrained perpendicular to $\boldsymbol{e_b}$ in order to preserve the length of the unit vector, since $\boldsymbol{e_b} \cdot \dot{\boldsymbol{e_b}} = \frac{1}{2} \frac{\mathrm{d}(\boldsymbol{e_b} \cdot \boldsymbol{e_b})}{\mathrm{d}t} = \frac{1}{2} \frac{\mathrm{d}}{\mathrm{d}t} 1 = 0$. Splitting the convective derivative as $(\boldsymbol{v} \cdot \boldsymbol{\nabla})\boldsymbol{e_b} = v_\parallel \nabla_\parallel \boldsymbol{e_b} + \boldsymbol{v}_\perp \cdot \boldsymbol{\nabla}_\perp \boldsymbol{e_b}$ will simplify the gyroaveraging procedure.

The parallel derivative $v_\parallel \nabla_\parallel \boldsymbol{e_b}$ represents the change of the direction of the magnetic field as the particle moves along the field line, which as a result of the rotational transform ι of the helical magnetic field is slowly twisting in the poloidal plane while moving along the field line. Consequently, the relevant cross product $\left[v_\parallel \nabla_\parallel \boldsymbol{e_b}\right] \times \boldsymbol{v} = \left[v_\parallel \nabla_\parallel \boldsymbol{e_b}\right] \times \left(v_\parallel \boldsymbol{e_b}\right)$ since the gyration takes place in the poloidal plane as well. It is custom to write $\nabla_\parallel \boldsymbol{e_b} = \boldsymbol{e_b} \cdot \boldsymbol{\nabla} \boldsymbol{e_b} \equiv \boldsymbol{\kappa}$ since this quantity represents the curvature of the magnetic field lines.

The perpendicular derivative $\boldsymbol{v}_\perp \cdot \boldsymbol{\nabla}_\perp \boldsymbol{e_b}$ is also a component of $\dot{\boldsymbol{e_b}}$ and therefore constrained perpendicular to the magnetic field, however unlike the parallel derivative $v_\parallel \nabla_\parallel \boldsymbol{e_b}$ it does not have a clear physical interpretation related to the twisting of the field line. Nevertheless, the gyroaveraging operation can be performed by realising that $\boldsymbol{\nabla} \boldsymbol{e_b}$ is a tensor containing the geometry information of how the direction of the magnetic field changes locally through space, and is therefore a fixed quantity for a given magnetic configuration at the guiding centre $\boldsymbol{R}$. However, $\boldsymbol{v}_\perp$ is the velocity associated with the gyromotion which continually changes direction depending on the gyro-angle ϑ. Since the magnetic moment $\mu = \frac{m v_\perp^2}{2B}$ is an adiabatic invariant of the motion, and the magnetic field strength cannot change abruptly along the helical trajectory of the particle during a single gyration ($\frac{v_\parallel}{\Omega} \ll \|\boldsymbol{\nabla} \ln B\|^{-1}$) the magnitude of $\boldsymbol{v}_\perp$ remains constant

during a gyration. Consequently during a single gyration $\boldsymbol{v}_\perp(\vartheta)\cdot\boldsymbol{\nabla}_\perp\boldsymbol{e_b}$ is scanning different components of the Jacobian matrix of the magnetic geometry ($\nabla\boldsymbol{e_b}$). Since after half a rotation the perpendicular velocity is in counter phase with itself $\boldsymbol{v}_\perp(\vartheta+\pi)=-\boldsymbol{v}_\perp(\vartheta)$ all the selected components of the Jacobian matrix during a gyration cancel out[71]. Consequently, after some effort the gyroaverage of term ii follows as

$$\left\langle\frac{\dot{\boldsymbol{e_b}}\times\boldsymbol{v}}{\Omega}\right\rangle_{\boldsymbol{R}}=\left\langle\frac{v_\parallel^2\boldsymbol{\kappa}\times\boldsymbol{e_b}}{\Omega}\right\rangle_{\boldsymbol{R}}+\left\langle\frac{(\boldsymbol{v}_\perp(\vartheta)\cdot\nabla_\perp)\,\boldsymbol{e_b}\times\boldsymbol{v}}{\Omega}\right\rangle_{\boldsymbol{R}}=\frac{v_\parallel^2\boldsymbol{\kappa}(\boldsymbol{R})\times\boldsymbol{e_b}(\boldsymbol{R})}{\Omega(\boldsymbol{R})}+\boldsymbol{0}. \tag{D.4}$$

Since the mass and charge of a given particle are constants, term iv can be reduced to $\frac{\boldsymbol{e_b}\times\boldsymbol{v}}{\Omega}\times\frac{1}{B}(\boldsymbol{v}\cdot\boldsymbol{\nabla})B$ where the first factor is the gyroradius vector $\boldsymbol{\rho}$ indicating the position of the particle on the gyration ring around the guiding center. Since for the gyroaveraging procedure the guiding center is kept fixed, the gyromotion can conveniently be described in a local Cartesian coordinate system $\{\boldsymbol{e_1},\boldsymbol{e_2},\boldsymbol{e_b}\}$ with its origin at $\boldsymbol{R}$ [6], such that the gyration is described by

$$\begin{aligned}\boldsymbol{\rho}&=\frac{v_\perp}{\Omega(\boldsymbol{R})}\left(\sin(\vartheta)\boldsymbol{e_1}+\cos(\vartheta)\boldsymbol{e_2}\right)\\ \boldsymbol{v}&=v_\parallel\boldsymbol{e_b}+v_\perp\left(\cos(\vartheta)\boldsymbol{e_1}-\sin(\vartheta)\boldsymbol{e_2}\right)\end{aligned}$$

which has the benefit that the unit vectors remain constant during gyroaveraging. Expanding term iv in this local Cartesian coordinate system gives

$$\begin{aligned}\frac{\boldsymbol{e_b}\times\boldsymbol{v}}{\Omega}\times\frac{1}{B}(\boldsymbol{v}\cdot\boldsymbol{\nabla})B=&\frac{v_\perp}{\Omega B}\boldsymbol{e_1}\left(v_\parallel\sin(\vartheta)\nabla_\parallel B+v_\perp\sin(\vartheta)\cos(\vartheta)\nabla_{e_1}B-v_\perp\sin(\vartheta)^2\nabla_{e_2}B\right)\\&+\frac{v_\perp}{\Omega B}\boldsymbol{e_2}\left(v_\parallel\cos(\vartheta)\nabla_\parallel B+v_\perp\cos(\vartheta)^2\nabla_{e_1}B-v_\perp\sin(\vartheta)\cos(\vartheta)\nabla_{e_2}B\right).\end{aligned}$$

The result of gyroaveraging is then readily obtained as

$$\left\langle\frac{\boldsymbol{e_b}\times\boldsymbol{v}}{\Omega}\times\frac{1}{B}(\boldsymbol{v}\cdot\boldsymbol{\nabla})B\right\rangle_{\boldsymbol{R}}=-\frac{v_\perp^2}{2\Omega(\boldsymbol{R})}\boldsymbol{e_1}\nabla_{e_2}\ln B(\boldsymbol{R})+\frac{v_\perp^2}{2\Omega(\boldsymbol{R})}\boldsymbol{e_2}\nabla_{e_1}\ln B(\boldsymbol{R}) \tag{D.5}$$

which is a direct consequence of the $\pi/2$ phase difference between the components of $\boldsymbol{\rho}$ and $\boldsymbol{v}_\perp$; the dot product leads to mixing of the components of $\boldsymbol{\rho}$ and $\boldsymbol{v}_\perp$ which are in phase and result in a non-vanishing average over a gyration. As the local Cartesian coordinate system is defined by $\boldsymbol{e_1}\times\boldsymbol{e_2}=\boldsymbol{e_b}$, Equation (D.5) can be generalised to an arbitrary coordinate system as

$$\left\langle\frac{\boldsymbol{e_b}\times\boldsymbol{v}}{\Omega}\times\frac{1}{B}(\boldsymbol{v}\cdot\boldsymbol{\nabla})B\right\rangle_{\boldsymbol{R}}=\frac{\boldsymbol{e_b}(\boldsymbol{R})}{\Omega(\boldsymbol{R})}\times\frac{v_\perp^2}{2}\boldsymbol{\nabla}\ln B(\boldsymbol{R}). \tag{D.6}$$

Combining Equations (D.2) to (D.6) gives the desired result for the gyroaveraged guiding center velocity

$$\left\langle\dot{\boldsymbol{R}}\right\rangle_{\boldsymbol{R}}=v_\parallel\boldsymbol{e_b}+\frac{\boldsymbol{e_b}\times\langle\boldsymbol{\nabla}\phi\rangle_{\boldsymbol{R}}}{B}+\frac{\boldsymbol{e_b}}{\Omega}\times\left(v_\parallel^2\boldsymbol{\kappa}+\frac{v_\perp^2}{2}\boldsymbol{\nabla}\ln B\right)$$

where the evaluation of the magnetic field at the guiding center has been suppressed since that is implied by the gyroaveraging procedure.

[71] This argument neglects the cross product with $\boldsymbol{v}$ which cannot be reduced to a cross product with just the gyrophase independent $v_\parallel\boldsymbol{e_b}$, since $\boldsymbol{v}_\perp\cdot\boldsymbol{\nabla}_\perp\boldsymbol{e_b}$ could also lie in the radial direction. Nevertheless, when $v_\perp$ is horizontal and the horizontal components of the Jacobian matrix are selected, the cross product with $v_\perp$ will select the vertical component, which is $\pi/2$ out of phase with its horizontal component. Consequently the average over a gyration of the cross product with $\boldsymbol{v}_\perp$ also vanishes since $\nabla\boldsymbol{e_b}$ is independent of gyrophase

E Derivation of dispersion relation for the basic drift wave

The dispersion relation for the basic drift wave mechanism can be derived fairly easily from the macroscopic MHD fluid equations for particle conservation and momentum balance, and what follows the procedure in [5, 12] will be closely followed. The MHD mass balance is given by [3]

$$\frac{\partial n_s}{\partial t} + \boldsymbol{\nabla} \cdot (n_s \boldsymbol{u_s}) = 0 \tag{E.1}$$

where n_s is the species density, and $\boldsymbol{u_s}$ is the macroscopic fluid velocity, which is equivalent to the average velocity in kinetic theory $\boldsymbol{u_s} = \int \boldsymbol{v} f_s \mathrm{d}^3\boldsymbol{v}/n_s$. The MHD momentum balance is given by [3]

$$m_s n_s \left(\frac{\partial}{\partial t} + \boldsymbol{u_s} \cdot \boldsymbol{\nabla} \right) \boldsymbol{u_s} = q_s n_s \left(\boldsymbol{E} + \boldsymbol{u_s} \times \boldsymbol{B} \right) - \boldsymbol{\nabla} p_s - m_s n_s \sum_{s'} \nu_{ss'} \left(\boldsymbol{u_s} - \boldsymbol{u_{s'}} \right) \tag{E.2}$$

where m_s, q_s are the species mass and charge respectively, $\boldsymbol{E}, \boldsymbol{B}$, $p_s = n_s T_s$ is the species pressure and T_s the species temperature, and $\nu_{ss'}$ is the net collision frequency for momentum exchange between species s and s'.

In the drift wave mechanism described in Section 2.1.1, it is the fast parallel motion of the electrons parallel to the field that is crucial for the generation of the electric field as a result of the much smaller inertia compared to ions. Thus neglecting the electron inertia and the collisions since they are not included in the basic drift wave mechanism, the parallel component of Equation (E.2) for electrons reduces to

$$0 \approx e n_e \boldsymbol{\nabla}_\parallel \phi - \boldsymbol{\nabla}_\parallel p_e \tag{E.3}$$

where the electrostatic approximation $\boldsymbol{E} = -\boldsymbol{\nabla}\phi$ was used. In the basic drift wave mechanism the temperature is uniform, the equilibrium density is taken to have a gradient perpendicular to the magnetic field, and in absence of a density perturbation there is no electrostatic potential ϕ such that the parallel momentum balance reduces to $0 = 0$ in equilibrium. In the presence of perturbations $n_e \to n_0 + \delta n$ and $\phi \neq 0$, and assuming these perturbations to be small $\delta n/n_0 \sim e\phi/T_e \sim \delta \ll 1$ Equation (E.3) can be solved perturbatively by neglecting δ^2 terms as

$$\frac{\delta n_e}{n_0} = \frac{e\phi}{T_e} \tag{E.4}$$

where $\boldsymbol{\nabla}_\parallel n_e = \boldsymbol{\nabla}_\parallel T_e = 0$ were used. Note that Equation (E.4) is simply the linearisation of the Boltzmann relation for electrons in equilibrium [218], which corresponds with the assumption that electrons respond adiabatically to equilibrate density differences.

Meanwhile the ions are dominated by their relatively large inertia, and will respond kinetically to the density perturbation. As a result from the electric field the ions will be affected by the $\boldsymbol{E} \times \boldsymbol{B}$ drift, which for a typical Maxwellian velocity distribution will be the mean velocity obtained from averaging over the distribution[72]. Consequently Equation (E.1) for the ions takes the form

$$\frac{\partial n_i}{\partial t} + \boldsymbol{\nabla} \cdot \left(n_i \frac{\boldsymbol{e_b} \times \boldsymbol{\nabla}\phi}{B} \right) = 0 \tag{E.5}$$

[72] In light of the theory presented Section 2.3 this is not completely true, since the kinetic response of the ions results in a distribution $f_i = f_{Mi} + f_{ad,i} + g_i$. Although for the first two terms which are of Maxwellian form it holds that $\boldsymbol{u_i} = \boldsymbol{v_E}$, the kinetic response function can also have a non-vanishing average parallel velocity. Nevertheless if the perturbations satisfy $\omega/k_\parallel \gg v_{th}$ the parallel motion of ions during a period of the oscillation will be negligible and on the timescale of the perturbation one can take $\boldsymbol{u_i} \approx \boldsymbol{v_E}$ [5]

where B is just the magnitude of the magnetic field and $\boldsymbol{e_b} = \boldsymbol{B}/B$ is the unit vector in the direction of the magnetic field. Assuming all perturbations to be of the form $f = \tilde{f}\exp(i\boldsymbol{k}\cdot\boldsymbol{x} - \omega t)$ for amplitude $\tilde{f}$, wavevector $\boldsymbol{k}$ and frequency ω, Equation (E.5) can also be solved perturbatively. Just as before using $n_i = n_0 + \delta n_i$, $e\phi/T_i \sim \delta n_i/n_0 \sim \delta$, and neglecting δ^2 effects, Equation (E.5) becomes

$$i\omega\delta n_i = \frac{\boldsymbol{e_b}\times\boldsymbol{k}}{B} i\phi\cdot\boldsymbol{\nabla}n_0 - \underbrace{\frac{\boldsymbol{e_b}\times\boldsymbol{k}}{B}\cdot\boldsymbol{k}}_{=0} n_0\phi$$

which is easily solved for the density perturbation as $\delta n_i = \frac{(\boldsymbol{e_b}\times\boldsymbol{k})\cdot\boldsymbol{\nabla}n_0}{\omega B}\phi$.

As a final ingredient, demanding the perturbations to maintain quasi-neutrality such that no macroscopically large electric fields will form along the magnetic field, results in

$$\left(\frac{(\boldsymbol{e_b}\times\boldsymbol{k})\cdot\boldsymbol{\nabla}n_0}{B\omega} - n_0\frac{e}{T_e}\right)\phi = 0$$

which should hold regardless of the form of the potential perturbation such that the frequency of the perturbation is found as

$$\omega = \frac{T_e}{e}\frac{(\boldsymbol{e_b}\times\boldsymbol{k})}{B}\cdot\boldsymbol{\nabla}\ln n_0, \tag{E.6}$$

i.e. the frequency is purely real corresponding to a stable travelling rather than an instability. Since the frequency was obtained with the same assumptions as the basic drift wave mechanism, namely adiabatic electrons and ions influenced by the $\boldsymbol{E}\times\boldsymbol{B}$ drift, it must be the drift wave frequency.

E.1 Translation to toroidal geometry

In the slab geometry the density gradient was taken to be in the x direction, which corresponds to the radial ψ direction in toroidal geometry, and a comparison with Equation (30) shows that the wavefrequency is the electron diamagnetic frequency $\omega_{\star e}$. Continuing the translation from slab to toroidal geometry, the wavevector in Equation (E.6) can be taken as $\boldsymbol{k}_\perp$ as the cross product would make any parallel component vanish, and the Clebsch representation of the magnetic field Equation (5) gives a natural choice for the perpendicular wavevector as $\boldsymbol{k}_\perp = k_\alpha\boldsymbol{\nabla}\alpha + k_\psi\boldsymbol{\nabla}\psi$, for which Equation (E.6) gives

$$\omega_{\star e} = \frac{T_e}{-e}\frac{(\boldsymbol{k}_\perp\times\boldsymbol{e_b})}{B}\cdot\boldsymbol{\nabla}\psi\frac{\mathrm{d}\ln n_e}{\mathrm{d}\psi} = \frac{T_e}{-e}k_\alpha\frac{\mathrm{d}\ln n_e}{\mathrm{d}\psi} \tag{E.7}$$

where the circular shift property of the scalar triple product, the definition of Clebsch coordinates $\boldsymbol{B} = \boldsymbol{\nabla}\psi\times\boldsymbol{\nabla}\alpha$ and $\boldsymbol{e_b} = \boldsymbol{B}/B$ have been used.

The fact that the perturbations move in the electron diamagnetic direction stems mathematically from Equation (E.4), namely that the perturbed electron density has exactly the same waveform as the potential perturbation (and by enforcing quasi neutrality so must the ion density). Physically it stems from the fact that the electrons quickly re-establish their density to the background density and thereby leave the ions behind at the perturbed density, so the wave will travel in the same direction along the field lines as the electrons do, with the phase speed $\omega/k_\parallel$.

E.2 Extension to $i\delta$ model

If the non-adiabatic nature of the electrons is accounted for by means of an $i\delta$ model, such that the electron density perturbation becomes

$$\frac{\delta n_e}{n_0} = \frac{e\phi}{T_e}e^{-i\delta} \approx \frac{e\phi}{T_e}(1 - i\delta)$$

for phase delay of $\delta \ll 1$, then the quasi-neutrality condition is changed to

$$\left[\frac{(\boldsymbol{e_b} \times \boldsymbol{k}) \cdot \boldsymbol{\nabla} n_0}{B\omega} - (1 - i\delta) n_0 \frac{e}{T_e}\right] \phi = 0$$

where the density perturbation for ions is the same as before. Factoring n_0, e, T_e out of the brackets to enforce Equation (E.6) as the definition for $\omega_{\star e}$ gives the new solution to the dispersion relation as

$$\frac{\omega}{\omega_{\star e}} = \frac{1}{1 - i\delta} \approx 1 + i\delta$$

where $\delta \ll 1$ was again used in the last step. The drift wave frequency now acquires an imaginary part which corresponds to a growth rate of $\gamma = \delta \times \omega_{\star e}$ leading to instability as a result of the non-adiabatic response of electrons provided that $\delta > 0$ and the density perturbation will lag the potential perturbation, i.e. the electrons cannot immediately establish equilibrium along the field line on the timescale of the perturbations. In the more general case where the phase delay is not small and the $\exp(-i\delta)$ phase factor cannot be expanded it is straightforward to show that the solution to the dispersion relation is given by

$$\frac{\omega}{\omega_{\star e}} = \exp(i\delta) \tag{E.8}$$

such that the non-adiabatic electron response leads to both a shift in the propagation frequency away from $\omega_{\star e}$ and a growth rate.

F Relaxation property of the BGK collision operator

In the absence of spatial gradients and electromagnetic fields[73] (i.e. a homogeneous, unmagnetised and quasi-neutral plasma) the kinetic equation Equation (10) reduces to the simple form

$$\frac{\partial f_s}{\partial t} = C_s. \tag{F.1}$$

By taking velocity moments of Equation (F.1) evolution equations for the density, mean velocity and temperature of species s are obtained

$$\begin{aligned} \frac{\partial}{\partial t}(n_s) &= \int C_s \mathrm{d}^3 \boldsymbol{v_s} \\ \frac{\partial}{\partial t}(n_s \boldsymbol{q_s}) &= \int \boldsymbol{v_s} C_s \mathrm{d}^3 \boldsymbol{v_s} \\ \frac{\partial}{\partial t}\left(\frac{3}{m_s} T_s + n_s \boldsymbol{q_s}^2\right) &= \int v_s^2 C_s \mathrm{d}^3 \boldsymbol{v_s} \end{aligned} \tag{F.2}$$

where the definition of the velocity moments of f_s from Equation (40) have been used. By using the BGK model Equation (38) for the collision operator C_s it follows from the standard velocity moments of the shifted Maxwellian

$$\int M[f_s] \mathrm{d}^3 \boldsymbol{v_s} = n_s \quad \int M[f_s] \boldsymbol{v_s} \mathrm{d}^3 \boldsymbol{v_s} = n_s \boldsymbol{q_s} \quad \int v^2 M[f_s] \mathrm{d}^3 \boldsymbol{v_s} = n_s \left(\frac{3T_s}{m_s} + \boldsymbol{q_s}^2\right) \tag{F.3}$$

[73] This is an idealisation that directly reduces the problem to an as simple as possible form. In actuality, spatial gradients can be allowed provided that they are sufficiently weak (i.e. long gradient lengths $L_{\boldsymbol{\nabla}}$) and the presence of magnetic field can also be allowed provided that is sufficiently strong, such that there is again a strong timescale separation $v_{Ts}/L_{\boldsymbol{\nabla}} \boldsymbol{\nabla}_{\boldsymbol{x}} \ll \nu_s \ll \Omega_s$ and the kinetic equation can be approximately reduced to Equation (F.1).

that all of the right-hand sides of Equation (F.2) vanish, which is a consequence of the conservative nature of the BGK model. This means that Equation (F.2) represent a set of conservation equations for the particle, momentum and energy densities, which can be reduced to

$$\frac{\partial n_s}{\partial t} = 0 \quad \frac{\partial \boldsymbol{q_s}}{\partial t} = 0 \quad \frac{\partial T_s}{\partial t} = 0$$

by substituting one equation into the next, and shows that the density, mean velocity and temperature are all individually all stationary (i.e. constant in time). As furthermore the plasma is taken to be homogeneous the the velocity of moments of f_s, which in general are a function of space and time since $f_s(\boldsymbol{x}, \boldsymbol{v}, t)$, are all just constants $n_{0s}, \boldsymbol{q_{0s}}, T_{0s}$, and therefore the equivalent Maxwellian Equation (39) is also constant $M_{0s} = M[f_s(\boldsymbol{v}, t)] = M(n_{0s}, \boldsymbol{q_{0s}}, T_{0s})$.

By explicitly writing out the BGK model in Equation (F.1) and plugging in the above results for the constant velocity moments gives

$$\frac{\partial f_s(\boldsymbol{v}, t)}{\partial t} = -\frac{1}{\tau_{rel,s}} \left(f_s(\boldsymbol{v}, t) - M_{0s}\right)$$

where because of the assumed spatial homogeneity the distribution function f_s can only be a function of time and velocity, for which can rather trivially be solved by means of substitution to the new variable $\Delta f_s(\boldsymbol{v}, t) \equiv f_s(\boldsymbol{v}, t) - M_{0s}$ in the reduced kinetic equation, resulting in

$$f_s(\boldsymbol{v}, t) = f_s(\boldsymbol{v}, 0) \exp\left(-\tfrac{t}{\tau_{rel,s}}\right) + n_{0s} \left(\tfrac{m_s}{2\pi T_{0s}}\right)^{3/2} \exp\left(-\tfrac{m_s(\boldsymbol{v_s} - \boldsymbol{q_{0s}})^2}{2T_{0s}}\right) \left(1 - \exp\left(-\tfrac{t}{\tau_{rel,s}}\right)\right) \quad \text{(F.4)}$$

where M_{0s} has been written out explicitly. From Equation (F.4) it can be seen that as $t \to \infty$ the distribution function tends to $f_s \to M_{0s}$ regardless of the initial distribution $f_s(\boldsymbol{v}, 0)$ and that the distribution function looses its initial character exponentially with an e-folding time $\tau_{rel,s}$.

G Details of derivation for interspecies BGK model

G.1 Constraints to the interspecies BGK model

The derivations of this section closely mirrors the one in [117,123], without assuming the collision frequencies ν_{12}, ν_{21} to be identical to respect the appearance of mass ratio in Equation (18).
The general strategy for determining the "hybrid" velocity moments of the equivalent Maxwellian $M_{ss'}$ appearing in the interspecies BGK collision model is best discussed step-by-step. First the exchange of particles, momentum and energy from one species to the other are calculated and the corresponding conservation requirements are set up in Appendix G.1.1. Then the process of relaxation towards a common equilibrium is discussed in Appendix G.1.2. Then lastly the postulates for the "hybrid" velocity moments are introduced in Appendix G.1.3 and their corresponding solutions from the constraints are obtained.

G.1.1 Conservation requirements

The exchanges of particles, momentum and energy as a result of the interspecies collisions follow from taking velocity moments of Equation (42), where the velocity moments of $M_{ss'}$ are the same as for M_s but with all species labels s in Equation (F.3) replaced by ss' and the velocity moments of f_s remain defined by Equation (40). Since any elastic scattering of particles cannot change the total number of particles, the "hybrid" densities can immediately be determined by requiring the vanishing of the zeroth velocity moment of Equation (42), resulting in

$$\int C_{ss',BGK} \mathrm{d}^3 \boldsymbol{v_s} = -\nu_{ss'} \left(n_{ss} - n_{ss'}\right)$$

where in the case $s = s'$ the result that self-collision conserve particles is recovered. Thus the "hybrid" densities are simply the particle density of each species n_{ss} which reflects the fact that since $\nu_{ss'}$ are constant collision rates there is no preferential group of particles that only scatter among themselves but not with the other species. Consequently double species labels on the density are redundant and will be dropped.

Net exchanges of momentum and energy between two species are however possible such that $C_{ss'}$ is not required to conserve momentum and energy. The resulting flows of momentum and energy from species s' to s follow as

$$\begin{aligned}\int m_s \boldsymbol{v_s} C_{ss'} \mathrm{d}^3 \boldsymbol{v_s} &= -\nu_{ss'} n_s \left(\boldsymbol{q_{ss}} - \boldsymbol{q_{ss'}}\right) \\ \int \frac{m_s v_s^2}{2} C_{ss'} \mathrm{d}^3 \boldsymbol{v_s} &= -\nu_{ss'} n_s \left(\frac{3}{2}\left[T_{ss} - T_{ss'}\right] + \frac{m_s}{2}\left[\boldsymbol{q_{ss}} \cdot \boldsymbol{q_{ss}} - \boldsymbol{q_{ss'}} \cdot \boldsymbol{q_{ss'}}\right]\right)\end{aligned} \tag{G.1}$$

where again in the case $s = s'$ the momentum and energy conservation of self-collisions is recovered. Since the collisions between ions and electrons are however elastic, the total momentum and energy in the system have to be conserved such that the total momentum lost by one species has to be gained by the other, which puts constraints on the "hybrid" moments in terms of the known moments of the distribution of each species. Conservation of total momentum and energy of the two species system follows from summing Equation (G.1) over both species which leads to

$$\sum_{(s,s')=1,2} \int m_s \boldsymbol{v_s} C_{ss'} \mathrm{d}^3 \boldsymbol{v_s} = \boldsymbol{0} = -\nu_{12} n_1 m_1 \left(\boldsymbol{q_{11}} - \boldsymbol{q_{12}}\right) - \nu_{21} n_2 m_2 \left(\boldsymbol{q_{22}} - \boldsymbol{q_{21}}\right) \tag{G.2}$$

$$\begin{aligned}&\sum_{(s,s')=1,2} \int \frac{m_s v_s^2}{2} C_{ss'} \mathrm{d}^3 \boldsymbol{v_s} = 0 \\ &= \nu_{12} n_1 \left(\frac{3}{2}\left[T_{11} - T_{12}\right] + \frac{m_1}{2}\left[\boldsymbol{q_{11}^2} - \boldsymbol{q_{12}^2}\right]\right) - \nu_{21} n_2 \left(\frac{3}{2}\left[T_{22} - T_{21}\right] + \frac{m_2}{2}\left[\boldsymbol{q_{22}^2} - \boldsymbol{q_{21}^2}\right]\right)\end{aligned} \tag{G.3}$$

These conservation requirements on the total momentum and energy in the system however gives only four equations to determine the eight unknown "hybrid" moments, such that additional constraints are required to uniquely determine all "hybrid" moments. These additional constraints come from a relaxation problem, which is worked out below

G.1.2 Relaxation towards common equilibrium

The continuous exchange of momentum and energy between the electrons and ions will eventually lead to an equilibrium situation where both species have the same temperature and mean velocity , such that on a statistical level momentum- and energy exchange between ion and electrons will cease [124]. To focus on the essential details of this process (slow time change to the distribution function as a result of collisions) the same simplification of a homogeneous plasma void of electromagnetic fields as in Appendix F is considered. Using Equation (G.1) the evolution equations for particle, momentum and energy density Equation (F.2) follow as

$$\begin{aligned}\frac{\partial}{\partial t}\left(n_s\right) &= 0 \\ \frac{\partial}{\partial t}\left(n_s \boldsymbol{q_{ss}}\right) &= -\sum_{s'=(1,2)} \nu_{ss'} n_s \left(\boldsymbol{q_{ss}} - \boldsymbol{q_{ss'}}\right) \\ \frac{\partial}{\partial t}\left(\frac{3}{m_s} T_{ss} + n_s \boldsymbol{q_{ss}^2}\right) &= -\sum_{s'=(1,2)} \nu_{ss'} n_s \left(\frac{3}{m_s}\left[T_{ss} - T_{ss'}\right] + \left[\boldsymbol{q_{ss}^2} - \boldsymbol{q_{ss'}^2}\right]\right).\end{aligned} \tag{G.4}$$

These evolution equations can similarly be reduced by substituting each equation in the next to give pure evolution equations for just the density, mean flow and temperature of species s

$$\frac{\partial n_s}{\partial t} = 0 \quad \frac{\partial \boldsymbol{q_{ss}}}{\partial t} = -\nu_{ss'}\left(\boldsymbol{q_{ss}} - \boldsymbol{q_{ss'}}\right) \quad \frac{\partial T_{ss}}{\partial t} = -\nu_{ss'}\left([T_{ss} - T_{ss'}] - \frac{m_s}{3}\left[\boldsymbol{q_{ss}} - \boldsymbol{q_{ss'}}\right]^2\right) \tag{G.5}$$

such that the evolution of the observables of interest of the distribution function are obtained. The difficulty in solving Equation (G.5) is that the evolution equations for T_s and $\boldsymbol{q_s}$ are coupled because of reshuffling of energy between deterministic part related to $\boldsymbol{q_s}$ and thermal part related to random motion. The main role of interspecies collisions will be to equilibrate the electrons with the ions and vice versa by exchanging energy and momentum until a common temperature and mean flow velocity are reached

$$\lim_{t\to\infty} \boldsymbol{q_{11}} = \lim_{t\to\infty} \boldsymbol{q_{22}} \equiv \boldsymbol{q_\infty} \quad \lim_{t\to\infty} T_{11} = \lim_{t\to\infty} T_{22} \equiv T_\infty. \tag{G.6}$$

To be a true equilibrium, the microscopic dynamics of ions and electrons which will continue to exchange momentum and energy on a single-particle level should no longer affect the macroscopic statistical properties of the electrons and ions on the collective level, such that the equilibrium must be steady-state. Therefore $\frac{\partial \boldsymbol{q_\infty}}{\partial t} = \boldsymbol{0}$ and $\frac{\partial T_\infty}{\partial t} = 0$, i.e. the moments of the distribution function should over time relax.

Enforcing steady-state on Equation (G.5) then places constraints on the long time behaviour of the "hybrid" moments

$$\lim_{t\to\infty} \boldsymbol{q_{ss'}} \to \boldsymbol{q_\infty} \quad \lim_{t\to\infty} T_{ss'} \to T_\infty \tag{G.7}$$

which means that the equivalent Maxwellians describing the scattering of each species among themselves and with each other will relax to the same distribution

$$\lim_{t\to\infty} M_{ss}[f_s] = \lim_{t\to\infty} M_{ss'}[f_s, f_{s'}] = M_{s,\infty}$$

which makes sense as the statisical information of the distribution functions $f_s, f_{s'}$, which in turn determine the statistical properties of $M_{ss'}$, are identical in the relaxed state. Equation (G.6) and Equation (G.7) can be compactly written as

$$\lim_{t\to\infty} \boldsymbol{q_{ss'}} \to \boldsymbol{q_\infty} \quad \forall (s, s') \in \{1, 2\} \otimes \{1, 2\} \tag{G.8}$$

$$\lim_{t\to\infty} T_{ss'} \to T_\infty \quad \forall (s, s') \in \{1, 2\} \otimes \{1, 2\} \tag{G.9}$$

which only gives information on the limiting time behaviour of the "hybrid" moments such that these cannot be used in conjunction to Equations (G.2) and (G.3) which have to be satisfied instantaneously and all reduce to zero in this relaxed state.

G.1.3 Form of the "hybrid" moments

The workaround to this issue which allows to use the relaxation problem as additional constraints to the conservation requirements is to decompose the "hybrid" moments in terms of the moments of the distribution of the two species (see Footnote 32 for motivation of this decomposition)

$$\begin{aligned} \boldsymbol{q_{12}} &= \alpha_{11}\boldsymbol{q_{11}} + \alpha_{12}\boldsymbol{q_{22}} \\ \boldsymbol{q_{21}} &= \alpha_{21}\boldsymbol{q_{11}} + \alpha_{22}\boldsymbol{q_{22}} \end{aligned} \tag{G.10}$$

$$\begin{aligned} T_{12} &= \beta_{11}T_{11} + \beta_{12}T_{22} + A\boldsymbol{q_{11}^2} + B\boldsymbol{q_{11}}\cdot\boldsymbol{q_{22}} + C\boldsymbol{q_{22}^2} \\ T_{21} &= \beta_{21}T_{11} + \beta_{22}T_{22} + D\boldsymbol{q_{11}^2} + E\boldsymbol{q_{11}}\cdot\boldsymbol{q_{22}} + F\boldsymbol{q_{22}^2} \end{aligned} \tag{G.11}$$

Because all time dependence in Equations (G.10) and (G.11) is relinquished to the time dependence of the temperature and mean velocity of each species and the coefficients are constant, the conservation requirements and relexation constraints can be applied to determine what these coefficients should be to reflect the proper physics and not be some arbitrary model parameter.

G.1.3.1 Solution for the "hybrid" mean velocities

The four α_{ij} coefficients are determined from momentum conservation Equation (G.2) and the velocity relaxation Equation (G.8). The steady-state requirement of the relaxation problem directly places a constraint on the α_{ij}'s since

$$\lim_{t\to\infty} \boldsymbol{q_{12}} = (\alpha_{11} + \alpha_{12})\boldsymbol{q_\infty} \to \boldsymbol{q_\infty}$$

must hold for arbitrary $\boldsymbol{q_\infty}$. Taking the same limit for $\boldsymbol{q_{21}}$ gives two constraint equations

$$\alpha_{11} + \alpha_{12} = 1, \quad \alpha_{21} + \alpha_{22} = 1 \tag{G.12}$$

Meanwhile the momentum conservation requirement Equation (G.2) becomes

$$\left(n_1 m_1 \nu_{12}\left[1-\alpha_{11}\right] - n_2\nu_{21}m_2\alpha_{21}\right)\boldsymbol{q_{11}} + \left(n_2\nu_{21}m_2\left[1-\alpha_{22}\right] - n_1\nu_{12}m_1\alpha_{12}\right)\boldsymbol{q_{22}} = \boldsymbol{0}$$

which should be satisfied instantaneously for any $\boldsymbol{q_{11}}, \boldsymbol{q_{22}}$ such that the constant coefficients in front of the mean flow velocities should vanish. However, using the earlier determined constraint on the α_{ij}'s Equation (G.12) this only produces one unique additional constraint coupling the two "hybrid" velocities $\boldsymbol{q_{12}}, \boldsymbol{q_{21}}$

$$\frac{\alpha_{21}}{\alpha_{12}} = \frac{n_1 m_1 \nu_{12}}{n_2 m_2 \nu_{21}} \tag{G.13}$$

which leaves one of the α_{ij}'s as a free model parameter, which is taken to be α_{12}.

G.1.3.2 Solution for the "hybrid" temperatures

The four β_{ij} coefficients and six Roman coefficients A-F are determined from energy conservation Equation (G.3) and the temperature relaxation Equation (G.9). Proceeding similarly as above, the steady-state requirement of the relaxation problem gives

$$\lim_{t\to\infty} T_{12} = (\beta_{11} + \beta_{12})T_\infty + (A + B + C)\boldsymbol{q_\infty^2} \to T_\infty$$

which must hold for arbitrary $\boldsymbol{q_\infty}, T_\infty$. Taking the same limit for T_{21} yields the four constraint equations

$$\begin{array}{cc} \beta_{11} + \beta_{12} = 1 & \beta_{21} + \beta_{22} = 1 \\ A + B + C = 0 & D + E + F = 0 \end{array} . \tag{G.14}$$

Meanwhile the energy conservation requirement Equation (G.3) becomes

$$\begin{aligned} &\frac{3}{2}\left(n_1\nu_{12}\left[1-\beta_{11}\right] - n_2\nu_{21}\beta_{21}\right)T_{11} + \frac{1}{2}\left(m_1 n_1 \nu_{12}\left[1-\alpha_{11}^2\right] - m_2 n_2 \nu_{21}\alpha_{21}^2 - 3n_1\nu_{12}A - 3n_2\nu_{21}D\right)\boldsymbol{q_{11}^2} + \\ &\frac{3}{2}\left(n_2\nu_{21}\left[1-\beta_{22}\right] - n_1\nu_{12}\beta_{12}\right)T_{22} + \frac{1}{2}\left(m_2 n_2 \nu_{21}\left[1-\alpha_{22}^2\right] - m_1 n_1 \nu_{12}\alpha_{12}^2 - 3n_1\nu_{12}C - 3n_2\nu_{21}F\right)\boldsymbol{q_{22}^2} + \\ &-\frac{1}{2}\left(3n_1\nu_{12}B + 3n_2\nu_{21}E + 2m_1 n_1 \nu_{12}\alpha_{12}\alpha_{11} + 2m_2 n_2 \nu_{21}\alpha_{21}\alpha_{22}\right)\boldsymbol{q_{11}}\cdot\boldsymbol{q_{22}} = 0 \end{aligned}$$

which should be statisfied instantaneously for any $T_{11}, T_{22}, \boldsymbol{q_{11}}, \boldsymbol{q_{22}}$ such the coefficients in front of every temperature and combination of flow velocity must vanish, yielding five additional constraint equations, which can be solved independently as Equation (G.14) decouples the β_{ij}'s from A-F. The constraint equations for the β_{ij}'s are isomorphic to the constraints for the α_{ij}'s such that only on additional constraint on the β_{ij}'s follows from energy conservation

$$\frac{\beta_{21}}{\beta_{12}} = \frac{n_1\nu_{12}}{n_2\nu_{21}} \tag{G.15}$$

which leaves β_{12} as a free model parameter.

The three remaining constraint on the Roman coefficents A-F are however coupled to the constraints on the α_{ij}'s such that these are not independent. Substituting the constraints on the α_{ij}'s then gives constraints equations on A-F in terms of the free parameter α_{12}

$$\begin{aligned} 3\left(n_1\nu_{12}A + n_2\nu_{21}D\right) =& \alpha_{12}m_1n_1\nu_{12}\left(2 - \alpha_{12}\left[1 + \frac{n_1m_1\nu_{12}}{n_2m_2\nu_{21}}\right]\right) \\ 3\left(n_1\nu_{12}C + n_2\nu_{21}F\right) =& \alpha_{12}m_1n_1\nu_{12}\left(2 - \alpha_{12}\left[1 + \frac{n_1m_1\nu_{12}}{n_2m_2\nu_{21}}\right]\right) \\ 3\left(n_1\nu_{12}B + n_2\nu_{21}E\right) =& -2\alpha_{12}m_1n_1\nu_{12}\left(2 - \alpha_{12}\left[1 + \frac{n_1m_1\nu_{12}}{n_2m_2\nu_{21}}\right]\right) \end{aligned} \tag{G.16}$$

which can be reduced to the "eyeballing solution"

$$A = C = -\frac{B}{2}, \quad D = F = -\frac{E}{2}$$

which is also a consistent solution to the relation constraint Equation (G.14), as each constraint in Equation (G.16) has the same right-hand side such that they are degenerate. This means that out of the six Roman coefficients A-F only two are unique and Equation (G.16) can be used to eliminate one of them which yields a third free model parameter

$$\frac{D}{A} = \frac{\alpha_{12}}{A}\frac{m_1n_1\nu_{12}}{3n_2\nu_{21}}\left(2 - \alpha_{12}\left[1 + \frac{n_1m_1\nu_{12}}{n_2m_2\nu_{21}}\right]\right) - \frac{n_1\nu_{21}}{n_2\nu_{21}} \tag{G.17}$$

which is chosen to be coefficient A.

G.2 Coupling of interspecies BGK model to exchange model

The fact that the BGK collision rates $\nu_{ss'}$ are free model parameters can cleverly be used to determine some of the remaining undetermined coefficients for the "hybrid" velocity moments Equations (G.10) and (G.11). This is because the undetermined parameters essentially are given the status of a free model parameter as well, but by substituting the results for the $\alpha_{ij}, \beta_{ij}, A-F$ from Appendix G.1 into Equation (G.1) it follows that the resulting exchange of momentum and energy from e.g. species 2 to 1 are given by

$$\int m_1\boldsymbol{v_1}C_{12}\mathrm{d}^3\boldsymbol{v_1} = -\nu_{12}n_1m_1\left(\boldsymbol{q_{11}} - \boldsymbol{q_{12}}\right) = -n_1m_1\alpha_{12}\nu_{12}\left(\boldsymbol{q_{11}} - \boldsymbol{q_{22}}\right) \tag{G.18}$$

$$\begin{aligned} \int \frac{m_1v_1^2}{2}C_{12}\mathrm{d}^3\boldsymbol{v_1} =& -\nu_{12}n_1\left(\frac{3}{2}\left[T_{11} - T_{12}\right] + \frac{m_1}{2}\left[\boldsymbol{q_{11}^2} - \boldsymbol{q_{12}^2}\right]\right) \\ =& -n_1\nu_{12}\beta_{12}\left[T_{11} - T_{22}\right] + n_1\nu_{12}\left(\frac{m_1}{2}\left[\boldsymbol{q_{11}} - \boldsymbol{q_{22}}\right]^2\right) \times \left(\frac{3A}{m_1} + \alpha_{12}^2\right) - n_1m_1\nu_{12}\alpha_{12}\left(\boldsymbol{q_{11}} - \boldsymbol{q_{22}}\right)\cdot\boldsymbol{q_{11}} \end{aligned} \tag{G.19}$$

Equation (G.18) shows that the actual momentum transform is determined by $\alpha_{12} \times \nu_{12}$ such that it is impossible for both α_{12}, ν_{12} to take on arbitrary values as the actual rate of momentum transfer between ions and electrons is determined by the details of their Coulomb interaction. Similarly Equation (G.19) shows that the energy flow has three channels of energy flow: transfer of thermal energy between the species, changes in the component of the relative velocity that species 1 carry and direct energy changes as a consequence from momentum transfer between the species. These channels have an energy flow propotional to the products $\nu_{12} \times \beta_{12}, \nu_{12} \times A, \nu_{12} \times \alpha_{12}$, whereas the actual rate of energy transfer between ions and electrons is also determined by the details of their Coulomb interaction. Therefore the model parameters $\alpha_{12}, \beta_{12}, A$ cannot truly be free as they will have to be adapted to the choice of ν_{12} to give the proper momentum and energy transfers.

G.2.1 Net exchange model for Coulomb collisions

The physical transfer of momentum and energy from the ions to the electrons due to collisions are semi-phenomonologically modelled as [3]

$$\frac{\mathrm{d}}{\mathrm{d}t}\left(n_e m_e \boldsymbol{q_e}\right) = -\, m_e n_e \overline{\nu_{ei}^m}\left(\boldsymbol{q_e} - \boldsymbol{q_i}\right) \tag{G.20}$$

$$\frac{\mathrm{d}}{\mathrm{d}t}\left(U_e\right) = -\, \overline{\nu_{ei}^{en}}\left(U_e - U_i\right) \tag{G.21}$$

where $U_s = \frac{3}{2} n_s T_s + \frac{1}{2} n_s m_s \boldsymbol{q_s}^2$ is the total energy density of species s and $\overline{\nu_{ei}^m}, \overline{\nu_{ei}^{en}}$ denote the effective exchange frequency of momentum and energy respectively. In fusion plasmas the mean flow is typically due to a toroidal rotation of the plasma that is externally induced to increase the macroscopic plasma stability [219]. In tokamaks this rotation speed can be a fraction of the ion thermal speed, but in stellarators it is typically inhibited [43]. Consequently the energy density is dominated by its thermal part such that $U_j \approx \frac{3}{2} n_j T_j$, which makes the coefficients A-F redundant. It might be objected that this would violate energy conservation since according to Equation (G.17) $A = 0$ does not imply that $D = 0$ as well, however in view of the inevitable linearisation of the BGK model which follows , the quadratic contributions in $\boldsymbol{q}$ to the "hybrid" temperature would be neglected anyway since these are $\mathcal{O}(\delta^2)$ [123]. Furthermore the fact that rotational velocities do not exceed only a fraction of the slowest ion thermal velocity is completely consistent with the linearisation of $\boldsymbol{q}[f]/v_{RMS} \approx \mathbf{0}$ from Section 2.5. By changing the species labels $e \to i,\ i \to e$ in Equations (G.20) and (G.21) completely analogous equations for the transfer of momentum and energy from electrons to ions are obtained, and conservation of the combined momentum and energy of electrons and ions fixes the relation between the exchange frequencies as

$$\begin{aligned} \frac{\mathrm{d}}{\mathrm{d}t}\left(n_e m_e \boldsymbol{q_e} + n_i m_i \boldsymbol{q_i}\right) = 0 \Rightarrow m_e \overline{\nu_{ei}^m} = m_i \overline{\nu_{ie}^m} \\ \frac{\mathrm{d}}{\mathrm{d}t}\left(U_e + U_i\right) = 0 \to \overline{\nu_{ei}^{en}} = \overline{\nu_{ie}^{en}} \end{aligned} \tag{G.22}$$

where quasi-neutrality $n_e \approx n_i$ has been used.

G.2.2 Matching of BGK to physical net exchange model

To match the BGK model to the exchange model a convention about the species labels will have to be adopted, and therefore the electrons are taken as species 1 and the ions as species 2. Comparing Equation (G.18) to Equation (G.20) then gives the undetermined α_{12} coefficient as

$$\alpha_{12} = \frac{\overline{\nu_{ei}^m}}{\nu_{12}}. \tag{G.23}$$

Similarly comparing the momentum flow from electrons to ions to the exchange model would give a match for$\alpha_{21} = \overline{\nu_{ie}^m}/\nu_{21}$ such that ratio of the two α_{ij} coefficients follows from Equation (G.22) as

$$\frac{\alpha_{21}}{\alpha_{12}} = \frac{\overline{\nu_{ie}^m}\nu_{12}}{\overline{\nu_{ei}^m}\nu_{21}} = \frac{m_e \nu_{12}}{m_i \nu_{21}}$$

which is consistent with the constraint Equation (G.13) under the same quasi-neutrality assumption.

For a consistent comparison of the energy exchange model Equation (G.21) with the energy flow from the BGK model Equation (G.19), the quadratic terms in the flow velocity will have to be

neglected in the latter, which would happen in linearisation anyway. Thus by retaining only the the first heat transfer term in Equation (G.19) the free parameter β_{12} is fixed as

$$\beta_{12} = \frac{\overline{\nu_{ei}^{en}}}{\nu_{12}} \tag{G.24}$$

and a similar analysis for the energy flow from electrons to ions gives a match for $\beta_{21} = \frac{\overline{\nu_{ie}^{en}}}{\nu_{21}}$ such that the ratio of the two β_{ij} coefficients follows from Equation (G.22) as

$$\frac{\beta_{21}}{\beta_{12}} = \frac{\overline{\nu_{ie}^{en}}\nu_{12}}{\overline{\nu_{ei}^{en}}\nu_{21}} = \frac{\nu_{12}}{\nu_{21}}$$

which is consistent with the constraint Equation (G.15) under the same quasi-neutrality assumption.

This method seems dubious at first as Equations (G.23) and (G.24) now express a previously free model parameter in the ratio between a seemingly phenomenological exchange rate and an equally free model parameter. The exchange model is however only semi-phenomological as the exchange frequencies can be determined from first principles, which involves averaging over the changes in velocity of individual test-electrons due to collisions with ions and is the natural extension to how the test particle collision frequencies Equation (16) are determined. The details of this calculation is rather lengthy and therefore deferred to Appendix H, which results in a coupling of the exchange frequencies to the rigorously physically interpretable 90° scattering frequency of electrons on ions as

$$\overline{\nu_{ei}^{en}} = 2\frac{m_e}{m_i}\overline{\nu_{ei}^{m}} = 2\frac{m_e}{m_i}\nu_{90^\circ}^{ei} \tag{G.25}$$

which again shows that energy transfer is slower than momentum transfer by the mass ratio. Furthermore Equation (G.25) allows to express α_{12} in terms of β_{12} as

$$\beta_{12} = 2\frac{m_e}{m_i}\alpha_{12}$$

which was not previously possible from the constraints on the interspecies BGK model. Within the framework of the linearisation to come this eliminates another coefficient of the "hybrid" moments for the interspecies BGK model such that all "hybrid moments" may be expressed in terms of β_{12}, which is in turn fixed through Equation (G.24) by any choice for the collision rate ν_{12} which is the conventional free parameter of the single-species BGK model. Consequently when linearised around $\boldsymbol{q_s}/v_{Ts} \ll 1$ the two-species BGK model is completely determined in terms of the four arbitrary collision rates $\nu_{ss'}$ only.

G.3 Linearisation of the interspecies BGK model

With the "hybrid" velocity moments for the equivalent Maxwellian $M_{ss'}$ of the scattered particles finally determined in terms of the known velocity moments of the ion and electron distribution functions the model can be subsequently linearised for its intended application of performing linear stability analysis on the GKE Equation (25).

G.3.1 Linearisation of the interspecies collision operator

Using the decomposition Equations (G.10) and (G.11), the solutions for the coefficients given in Appendices G.1 and G.2 and the linearised solution for the functionals Equation (40) (corresponding to linearised velocity moments of f_s) of each species determined in Section 2.5.1, the

"hybrid" moments follow as

$$
\begin{aligned}
n_{12} =& n_e = n_{0e}\left(1+\frac{e\phi}{T_e}\right) & n_{21} =& n_i = n_{0i}\left(1-\frac{e\phi}{T_i}\right)\\
\boldsymbol{q_{12}} \approx& \mathbf{0} & \boldsymbol{q_{21}} \approx& \mathbf{0}\\
T_{12} \approx& \beta_{12}T_i + (1-\beta_{12})T_e & T_{21} \approx& \beta_{12}\frac{\nu_{12}}{\nu_{21}}T_e + \left(1-\beta_{12}\frac{\nu_{12}}{\nu_{21}}\right)T_i
\end{aligned}
$$

where species 1 is taken to be the electrons and species 2 is taken to be the ions. The issue with the coupled arbitrariness of β_{12} to the free choice of the collision rate ν_{12} can be closed by introducing the temperature ratio $\tau = T_{0i}/T_{0e}$ such that the "hybrid" temperatures for scattered electrons can be written in terms of the electron temperature, and vice versa for the ions

$$
T_{12} = T_e\left(1+\beta_{12}\left(\tau-1\right)\right) \quad T_{21} = T_i\left(1+\beta_{21}\frac{1-\tau}{\tau}\right).
$$

Under typical fusion reactor conditions the temperature ratio satisfies $\tau \approx 1$, see Figure 1b, such that the "hybrid" Maxwellians can be expanded around $\tau = 1$ such that the linearised BGK operator for e.g. electron-ion collisions becomes

$$
C_{ei,BGK} = -\nu_{12}g_e + \nu_{12}\beta_{12}\left(\tau-1\right)F_{Me}\left(1+\frac{e\phi}{T_{e0}}\right)\left[\frac{m_e v_e^2}{2T_e}-\frac{3}{2}\right] \equiv C^{\delta}_{ei,BGK} + C^{0}_{ei,BGK} \quad \text{(G.26)}
$$

which consists of a fluctuating part $C^{\delta}_{ei,BGK}$ that is linear in the perturbations g_s, ϕ and an equilibrium $C^{0}_{ei,BGK}$ part that only contains the Maxwellian F_{Me}. As this part is unrelated to the fluctuations that are intended to be studied with Equation (G.26) its role is first investigated in detail below by taking the equilibrium limit of $g_e, \phi \to 0$.

G.3.2 Understanding the equilibrium contribution

The effect of the leading order equilibrium part of the linearised BGK operator for electron-ion collisions

$$
C^{0}_{ei,BGK} = \nu_{12}\beta_{12}\left(\tau-1\right)F_{Me}\left(\frac{m_e v_e^2}{2T_e}-\frac{3}{2}\right). \quad \text{(G.27)}
$$

becomes clear by taking its moments velocity moments. The zeroth velocity moment follows as

$$
\begin{aligned}
\int C^{0}_{ei,BGK}\mathrm{d}^3\boldsymbol{v_e} &= \nu_{12}\beta_{12}\left(\tau-1\right)n_{e0}\left(\frac{m_e}{2\pi T_{e0}}\right)^{3/2}\int \exp\left(-\frac{m_e v_e^2}{2T_{e0}}\right)\left(\frac{m_e v_e^2}{2T_{e0}}-\frac{3}{2}\right)\mathrm{d}^3\boldsymbol{v_e}\\
&= \nu_{12}\beta_{12}\left(\tau-1\right)n_{e0}\frac{2}{\sqrt{\pi}}\int_0^{\infty}\sqrt{\mu}\exp(-\mu)\left(\mu-\frac{3}{2}\right)\mathrm{d}\mu\\
&= \nu_{12}\beta_{12}\left(\tau-1\right)n_{e0}\frac{2}{\sqrt{\pi}}\left(\Gamma(5/2)-\frac{3}{2}\Gamma(3/2)\right) = 0
\end{aligned}
$$

where spherical velocity coordinates are used to exploit the isotropy of the Maxwellian, $\mu = m_e v_e^2/2T_e$ has been introduced to map the remaining integral onto gamma functions, and the last step follows from the recursive property of the gamma function $\Gamma(n+1) = n\Gamma(n)$. As the zeroth velocity moment vanishes, Equation (G.27) is particle conserving.

The first velocity moment of Equation (G.27) $\int C^{0}_{ei} m_e \boldsymbol{v_e}\mathrm{d}^3\boldsymbol{v_e} = \mathbf{0}$ as the integrand is anti-symmetric, such that in equilibrium there is no momentum exchange with the ions. As the ions are also taken to be given by a Maxwellian distribution without mean velocity, this is consistent with the exchange model Equation (G.20). This could be expected as the Maxwellian Equation (23) is taken to have zero mean velocity for both ions and electrons, such that the

electrons and ion do not cary any net macroscopic momentum and this neatly shows that there is no spurious macroscopic momentum generated for the electrons (and hence also not for ions to conserve total momentum).

Meanwhile the second velocity moment of Equation (G.27) is given by

$$\begin{aligned}\int C^0_{ei}\frac{m_e v_e^2}{2}\mathrm{d}^3\boldsymbol{v_e} &= \nu_{12}\beta_{12}\left(\tau-1\right)n_{e0}\frac{m_e}{2}\left(\frac{m_e}{2\pi T_{e0}}\right)^{3/2}\int\exp\!\left(-\frac{m_e v_e^2}{2T_{e0}}\right)\left(\frac{m_e v_e^2}{2T_{e0}}-\frac{3}{2}\right)v_e^2\mathrm{d}^3\boldsymbol{v_e}\\ &= \nu_{12}\beta_{12}\left(\tau-1\right)n_{e0}\frac{2T_{e0}}{\sqrt{\pi}}\int_0^\infty\mu^{3/2}\exp(-\mu)\left(\mu-\frac{3}{2}\right)\mathrm{d}\mu\\ &= \nu_{12}\beta_{12}\left(\tau-1\right)n_e\frac{2T}{\sqrt{\pi}}\left(\underbrace{\Gamma(7/2)}_{=15\sqrt{\pi}/8}-\frac{3}{2}\underbrace{\Gamma(5/2)}_{=3\sqrt{\pi}/4}\right)\\ &= \nu_{12}\beta_{12}\left(\tau-1\right)n_e\frac{3T_{e0}}{2}\end{aligned}$$

upon using Equation (G.24) and $\tau = T_{i0}/T_{e0}$ it follows that the energy exchange resulting from Equation (G.27) is exactly the energy exchange model Equation (G.21). The fact that the BGK model is consistent with the exchange model should not be completely surprising as the BGK model is fitted to match the exchange model and the exchange frequencies are rigorously calculated by averaging the energy and momentum exchanges over the Maxwellian distribution.

Furthermore, if the electron Maxwellian is given by Equation (23), repeated here for convenience

$$F_{Me} = n_{0e}(\psi)\left(\frac{m_e}{2\pi T_{0e}(\psi,t)}\right)^{3/2}\exp\!\left(-\frac{m_e v_e^2}{2T_{0e}(\psi,t)}\right)$$

then it follows that in equilibrium

$$\frac{\mathrm{d}F_{Me}}{\mathrm{d}t} = n_{e0}\left(\frac{m_e}{2\pi T_{0e}(\psi,t)}\right)^{3/2}\exp\!\left(-\frac{m_e v_e^2}{2T_{0e}(\psi,t)}\right)\left(\frac{m_e v^2}{2T_{0e}}-\frac{3}{2}\right)\frac{\mathrm{d}T_{e0}}{\mathrm{d}t}/T_{e0} \tag{G.28}$$

where for flux functions $P(\psi,t)$ the convective part of the total time derivative $\frac{\mathrm{d}P}{\mathrm{d}t} = \frac{\partial P}{\partial t} + \dot{\psi}\frac{\partial P}{\partial \psi}$ will vanish if averaged over some suitable intermediate time interval since to have proper particle confinement the magnetic geometry is constructed to make the average radial drifts vanish[74]. If the energy exchange model Equation (G.21) is substituted for $\frac{\mathrm{d}T_{e0}}{\mathrm{d}t}$, where for the equilibrium Maxwellian the energy density is exactly $U_j = \frac{3}{2}n_{0j}T_{0j}$ because there is no mean flow, Equation (G.28) becomes

$$\frac{\mathrm{d}F_{Me}}{\mathrm{d}t} = -F_{Me}\overline{\nu^{en}_{ei}}\left(\frac{m_e v^2}{2T_{0e}}-\frac{3}{2}\right)\left(T_{e0}-T_{i0}\right)/T_{e0} = C^0_{ei,BGK} \tag{G.29}$$

where the last step follows by substitution of Equation (G.24) and definition $\tau = T_{i0}/T_{e0}$. That is Equation (G.29) is essentially the kinetic equation[75] for the equilibrium Maxwellian, and the purpose of the equilibrium part of the BGK operator Equation (G.27) is to slowly equilibrate the electron temperature to the ion temperature over time as it will completely vanish when $\tau = 1$, which was alluded to in Section 2.3 when the Maxwellian Equation (23) was introduced.

[74] Rather in the context of Appendix C.2 this radial drift would lead to a small deviation from the Maxwellian resulting in neoclassical transport, but this has been omitted throughout the thesis.

[75] Not in the sense of a direct comparison with Equation (10) which is valid in a general situation, but rather in the sense of Equation (C.2) taking into account the previous comment about omitting the neoclassical correction or averaging over a suitable intermediate time window.

G.3.3 Simplifying the fluctuating contribution

As the equilibrium can be considered as "frozen" on the timescale of the perturbations, for the purpose of linear stability the contribution from $C^0_{ei,BGK}$ to Equation (G.26) can be neglected such that the BGK model is completely determined by its fluctuating part $C^\delta_{ei,BGK}$. There is however an inbalance between these terms as both $g_s/F_{Ms} \sim e\phi/T_{e0} \sim \delta \ll 1$ but the second term is still multiplied by $\tau - 1$ which tends to zero when $\tau \approx 1$ and consequently will be significantly smaller. Therefore combining the above statements then leads to the total linearised BGK operator for electron-ion collisions as

$$C_{ei,BGK} \approx -\nu_{12} g_e + \nu_{12}\beta_{12}\left(\tau - 1\right) F_{Me} \frac{e\phi}{T_{e0}} \left[\frac{m_e v_e^2}{2T_e} - \frac{3}{2}\right] \approx -\nu_{12} g_e$$

which eliminates β_{12} completely from the collision operator, such that it is merely described by its free parameter collision rate ν_{12}. This analysis has focused on the electron-ion term since it contains the somewhat annoying β_{12} parameter which has to be determined from the choice of ν_{12} and the energy exchange frequency $\overline{\nu^{en}_{ei}}$, but is straightforward to show that for the ion-electron collisions effectively the labels $e \to i, 12 \to 21$ and $\tau \to 1/\tau$ are changed in all formulas above such that analogously the lowest order contribution to the linearised BGK operator for ion-electrons collisions is just $C_{ie,BGK} \approx -\nu_{21} g_i$.

H Calculation of the macroscopic exchange frequencies

In the derivations that follow, the integral strategy from Chapter 9.7 of [3] is closely followed, but has been reformulated in terms of the theory of binary collisions from Appendix B and extended to the more general case where the mean velocities are not aligned with one of the coordinate axes.

H.1 The momentum exchange frequency

The net change in the macroscopic momentum density of electrons due to binary collisions with ions is simply a suitable average of the microscopic momentum gained by a test-electron from collisions with the population of target-ions over the electron distribution function

$$\begin{aligned} \frac{\mathrm{d}}{\mathrm{d}t}\left(n_e m_e \boldsymbol{q_e}\right) &= \int \Bigg\langle \underbrace{\frac{m_e\left(\boldsymbol{v_e} + \boldsymbol{\Delta v_e}\right) - m_e \boldsymbol{v_e}}{\Delta t}}_{=\frac{\Delta(m_e \boldsymbol{v_e})}{\Delta t}} \Bigg\rangle^{ei} f_e \mathrm{d}^3\boldsymbol{v_e} \\ &= -\frac{L^{ei}}{4\pi}\left(1 + \frac{m_e}{m_i}\right) m_e \iint \frac{\boldsymbol{u}}{u^3} f_e f_i \mathrm{d}^3\boldsymbol{v_e} \mathrm{d}^3\boldsymbol{v_i} \end{aligned} \tag{H.1}$$

where Equation (B.5) has been used for the statistical change in the velocity of a test-electron due to collisions with all the ions. Calculating Equation (H.1) in general for arbitrary distribution is not feasible, therefore the ions and electrons are assumed to have a shifted Maxwellian distribution to allow for a macroscopic flow of ions and electrons such that there is a non-zero macroscopic momentum. In line with the observation that the toroidal plasma rotation is typically only a fraction of the ion thermal velocity at most the mean velocities are ordered as $\|\boldsymbol{q_s}\|/v_{Ts} \ll 1$ for both species. Additionally in accordance with the typical reactor conditions the temperature difference between ion and electrons is assumed to be small such that

$$\frac{\left(T_e - T_i\right)}{\left(T_e + T_i\right)/2} \equiv \frac{\Delta T}{T_0} \ll 1$$

where T_0 is a measure for the average temperature in the plasma and the electron and ion temperature follow from this definition as $T_e = T_0 + \Delta T/2$ and $T_i = T_0 - \Delta T/2$. With these

assumption the distribution function for ions and electrons can be expanded to first order in $\boldsymbol{q_s}/v_{Ts}, \Delta T/T_0$ resulting in

$$f_s(\boldsymbol{v_s}) \approx n_s \left(\frac{m_s}{2\pi T_0}\right)^{3/2} \exp\left(-\frac{m_s v_s^2}{2T_0}\right) \times \left(1 \pm \frac{\Delta T}{2T_0}\left[\frac{m_s v_s^2}{2T_0} - \frac{3}{2}\right] + \frac{m_s \boldsymbol{v_s}\cdot\boldsymbol{q_s}}{T_0}\right)$$

where the the plus sign holds for electrons and the minus sign for ions.

Because the integration in Equation (H.1) involves the relative velocity $\boldsymbol{u}$ and the individual velocities of both species it is best handled with a change of coordinates that reflects the form of the integrand. This is facilitated by the coordinate transform $(\boldsymbol{v_e}, \boldsymbol{v_i}) \to (\boldsymbol{V}, \boldsymbol{u})$ determined by

$$\begin{aligned} \boldsymbol{v_e} &= \boldsymbol{V} + \frac{m_i}{m_e+m_i}\boldsymbol{u} & \qquad \boldsymbol{V} &= \frac{m_e\boldsymbol{v_e} + m_i\boldsymbol{v_i}}{m_e+m_i} \\ \boldsymbol{v_i} &= \boldsymbol{V} - \frac{m_e}{m_e+m_i}\boldsymbol{u} & \qquad \boldsymbol{u} &= \boldsymbol{v_e} - \boldsymbol{v_i} \end{aligned} \tag{H.2}$$

where $\boldsymbol{V}$ is the centre of mass velocity and $\boldsymbol{u}$ is the relative velocity. To correctly transform the velocity volume element $\mathrm{d}^3\boldsymbol{v_e}\mathrm{d}^3\boldsymbol{v_e} \to \left|\det \underline{\underline{J}}\right| \mathrm{d}^3\boldsymbol{u}\mathrm{d}^3\boldsymbol{V}$ the determinant of the 6×6 Jacobian matrix $\underline{\underline{J}}$ is required. Fortunately this can be done in an elegant way by realising there is no mixing of components in the coordinate transformation Equation (H.2), consequently the Jacobian matrix $\underline{\underline{J}}$ will be very sparse and can be arranged to have a block-diagonal structure of three 2×2 matrices for each direction and the determinant is simply $\det \underline{\underline{J}} = J_x J_y J_z$ where

$$J_k = \det \frac{\partial(v_{e,k}, v_{i,k})}{\partial(V_k, u_k)} = \det \begin{bmatrix} 1 & \frac{m_i}{m_e+m_i} \\ 1 & -\frac{m_e}{m_e+m_i} \end{bmatrix} = -1 \quad k = x, y, z$$

is identical for each 2×2 sub-matrix due to absence of component mixing and is a simple multiplicative factor because the transforms Equation (H.2) are linear. As a last prepratory before calculating the integral the product of distribution functions $f_e f_i$ is also written as a function of $\boldsymbol{u}, \boldsymbol{V}$

$$\begin{aligned} f_e f_i \approx & n_e n_i \left(\frac{m_e m_i}{(2\pi T_0)^2}\right)^{3/2} \exp\left(-\frac{m_e v_e^2 + m_i v_i^2}{2T_0}\right)\left(1 + \frac{m_e\boldsymbol{v_e}\cdot\boldsymbol{q_e} + m_i\boldsymbol{v_i}\cdot\boldsymbol{q_i}}{T_0} + \frac{m_e v_e^2 - m_i v_i^2}{2T_0}\frac{\Delta T}{2T_0}\right) \\ = & n_e n_i \left(\frac{m_e m_i}{(2\pi T_0)^2}\right)^{3/2} \exp\left(-\frac{(m_i+m_e)\,V^2}{2T_0}\right)\exp\left(-\frac{m_\star u^2}{2T_0}\right)\left(1 + \frac{\boldsymbol{V}\cdot(m_e\boldsymbol{q_e} + m_i\boldsymbol{q_i})}{T_0} + \right. \\ & \left. \frac{m_\star \boldsymbol{u}\cdot(\boldsymbol{q_e} - \boldsymbol{q_i})}{T_0} + \frac{\Delta T}{2T_0}\left[\frac{(m_e-m_i)V^2}{2T_0} + \frac{4m_\star \boldsymbol{V}\cdot\boldsymbol{u}}{2T_0} + \frac{u^2 m_\star \frac{m_i-m_e}{m_i+m_e}}{2T_0}\right]\right) \\ \equiv & n_e n_i \left(\frac{m_e m_i}{(2\pi T_0)^2}\right)^{3/2} \exp\left(-\frac{(m_i+m_e)\,V^2}{2T_0}\right)\exp\left(-\frac{m_\star u^2}{2T_0}\right) F(\boldsymbol{V}, \boldsymbol{u}) \end{aligned} \tag{H.3}$$

where only terms to first order in $\boldsymbol{q_s}/v_{Ts}, \delta T/T_0$ are retained and the reduced mass $m_\star = m_i m_e/(m_i+m_e)$ has been introduced.

The resulting integral $\iint \frac{\boldsymbol{u}}{u^3} f_e f_i \mathrm{d}^3\boldsymbol{u}\mathrm{d}^3\boldsymbol{V}$ can now easily be carried out by substituting Equation (H.3) and realising that the prefactor $\frac{\boldsymbol{u}}{u^3}\exp\left(-\frac{m_\star u^2}{2T_0}\right)$ is anti-symmetric in $\boldsymbol{u}$, such that the only non-vanishing contribution to the integral over $\mathrm{d}^3\boldsymbol{u}$ comes from the expansion terms in $F(\boldsymbol{u}, \boldsymbol{V})$ that are also anti-symmetric in $\boldsymbol{u}$. Similarly the prefactor $\exp\left(-\frac{(m_i+m_e)V^2}{2T_0}\right)$ is symmetric in $\boldsymbol{V}$, such that the only non-vanishing contribution to the integral over $\mathrm{d}^3\boldsymbol{V}$ comes from the expansion terms in $F(\boldsymbol{u}, \boldsymbol{V})$ that are also symmetric in $\boldsymbol{V}$. There is only one term in the

expansion $F(\boldsymbol{u},\boldsymbol{V})$ which satisfies both symmetry requirements, such that the integral simplifies to

$$\iint \frac{\boldsymbol{u}}{u^3} f_e f_i \mathrm{d}^3\boldsymbol{u}\mathrm{d}^3\boldsymbol{V} = n_e n_i \left(\frac{m_e m_i}{(2\pi T_0)^2}\right)^{3/2} \iint \frac{\boldsymbol{u}}{u^3} \exp\!\left(-\frac{(m_i+m_e)\,V^2}{2T_0}\right) \exp\!\left(-\frac{m_\star u^2}{2T_0}\right) \frac{m_\star \boldsymbol{u}\cdot(\boldsymbol{q_e}-\boldsymbol{q_i})}{T_0} \mathrm{d}^3\boldsymbol{u}\mathrm{d}^3\boldsymbol{V}$$

which factors itself into a $\boldsymbol{V}$ dependent integral and a $\boldsymbol{u}$ dependent integral that can be evaluated separately in spherical velocity coordinates

$$\mathrm{d}^3\boldsymbol{V} \to V^2 \sin\Theta\,\mathrm{d}V\,\mathrm{d}\Theta\,\mathrm{d}\Phi \qquad \mathrm{d}^3\boldsymbol{u} \to u^2 \sin\theta\,\mathrm{d}u\,\mathrm{d}\theta\,\mathrm{d}\phi$$

The integral over $\mathrm{d}^3\boldsymbol{V}$ is the most straightforward

$$\begin{aligned}\int_0^{2\pi}\int_0^{\pi}\int_0^{\infty} \exp\!\left(-\frac{(m_i+m_e)\,V^2}{2T_0}\right) V^2\sin\Theta\,\mathrm{d}V\,\mathrm{d}\Theta\,\mathrm{d}\Phi &= 4\pi\left(\frac{2T_0}{m_e+m_i}\right)^{3/2}\int_0^{\infty} W^2\exp\!\left(-W^2\right)\mathrm{d}W \\ &= 4\pi\left(\frac{2T_0}{m_e+m_i}\right)^{3/2}\left(\frac{1}{2}\underbrace{\int_0^{\infty}\sqrt{\xi}\exp(-\xi)}_{=\Gamma(3/2)=\sqrt{\pi}/2}\right) = \left(\frac{2\pi T_0}{m_e+m_i}\right)^{3/2}\end{aligned}$$

where in the first step the information over angle is performed and a change of variables $W = \sqrt{(m_e+m_i)/2T_0}V$ has been performed, and in the second step another change of variables $\xi = W^2$ is performed to map the integral onto a standard Gamma function.

The integral over $\mathrm{d}^3\boldsymbol{u}$ requires some more effort to work out since it also depends on the direction of $\boldsymbol{u}$, which can be accounted for by expanding $\boldsymbol{u}$ and $\boldsymbol{q_{e,i}}$ in their Cartesian components

$$\int_0^{\infty}\tfrac{m_\star u}{T_0}\exp\!\left(-\tfrac{m_\star u^2}{2T_0}\right)\mathrm{d}u \times \int_0^{2\pi}\int_0^{\pi}\sin\theta\,(\sin\theta\cos\phi\boldsymbol{e_x}+\sin\theta\sin\phi\boldsymbol{e_y}+\cos\theta\boldsymbol{e_z})\times([q_{e,x}-q_{i,x}]\sin\theta\cos\phi+[q_{e,y}-q_{i,y}]\sin\theta\sin\phi+[q_{e,z}-q_{i,z}]\cos\theta)\,\mathrm{d}\theta\,\mathrm{d}\phi$$

which can be straightforward integrated over ϕ to cancel out the majority of the terms

$$\begin{aligned}&= \underbrace{\int_0^{\infty}\exp(\eta)\,\mathrm{d}\eta}_{=\Gamma(1)=1} \times\pi\int_0^{\pi}\sin\theta\left([q_{e,x}-q_{i,x}]\,\boldsymbol{e_x}\sin^2\theta+[q_{e,y}-q_{i,y}]\,\boldsymbol{e_y}\sin^2\theta+[q_{e,z}-q_{i,z}]\,\boldsymbol{e_z}2\cos^2\theta\right) \\ &= \pi\int_{-1}^{1}\left([q_{e,x}-q_{i,x}]\,\boldsymbol{e_x}(1-\alpha^2)+[q_{e,y}-q_{i,y}]\,\boldsymbol{e_y}(1-\alpha^2)+[q_{e,z}-q_{i,z}]\,\boldsymbol{e_z}2\alpha^2\right)\mathrm{d}\alpha = \frac{4\pi}{3}\left(\boldsymbol{q_e}-\boldsymbol{q_i}\right)\end{aligned}$$

where the new variables $\eta = m_\star u^2/2T_0,\ \alpha = \cos\theta$ have been introduced to reduce the integrals to elementary forms.

Combining the factorised integrals over $\boldsymbol{u}$ and $\boldsymbol{V}$ then gives the rate of change in macroscopic electron momentum density as

$$\frac{\mathrm{d}}{\mathrm{d}t}\left(n_e m_e \boldsymbol{q_e}\right) = -\frac{L^{ei}}{4\pi}\left(1+\frac{m_e}{m_i}\right)m_e \times n_e n_i\left(\frac{m_e m_i}{(2\pi T_0)^2}\right)^{3/2} \times \left(\frac{2\pi T_0}{m_e+m_i}\right)^{3/2} \times \frac{4\pi}{3}\left(\boldsymbol{q_e}-\boldsymbol{q_i}\right). \quad \text{(H.4)}$$

Comparing Equation (H.4) with the phenomological form of the exchange model Equation (G.20) then gives the effective momentum exchange frequency between ions and electrons as

$$\overline{\nu_{ei}^m} = \frac{L^{ei}}{3}\left(1+\frac{m_e}{m_i}\right)n_i\left(\frac{m_\star}{2\pi T_0}\right)^{3/2} \approx \frac{n_i}{3}\left(\frac{e^2}{\epsilon_0 m_e}\right)^2 \frac{1}{\pi^{3/2}v_{Te}^3}\ln\Lambda = \nu_{90^\circ}^{ei} \quad \text{(H.5)}$$

where the mass ratio expansion $m_e/m_i \ll 1$ has been performed, the definition of L^{ei} given below Equation (B.3) and Equation (17) for the definition of the 90° scattering frequency have been used.

H.2 The energy exchange frequency

The calculation of the energy exchange frequency proceeds much analogous to the calculation of the momentum exchange frequency. Departing from averaging the change in test-electron energy due to collisions with the target-ion population

$$\begin{aligned}\frac{\mathrm{d}}{\mathrm{d}t}U_e &= \int \Bigg\langle \underbrace{\frac{m_e\left(\boldsymbol{v_e}+\boldsymbol{\Delta v_e}\right)^2/2 - m_e\boldsymbol{v_e}^2/2}{\Delta t}}_{=\frac{\Delta(m_e v_e^2/2)}{\Delta t}} \Bigg\rangle^{ei} f_e \mathrm{d}^3\boldsymbol{v_e} \\ &= \int f_e m_e \boldsymbol{v_e}\cdot\left\langle\frac{\Delta\boldsymbol{v_e}}{\Delta t}\right\rangle^{ei}\mathrm{d}^3\boldsymbol{v_e} + \int f_e m_e \left\langle\frac{(\Delta\boldsymbol{v_e})^2}{2\Delta t}\right\rangle^{ei}\mathrm{d}^3\boldsymbol{v_e} \\ &= -\frac{L^{ei}}{4\pi}\left(1+\frac{m_e}{m_i}\right)m_e\int\int \boldsymbol{v_e}\cdot\frac{\boldsymbol{u}}{u^3}f_i f_e \mathrm{d}^3\boldsymbol{v_e}\mathrm{d}^3\boldsymbol{v_i} + \frac{L^{ei}}{8\pi}m_e\int\int\frac{2}{u}f_i f_e\mathrm{d}^3\boldsymbol{v_e}\mathrm{d}^3\boldsymbol{v_i}\end{aligned} \tag{H.6}$$

where Equations (B.5) and (B.6) have been used for the statistical changes in electron velocity. Equation (H.6) shows the test-electron energy can either change by direct momentum transfer resulting in a power $P = \frac{\partial m_e \boldsymbol{v_e}}{\partial t}\cdot\boldsymbol{v_e}$ and indirect velocity diffusion.

When transforming to the new velocity variables $(\boldsymbol{v_e},\boldsymbol{v_i})\rightarrow(\boldsymbol{V},\boldsymbol{u})$ these different contributions partially cancel leaving only

$$\frac{\mathrm{d}}{\mathrm{d}t}U_e = -\frac{L^{ei}}{4\pi}\left(1+\frac{m_e}{m_i}\right)m_e\int\int\frac{\boldsymbol{u}\cdot\boldsymbol{V}}{u^3}f_i f_e\mathrm{d}^3\boldsymbol{u}\mathrm{d}^3\boldsymbol{V}$$

which is a consequence of the fact that the small velocity deflection in binary Coulomb collisions conserve both the centre of mass velocity $\boldsymbol{V}$ and the magnitude of the relative velocity $\|\boldsymbol{u}\|^2$ such that only the direction of $\boldsymbol{u}$ w.r.t. $\boldsymbol{V}$ can change in a collisions [3].

Substituting Equation (H.3) and considering the symmetry requirement that only expansion terms in $F(\boldsymbol{u},\boldsymbol{V})$ that are odd in both $\boldsymbol{u},\boldsymbol{V}$ will give a non-vanishing contribution to the integral leaves again only a single integral to evaluate

$$\int\int\frac{\boldsymbol{u}\cdot\boldsymbol{V}}{u^3}f_i f_e\mathrm{d}^3\boldsymbol{u}\mathrm{d}^3\boldsymbol{V} = n_e n_i\left(\frac{m_e m_i}{(2\pi T_0)^2}\right)^{3/2}\iint\frac{\boldsymbol{V}\cdot\boldsymbol{u}}{u^3}\exp\!\left(-\frac{(m_i+m_e)\,V^2}{2T_0}\right)\exp\!\left(-\frac{m_\star u^2}{2T_0}\right)\frac{m_\star\boldsymbol{u}\cdot\boldsymbol{V}\Delta T}{T_0^2}\mathrm{d}^3\boldsymbol{u}\mathrm{d}^3\boldsymbol{V}$$

which can again be done in spherical velocity coordinates for both $\boldsymbol{V},\boldsymbol{u}$ but results in a more involved angular as the direction of both $\boldsymbol{u},\boldsymbol{V}$ will have to be accounted for. Nevertheless using spherical facilitates to factorise the integral into an angular (direction) part, and two magnitude (speed) parts. The latter can be cast in the form of gamma functions

$$\int_0^\infty V^4\exp\!\left(-\frac{(m_i+m_e)\,V^2}{2T_0}\right)\mathrm{d}V = \left(\frac{2T_0}{m_i+m_e}\right)^{5/2}\left(\frac{1}{2}\underbrace{\int_0^\infty\xi^{3/2}\exp(\xi)}_{=\Gamma(5/2)=3\sqrt{\pi}/4}\right) = \frac{3\sqrt{\pi}}{8}\left(\frac{2T_0}{m_i+m_e}\right)^{5/2}$$

$$\int_0^\infty\frac{m_\star\Delta T}{T_0^2}u\exp\!\left(-\frac{m_\star u^2}{2T_0}\right)\mathrm{d}u = \frac{\Delta T}{T_0}\underbrace{\int_0^\infty\exp(-\eta)\mathrm{d}\eta}_{=\Gamma(1)=1} = \frac{\Delta T}{T_0}$$

by using $\xi=(m_i+m_e)\,V^2/2T_0, \eta = m_\star u^2/2T_0$ again. The angular part is more involved

$$\int_0^{2\pi}\int_0^{2\pi}\int_0^{\pi}\int_0^{\pi}\left(\cos^2(\Phi-\phi)\left[1-\cos^2\theta-\cos^2\Theta\right]+\cos^2\Theta\cos^2\theta\left[1+\cos^2(\Phi-\phi)\right]+\tfrac{1}{2}\cos(\Phi-\phi)\sin(2\theta)\sin(2\Theta)\right)\sin\theta\sin\Theta\,\mathrm{d}\Theta\,\mathrm{d}\theta\,\mathrm{d}\Phi\,\mathrm{d}\phi$$

$$= 2\pi^2\int_0^\pi\int_0^\pi\left(1-\cos^2\theta-\cos^2\Theta+3\cos^2\theta\cos^2\Theta\right)\sin\theta\sin\Theta\mathrm{d}\theta\mathrm{d}\Theta = 2\pi^2\int_{-1}^1\int_{-1}^1\left(1-\alpha^2-\beta^2+3\alpha^2\beta^2\right)\mathrm{d}\alpha\mathrm{d}\beta = \frac{16\pi^2}{3}$$

which is calculated by first carrying out the integral over Φ, ϕ by expanding $\cos(\Phi - \phi)$ into elementary trigonometric functions, and then transforming the remaining integral over θ, Θ with the substitutions $\alpha = \cos\theta, \beta = \cos\Theta$. Combining the above integrals then gives the rate of change in macroscopic electron energy density as

$$\frac{\mathrm{d}}{\mathrm{d}t}U_e = -\frac{L^{ei}}{4\pi}\left(1+\frac{m_e}{m_i}\right)m_e \times n_e n_i \left(\frac{m_e m_i}{(2\pi T_0)^2}\right)^{3/2} \times \frac{\Delta T}{T_0} \times 3\sqrt{\pi}8\left(\frac{2T_0}{m_i+m_e}\right)^{5/2} \times \frac{16\pi^2}{3}. \tag{H.7}$$

To compare Equation (H.7) with the phenomological form of the exchange model, the small mean flow assumption $\|\boldsymbol{q_s}\|/v_{Ts} \ll 1$ is made such that $U_j \approx \frac{3}{2}n_j T_j$ and the effective energy exchange frequency follows as

$$\overline{\nu_{ei}^{en}} = \frac{2L^{ei}}{3}n_i\left(\frac{m_\star}{2\pi T_0}\right)^{3/2}\frac{m_e}{m_i} \approx \frac{2n_i}{3}\left(\frac{e^2}{\epsilon_0 m_e}\right)^2 \frac{1}{\pi^{3/2}v_{Te}^3}\ln\Lambda\frac{m_e}{m_i} = 2\frac{m_e}{m_i}\nu_{90^\circ}^{ei} \tag{H.8}$$

where again the mass ratio expansion $m_e/m_i \ll 1$ is performed and Equation (17) for the definition of the 90° scattering frequency have been used. A comparison of Equation (H.8) with Equation (H.5) shows that the exchange frequencies are related by

$$\overline{\nu_{ei}^{en}} = 2\frac{m_e}{m_i}\overline{\nu_{ei}^{m}}.$$

I Explicit calculation of the ion velocity integral

Departing from the ion velocity integral on the right-hand side of Equation (56) and substituting for the temperature dependent diamagnetic velocity Equation (30) splitting for its energy dependent and independent parts results in the following integrals

$$\left(1-\frac{\omega_{\star i}}{\omega}\right)\int\left(1+\frac{\omega_{di}}{\omega}-i\frac{\nu^{ie}}{\omega}\right)\left(\frac{1}{\pi v_{Ti}^2}\right)^{3/2}\exp\left(-\frac{v_i^2}{v_{Ti}^2}\right)J_0\left(k_\perp\frac{v_{\perp,i}}{\Omega_i}\right)^2\mathrm{d}^3\boldsymbol{v_i}$$
$$-\eta_i\omega_{\star i}\int\left(\frac{v_i^2}{v_{Ti}^2}-\frac{3}{2}\right)\left(1+\frac{\omega_{di}}{\omega}-i\frac{\nu^{ie}}{\omega}\right)\left(\frac{1}{\pi v_{Ti}^2}\right)^{3/2}\exp\left(-\frac{v_i^2}{v_{Ti}^2}\right)J_0\left(k_\perp\frac{v_{\perp,i}}{\Omega_i}\right)^2\mathrm{d}^3\boldsymbol{v_i}$$

where all velocity independent factors have been taken out of the integral and the thermal velocity $v_{Ti} = \sqrt{2T_{i0}/m_i}$ was used for compressed notation of the Maxwellian. This notation further facilitates the use of normalised cylindrical velocity coordinates $\mathrm{d}^3\boldsymbol{v_i} \to v_{Ti}^3\,\mathrm{d}\vartheta\,x_\perp\,\mathrm{d}x_\perp\,\mathrm{d}x_\parallel$ where $x_\parallel = v_\parallel/v_{Ti}, x_\perp = v_\perp/v_{Ti}$ since the Bessel function depends only on the perpendicular speed and the magnetic drift velocity splits in a contribution from parallel and perpendicular motion, resulting in

$$\left(1-\frac{\omega_{\star i}}{\omega}\right)\frac{2}{\sqrt{\pi}}\int_\infty\int_0^\infty\left(1+\frac{\omega_{di}(x_\perp,x_\parallel)}{\omega}-i\frac{\nu^{ie}(x_\perp,x_\parallel)}{\omega}\right)\exp\left(-x_\parallel^2+x_\perp^2\right)J_0\left(k_\perp\rho_{Ti}x_\perp\right)^2 x_\perp\,\mathrm{d}x_\perp\,\mathrm{d}x_\parallel$$
$$-\eta_i\omega_{\star i}\frac{2}{\sqrt{\pi}}\int_\infty\int_0^\infty\left(x_\parallel^2+x_\perp^2-\frac{3}{2}\right)\left(1+\frac{\omega_{di}(x_\perp,x_\parallel)}{\omega}-i\frac{\nu^{ie}(x_\perp,x_\parallel)}{\omega}\right)\exp\left(-x_\parallel^2+x_\perp^2\right)J_0\left(k_\perp\rho_{Ti}x_\perp\right)^2 x_\perp\,\mathrm{d}x_\perp\,\mathrm{d}x_\parallel$$

where the integral over the gyrophase just gives a 2π prefactor as by construction the kinetic response $\hat{g}_i$ is gyrophase independent and the dependence of collision frequency and drift frequency is made explicit. Upon using the "vacuum plasma" approximation for the magnetic drift frequency, the integrals over perpendicular and parallel direction become factorisable into the

following standard integrals

$$
\begin{aligned}
\int_{-\infty}^{\infty} \xi^{2n} \exp\bigl(-\xi^2\bigr)\,\mathrm{d}\xi &= \int_0^{\infty} \zeta^{n-1/2} \exp(-\zeta)\,\mathrm{d}\zeta = \Gamma\left(n+1/2\right) \\
\int_0^{\infty} \exp\bigl(-\xi^2\bigr)\xi J_0(a\xi)^2\,\mathrm{d}\xi &= \frac{1}{2}\exp\left(-\frac{a^2}{2}\right) I_0\left(\frac{a^2}{2}\right) \\
\int_0^{\infty} \exp\bigl(-\xi^2\bigr)\xi^3 J_0(a\xi)^2\,\mathrm{d}\xi &= \frac{1}{2}\exp\left(-\frac{a^2}{2}\right)\left[\frac{a^2}{2} I_1\left(\frac{a^2}{2}\right) + (1-\frac{a^2}{2}) I_0\left(\frac{a^2}{2}\right)\right] \\
\int_0^{\infty} \exp\bigl(-\xi^2\bigr)\xi^5 J_0(a\xi)^2\,\mathrm{d}\xi &= \exp\left(-\frac{a^2}{2}\right)\left[(1-\frac{a^2}{2})^2 I_0\left(\frac{a^2}{2}\right) - \frac{a^2}{2}(\frac{a^2}{2}-\frac{3}{2}) I_1\left(\frac{a^2}{2}\right)\right]
\end{aligned}
\tag{I.1}
$$

where $\Gamma(n)$ is the Gamma function and I_n denotes the modified Bessel function of order n and $a > 0$. In terms of these standard integrals the constant and drift terms of the velocity integral evaluate to

$$
\int_{\infty}^{\infty}\int_0^{\infty} 1 \times \exp\bigl(-x_\parallel^2 + x_\perp^2\bigr) J_0\left(k_\perp \rho_{Ti} x_\perp\right)^2 x_\perp\,\mathrm{d}x_\perp\,\mathrm{d}x_\parallel = \frac{\sqrt{\pi}}{2}\exp\left(-\frac{\left(k_\perp\rho_{Ti}\right)^2}{2}\right) I_0\left(\frac{\left(k_\perp\rho_{Ti}\right)^2}{2}\right)
$$

$$
\frac{\hat{\omega}_{di}}{\omega}\int_{\infty}^{\infty}\int_0^{\infty}\left(x_\parallel^2 + \frac{x_\perp^2}{2}\right) \times \exp\bigl(-x_\parallel^2 + x_\perp^2\bigr) J_0\left(k_\perp \rho_{Ti} x_\perp\right)^2 x_\perp\,\mathrm{d}x_\perp\,\mathrm{d}x_\parallel =
$$

$$
\frac{\omega\hat{_{di}}}{\omega}\frac{\sqrt{\pi}}{4}\left[\frac{\left(k_\perp\rho_{Ti}\right)^2}{2} I_1\left(\frac{\left(k_\perp\rho_{Ti}\right)^2}{2}\right) + (2-\frac{\left(k_\perp\rho_{Ti}\right)^2}{2}) I_0\left(\frac{\left(k_\perp\rho_{Ti}\right)^2}{2}\right)\right]
$$

$$
\int_{\infty}^{\infty}\int_0^{\infty}\left(x_\parallel^2 + x_\perp^2 - \frac{3}{2}\right) \times \exp\bigl(-x_\parallel^2 + x_\perp^2\bigr) J_0\left(k_\perp \rho_{Ti} x_\perp\right)^2 x_\perp\,\mathrm{d}x_\perp\,\mathrm{d}x_\parallel =
$$

$$
\frac{\left(k_\perp\rho_{Ti}\right)^2}{4}\sqrt{\pi}\exp\left(-\frac{\left(k_\perp\rho_{Ti}\right)^2}{2}\right)\left[I_1\left(\frac{\left(k_\perp\rho_{Ti}\right)^2}{2}\right) - I_0\left(\frac{\left(k_\perp\rho_{Ti}\right)^2}{2}\right)\right]
$$

$$
\frac{\hat{\omega}_{di}}{\omega}\int_{\infty}^{\infty}\int_0^{\infty}\left(x_\parallel^2 + x_\perp^2 - \frac{3}{2}\right) \times \left(x_\parallel^2 + \frac{x_\perp^2}{2}\right) \times \exp\bigl(-x_\parallel^2 + x_\perp^2\bigr) J_0\left(k_\perp \rho_{Ti} x_\perp\right)^2 x_\perp\,\mathrm{d}x_\perp\,\mathrm{d}x_\parallel =
$$

$$
\frac{\sqrt{\pi}}{2}\exp\left(-\frac{\left(k_\perp\rho_{Ti}\right)^2}{2}\right)\left[\left(1-\frac{\left(k_\perp\rho_{Ti}\right)^2}{2}\right)^2 I_0\left(\frac{\left(k_\perp\rho_{Ti}\right)^2}{2}\right) - \frac{\left(k_\perp\rho_{Ti}\right)^2}{2}\left(\frac{\left(k_\perp\rho_{Ti}\right)^2}{2} - \frac{3}{2}\right) I_1\left(\frac{\left(k_\perp\rho_{Ti}\right)^2}{2}\right)\right]
$$

For the ion-electron frequency the velocity dependence $\propto (v_{Ti}/v_i)^2$ is prevents factorisation of the parallel and perpendicular velocity integrals. Nevertheless as it turns it the double integral over both velocity components evaluates to a more generalised hypergeometric function ${}_pF_q$

$$
\int_{-\infty}^{\infty}\int_0^{\infty} \exp\bigl(-\xi^2\bigr)\exp\bigl(-\zeta^2\bigr)\frac{\xi}{\xi^2+\zeta^2} J_0(a\xi)^2\,\mathrm{d}\xi\,\mathrm{d}\zeta = \sqrt{\pi} \times {}_2F_2\left[\begin{matrix}1/2 & 1/2\\ 1 & 3/2\end{matrix}; -a^2\right]
$$

such that the two remaining integrals involving the collision frequency become

$$
\frac{\tilde{\nu}^{ie}}{\omega}\int_{\infty}^{\infty}\int_0^{\infty}\frac{1}{x_\parallel^2+x_\perp^2} \times \exp\bigl(-x_\parallel^2 + x_\perp^2\bigr) J_0\left(k_\perp \rho_{Ti} x_\perp\right)^2 x_\perp\,\mathrm{d}x_\perp\,\mathrm{d}x_\parallel = \sqrt{\pi}{}_2F_2\left[\begin{matrix}1/2 & 1/2\\ 1 & 3/2\end{matrix}; -\left(k_\perp\rho_{Ti}\right)^2\right]
$$

$$
\frac{\tilde{\nu}^{ie}}{\omega}\int_{\infty}^{\infty}\int_0^{\infty}\frac{1}{x_\parallel^2+x_\perp^2} \times \left(x_\parallel^2 + x_\perp^2 - \frac{3}{2}\right) \times \exp\bigl(-x_\parallel^2 + x_\perp^2\bigr) J_0\left(k_\perp \rho_{Ti} x_\perp\right)^2 x_\perp\,\mathrm{d}x_\perp\,\mathrm{d}x_\parallel =
$$

$$
\sqrt{\pi}\left(\frac{\exp\left(\frac{\left(k_\perp\rho_{Ti}\right)^2}{2}\right)}{2} I_0\left(\frac{\left(k_\perp\rho_{Ti}\right)^2}{2}\right) - \frac{3}{2}{}_2F_2\left[\begin{matrix}1/2 & 1/2\\ 1 & 3/2\end{matrix}; -\left(k_\perp\rho_{Ti}\right)^2\right]\right)
$$

where $\tilde{\nu}^{ie} = \nu_D^{ie}(v_{Ti}) = \hat{\nu}^{ie}\frac{4}{3\sqrt{\pi}}\sqrt{m_e/m_i}\sqrt{T_{i0}/T_{e0}}$ by using Equation (18). Multiplying the above integrals by the common $2/\sqrt{\pi}$ prefactor and adding them leads to Equation (59).

J Effects of finite temperature gradient on leading order dispersion relation solution

The role of finite temperature gradient will enter the solution to the leading order dispersion relation Equation (60) through the ion gradient length scale ratio $\eta_i = \frac{\mathrm{d}\ln T_i}{\mathrm{d}\psi} / \frac{\mathrm{d}\ln n_i}{\mathrm{d}\psi} = L_n/L_T$ (presuming the density gradient is non-zero). As the solution for ω_0 in absence of temperature gradient Equation (61) is found to be rather insensitive to the temperature ratio, the role of finite η_i is investigated at a fixed temperature of $\tau = 1.0$. The three contributions to Equation (60) are plotted versus $k_\perp \rho_{Ti}$ for various ion gradient length ratios η_i in Figure J.1.

Unlike the temperature ratio τ is can be seen that the temperature gradient has a significant influence on the solution to the dipersion relation $D_0(\omega, \boldsymbol{k}_\perp, \hat{\phi}) = 0$. Increasing η_i results in a downward shift of the mode frequency compared to the pure density gradient case ($\eta_i = 0$) until above a certain critical value of η_i the mode frequency starts to propagates in the ion diamagnetic direction ($\omega_0/\omega_{\star e} < 0$). This behaviour is more closely investigated by slowly varying η_i, from which it is found that this transition occurs near $k_\perp \rho_{Ti} \approx 2$ for a critical temperature gradient of $\eta_{i,crit} \approx 1.64$. This is as result of the opposite signs that the integrals S_1, S_4 have (see Figure 11). For temperature gradients above critical the wavelength window where the mode frequency changes sign becomes wider and the frequency becomes ever directed in the ion diamagnetic direction. This change of sign of the mode frequency to the ion diamagnetic direction is indicative of the mode being an ITG rather than a TEM [76, 96, 220]. Even though treating the electrons adiabatically is appropriate for ITGs [36], the obtained solution $D_0(\omega_0, \boldsymbol{k}_\perp, \hat{\phi}) = 0$ does not accurately describe the ITG instability as a resonance with ion drift or longitudinal motion (in case of slab ITG) is not possible with the $\omega_{di}/\omega \ll 1, v_{Ti}/k_\parallel \ll \omega$ assumptions [83].

As a result of the frequency crossing through zero as the temperature gradient is increased, the approximation of small collision frequency and small drift break down, which is seen from the discontinuity and divergence in the two bottom plots of Figure J.1 which coincide with the wavenumber $(k_\perp \rho_{Ti})_{trans}$ for which the mode changes from TEM to ITG. In the vicinity of this transition region the solutions have to be discarded, but in the remaining regions where ω_0 is either strongly in the ion diamagnetic region or electron diamagnetic region they provide proper solutions. Most interestingly it can be seen that a finite temperature gradient spoils the stabilising influence collisions have in the pure density gradient case, with the growth rate becoming positive. This already occurs for temperature gradients below the critical value for TEM→ITG transition and is determined similarly by the opposite signs of the integrals S_3, S_6 which lead to a threshold temperature gradient for instability of $\eta_{i,thres} \approx 0.75$. At temperature gradients above the TEM→ITG transition there is however a competing effect in the growth rate, as η_i enters $\mathrm{Im}[\omega_0]$ through the ratio $(S_3 + \eta_i S_6)/(S_1 + \eta_i S_4)$ which changes its sign twice as η_i is increased, such that collisions always have a damping effect in the ITG regime.

K Marginal stability evaluation of collisionless TEM

The method presented here is inspired by the one presented in [221] where the pole of the integrand occurs at zero along the real line rather than shifted at x_{res}.

Allowing for a small imaginary part $i\delta\gamma$ in the denominator of the trapped electron response, the integral over particle energies in the collisionless limit becomes $\int_0^\infty \mathrm{d}x \, \frac{x^2 \exp(-x^2)}{\omega_0 - \overline{\omega_{de}} + i\delta\gamma}$ which can be explicitly split in its real and imaginary parts by expanding the denominator

$$\int_0^\infty \mathrm{d}x \, \frac{x^2 \exp(-x^2)}{\omega_0 - \overline{\omega_{de}} + i\delta\gamma} = \int_0^\infty \mathrm{d}x \, \frac{(\omega_0 - \overline{\omega_{de}})\, x^2 \exp(-x^2)}{(\omega_0 - \overline{\omega_{de}})^2 + (\delta\gamma)^2} - \int_0^\infty \mathrm{d}x \, \frac{i\delta\gamma x^2 \exp(-x^2)}{(\omega_0 - \overline{\omega_{de}})^2 + (\delta\gamma)^2}. \quad \text{(K.1)}$$

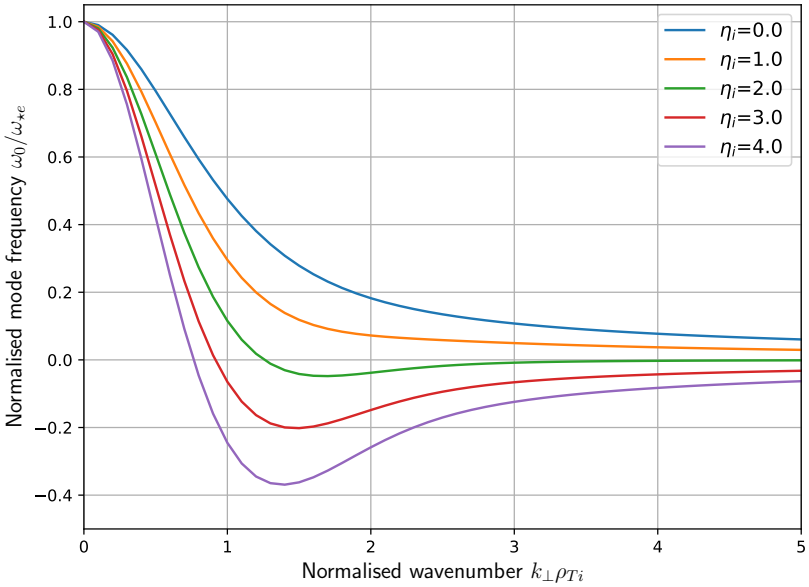

(a)

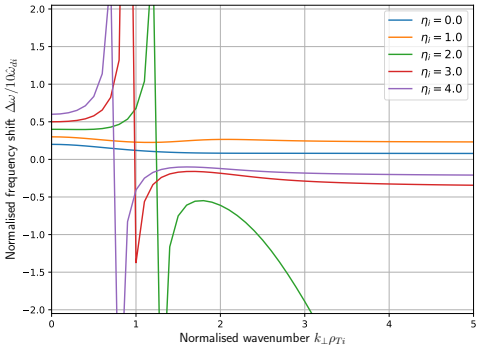

(b)

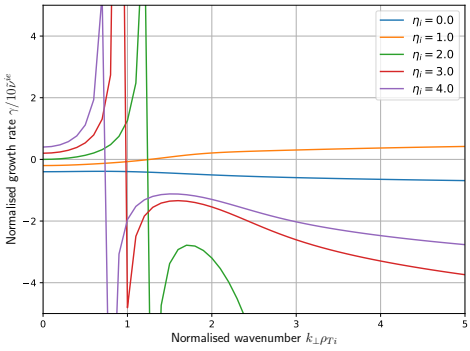

(c)

Figure J.1: Contributions to the leading order dispersion relation $D_0(\omega, \boldsymbol{k}_\perp, \hat{\phi}) = 0$ for a temperature ratio of $\tau = 1$ (a) the lowest order (real) frequency in absence of ion drift and collisions, (b) the shift in (real) frequency due to correction from ion drift, and (c) the growth rate due to correction from collisions for various temperature gradient ratios $\eta_i = \|\boldsymbol{\nabla} \ln T_i\| / \|\boldsymbol{\nabla} \ln n_i\|$. Note that the axis in (b),(c) have been scaled by a factor of 10 and the curves for $\eta_i = 0.0$ correspond to those of Figure 12.

The behaviour of these integrals can then be investigated separately in the limit of marginal stability. Starting with the real part, it is most convenient to break up the integration interval in three regions around the resonance x_{res}

$$\int_0^{x_{res}-\delta x} \mathrm{d}x\, \frac{(\omega_0-\overline{\omega_{de}})\,x^2\exp\left(-x^2\right)}{(\omega_0-\overline{\omega_{de}})^2+\delta\gamma^2} + \int_{x_{res}-\delta x}^{x_{res}+\delta x} \mathrm{d}x\, \frac{(\omega_0-\overline{\omega_{de}})\,x^2\exp\left(-x^2\right)}{(\omega_0-\overline{\omega_{de}})^2+\delta\gamma^2} + \int_{x_{res}+\delta x}^{\infty} \mathrm{d}x\, \frac{(\omega_0-\overline{\omega_{de}})\,x^2\exp\left(-x^2\right)}{(\omega_0-\overline{\omega_{de}})^2+\delta\gamma^2}$$

where $\delta x > 0$ is in principle arbitrary. In the outer two integrals the resonance is avoided and the limit of marginal stability can safely be applied by simply setting $\delta\gamma = 0$ directly in the integrand. Meanwhile if the width of the central region around x_{res} is taken to be small by letting the arbitrary parameter $\delta x/x_{res} \ll 1$ then the part from the Maxwellian function will hardly vary in the integration interval compared to the variation in $(\omega_0 - \overline{\omega_{de}})$ such that such that the central integral can be approximated by

$$\begin{aligned}\int_{x_{res}-\delta x}^{x_{res}+\delta x} \mathrm{d}x\, \frac{(\omega_0-\overline{\omega_{de}})\,x^2\exp\left(-x^2\right)}{(\omega_0-\overline{\omega_{de}})^2+\delta\gamma^2} \approx & x_{res}^2\exp\left(-x_{res}^2\right)\int_{x_{res}-\delta x}^{x_{res}+\delta x} \mathrm{d}x\, \frac{(\omega_0-\overline{\omega_{de}})}{(\omega_0-\overline{\omega_{de}})^2+\delta\gamma^2} \\ = & \frac{x_{res}^2\exp\left(-x_{res}^2\right)}{\overline{\omega_{de}^T}}\int_{x_{res}-\delta x}^{x_{res}+\delta x} \mathrm{d}x\, \frac{\left(x_{res}^2-x^2\right)}{\left(x_{res}^2-x^2\right)^2+\frac{\delta\gamma^2}{\overline{\omega_{de}^T}^2}}\end{aligned}$$

where Equations (67) and (68) where substituted for $\overline{\omega_{de}}, \omega_0$ respectively. Now as the integration interval becomes increasingly small around x_{res} the integrand will ever closer become antisymmetric around x_{res} such that the integral becomes asymptotically zero[76]. Consequently in the simulataneoous limit $\delta x, \delta\gamma \to 0$ the real part of the integral reduces to

$$\lim_{\delta x\downarrow 0}\left(\lim_{\delta\gamma\downarrow 0}\int_0^{\infty} \mathrm{d}x\, \frac{(\omega_0-\overline{\omega_{de}})\,x^2\exp\left(-x^2\right)}{(\omega_0-\overline{\omega_{de}})^2+(\delta\gamma)^2}\right) \to \frac{1}{\overline{\omega_{de}^T}}\left[\lim_{\delta x\downarrow 0}\int_0^{x_{res}-\delta x} \mathrm{d}x\, \frac{x^2\exp\left(-x^2\right)}{x_{res}^2-x^2} + \int_{x_{res}+\delta x}^{\infty} \mathrm{d}x\, \frac{x^2\exp\left(-x^2\right)}{x_{res}^2-x^2}\right]$$

where the term in square bracket defines the Cauchy Principal Value $\mathcal{P}$ of the integral $\int \mathrm{d}x\, \frac{x^2\exp\left(-x^2\right)}{x_{res}^2-x^2}$.

The procedure for the imaginary part of Equation (K.1) is much the same, with the slight subtlety that in the limit of marginal stability the $\delta\gamma$ prefactor makes the integral vanishingly small except near x_{res} where the integral will diverge as $1/\delta\gamma$. Consequently the procedure for the integrand used in the central regime above is in fact appropriate for the full integration range as in the limit of marginal stability it is only the narrow region near x_{res} that will give a finite contribution to the complete integral

$$\int_0^{\infty} \mathrm{d}x\, \frac{\delta\gamma x^2\exp\left(-x^2\right)}{(\omega_0-\overline{\omega_{de}})^2+(\delta\gamma)^2} \approx \frac{\delta\gamma}{2\overline{\omega_{de}^T}}\sqrt{z_{res}}\exp(-z_{res})\int_0^{\infty} \frac{\mathrm{d}z}{(z_{res}-z)^2+\frac{\delta\gamma^2}{\overline{\omega_{de}^T}^2}} \tag{K.2}$$

where the change of variables $z = x^2$ was made. This change of variables facilitates the use of standard integrals as it reduces the definition of arctan function such that

$$\int_0^{\infty} \frac{\mathrm{d}z}{(z_{res}-z)^2+\frac{\delta\gamma^2}{\overline{\omega_{de}^T}^2}} = \left.\frac{\arctan\left(\frac{z-z_{res}}{\delta\gamma/\overline{\omega_{de}^T}}\right)}{\delta\gamma/\overline{\omega_{de}^T}}\right|_0^{\infty} = \frac{\pi}{2}\,\mathrm{sgn}\left(\frac{\delta\gamma}{\overline{\omega_{de}^T}}\right) + \arctan\left(\frac{z_{res}}{\delta\gamma/\overline{\omega_{de}^T}}\right)$$

where sgn is the signum function defined such that $\mathrm{sgn}(x>0) = +1, \mathrm{sgn}(x<0) = -1, \mathrm{sgn}(x = 0) = 0$. In the limit of marginal stability this integral simply reduced to π which shows the

[76] More precisely, the smaller δx the better the integrand is approximated by an arbitrary truncation of its Taylor expansion around x_{res} which is straightforward to integrate around the interval $x_{res} \pm \delta x$. Only the even terms give a non-vanishing contributions to the integral and result in a polynomial in $\delta x^{2n+1}/\delta\gamma^{2n}$ $(n \geq 1)$ which vanishes in the limit that $\delta x \to 0$ even if $\delta\gamma \to 0$ as well.

factor $\frac{1}{\pi}\frac{\delta\gamma/\overline{\omega_{de}^T}}{(z_{res}-z)^2+\left(\delta\gamma/\overline{\omega_{de}^T}\right)^2}$ in Equation (K.2) effectively acts a Dirac delta function to sift out the resonance in the limit of $\delta\gamma \to 0$. This is not surprising since this "magic" factor is the Lorentzian/Cauchy distribution $\mathcal{L}$ representing a probability density function with the property that $\int \mathcal{L}\,\mathrm{d}\xi = 1$, where the factor $\delta\gamma/\overline{\omega_{de}^T}$ acts as the characteristic width of the distribution. It is a common property of many distribution functions that they reduce to a Dirac delta function as their width is taken as infinitesimally small provided that they peak at a single well defined point [222], which is satisfied by the Lorentzian.

Putting these results back together into Equation (K.1) then gives the collisionless resonant integral in the limit of marginal stability

$$\lim_{\delta\gamma\downarrow 0}\int_0^\infty \mathrm{d}x\,\frac{x^2\exp\left(-x^2\right)}{\omega_0-\overline{\omega_{de}}+i\delta\gamma} = \frac{1}{\overline{\omega_{de}^T}}\mathcal{P}\left\{\int_0^\infty \mathrm{d}x\,\frac{x^2\exp\left(-x^2\right)}{x_{res}^2-x^2}\right\} - i\frac{\pi}{\overline{\omega_{de}^T}}\int\frac{\sqrt{z}}{2}\exp(-z)\delta(z-z_{res})$$

if the latter integral is transformed back from $z = x^2$ to x and $\overline{\omega_{de}^T}$ is absorbed into the principal value Equation (69) is recovered.

L Validation of the domain splitting approximation

L.1 Validity of the approximation

The domain splitting approximation makes use of the qualitatively different dependence on the particle speed of the electron-ion collision frequency $\nu_e(x) \propto 1/x^3$ and electron drift frequency $\omega_{de} \propto x^2$ to split the integral over particle speed as

$$\int_{x_{cut}}^\infty \mathrm{d}x\,\frac{x^2\exp\left(-x^2\right)}{\omega_0-\overline{\omega_{de}}+i\nu^{ei}} = \int_{x_{cut}}^{x_{crit}} \mathrm{d}x\,\underbrace{\frac{x^2\exp\left(-x^2\right)}{\omega_0-\overline{\omega_{de}}+i\nu^{ei}}}_{\nu^{ei}>|\overline{\omega_{de}}|} + \int_{x_{crit}}^\infty \mathrm{d}x\,\underbrace{\frac{x^2\exp\left(-x^2\right)}{\omega_0-\overline{\omega_{de}}+i\nu^{ei}}}_{|\overline{\omega_{de}}|>\nu^{ei}}$$

$$\approx \int_{x_{cut}}^{x_{crit}} \mathrm{d}x\,\frac{x^2\exp\left(-x^2\right)}{\omega_0+i\nu^{ei}}\left[1+\frac{\overline{\omega_{de}}}{\omega_0+i\nu^{ei}}\right] + \int_{x_{crit}}^\infty \mathrm{d}x\,\frac{x^2\exp\left(-x^2\right)}{\omega_0-\overline{\omega_{de}}}\left[1-\frac{i\nu^{ei}}{\omega_0-\overline{\omega_{de}}}\right].$$

where the critical speed is defined as the speed where the magnitude of both frequencies will be equal $\hat{\nu}(x_{crit}) = |\overline{\omega_{de}}(x_{crit})|$ with the absolute value taking care of the sign of $\overline{\omega_{de}}$, as collision frequencies are strictly positive. Treating the drift/collision frequency as a small correction helps to not complete discard part of the physics in either regime and helps to make a more smooth "connection" between the dissipative and collisionless regimes as integrands would change in a rather discrete way between regimes if the denominators were only expanded to zeroth order. Nevertheless close to x_{crit} where $\hat{\nu}^{ei} \sim |\overline{\omega_{de}}|$ and this approximation is not justifiable and likely to fail. To investigate this the approximate integrands just above and below regime transition are compared to the exact integrand at regime transition

$$\begin{cases} \frac{x^2\exp\left(-x^2\right)}{\omega_0-\overline{\omega_{de}}+i\nu^{ei}} = \frac{x_{crit}^2\exp\left(-x_{crit}^2\right)}{\omega_0}\frac{1}{1+\xi(i\mp 1)} & \text{exact for } x = x_{crit} \\ \frac{x^2\exp\left(-x^2\right)}{\omega_0-\overline{\omega_{de}}+i\nu^{ei}} \approx \frac{x_{crit}^2\exp\left(-x_{crit}^2\right)}{\omega_0}\frac{1+\xi(i\pm 1)}{(1+i\xi)^2} & \text{approximation for } 0 < \frac{x_{crit}-x}{x_{crit}} \ll 1 \\ \frac{x^2\exp\left(-x^2\right)}{\omega_0-\overline{\omega_{de}}+i\nu^{ei}} \approx \frac{x_{crit}^2\exp\left(-x_{crit}^2\right)}{\omega_0}\frac{1-\xi(i\pm 1)\xi}{(1\mp\xi)^2} & \text{approximation for } 0 < \frac{x-x_{crit}}{x_{crit}} \ll 1 \end{cases} \tag{L.1}$$

where all factors are approximated by their value at critical speed since they vary smoothly over the regime transition in contrast to the actual integrands themselves. In Equation (L.1) the parameter $\xi = \nu(x_{crit})/\omega_0 = |\overline{\omega_{de}}(x_{crit})|/\omega_0$ is introduced and the different sign conventions account for the sign of $\overline{\omega_{de}}(x_{crit})$ with the top signs corresponding to $\overline{\omega_{de}}(x_{crit}) > 0$.

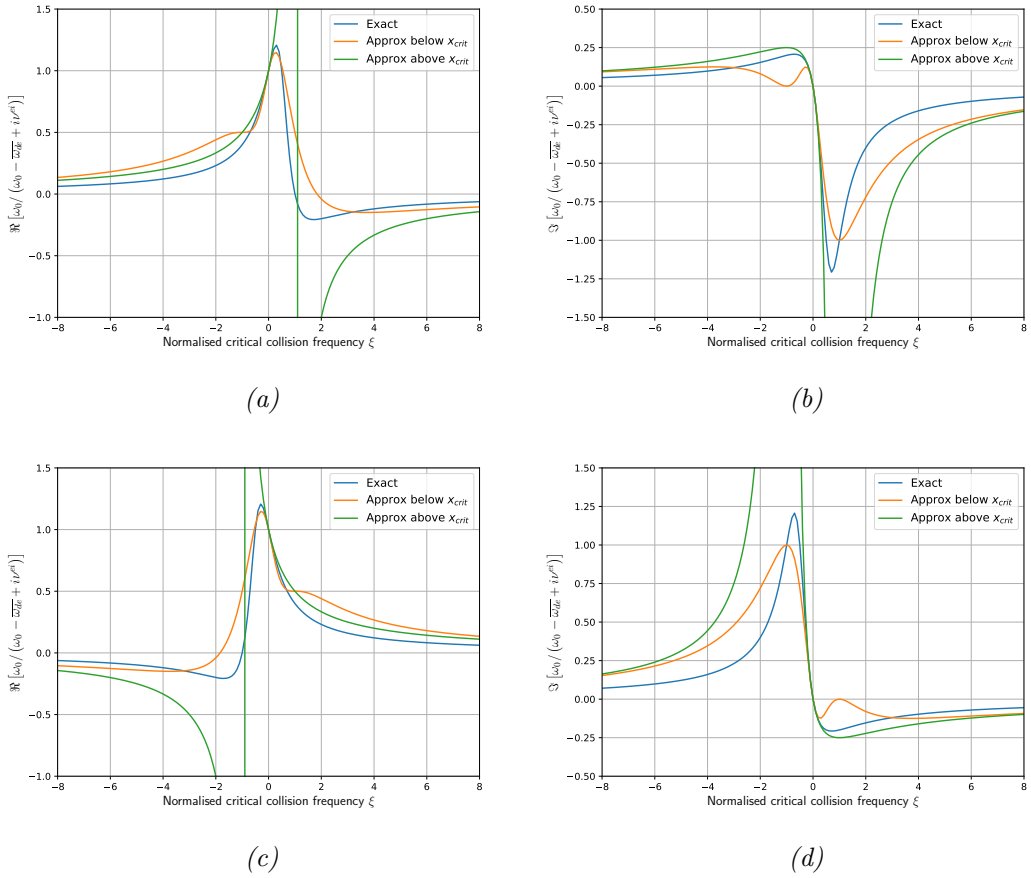

Figure L.1: Comparison of the behaviour of different integrands near regime transition at x_{crit} as a function of normalised critical frequency ξ, showing for the case when $\overline{\omega_{de}}(x_{crit}) > 0$ the (a) real and (b) imaginary parts, and for the case when $\overline{\omega_{de}}(x_{crit}) < 0$ (c) real and (d) imaginary parts.

The quality of the approximation is then visually assessable by comparing how well the approximate ξ functions match the exact ξ function, which is shown in Figure L.1 for both signs of $\overline{\omega_{de}}(x_{crit})$. It can be seen that the approximations for the integrand in both regimes are a decent match except when $\xi = \pm 1$, which exactly corresponds to resonance at the critical speed $\overline{\omega_{de}}(x_c rit) = \omega_0$. Furthermore it can be seen that the largest discrepancy due to resonance comes form the approximation in the collisionless regime, which is because the resonance is amplified by the domain splitting regime since it enters as $1/(1 \pm \xi)^2$ which strongly increases its locality compared to the exact case where the inclusion of $i\nu_e$ in the denominator smoothens out the resonance by increasing its width but decreases its amplitude. For either case it also follows that at the opposite side of the resonance (different sign of ξ) the approximations in both regimes decently match the exact integrand. Consequently near the transition region the domain splitting approximation will be a decent tool provided that the transition will not occur near the resonance (if it exists).

L.2 Verification of the threshold collision frequency

The threshold frequency prediction Equation (76) is still based on the domain splitting approximation of Equation (74) rather than the exact denominator. Based on the verification of this approximation above it should be expected that this prediction decently holds, but as the approximation is shown to break down near resonance it is of interest to investigate how well the

prediction holds in general. Fortunately this can be verified by means of numerically integrating $\int_{x_{cut}}^{\infty} \mathrm{d}x \, \frac{\omega_0 x^2 \exp\left(-x^2\right)}{\omega_0 - \overline{\omega_{de}} + i\nu_e}$ for various speed parameters x_{res}, x_ν such that both cases where x_ν and x_{res} are well separated (and the domain splitting approximation will decently hold), and cases where $x_\nu \sim x_{res}$ (and the domain splitting approximation is not accurate) are excluded. Since both parameters represent a normalised speed they are scanned over within the range $|x_{\nu,res}| \leq 5$, covering both resonant and non-resonant cases as well as configurations with a standard density profile where $\omega_{\star e} > 0$ and configurations with off-centre density peak where $\omega_{\star e} < 0$. In order to numerically capture the resonance, an artificially small 1×10^{-6} imaginary part is added to the denominator, which has been tested to correctly reproduce the expected result from the Sokhotski-Plemelj theorem in the absence of collisions while not affecting the outcome of the integral when a finite collision parameter x_ν of at least 1×10^{-4} is included. The results are shown in Figure L.2 where a real/imaginary valued x_{res} correspond to cases the resonance can/cannot occur, while positive/negative values of x_ν correspond to centred/off-centre density profiles. It can immediately be seen that whether or not a resonance is possible has a large influence on the trapped electron response with both real and imaginary parts being much larger in the resonant case. Furthermore reversal of the density gradient gives a sign change in x_ν and essentially produces complex conjugation of $\delta\omega$ as seen from the symmetry in Figures L.2a and L.2b and asymmetry in Figures L.2c and L.2d around $x_\nu = 0$, which is a consequence of the way the collision frequency enters the GKE by using a simplified BGK operator. However, as ω_0 is effectively taken out of this integral to provide normalisation, such sign changes in the imaginary part would ultimately cancel in the actual frequency shift Equation (65) which is normalised by $1/\omega_0$. The condition for the threshold collision frequency $|x_\nu| > |x_{res}|$ to avoid a resonance is neatly reproduced in Figures L.2a and L.2c where the magnitude of the integral quickly fades outside of the threshold region corresponding to the diagonal. However, perhaps more importantly it seems that in the case of a resonance the growth rate is actually worsened by the introduction of a small collision freqeuncy below the threshold of Equation (76), as seen by the spreading of the contours in Figure L.2c.

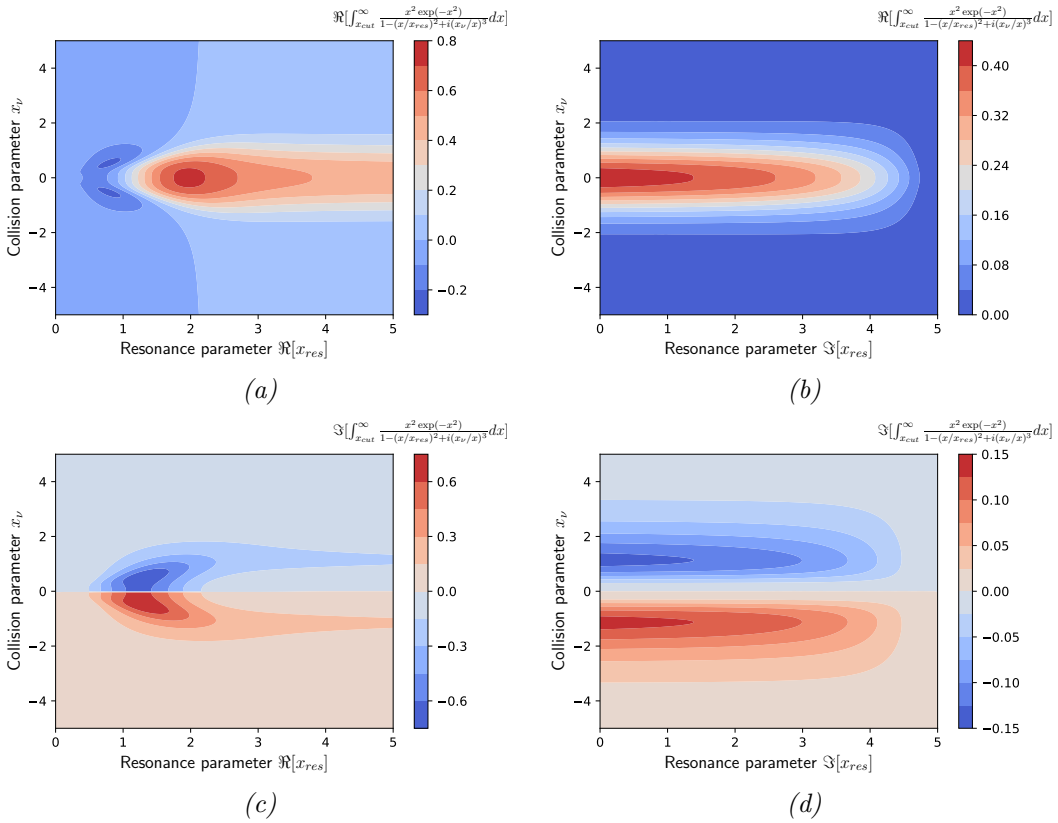

Figure L.2: Results of numerical integration over the particle energy for various x_{res}, x_ν parameters, showing (a) the real part of the integral in case of resonance, (b) the real part of the integral for the off-resonant case, (c) the imaginary part of the integral in case of resonance, and (d) the imaginary part of the integral in the off-resonant case. Notice the disparity in contour levels for both real and imaginary parts showing the importance of resonance.

M Normalisations procedures of the numerical methods

M.1 Normalisations used in GENE

The normalisation procedure of GENE is two-fold where first the independent variables are normalised by selecting appropriate reference scales, and then the remaining independent variables are normalised [158,162]. There are several layers to the reference values where first fundamental reference values for the mass and charge are chosen, defined by the particle species. Next a set of reference scales are determined by the macroscopic plasma equilibrium such as the density, temperature, magnetic field strength and an equilibrium length scale L_{ref} (which is typically the major/minor radius). Based on the combination of fundamental and equilibrium reference scales a set of reference scales related to the gyromotion are created

$$c_{\mathrm{ref}} = \sqrt{\frac{T_{\mathrm{ref}}}{m_{\mathrm{ref}}}} \quad \Omega_{\mathrm{ref}} = \frac{eB_{\mathrm{ref}}}{m_{\mathrm{ref}}} \quad \rho_{\mathrm{ref}} = \frac{c_{\mathrm{ref}}}{\Omega_{\mathrm{ref}}}$$

where in the typical case of a plasma consisting of a single ion species $m_{\mathrm{ref}} = m_i$, $T_{\mathrm{ref}} = T_e$ such that c_{ref} is simply the ion sound speed, and consequently ρ_{ref} is simply the ion gyroradius at sound speed. The independent quantities are then normalised as follows [16]

$$\tilde{y} = \frac{y}{\rho_{\mathrm{ref}}} \quad \tilde{x} = \frac{x}{\rho_{\mathrm{ref}}} \quad \tilde{z} = z \quad \tilde{v_{\parallel}} = \frac{v_{\parallel}}{v_{Ts}} \quad \tilde{\mu} = \frac{\mu}{T_{0s}/B_{\mathrm{ref}}} \quad \tilde{t} = \frac{t}{L_{\mathrm{ref}}/c_{\mathrm{ref}}}$$

where quantities in tildes refer to normalised quantities, the parallel z direction does not require normalisation as it measures the poloidal angle along the field line (see explanation of flux tube in Appendix N), and the velocity dimensions are normalised per species[77] such that a single velocity grid for both species can be used.

Next with the independent variables normalised and dimensionless, the remainder of the GKE is then suitably normalised by making the dependent variables dimensionless as well, which for electrostatic turbulence means [16]

$$\tilde{F_{Ms}} = \frac{n_{0s}}{v_{Ts}^3} F_{Ms} \quad \tilde{g_s} = \frac{n_{0s}}{v_{Ts}^3} g_s \frac{\rho_{\mathrm{ref}}}{L_{\mathrm{ref}}} \quad \tilde{\phi} = \frac{T_{ref}}{e}\phi \frac{\rho_{\mathrm{ref}}}{L_{\mathrm{ref}}}$$

where perturbed quantities are intrinsically normalised to the already dimensionless $\rho_{\mathrm{ref}}/L_{\mathrm{ref}}$ factor to incorporate the $\delta \ll 1$ ordering parameter for perturbations. Meanwhile the the important derivatives of the magnetic field which determine the curvature and $\boldsymbol{\nabla} B$ drifts and plasma profiles that determine the driving factors are normalised according to

$$\frac{\partial \tilde{B}}{\partial x} = \frac{L_{\mathrm{ref}}}{B_{\mathrm{ref}}} \frac{\partial B}{\partial x} \quad \frac{\partial \tilde{B}}{\partial y} = \frac{L_{\mathrm{ref}}}{B_{\mathrm{ref}}} \frac{\partial B}{\partial y} \quad \frac{\partial \tilde{B}}{\partial z} = \frac{1}{B_{\mathrm{ref}}} \frac{\partial B}{\partial x}$$

$$\tilde{\omega_n} = -\frac{L_{\mathrm{ref}}}{B_{\mathrm{ref}}} \frac{\mathrm{d}n_{0s}}{\mathrm{d}x} \qquad \tilde{\omega_T} = -\frac{L_{\mathrm{ref}}}{T_{\mathrm{ref}}} \frac{\mathrm{d}T_{0s}}{\mathrm{d}x}$$

and the Jacobian which maps the volume elements in (x, y, z) space to a 3D volume in the torus is normalised according to $\tilde{J} = L_{\mathrm{ref}} J$.

When these normalisations are applied to the GKE three natural dimensionless quantities appear[78]

$$\beta = \frac{n_{\mathrm{ref}} T_{\mathrm{ref}}}{B_{\mathrm{ref}}^2/2\mu_0} \quad \tilde{\nu_c} = \frac{e^4 \ln \Lambda L_{\mathrm{ref}} n_{\mathrm{ref}}}{32\sqrt{2}\pi T_{\mathrm{ref}}^2 \epsilon_0^2} \quad \tilde{\lambda_D} = \sqrt{\frac{B_{\mathrm{ref}}^2 \epsilon_0}{m_{\mathrm{ref}} n_{\mathrm{ref}}}}$$

[77] This essentially entails an additional normalisation step of the species mass and temperature in terms of the reference quantities m_{ref},T_{ref}, such that e.g. the thermal velocity v_{Ts} is first made dimensionless through terms of c_{ref} and the velocity grid is then normalised to the dimensionless thermal velocity.

[78] For modern convenience these have been converted into SI units. GENE, much like the literature on plasma turbulence, still uses CGS units such that the actual dimensionless quantities are $\beta = 8\pi n_{\mathrm{ref}} T_{\mathrm{ref}}/B_{\mathrm{ref}}^2$, $\tilde{\nu_c} =$

which give respectively the ratio between plasma pressure to magnetic pressure, the collision frequency normalised to the time unit $L_{\text{ref}}/c_{\text{ref}}$ and the ratio of Debye length to ρ_{ref}. These three quantities influence the simulations in terms of the equations that are solved as they are effectively applied weights to the normalised terms of the GKE. A non-zero β will switch on electromagnetic perturbations, a non-zero $\tilde{\lambda_D}$ takes into account deviations from quasi-neutrality within the the flux tube (by retaining $\nabla^2\phi$ terms), and a non-zero $\tilde{\nu_c}$ will take the collision operator into account.

In particular the value of $\tilde{\nu_c}$ will be tweaked to explore the influence of collisionality. For the interpretation of results it is most useful to map the input collision frequency to a sensible physical collision frequency. This connection is given by [157]

$$\hat{\nu}^{ei} = 4\frac{n_i}{n_{\text{ref}}}\left(\frac{T_{\text{ref}}}{T_e}\right)^{3/2}\sqrt{\frac{m_{\text{ref}}}{m_e}}\tilde{\nu_c}\frac{c_{\text{ref}}}{L_{\text{ref}}} \approx 171\sqrt{A}\tilde{\nu_c}\frac{c_{\text{ref}}}{L_{\text{ref}}} \tag{M.1}$$

where the last step follows for the typical single ion species case with $m_{\text{ref}} = m_i, T_{\text{ref}} = T_e$ and quasi-neutrality $n_{0i} \approx n_{0e} = n_{\text{ref}}$, with A being the ion species mass number. In particular if the reference density, temperature and length scale are expressed in 10^{19}m^{-3}, keV and m respectively, the numerical value of $\tilde{\nu_c}$ follows as

$$\tilde{\nu_c} = 2.303\,08 \times 10^{-5}\frac{n_{\text{ref}}[10^{19}\text{m}^{-3}]L_{\text{ref}}[\text{m}]}{T^2_{\text{ref}}[\text{keV}]}\ln\Lambda$$

which can be used to straightforward obtain a realistic values of $\tilde{\nu_c}$ from pressure profiles.

M.2 Normalisations used for integrating the perturbative frequency shift

The normalised frequency shift is calculated according to Equation (79) which is repeated below for convenience

$$\frac{\delta\omega}{\omega_0} = \frac{2}{\sqrt{\pi}}\frac{\left\langle\frac{\omega_0}{\omega_{\star e}}\right\rangle - 1}{\langle\Gamma_0\rangle}\left\langle\frac{\omega_0}{\omega_{\star e}}\right\rangle\int_{1/B_{max}}^{1/B_{min}}\mathrm{d}\lambda\sum_{w(\lambda)}\int_{x_{cut}}^{\infty}\mathrm{d}x\,\frac{x^2\exp\left(-x^2\right)}{\left\langle\frac{\omega_0}{\omega_{\star e}}\right\rangle - \frac{\overline{\omega_{de}}}{\omega_{\star e}} + i\frac{\nu_e}{\omega_{\star e}}}\left|\overline{\hat{\phi}}\right|^2 L_{eff[w]}\Big/\oint\left|\hat{\phi}\right|^2\frac{\mathrm{d}l}{B}. \tag{M.2}$$

As the GIST code is used to "feed" the geometry info to the integral to calculate all electron bounce quantities, and GIST is coupled to GENE, most of the normalisations from Appendix M.1 have to be directly applied. A few things require additional care however. For all integrals along the field line the proper integration variable is the arc length along the magnetic field $\mathrm{d}l$. Rather in the flux tube, the parallel field coordinate is taken to be the poloidal angle $\mathrm{d}\theta$. As the field lines are helical, a variation in the poloidal angle directly relates to a variation in the length along the magnetic field according to [46]

$$\mathrm{d}l = \sqrt{g}B\frac{\mathrm{d}\theta}{\iota} \tag{M.3}$$

where $\sqrt{g}$ is the Jacobian that maps the 3D volume element in a torus to the (ψ, α, θ) coordinates $\mathrm{d}V = \sqrt{g}\,\mathrm{d}\psi\,\mathrm{d}\alpha\,\mathrm{d}\theta$, B is the local value of the magnetic field strength along the field line and ι is the rotational transform of the field (which in terms of the flux-tube coordiantes is $1/q_0$). Consequently all integrals along the field line have to be transformed to integrals over the

$\pi e^4\ln\Lambda L_{\text{ref}}n_{\text{ref}}/2^{3/2}T^2_{\text{ref}}$, $\tilde{\lambda_D} = \sqrt{B^2_{\text{ref}}/4\pi c^2 m_{\text{ref}}n_{\text{ref}}}$. This distinction matters little as regardless of the system of units, simulations are performed using $\beta = \tilde{\lambda_D} = 0$ and introducing convenient renormalisations for $L_{\text{ref}}.n_{\text{ref}}, T_{\text{ref}}$ of $1\,\text{m}, 1\times10^{19}\,\text{m}^{-3}, 1\,\text{keV}$ respectively based on typical fusion plasma parameters. With these renormalisations of the reference values for $\hat{\nu_c}$, the dimensionless collision frequency has the same numerical prefactor of 2.303×10^{-5} in both CGS and SI units.

poloidal angle which spans on poloidal turn $\theta \in [-\pi, \pi]$. The Jacobian which is provided by GIST code is however the Jacobian for how the volume span by flux tube coordinates (x, y, z) changes to a physical 3D volume element in the torus, which by using Equation (N.7) means that the "Jacobian" from GIST is actually[79] $J^{\text{flux-tube}} = 1/B_0\sqrt{g} = \tilde{J}^{\text{GIST}}/L_{\text{ref}}$ with B_0 the magnetic field strength on axis. Consequently the arc length element is given in terms of GIST parameters as

$$\mathrm{d}l = \frac{B}{B_0}\frac{L_{\text{ref}}}{\tilde{J}^{\text{GIST}}} q_0 \,\mathrm{d}\theta = L_{\text{ref}} \underbrace{q_0 \tilde{B} \frac{B_{\text{ref}}}{B_0} \,\mathrm{d}\theta}_{=\mathrm{d}\tilde{l}} \tag{M.4}$$

where $\tilde{B} = B/B_{\text{ref}}$ is the normalised magnetic field in GENE units and a dimensionless arclength $\mathrm{d}\tilde{l}$ is identified.

With Equation (M.4) the most painful part of the normalisation process is complete, as the remainder of the normalisations are quite straightforward. The frequency ratio $\omega_0/\omega_{\star e}$ already has a normalised expression Equation (61) which is expressed in terms of functions of $k_\perp \rho_{Ti}$. There are two translations which have to be made to Equation (61) to make it compatible with GENE/GIST normalisations. First the perpendicular wavenumber should be properly averaged along the field line according to Equation (78) with $k_\perp$ given by Equation (77). As the wavenumbers are inherently normalised to the ρ_{ref} this means the averaging procedure actually calculates $\left\langle (k_\perp \rho_{\text{ref}})^2 \right\rangle$, whereas the $\langle \omega_0/\omega_{\star e} \rangle$ and $\langle \Gamma_0 \rangle$ are functions of $(k_\perp \rho_{Ti})^2$. The function argument is straightforwardly translated as

$$\langle k_\perp \rho_{Ti} \rangle = \langle k_\perp \rho_{\text{ref}} \rangle \sqrt{\frac{2T_{i0} m_{\text{ref}}}{T_{\text{ref}} m_i}} \tag{M.5}$$

where the translation factor reduces to $\sqrt{2\tau}$ in the standard case of single ion species plasma. For the integral to determine the average wavenumber Equation (78) however the electrostatic potential has to be normalised[80], where the obvious choice for normalisation from the discussion of quasi-neutrality condition Section 2.4 where the dimensionless potential $\Phi = e\phi/T_{e0}$ was used, which immediately corresponds to the GENE units as the electron temperature is taken as the reference scale such that $\hat{\tilde{\phi}} = e\hat{\phi}/T_{\text{ref}}$. For the remaining frequency ratios an explicit expression of the electron diamagnetic frequency is required, which from Equation (E.7) is given in terms of Clebsch coordinates as

$$\omega_{\star e} = \frac{T_e}{-e} k_\alpha \frac{\mathrm{d}\ln n_e}{\mathrm{d}\psi} = -\frac{T_e}{eB_0} k_y \frac{\mathrm{d}\ln n_e}{\mathrm{d}x} = \underbrace{\frac{T_e}{eB_0 L_{\text{ref}} \rho_{\text{ref}}}}_{=\omega_{\star e}^{\text{phys}}} (k_y \rho_{\text{ref}}) \, \tilde{\omega_n} \tag{M.6}$$

where again the translation from (ψ, α) Clebsch coordinates to (x, y) flux-tube coordinates has been made, and a basic diamagnetic drift frequency with dimension of Hz corresponding the diamagnetic drift for $\tilde{\omega_n} = \tilde{k_y} = 1$ naturally defines itself. It is this basic diamagnetic drift frequency that provides the most sensible normalisation for the collision frequency as it removes any intrinsic scaling on the driving gradient strength and spatial extent of the perturbations. Consequently the collision frequency term in Equation (M.2) is normalised as

$$\frac{\nu_e(x)}{\omega_{\star e}} = \frac{\hat{\nu}^{ei}}{\omega_{\star e}^{\text{phys}}} \frac{1}{x^3 \tilde{k_y} \tilde{\omega_n}} \equiv \frac{\tilde{\nu}_{\text{scan}}}{x^3 \tilde{k_y} \tilde{\omega_n}}$$

[79] The normalisation follows from dimensional analysis of the volume element $\mathrm{d}V = \sqrt{g}\,\mathrm{d}\psi\,\mathrm{d}\alpha\,\mathrm{d}\theta$ which shows that $B_0\sqrt{g}$ has the dimension of m and is the actual Jacobian J which is normalised by L_{ref} in the GENE normalisation of Appendix M.1.

[80] Technically the electrostatic completely cancels out from all equations as a result of the "flute-mode" approximation, but for future improvements a variation of the electrostatic potential along the field line can be considered and the normalisation issue becomes relevant again.

where $\tilde{\nu}_{\text{scan}}$ is the dimensionless collision frequency which is varied in Section 3.5.

For the remaining frequency ratio between the precession frequency and the diamagnetic frequency is most sensible if the precession frequency is explicitly written out. For this exercise it is most convenient to express the precession frequency in Clebsch coordinates Equation (71) since the bounce average drifts in (ψ, α) are related to the derivatives of the second adiabatic invariant $\mathcal{J}$. Starting from its definition Equation (7) and using pitch-angle coordinates it follows that $\mathcal{J} = \int_a^b \sqrt{2mE}\sqrt{1-\lambda B}\,\mathrm{d}l$. Taking its derivative at constant ψ, μ, α gives the bounce time τ_b

$$\begin{aligned}\left(\frac{\partial \mathcal{J}}{\partial E}\right)_{\psi,\mu,\alpha} &= \sqrt{\frac{m}{2E}}\int \sqrt{1-\lambda B}\,\mathrm{d}l + \sqrt{\frac{mE}{2}}\int \frac{-B}{\sqrt{1-\lambda B}}\frac{\partial \lambda}{\partial E} \\ &= \sqrt{\frac{m}{2E}}\int \left(\sqrt{1-\lambda B} + \frac{\lambda B}{\sqrt{1-\lambda B}}\right) = \sqrt{\frac{m}{2E}}\int \frac{\mathrm{d}l}{\sqrt{1-\lambda B}} = \int \frac{\mathrm{d}l}{v_\parallel}\end{aligned}$$

where the proper energy dependence of the pitch-angle $\lambda = \mu/E$ has to be accounted for. At the same time its derivative w.r.t. the Clebsch coordinates while holding the other variables constant follow similarly as

$$\left(\frac{\partial \mathcal{J}}{\partial \psi}\right)_{E,\mu,\alpha} = \sqrt{\frac{mE}{2}}\int \frac{-\lambda\frac{\partial B}{\partial \psi}}{\sqrt{1-\lambda B}}\,\mathrm{d}l \qquad \left(\frac{\partial \mathcal{J}}{\partial \alpha}\right)_{E,\mu,\psi} = \sqrt{\frac{mE}{2}}\int \frac{-\lambda\frac{\partial B}{\partial \alpha}}{\sqrt{1-\lambda B}}\,\mathrm{d}l\,.$$

Consequently the α component of the precession drift then follows as

$$k_\alpha \overline{\boldsymbol{v_{ds}}\cdot\boldsymbol{\nabla}\alpha} = \frac{k_\alpha}{e\tau_b}\left(\frac{\partial \mathcal{J}}{\partial \psi}\right)_{E,\mu,\alpha} = \frac{k_\alpha E}{e}\frac{\int -\lambda\frac{\partial B}{\partial \psi}/\sqrt{1-\lambda B}\,\mathrm{d}l}{\int \mathrm{d}l\,/\sqrt{1-\lambda B}} \tag{M.7}$$

which takes precisely the form of a bounce average in pitch-angle coordinates, and similarly for the ψ component by replacing the indices $\psi \leftrightarrow \alpha$. As only $k_\psi = 0$ modes are considered in the the calculation, the α component of the drift is the only one that matters such that the ratio $\overline{\omega_{de}}/\omega_{\star e}$ follows as[81]

$$\frac{\overline{\omega_{de}}}{\omega_{\star e}} = \frac{k_y E}{eB_0}\frac{\int -\lambda\frac{\partial B}{\partial x}/\sqrt{1-\lambda B}\,\mathrm{d}l}{\int \mathrm{d}l\,/\sqrt{1-\lambda B}}\Bigg/\omega_{\star e}^{\text{phys}}\tilde{k_y}\tilde{\omega_n} = \frac{E}{T_e}L_{\text{ref}}\frac{\int -\lambda\frac{\partial B}{\partial x}/\sqrt{1-\lambda B}\,\mathrm{d}l}{\int \mathrm{d}l\,/\sqrt{1-\lambda B}}\Bigg/\tilde{\omega_n}$$

where again the translation between Clebsch-coordinates and flux-tube coordinates Equation (N.7) has been made, and the explicit expression for $\omega_{\star e}^{\text{phys}}$ Equation (M.6) is substituted. As the magnetic field is normalised to B_{ref} it follows that the pitch angle must be normalised according to $\tilde{\lambda} = \lambda/B_{\text{ref}}$ which follows either from dimensional analysis of $\lambda = \mu/E$ or the fact that the product $\lambda B = 1$ has to keep defining the bounce points even in normalised units, and correspondingly the ratio is given in dimensionless units as provided by GIST

$$\frac{\overline{\omega_{de}}}{\omega_{\star e}} = x^2\frac{\int -\tilde{\lambda}\frac{\tilde{\partial B}}{\partial x}/\sqrt{1-\tilde{\lambda}\tilde{B}}d\tilde{d}l}{\int \tilde{\mathrm{d}}l/\sqrt{1-\tilde{\lambda}\tilde{B}}}\Bigg/\tilde{\omega_n}$$

where the definition of the normalised velocity $x = v/v_{Te}$ and the normalisation of the magnetic gradient according to Appendix M.1 are used and the dimensional factor to translate $\mathrm{d}l \to \tilde{\mathrm{d}}l$ simply cancels as it appears in both the numerator and denominator. For exactly the same reason, making the bounce average of the potential dimensionless results only in a prefactor related to normalisation of the potential $\overline{\tilde{\phi}} \to T_{\text{ref}}/e\overline{\tilde{\phi}}$ which is cancelled by the same prefactor that will appear in the denominator of Equation (M.2).

[81] In case that a radial wave number would be included it is fairly straightforward to show by the same process that this would result in an additional term where with $\frac{\tilde{\partial B}}{\partial x}$ replaced by $(k_x/k_y)\frac{\tilde{\partial B}}{\partial y}$.

This leaves two normalisations left undetermined which are closely related to each other. First the "effective well length" normalisation follows directly from the normalisations that have been introduced so far

$$L_{eff[w]} = \int_{l_1[w]}^{l_2[w]} \frac{\mathrm{d}l}{\sqrt{1-\lambda B}} \rightarrow L_{\mathrm{ref}} \int_{l_1[w]/L_{\mathrm{ref}}}^{l_2[w]/L_{\mathrm{ref}}} \frac{\tilde{\mathrm{d}}l}{\sqrt{1-\tilde{\lambda}\tilde{B}}} \equiv L_{\mathrm{ref}} \tilde{L}_{eff[w]}$$

where the integration boundaries naturally define the dimensionless bounce point locations $\tilde{l}_{1,2}[w]$. This is not surprising since $L_{eff[w]}$ represents the physical length of an electron orbit along a fraction of the field line which can be comparable to macroscopic plasma scales unless the particles are deeply trapped. The remaining normalisation concerns the energy cut-off in the integration $x_{cut} = \sqrt[4]{\hat{\nu}^{ei}/\omega_{be}(\lambda)^T}$ which because of the choice to normalise the collision frequency w.r.t. $\omega_{\star e}^{\mathrm{phys}}$ is no longer free to be normalised at will. Rather it would be more correct to use the proper bounce frequency for each magnetic well w and particles trapped with the same pitch angle λ will have a different bounce frequency in a wide and compressed well with the same depth. Consequently $\omega_{be}[w]^T(\lambda) = 2\pi v_{Te} / \int_{l_1[w]}^{l_2[w]} \frac{\mathrm{d}l}{\sqrt{1-\lambda B}} = 2\pi v_{Te}/L_{eff[w]}$ and the collisional cut-off is given by $x_{cut} = \sqrt[4]{\tilde{\nu}_{\mathrm{scan}} G[w](\lambda)}$ where the function $G[w](\lambda)$ is given by

$$G[w](\lambda) = \frac{\omega_{\star e}^{\mathrm{phys}}}{\omega_{be}^T[w](\lambda)} = \frac{\frac{T_e}{\sqrt{T_{\mathrm{ref}} m_{\mathrm{ref}}}} \frac{B_{\mathrm{ref}}}{B_0} L_{eff[w]}}{2\pi\sqrt{2T_e/m_e} L_{\mathrm{ref}}} = \frac{\sqrt{\frac{m_e}{m_{\mathrm{ref}}}}\sqrt{\frac{T_e}{T_{\mathrm{ref}}}}}{2\pi\sqrt{2}} \frac{B_{\mathrm{ref}}}{B_0} \tilde{L}_{eff[w]} \tag{M.8}$$

which follows by explicitly writing out $\omega_{\star e}^{\mathrm{phys}}$ Equation (M.6) along with $\rho_{\mathrm{ref}} = c_{\mathrm{ref}}/\Omega_{\mathrm{ref}}$ and the thermal electron velocity. In the typical case of a single ion plasma where $m_{\mathrm{ref}} = m_i$ and $T_{\mathrm{ref}} = T_e$ this weighing function $\tilde{\nu}_{scan}$ to the cut-off velocity will be very small such that it would be appropriate to set[82] $B_{\mathrm{ref}}/B_0 \approx 1$ as order unity factors would not significantly affect x_{cut} or the total end result.

After a lengthy process this then leads to the dimensionless integral

$$\frac{\delta\omega}{\omega_0} = \frac{2}{\sqrt{\pi}} \frac{\left\langle \frac{\omega_0}{\omega_{\star e}} \right\rangle - 1}{\langle \Gamma_0 \rangle} \left\langle \frac{\omega_0}{\omega_{\star e}} \right\rangle \int_{1/\tilde{B}_{max}}^{1/\tilde{B}_{min}} \mathrm{d}\tilde{\lambda} \sum_{w(\tilde{\lambda})} \int_{\sqrt[4]{\tilde{\nu}_{scan} G[w](\tilde{\lambda})}}^{\infty} \mathrm{d}x \frac{x^2 \exp(-x^2)}{\left\langle \frac{\omega_0}{\omega_{\star e}} \right\rangle - x^2 \frac{\int -\tilde{\lambda} \frac{\partial \tilde{B}}{\partial x} / \sqrt{1-\tilde{\lambda}\tilde{B}} \tilde{\mathrm{d}}l}{\int \tilde{\mathrm{d}}l / \sqrt{1-\tilde{\lambda}\tilde{B}} \times \tilde{\omega_n}} + i \frac{\tilde{\nu}_{scan}}{x^3 \tilde{k}_y \tilde{\omega_n}}} \tilde{L}_{eff[w]} \Big/ \oint \frac{\tilde{\mathrm{d}}l}{\tilde{B}}$$

where the "flute-mode" approximation is invoked to get rid of the terms involving the electrostatic potential and all functions of $k_\perp \rho_{Ti}$ are evaluated at $\langle k_\perp \rho_{ci} \rangle \sqrt{2\tau}$. The numerical integration is performed using a hybrid of python/MATLAB, since MATLAB turned out to possess the most robust "black box" numerical integration method for handling the resonance at low collisionality, whereas Python is used to load in the geometry, identify the different wells and corresponding bounce points along with the gyroaverages, and performs the final integration over pitch angle.

M.3 Matching of the GENE and perturbative frequency normalisations

For fair comparison between the solutions for the two numerical methods the collision frequency and growth rates have to be expressed in the same basis. The values of the GENE collision

[82] There are strict reasons inherent to the GENE normalisation why one cannot set the reference magnetic field strength equal to the magnetic field strength on axis [159]. However as the magnetic field is generated by coils some distance from the plasma a simple $\propto 1/r$ estimate for the magnetic field strength shows that $B_0/B_{\mathrm{ref}} = 1 + \delta r/R_0$ where R_0 is the major radius and δr is the deviation of the reference position from the magnetic axis, which can be at most the plasma minor radius at the edges. As the aspect ratio a/R_0 is typically small for most devices, it follows that $B_0/B_{\mathrm{ref}} \approx 1$ will not be a severe approximation given that the other contribution factors to x_{cut} are small or $\mathcal{O}(1)$ themselves.

frequency $\tilde{\nu}_c$ are straightforward expressed in terms of $\tilde{\nu}_{\text{scan}}$ by using Equation (M.1), which only requires to ratio of $(c_{\text{ref}}/L_{\text{ref}})/\omega_{\star e}^{\text{phys}}$. Using Equation (M.6) it follows that

$$\frac{c_{\text{ref}}/L_{\text{ref}}}{\omega_{\star e}^{\text{phys}}} = \frac{c_{\text{ref}}/L_{\text{ref}}}{T_e/eB_0 L_{\text{ref}}\rho_{\text{ref}}} = \frac{B_0 c_{\text{ref}}^2 m_{\text{ref}}}{T_e B_{\text{ref}}} \tag{M.9}$$

where the gyroradius was expressed in terms of the reference speed and reference gyrofrequency. Consequently the GENE collision frequency can be mapped to the perturbative collision frequency by

$$\tilde{\nu}_{\text{scan}} = 4\frac{n_i}{n_{\text{ref}}}\left(\frac{T_{\text{ref}}}{T_e}\right)^{5/2}\sqrt{\frac{m_{\text{ref}}}{m_e}}\tilde{\nu_c}\frac{B_0}{B_{\text{ref}}} \approx 171\sqrt{A}\tilde{\nu_c}\frac{B_0}{B_{\text{ref}}}$$

where c_{ref} was expressed in terms of the reference mass and temperature in Equation (M.9) and the last step corresponds to the usual case of a single ion species plasma simulation where $T_{\text{ref}} = T_e, m_{\text{ref}} = m_i$.

To convert the growth rates from the perturbative calculation to the GENE normalisation, $\langle\omega_0\rangle$ has to be expressed in terms of $c_{\text{ref}}/L_{\text{ref}}$. Rather what the leading order solution of the perturbative calculation gives is $\omega_0/\omega_{\star e}$, however as a result of flux surfaces being isobars and $k_y\rho_{\text{ref}}$ being a fixed quantity in the flux-tube the diamagnetic frequency is fortunately constant along the field line such that $\langle\omega_0/\omega_{\star e}\rangle = \langle\omega_0\rangle/\omega_{\star e}$, and the normalised solution for the leading order dispersion relation for the average perpendicular wavenumber Equation (M.5) can be used. From Equation (M.6) it then follows that the growth rates are also translated by the ratio of $(c_s/a)/\omega_{\star e}^{\text{phys}}$ according to

$$\tilde{\gamma}_{\text{perturb}} = \frac{\gamma}{\langle\omega_0\rangle} = \left[\frac{c_{\text{ref}}/L_{\text{ref}}}{\omega_{\star e}\langle\omega_0/\omega_{\star e}\rangle}\right]\frac{\gamma}{c_{\text{ref}}/L_{\text{ref}}} = \frac{T_{\text{ref}}B_0}{T_e B_{\text{ref}}(k_y\rho_{\text{ref}})\tilde{\omega_n}\langle\omega_0/\omega_{\star e}\rangle}\tilde{\gamma}_{GENE}$$

where Equations (M.6) and (M.9) have been used and in the usual case of single ion species the temperature ratio disappears.

N Mathetmatical details of the flux-tube geomtetry

Note: due to historic reasons the notation for the Clebsch representation in this section deviates from notations elsewhere in the thesis, such that α, ψ have different meaning, and the safety factor q is used rather than rotational transform ι. To be consistent $\tilde{\alpha} = -\alpha/\iota$ and $\tilde{\psi} = \chi$ where tildes indicate the notation used within this section. This section is largely based on [68] unless otherwise stated.

N.1 Choice and implications of coordinates

The flux tube geometry is able to minimise the required simulation volume to resolve plasma microturbulence by considering a box whose sizes are (slightly larger than) the correlation length of the turbulent eddies perpendicular to the magnetic field (typically the gyroradius), which wraps around the field line for one or several poloidal revolution (such that $k_\parallel L_\parallel \sim 1$) as well. Then the turbulence statistics outside of this box will be the identical to the those within the box and the simulation results become practically insensitive to the box size.

The flux tube formalism is based on the Clebsch representation of the magnetic field as $\boldsymbol{B} = \boldsymbol{\nabla}\alpha \times \boldsymbol{\nabla}\psi$ with ψ denoting the poloidal flux and $\alpha = \zeta - q(\psi)\theta$ the field line label, with ζ, θ the toroidal and poloidal Boozer angle (as usual, no change in definition), and $q(\psi) = 1/\iota(\psi)$ the safety factor. Because from the Clebsch representation it follows that $\boldsymbol{B} \cdot \boldsymbol{\nabla}\alpha = \boldsymbol{B} \cdot \boldsymbol{\nabla}\psi = 0$ such that α, ψ are constant on a particular field line, this naturally gives ψ, α as choices for the perpenedicular coordinates of the flux-tube. Within the flux tube then ψ is a radial coordinate since the enclosed magnetic flux will increase with further distance from the magnetic axis. This leaves α is the so-called binormal coordinate, as it is a second dimension perpendicular to the magnetic field line. Only a third coordinate z has to be chosen to represent the distance along the field line. Although the arc length along the field line would be the most intuitive choice, it is more convenient to use the poloidal Boozer angle[83] $z = \theta$, and as a result the actual physical length scale of the parallel direction will enter through the normalisation of the metric [154]. Since the Boozer coordinates (ψ, ζ, θ) themselves are non-orthogonal[84], the flux tube coordinates (ψ, α, z) form a non-mutually orthogonal curvilinear coordinate system as well. Therefore that the information of the metric tensor $\underline{\underline{g}}(\psi, \alpha, z)$ mapping (ψ, α, z) to physical lab frame (in which the volume and shape of the torus are defined) is of importance. Specifically the value of the Jacobian $J(\psi, \alpha, z) = [(\boldsymbol{\nabla}\alpha \times \boldsymbol{\nabla}\psi) \cdot \boldsymbol{\nabla}z]^{-1}$ which maps the volume of the flux tube to the physical volume that is wrapped along of the field line in the torus has a large influence. As a consequence of $J(\psi, \alpha, z)$ the rectangular volume of the flux tube geometry is transformed into a sheared and curved box inside the torus which is embedded in the fixed lab frame (see Figure 16). In principle other choices of the third coordinate z can be made, but each choice will affect the explicit form of the metric tensor $\underline{\underline{g}}$ and the Jacobian J, but the choice of the poloidal Boozer angle is most convenient as it directly links the flux tube coordinates (ψ, α, z) to MHD equilibria configurations of the magnetic field [139] and makes the Fourier modes closely related to the ballooning mode formalism [68].

With the formalities and intricacies of the coordinate system out of the way, the flux tube

[83] Note that with this choice z is not a strictly parallel coordinate like $\boldsymbol{e_b}$ since $\boldsymbol{B} \cdot \boldsymbol{\nabla}z/\|\boldsymbol{B}\|\|\boldsymbol{\nabla}z\| \neq 1$, but the fact that $\boldsymbol{B} \cdot \boldsymbol{\nabla}z \neq 0$ means that $\boldsymbol{\nabla}z$ has a finite projection onto the magnetic field line, and can thus be used to parameterise the distance along the field as the other coordinates are strictly perpendicular to $\boldsymbol{B}$. Note that changes in θ indeed correspond to changes of the arc length along the magnetic field through Equation (M.3), and it is only the variation of the Jacobian and the magnetic field strength with θ which spoils a direct correspondence between θ and the parallel direction.

[84] This is what leads to the different representations of the magnetic field in its usual contravariant/Clebsch form in fluxes and covariant form in terms of currents [45, 47].

formalism can be constructed. The idea is to take a volume that is enclosed by

$$\alpha_0 - \Delta\alpha \leq \alpha \leq \alpha + \Delta\alpha_0 \quad \psi_0 - \Delta\psi \leq \psi \leq \psi_0 + \Delta\psi \quad -z_0 \leq z \leq z_0 \tag{N.1}$$

which describes a box with area $\Delta\psi\Delta\alpha$ centred around a magnetic field line described by ψ_0, α_0, which is then extended $2z_0$ along the field. Since the perpendicular correlation length is much smaller than the equilibrium length scales of density and temperature profiles, the turbulence can be considered to be locally driven as the gradients do not vary over the correlation length. Within this approximation the equilibrium quantities can then be expanded to lowest order around the central field line as

$$n \approx n_0 + \left.\frac{\mathrm{d}n}{\mathrm{d}\psi}\right|_{\psi=\psi_0} (\psi - \psi_0) \quad T \approx T_0 + \left.\frac{\mathrm{d}T}{\mathrm{d}\psi}\right|_{\psi=\psi_0} (\psi - \psi_0)$$

making use of the flux surface property that $\boldsymbol{B} \cdot \boldsymbol{\nabla} p = 0$ such that the pressure profile depends only on the flux surface label ψ. A similar approximation is also applied to the metric tensor $\underline{\underline{g}}$, as the coordinates are defined on the equilibrium magnetic field which also varies on the same equilibrium scale according to the MHD force balance $\boldsymbol{j} \times \boldsymbol{B} = \boldsymbol{\nabla} p$, such that all geometric quantities are independent of ψ, α and only depend on their local value along the field line [153]. Specifically this means that throughout the full flux tube

$$\underline{\underline{g}}(\psi, \alpha, z) \approx \underline{\underline{g}}(\psi_0, \alpha_0, z) \quad J(\psi, \alpha, z) \approx J(\psi_0, \alpha_0, z)$$

and as a consequence the transformed spatial differential operators expressed in (α, ψ, z) coordinates (which involve the elements of the metric tensor) have no explicit dependence on α, ψ anymore, which leads to a reduction in the number of computational operations that have to be performed in the simulation.

N.2 Boundary conditions

As the flux tube does not simulate the full torus where natural/physical boundary conditions would arise (e.g. pressure vanishing at the edge), a set of suitable boundary conditions for the flux tube have to be implemented. These boundary conditions should be chosen such that this reduction in simulation domain has a negligible influence on the results[85]. As the flux tube is based on the idea of turbulence correlation length, such that the turbulence statistics at $\psi + 2\Delta\psi$ are identical to those at ψ, motivating the use of periodic boundary conditions[86] in ψ and for completely analogous reasons periodic boundary conditions in α. This periodicity and the fact that the differential operators do not explicitly depend on α, ψ make the decomposition of all turbulent quantities A in terms of a Fourier series attractive

$$A(\psi, \alpha, z, t) = \sum_{n=-\infty}^{\infty} \sum_{m=-\infty}^{\infty} \hat{A}_{n,m}(z, t) \exp\left(i2\pi n \frac{(\psi - \psi_0)}{2\Delta\psi} + i2\pi m \frac{\alpha - \alpha_0}{2\Delta\alpha} \right). \tag{N.2}$$

Although Equation (N.2) implies plane waves in (ψ, α), the actual waves inside the torus can be highly distorted due to the shearing of the flux tube volume.

More complicated is the parallel boundary condition. Since the parallel length of the box is also taken to be longer than the parallel correlation length, a parallel periodic boundary condition can also be used. However, there is a two-fold subtlety about this periodicity. First if periodicity were to be enforced in within the flux tube coordinates, it is implied that $A(\psi_0, \alpha_0, +z_0) =$

[85] For instance this means that fixed boundary conditions like for the full torus should be avoided, as they can unphysically prevent fluxes of heat and particles out of the simulation box.

[86] Furthermore such periodic boundary conditions would prevent the accumulation of heat and particles which could alter the fixed gradients in the local approach [16].

$A(\psi_0, \alpha_0, -z_0)$, and as $2z_0$ is an integer number of poloidal revolutions this would imply that all field lines "bite their own tail" after an integer number of poloidal revolutions, i.e. that every field line has a rational q_0. Secondly, since the magnetic field line is twisting in real space during a poloidal revolution, the physical turbulence structures which are elongated along the field line do also twist in real space, and it is the periodicity in the turbulence structures that should be enforced (as beyond a parallel correlation length, the turbulence properties along the field line will be the same). Therefore the parallel boundary condition should be applied using physical (ψ, ζ, θ) coordinates, as the turbulent eddies in the (ψ, ζ) plane[87] should be identical after an integer number of poloidal revolutions as this returns to the same (ψ, ζ) plane in the torus. As a consequence thus, the parallel periodic boundary condition for $N_p \in \mathbb{N}$ poloidal revolutions of the flux tube becomes

$$A\left(\psi, \alpha(\theta, \zeta), z(\theta)\right) = A\left(\psi, \alpha(\theta + 2\pi N_p, \zeta), z(\theta + 2\pi N_p)\right). \tag{N.3}$$

To enforce the boundary condition Equation (N.3), the safety factor can also be expanded as $q \approx q_0 + \frac{\partial q}{\partial \psi}|_{\psi=\psi_0}(\psi - \psi_0)$ just like the equilibrium quantities n, T since the geometry of the equilibrium magnetic field line hardly changes within the extend of the flux tube. As a consequence the radial and poloidal coordinate get mixed in the Fourier representation of Equation (N.2)

$$\begin{aligned} A(\psi, \alpha(\theta, \zeta), z(\theta), t) &= \sum_{n=-\infty}^{\infty} \sum_{m=-\infty}^{\infty} \hat{A}_{n,m}(\theta, t) \exp\left(i2\pi n \frac{\psi - \psi_0}{2\Delta\psi} + i2\pi m \frac{\zeta - \zeta_0}{2\delta\alpha} - i2\pi m q_0 \frac{\theta - \theta_0}{2\Delta\alpha} - i2\pi m \frac{\mathrm{d}q}{\mathrm{d}\psi}(\psi - \psi_0) \frac{\theta - \theta_0}{2\Delta\alpha} \right) \\ &= \sum_{n=-\infty}^{\infty} \sum_{m=-\infty}^{\infty} \hat{A}_{n,m}(\theta, t) \exp\left(i2\pi \frac{\psi - \psi_0}{2\Delta\psi} \left[n - m \frac{\mathrm{d}q}{\mathrm{d}\psi}(\theta - \theta_0) \frac{2\Delta\psi}{2\Delta\alpha} \right] + i2\pi m \frac{\zeta - \zeta_0}{2\delta\alpha} - i2\pi m q_0 \frac{\theta - \theta_0}{2\Delta\alpha} \right) \end{aligned}$$

where in the second line all factors of $\psi - \psi_0$ have been gathered in favour to apply the boundary condition Equation (N.3), since the boundary condition is taken at constant ψ, ζ. A similar expansion of at a poloidal angle of $\theta + 2\pi N_p$ gives

$$\begin{aligned} &A(\psi, \alpha(\theta + 2\pi N_p, \zeta), z(\theta + 2\pi N_p), t) = \\ &\sum_{n=-\infty}^{\infty} \sum_{m=-\infty}^{\infty} \hat{A}_{n,m}(\theta + 2\pi N_p, t) \exp\left(i2\pi \frac{\psi - \psi_0}{2\Delta\psi} \left[n - m \frac{\mathrm{d}q}{\mathrm{d}\psi}(\theta - \theta_0) \frac{2\Delta\psi}{2\Delta\alpha} - m \frac{\mathrm{d}q}{\mathrm{d}\psi} 2\pi N_p \frac{2\Delta\psi}{2\Delta\alpha} \right] + i2\pi m \frac{\zeta - \zeta_0}{2\delta\alpha} - i2\pi m q_0 \frac{\theta - \theta_0}{2\Delta\alpha} - i2\pi m q_0 \frac{2\pi N_p}{2\Delta\alpha} \right) \\ &\sum_{n'=-\infty}^{\infty} \sum_{m=-\infty}^{\infty} \hat{A}_{n'+\delta n,m}(\theta + 2\pi N_p, t) \exp\left(i2\pi \frac{\psi - \psi_0}{2\Delta\psi} \left[n' - m \frac{\mathrm{d}q}{\mathrm{d}\psi}(\theta - \theta_0) \frac{2\Delta\psi}{2\Delta\alpha} \right] + i2\pi m \frac{\zeta - \zeta_0}{2\Delta\alpha} - i2\pi m q_0 \frac{\theta - \theta_0}{2\Delta\alpha} - i2\pi m q_0 \frac{2\pi N_p}{2\Delta\alpha} \right) \end{aligned}$$

where a shift index $n' = n - \delta n$ was introduced in the last line with

$$\delta n = m \frac{\mathrm{d}q}{\mathrm{d}\psi} 2\pi N_p \frac{2\Delta\psi}{2\Delta\alpha}. \tag{N.4}$$

After this effort, the boundary condition Equation (N.3) can then be straightforwardly applied by comparing the expressions for $A(\psi, \alpha(\theta, \zeta), z(\theta, t)$ and $A(\psi, \alpha(\theta + 2\pi N, \zeta), z(\theta + 2\pi N, t)$: because the start point (ψ, ζ, θ) was identical the coefficients in front of each of the $\psi - \psi_0,\ \zeta - \zeta_0,\ \theta - \theta_0$ terms in the exponential should be identical. This leads to the following condition

$$\hat{A}_{n,m}(\theta, t) = \hat{A}_{n+\delta n,m}(\theta + 2\pi N_p, t) \exp\left(-i2\pi m q_0 \frac{2\pi N}{2\Delta\alpha} \right) \tag{N.5}$$

with δn given by Equation (N.4). Essentially this means that Fourier modes in the ψ direction become coupled at the parallel ends of the flux tube, even though they are decoupled within the interior (at least as long as the $\boldsymbol{E} \times \boldsymbol{B}$ non-linearity is not in play). The physical reason for this coupling is that as a result of shearing of the cross section of the flux tube in the torus through

[87] Since ψ is a radial coordinate, and ζ the Boozer toroidal angle, this plane characterises a slice going around the torus the long way which extends from the magnetic axis to the edge and thus samples full physical eddies in the plasma except for poloidal asymmetries.

the metric elements $\underline{\underline{g}}(z)$ gets distorted, and a matching of these surfaces (as implied by the parallel boundary condition) requires a shift in the binormal coordinate α that depends on the radial ψ coordinate [16]. Such shifts in physical space then correspond to an shift "the other way around" in Fourier space, as the index δn is shifted, essentially the wavenumber $k_\psi = n2\pi/2\Delta\psi$ in the ψ direction is shifted.

The most important consequence of the parallel boundary condition is that the box sizes of the flux tube in the two perpendicular directions are constraint by the $\frac{\mathrm{d}q}{\mathrm{d}\psi}$ of the central field line. This is because the index shift δn must be an integer, such that Equation (N.4) requires that

$$2\pi\frac{\mathrm{d}q}{\mathrm{d}\psi}\frac{2\Delta\psi}{2\Delta\alpha} \in \mathbb{Z} \tag{N.6}$$

since both m, N_p are already integers. Another indirect consequence of the parallel boundary condition Equation (N.5) is that even for a linear simulation in which the Fourier modes are decoupled in the interior of the flux tube, an envelope of k_ψ modes (corresponding to different n's in Equation (N.2)) is always required even for a single k_α mode (corresponding to different m's in Equation (N.2)). This then gives the very pragmatic way of handling the constraint on the box sizes Equation (N.6) to minimise the simulation volume: the wave-number k_α of the mode determines the minimum resolution in the binormal direction through $2\Delta\alpha_{\min} = 2\pi/k_\alpha$ to resolve at least one period of the eddy in the binormal direction, and Equation (N.6) then determines the box size in the radial direction $2\Delta\psi$, with the minimum box size corresponding to an index shift of $|\delta n| = 1$, leading to a minimum radial box size of

$$2\Delta\psi_{\min} = \frac{2\Delta\alpha_{\min}}{2\pi\left|\frac{\mathrm{d}q}{\mathrm{d}\psi}\right|}.$$

N.3 Transformation to practical coordinates

In principle the above method completes the characterisation of the flux tube, but it is not the most practical description. The range of (α, ψ, z) describing the flux-tube do not enclose the origin and more importantly the two perpendicular coordinates have different dimensions, which makes normalisation bothersome. As plasma microturbulence is characterised by $k_\perp\rho \sim 1$ and the ion gyroradius is used in the normalisation of length scales, it makes sense to transform to new perpendicular coordinates (x, y) which have the normal dimension of m. These normalisation-friendly are

$$x = \frac{q_0}{B_0 r_0}(\psi - \psi_0) \quad y = \frac{r_0}{q_0}(\alpha - \alpha_0) \tag{N.7}$$

with B_0 the magnetic field strength at the magnetic axis and r_0 the distance from the magnetic axis to the central field line of the flux-tube (characterised by (α_0, ψ_0)). As the poloidal flux scales as $\psi \sim B_{\mathrm{pol}} r^2$ with r the distance from the magnetic axis, it can be seen that x is a physical radial coordinate by expanding $\psi - \psi_0$ for $r = r_0 + \delta r$

$$x \sim \frac{q_0}{B_0 r_0} B_{\mathrm{pol}}\left([r_0 + \delta r]^2 - r_0^2\right) = \frac{q_0 B_{\mathrm{pol}}}{B_0}\delta r\left(2 + \frac{\delta r}{r_0}\right)$$

as at the magnetic axis the magnetic field is purely toroidal the q_0 makes the prefactor unity as a result of Equation (4). Together with the small perpendicular extent of the box such that $\delta r/r_0 \ll 1$ it follows that x is the radial deviation from the central field line within the flux tube. Similarly for the y coordinate the factor r_0 transfer the deviation in binormal coordinate $\alpha - \alpha_0$ to an arc length since α is an angle, which in the limit of small $\delta\alpha$ deviations from α_0 are straightline segments. The additional appearance of the safety factor q_0 in the y coordinate is

to facilitate normalisation of the the constraint on box sizes due to parallel boundary condition Equation (N.6). Equation (N.7) implies physical box sizes of $L_x = 2\Delta x = q_0 2\Delta\psi / B_0 r_0$ and $L_y = r_0 2\Delta\alpha / q_0$, such that Equation (N.6) in terms of the new coordinates becomes

$$2\pi \frac{\mathrm{d}q}{\mathrm{d}\psi} \frac{B_0 r_0^2}{q_0^2} \frac{L_x}{L_y} = 2\pi \frac{\mathrm{d}q}{\mathrm{d}x} \frac{r_0}{q_0} \frac{L_x}{L_y} \in \mathbb{Z} \tag{N.8}$$

where the derivative of the safety factor has also been changed to the new radial coordinate x. The quantity $\frac{\mathrm{d}q}{\mathrm{d}x}|_{x=0} \frac{r_0}{q_0} \equiv \hat{s}$ is intrinsically dimensionless and is known as the global magnetic shear (since the derivative at $x = 0$ is equivalent to a radial derivative at $r = r_0$), indicating how the twisting of the magnetic field changes through the torus. Equation (N.8) is an implementation friendly way of determining the radial box-size L_x since the shear $\hat{s}$ is one of the equilibrium MHD quantities of the central field line available from the GIST interface. Similarly also the position of the flux within the torus given by x_0 can be obtained from the GIST file, as the field line is characterised by the normalised enclosed flux $s_0 = \psi / \psi_{\mathrm{edge}} = r_0^2 / a^2$ of its flux surface.

In these new physical coordinates, the perpendicular periodic boundary conditions don't change such that Equation (N.2) can be recast as

$$A(x, y, z, t) = \sum_{k_x=-\infty}^{\infty} \sum_{k_y=-\infty}^{\infty} \hat{A}_{k_x, k_y}(z, t) \exp(i k_x x + i k_y y) \tag{N.9}$$

where the wave numbers $k_x = n 2\pi / L_x,\ k_y = m 2\pi / L_y$ are related to the n, m indices of Equation (N.2), and the shift condition Equation (N.4) translates to a shift in k_x. Within these new coordinates the equilibrium quantities n, T can then be extended in the radial direction as opposed to the flux label ψ

$$n \approx n_0 \left.\frac{\mathrm{d}n}{\mathrm{d}r}\right|_{r=r_0} (r - r_0) \quad T \approx T_0 + \left.\frac{\mathrm{d}T}{\mathrm{d}r}\right|_{r=r_0} (r - r_0)$$

which has the benefit that radial profile derivatives are easily obtained from e.g. experimental measurements, and that the gradient lengths $\frac{\mathrm{d}\ln n}{\mathrm{d}r}$ are straightforward to normalise to the machine size.

O Cross-phase data for the collisional simulations

The dependence of the weighted average cross-phase data on wavenumber and collision frequency for the collisional simulation for DIII-D, HSX and W7-X are shown in Figures O.1 to O.3 respectively. The axes have been fixed to $[-\pi, +\pi]$ to include all possible phases and make direct comparison between plots possible.

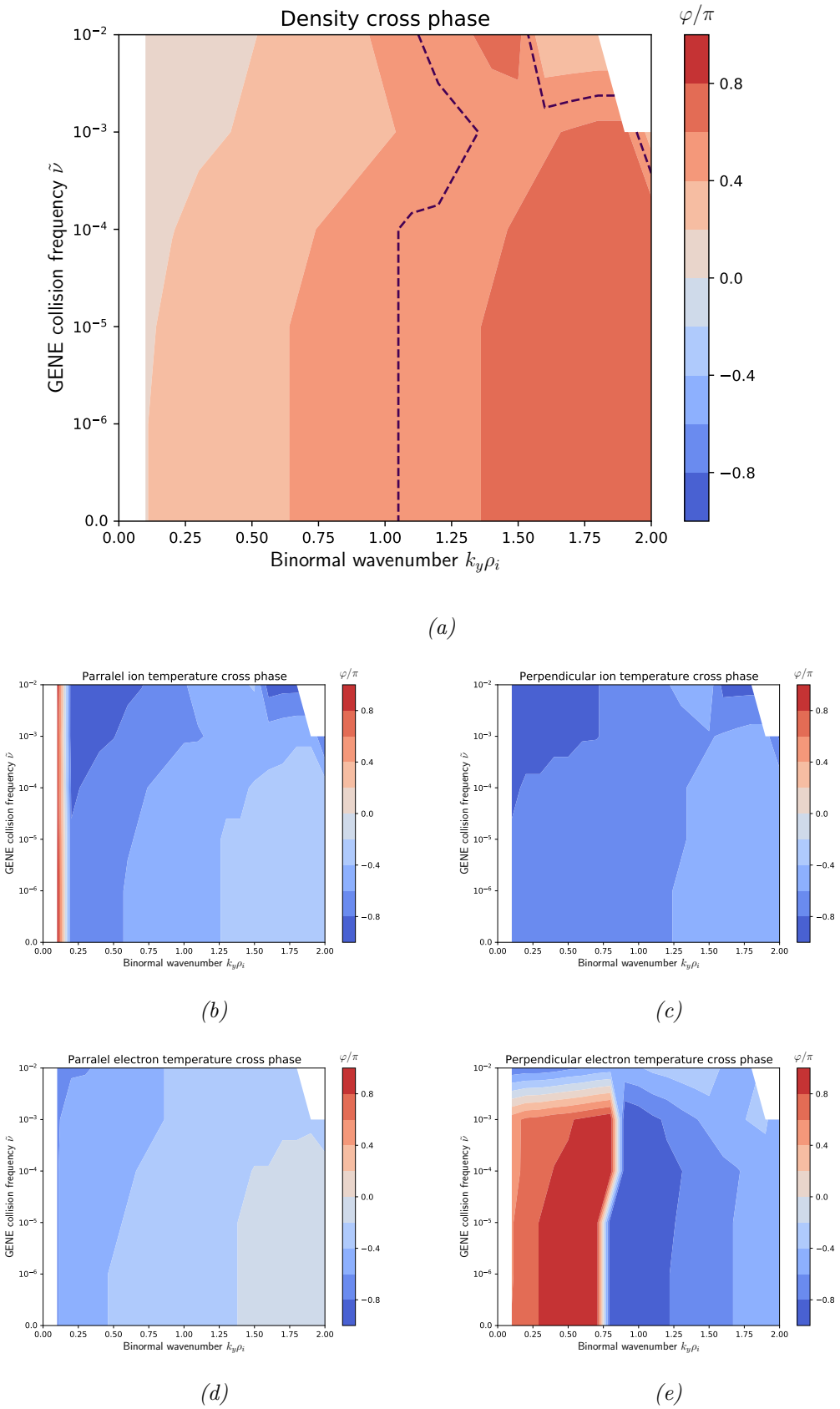

Figure O.1: Cross-phases between the electrostatic potential and (a) density, (b) parallel ion temperature, (c) perpendicular ion temperature, (d) parallel electron temperature and (e) perpendicular electron temperature perturbations in DIII-D.

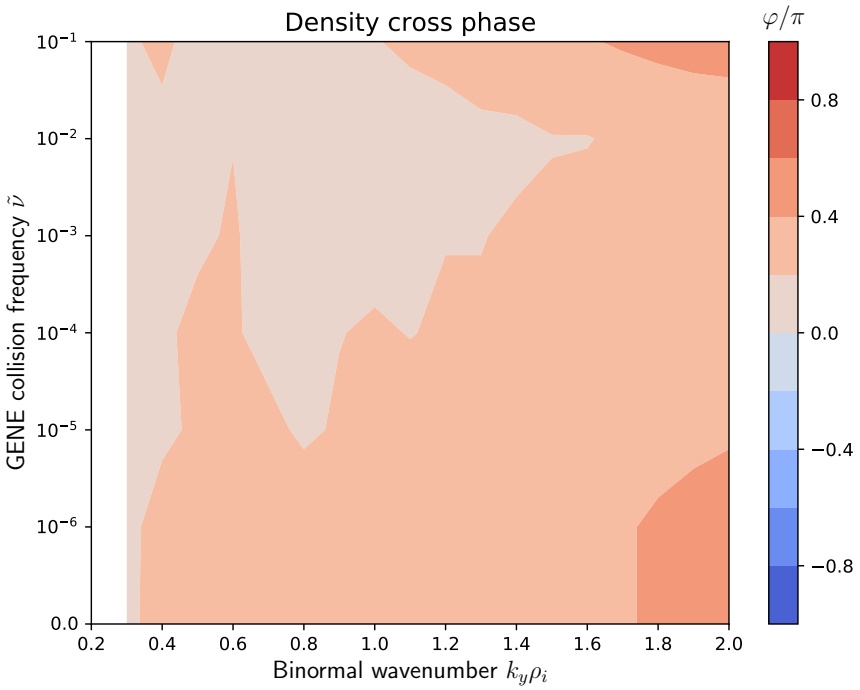

(a)

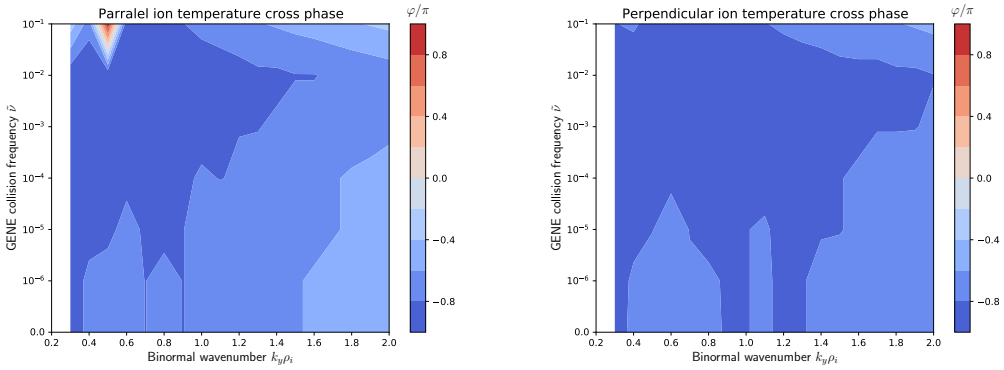

(b) *(c)*

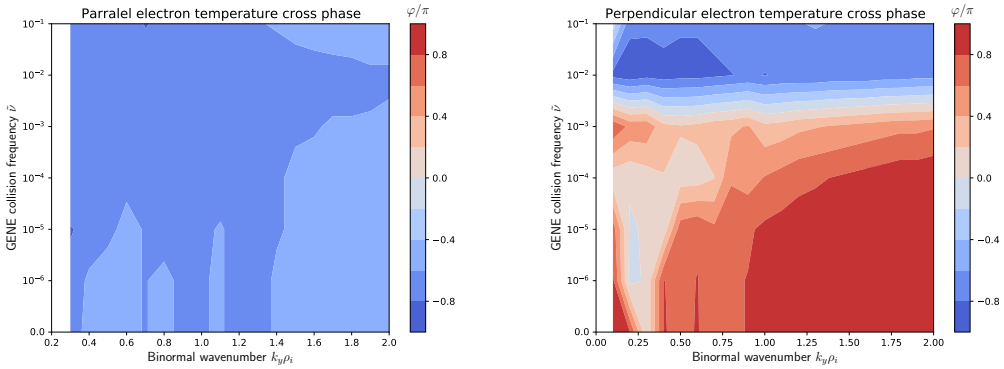

(d) *(e)*

Figure O.2: Cross-phases between the electrostatic potential and (a) density, (b) parallel ion temperature, (c) perpendicular ion temperature, (d) parallel electron temperature and (e) perpendicular electron temperature perturbations in HSX.

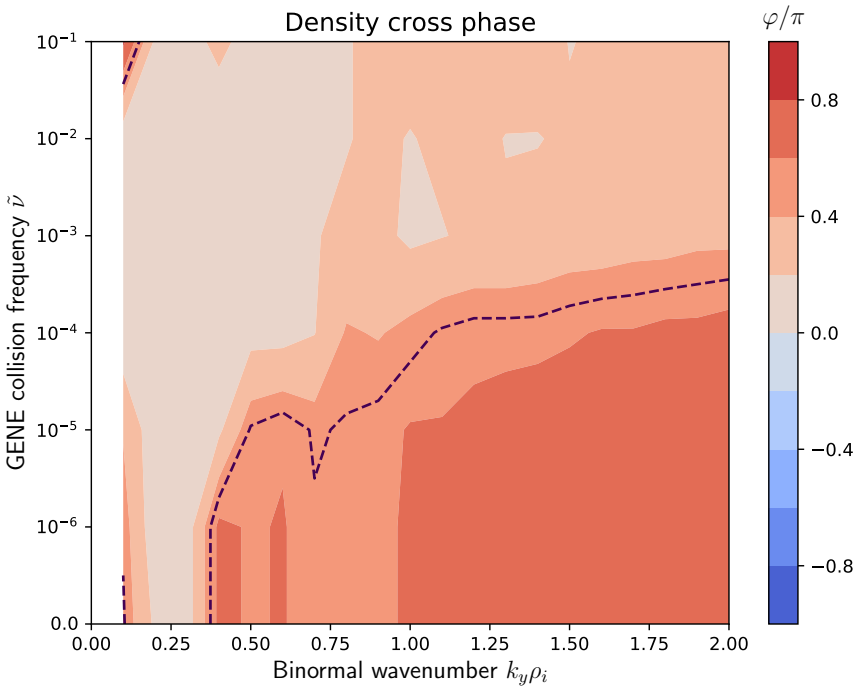

(a)

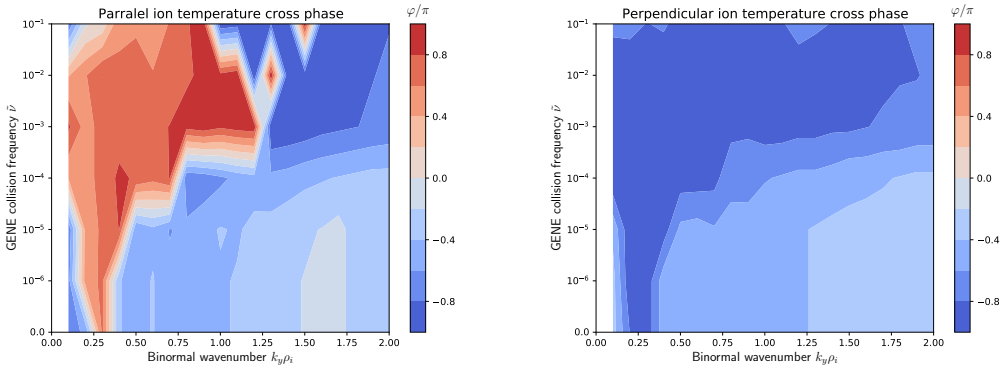

(b) *(c)*

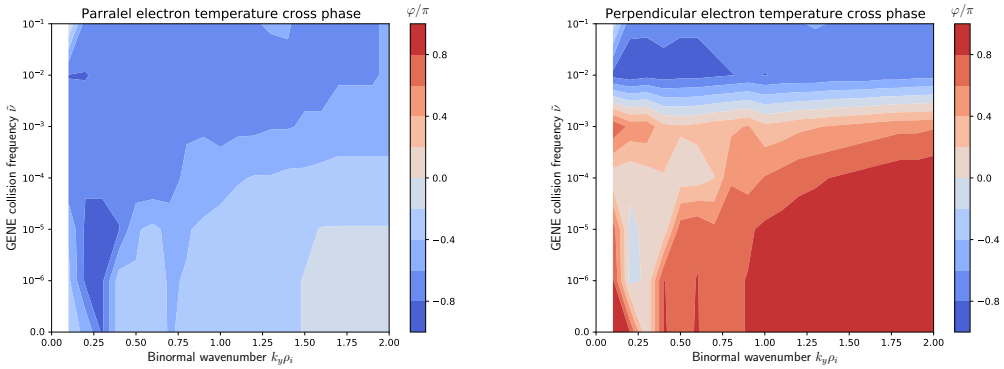

(d) *(e)*

Figure O.3: Cross-phases between the electrostatic potential and (a) density, (b) parallel ion temperature, (c) perpendicular ion temperature, (d) parallel electron temperature and (e) perpendicular electron temperature perturbations in W7-X.

P Validity limits of the perturbative calculation

The validity of the perturbative approach extends only to small frequency shifts, which can be most consistently assessed by the absolute value of the complex frequency shift $|\delta\omega| = \sqrt{\mathrm{Re}[\delta\omega]^2 + \mathrm{Im}[\delta\omega]^2}$ which weights the real and imaginary parts equally. Taken $|\delta\omega| / \langle\omega_0\rangle = 10^{-0.5} \approx 0.3$ as a generous measure for the validity range of small perturbations, it can be seen from Figure P.1 that this the perturbations over a large range of parameter space are larger than acceptable to justify the perturbative approach. Note that the absolute frequency shift in HSX and W7-X are near identical, which can be explained by the similar shape of the contours for real and imaginary parts of the frequency shift of Figure 14 where the fact that $\mathrm{Re}[\delta\omega / \langle\omega_0\rangle]$ is typically smaller in HSX than in W7-X is compensated in the absolute value by the fact that $\mathrm{Im}[\delta\omega / \langle\omega_0\rangle]$ is larger in HSX than in W7-X in the absolute value.

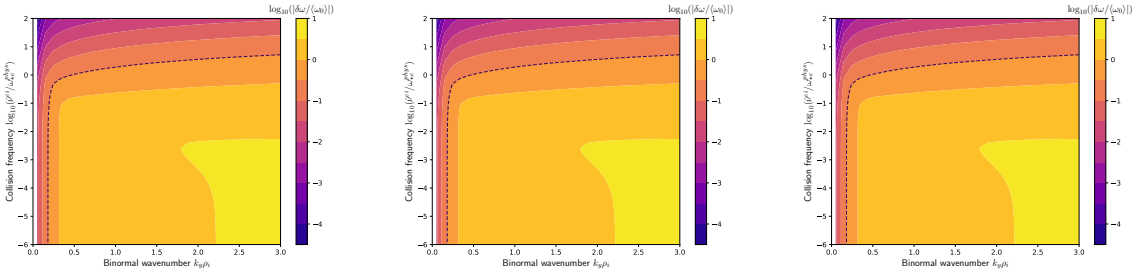

(a) *(b)* *(c)*

Figure P.1: Absolute value of the normalised complex frequency shift as a function of the binormal wavenumber and collision frequency in (a) DIII-D, (b) HSX and (c) W7-X, where the dotted line indicates the 30% mark within which the perturbative approach is justified.

Q Work on free energy description of TEMs

An alternative toolbox to describe microinstabilities is the so-called free energy that is stored in the perturbations, which will increase/decrease in time as the perturbations are destabilised/-damped respectively. This framework is based on a statistical thermodynamic description of the plasma, and starts from the gyroaveraged Hamiltonian [190]

$$H = \frac{1}{2}mv^2 + q\left\langle\phi\right\rangle_{\boldsymbol{R}} - \frac{e^2}{2B}\frac{\partial}{\partial\mu}\left(\left\langle\phi\right\rangle_{\boldsymbol{R}}^2 - \left\langle\phi^2\right\rangle_{\boldsymbol{R}}\right) = H_0 + q\left\langle\phi\right\rangle_{\boldsymbol{R}} - \frac{e^2}{2B}\frac{\partial}{\partial\mu}\left(\left\langle\phi\right\rangle_{\boldsymbol{R}}^2 - \left\langle\phi^2\right\rangle_{\boldsymbol{R}}\right) \quad \text{(Q.1)}$$

where H_0 is simply the unperturbed particle energy. From the Hamiltonian the total energy of the plasma can be constructed by integrating the single particle Hamiltonian over the distribution function in phase space $E = \sum_s \int \mathrm{d}^6\Lambda H f_s$, where $\mathrm{d}^6\Lambda = \mathrm{d}^3\boldsymbol{v}\mathrm{d}^3\boldsymbol{x}$. By splitting the distribution in its equilibrium and perturbed part $f_s = F_{Ms} + \delta f_s$ and subsequently linearising this gives the total plasma energy as [190]

$$E = \sum_s \int \mathrm{d}^6\Lambda \left[H_0 F_{Ms} + H_0\delta f_s + \frac{q_s^2}{2T}F_{Ms}(\phi^2 - \left\langle\phi\right\rangle_{\boldsymbol{R}}^2)\right]. \quad \text{(Q.2)}$$

As the first term to Equation (Q.2) is simply the total kinetic energy of the plasma in equilibrium, the free energy of the perturbations is then subsequently defined as the difference $\mathcal{E} = E - \sum_s \int \mathrm{d}^6\Lambda H_0 F_{Ms}$, and consists of two contributions the kinetic energy of the perturbed particles which as a result of lack of equilibrium will establish itself as entropy and the energy stored within the electric field given by the second and third term of Equation (Q.2) respectively [189].

Note that the free energy $\mathcal{E}$ is defined in real-space using the potential ϕ rather than its Fourier components $\hat{\phi}$. This is because the free energy is a so-called non-linear invariant of the GKE, which is conserved by the convective $\boldsymbol{E}\times\boldsymbol{B}$ non-linearity [193, 194]. This is because in terms of Fourier modes the neglected $\boldsymbol{E}\times\boldsymbol{B}$ non-linearity becomes a convolution in wavenumber-space, given by [191]

$$(\boldsymbol{v}_{\boldsymbol{E}}\cdot\boldsymbol{\nabla}g_s)_{\boldsymbol{k}_\perp} = -\frac{1}{B^2}\sum_{\boldsymbol{k}'_\perp}\boldsymbol{B}\cdot\left(\boldsymbol{k}'_\perp\times\left[\boldsymbol{k}_\perp - \boldsymbol{k}'_\perp\right]\right)J_0(k'_\perp\rho_s)\hat{\phi}_{\boldsymbol{k}'_\perp}\hat{g}_{s,\boldsymbol{k}_\perp-\boldsymbol{k}'_\perp} \quad \text{(Q.3)}$$

which can only shuffle (free) energy between Fourier modes rather than create/dissipate it and is responsible for eventual saturation of turbulence [192]. This is much in analogy with fluid turbulence, where the kinetic energy $mu^2/2$ is also a non-linear invariant of the Navier-Stokes equations as it is conserved by the $\boldsymbol{u}\cdot\boldsymbol{\nabla}\boldsymbol{u}$ non-linearity [8, 192, 193]. Just as in fluid turbulence where the evolution equation of kinetic energy follows by multiplying the Navier-Stokes equation with $\boldsymbol{u}$ and averaging over space [223], the evolution for the free energy in plasma follows by multiplying the GKE Equation (25) with factors that are preserved by the non-linearity, which are[88] the kinetic response $T_s g_s/F_{Ms}$ and the electrostatic potential perturbation $q_s\left\langle\phi\right\rangle_{\boldsymbol{R}}$ and integrating over phase-space (where the additional prefactors make sure that the free energy $\mathcal{E}$ has the proper dimension).

[88] This is because in a formal formulation of gyrokinetics the advective non-linearity can be expressed as a Poisson bracket $\left\{\left\langle\phi\right\rangle_{\boldsymbol{R}}, g_s\right\}$ [67] which has the property that it will vanish when multiplied by any commuting quantity and integrated over space [111, 190]. This does leave room for some discrepancy about the adiabatic response in literature [109], where the adiabatic response as used in this thesis is the particle adiabatic response related to the particle distribution function while in free-energy literature the guiding-center adiabatic response is considered based on both the energy form in the Hamiltonian Equation (Q.1) and the appearance of $\left\langle\phi\right\rangle_{\boldsymbol{R}}$ in the Poisson bracket. This does create an inconsistency in evolution equations of free energy, as the adiabatic response of the distribution function is also taken as $-q_s\left\langle\phi\right\rangle_{\boldsymbol{R}}/T_{s0}F_{Ms}$ which alters the form of Poisson's equation Equation (37), and results in a single evolution equation for both free energy forms [189, 190, 193, 195]. If the adiabatic response of the distribution function is however properly kept as $-q_s\phi/T_{s0}F_{Ms}$ the same derivation results in two separate evolution equations for the free energy quantities as also obtained by [111] which consider a uniform equilibrium magnetic field and kinetic profiles.

Q.1 Derivation of free energy evolution equations

As the $\boldsymbol{E} \times \boldsymbol{B}$ non-linearity conserves the free energy $\mathcal{E}$, the linearised gyrokinetic equation Equation (34) can be used to derive the evolution equations for the free energy, provided that the result is summed over all wavenumbers such that the neglected influence of the non-linearity is effectively "washed out"[89]. Rather than multiplying the GKE with $T_s g_s / F_{Ms}$ and $q_s \langle \phi \rangle_{\boldsymbol{R}}$ to derive the evolution equation for the free energy, the linearised GKE Equation (34) is multiplied by $T_s \hat{g_s}^* / F_{Ms}$ and $q_s J_0 \hat{\phi}^*$ instead and taking the real part of the phase space integral [191, 195]. Doing so would only result in the free energy associated with one particular species, so to get the total free energy one finally has to sum over all species, just like with the total plasma energy Equation (Q.2). Physically this is motivated with the foresight that $\mathcal{E}_{\delta f}$ is an entropy-like quantity and the total entropy of a system that is divisible in subsystems is the the sum of individual entropies [224].

Since the free energy is quadratic in the perturbations (as will be clear shortly) this equivalence between treating the total free energy $\mathcal{E}$ and the combined free energy per Fourier mode $\sum_{\boldsymbol{k}_\perp} \mathcal{E}_{\boldsymbol{k}_\perp}$ is due to Parseval's theorem [193]. Consequently the integration over phase space and spatial averaging can be replaced by $\int \cdots \mathrm{d}^6\Lambda / \int \mathrm{d}^3\boldsymbol{x} = \iint \cdots \mathrm{d}^3\boldsymbol{v} \mathrm{d}^3\boldsymbol{x} \to \sum_{\boldsymbol{k}_\perp} \iint (\cdots)_{\boldsymbol{k}_\perp} \mathrm{d}^3\boldsymbol{v} \frac{\mathrm{d}l}{B} / \int \frac{\mathrm{d}l}{B}$ since the wavevector only accounts for the cross-field variations as a result of the WKB formalism for the perturbations Equation (28). Since however $\boldsymbol{k} \approx \boldsymbol{k}_\perp$, the distinction between $\boldsymbol{k}$ and $\boldsymbol{k}_\perp$ will henceforth be suppressed for notational convenience, unless it is particularly illuminating to do so.

Q.1.1 Derivation of entropy evolution equation

Starting with the entropy-like quantity, multiplying Equation (34) with $T_s \hat{g_s}^* / F_{Ms}$, adding the integrals/summations and taking the real part gives

$$\begin{aligned} \sum_s \sum_{\boldsymbol{k}} \mathrm{Re} \left[\int \mathrm{d}^3\boldsymbol{v} \int \frac{\mathrm{d}l}{B} T_s \frac{\hat{g}^*_{s,\boldsymbol{k}}}{F_{Ms}} v_\parallel \boldsymbol{\nabla}_\parallel \hat{g}_{s,\boldsymbol{k}} - T_s \frac{\hat{g}^*_{s,\boldsymbol{k}}}{F_{Ms}} i \left(\omega_{\boldsymbol{k}} - \omega_{d,s} \right) \hat{g}_{s,\boldsymbol{k}} - T_s \frac{\hat{g}^*_{s,\boldsymbol{k}}}{F_{Ms}} \hat{C}_{\boldsymbol{k}} \right] = \\ - \sum_s \sum_{\boldsymbol{k}} \mathrm{Re} \left[\int \mathrm{d}^3\boldsymbol{v} \int \frac{\mathrm{d}l}{B} i T_s \frac{\hat{g}^*_{s,\boldsymbol{k}}}{F_{Ms}} \frac{q_s}{T_s} J_0 \hat{\phi}_{\boldsymbol{k}} \left(\omega_{\boldsymbol{k}} - \omega^T_{\star s} \right) F_{Ms} \right] \end{aligned} \tag{Q.4}$$

which is best expanded on a term-by-term basis. Starting with the parallel dynamics term on the left-hand side of Equation (Q.4), and splitting the integration over position and velocity variables gives

$$\mathrm{Re} \left[\int \mathrm{d}^3\boldsymbol{v} \int \frac{dl}{B} \frac{T_s}{F_{Ms}} v_\parallel \hat{g}^*_{s,\boldsymbol{k}} \boldsymbol{\nabla}_\parallel \hat{g}_{s,\boldsymbol{k}} \right] = \mathrm{Re} \left[\int \mathrm{d}^3\boldsymbol{v} \frac{T_s}{F_{Ms}} v_\parallel \int \frac{\mathrm{d}l}{B} \hat{g}^*_{s,\boldsymbol{k}} \boldsymbol{\nabla}_\parallel \hat{g}_{s,\boldsymbol{k}} \right]$$

If pitch-angle velocity coordinates are used for the velocity integral, then as a result of the Jacobian $\mathrm{d}^3\boldsymbol{v} \to \sum_{\sigma=\pm} \pi v^2 B / \sqrt{1 - \lambda B} \, \mathrm{d}v \, \mathrm{d}\lambda$ the $1/B$ factor will cancel such that the integration along the field line can be performed using integration by parts [195]

$$\int_{-\infty}^{\infty} \mathrm{d}l \, \hat{g}^*_{s,\boldsymbol{k}} \boldsymbol{\nabla}_\parallel \hat{g}_{s,\boldsymbol{k}} = \left| \hat{g}_{s,\boldsymbol{k}} \right|^2 \Big|_{l=-\infty}^{l=+\infty} - \int_{-\infty}^{\infty} \mathrm{d}l \, \hat{g}_{s,\boldsymbol{k}} \boldsymbol{\nabla}_\parallel \hat{g}^*_{s,\boldsymbol{k}} = - \left(\int_{-\infty}^{\infty} \mathrm{d}l \, \hat{g}_{s,\boldsymbol{k}} \boldsymbol{\nabla}_\parallel \hat{g}^*_{s,\boldsymbol{k}} \right)^*$$

[89] Mathematically this follows from a summation of Equation (Q.3) over wavenumbers $\boldsymbol{k}$, such that the double sum $\sum_{\boldsymbol{k}} \sum_{\boldsymbol{k}'}$ will repeat every possible $(\boldsymbol{k}, \boldsymbol{k}')$ pair and will vanishes as the cross-product is reversed in the outer sum. Physically this is because the $\boldsymbol{E} \times \boldsymbol{B}$ non-linearity only exchanges free energy between different modes such that an inclusion of Equation (Q.3) to the linearised GKE Equation (34) would result in an additional source/sink in the evolution equation for the free energy for each Fourier mode $\frac{\partial \mathcal{E}_{\boldsymbol{k}}}{\partial t}$, but all these internal sources/sinks cancel when adding up the free energy stored in each Fourier mode to get the evolution total free energy $\frac{\partial \mathcal{E}}{\partial t} = \sum_{\boldsymbol{k}} \frac{\partial \mathcal{E}_{\boldsymbol{k}}}{\partial t}$, similarly to how in Classical Mechanics all internal forces between particles cancel and the dynamics of a multibody system is given by Newton's equation of motion for the centre of mass acted upon only by the external forces [108].

where the boundary term vanishes since $l = \pm\infty$ correspond to the points where a field-line will bite its own tail[90] As this integral is the opposite of its own complex conjugate it must be purely imaginary, and consequently its real part vanishes.

Moving on to the second term on the left-hand side of Equation (Q.4), the procedure of simplifying the integral is more straightforward

$$\mathrm{Re}\left[\int \mathrm{d}^3\boldsymbol{v} \int \frac{\mathrm{d}l}{B} \frac{T_s}{F_{Ms}} \hat{g}^*_{s,\boldsymbol{k}} i(\omega_{\boldsymbol{k}} - \omega_{d,s}) \hat{g}_{s,\boldsymbol{k}}\right] = -\gamma_{\boldsymbol{k}} \int \mathrm{d}^3\boldsymbol{v} \int \frac{\mathrm{d}l}{B} \frac{T_s}{F_{Ms}} |\hat{g}_{s,\boldsymbol{k}}|^2$$

by using the complex frequency $\omega = \omega_R + i\gamma$, and the fact that $|\hat{g}_{s,\boldsymbol{k}}|^2 \in \mathbb{R}$ along with all other equilibrium quantities including the magnetic drift frequency.

The term involving the collision operator cannot be simplified by exploiting a splitting in real/imaginary parts without specifying a collision operator so it will be left as is. Moving on to the right-hand side of Equation (Q.4) there is only a a single term, however it cannot be straightforwardly simplified like the other terms above by identifying its real and imaginary parts since those depend on the phase between $\hat{g}_{\boldsymbol{k}}, \hat{\phi}_{\boldsymbol{k}}$. This phase cannot be arbitrary however as the (charge) density perturbations are directly linked to perturbations in the electrostatic potential through the quasi-neutrality condtion Equation (37). Therefore by explicitly including the sum over species this time the first term from the angular brackets can be rewritten as

$$\begin{aligned}\sum_s \mathrm{Re}\left[i\omega_{\boldsymbol{k}} \int \frac{\mathrm{d}l}{B} \hat{\phi}_{\boldsymbol{k}} q_s \int \mathrm{d}^3\boldsymbol{v} \hat{g}^*_{s,\boldsymbol{k}} J_0\right] &= \mathrm{Re}\left[i\omega_{\boldsymbol{k}} \int \frac{\mathrm{d}l}{B} \hat{\phi}_{\boldsymbol{k}} \sum_s \left(q_s \int \mathrm{d}^3\boldsymbol{v} \hat{g}^*_{s,\boldsymbol{k}} J_0\right)\right] \\ &= \mathrm{Re}\left[i\omega_{\boldsymbol{k}} \int \frac{\mathrm{d}l}{B} \hat{\phi}_{\boldsymbol{k}} \sum_s n_s \frac{q_s^2}{T_s} \hat{\phi}^*_{\boldsymbol{k}}\right] = -\gamma_{\boldsymbol{k}} \sum_s \int \frac{\mathrm{d}l}{B} \frac{n_s q_s^2}{T_s} \left|\hat{\phi}_{\boldsymbol{k}}\right|^2\end{aligned}$$

where the quasi-neutrality condition eliminates the kinetic response and leaves $\omega_{\boldsymbol{k}}$ as the only complex value under the $\mathrm{Re}[\cdots]$ operator. The remaining term on the left-hand side involving the diamagnetic frequency $\omega^T_{\star s}$ cannot be rewritten in a similar way, as unlike $\omega_{\boldsymbol{k}}$ it cannot be evacuated from the velocity integral because of its velocity dependence, and it thus cannot be cast in terms of the quasi-neutrality condition. The imaginary unit i can however be removed from this expression by using $\mathrm{Re}[i\zeta] = \mathrm{Im}[\zeta^*]$ which holds for any $\zeta \in \mathbb{C}$, which will be more advantageous for identifying its physical significance.

Compiling all of the above intermediate results and substituting them back in Equation (Q.4) then leads to the "evolution" equation

$$\begin{aligned}&\sum_{\boldsymbol{k}} \gamma_{\boldsymbol{k}} \sum_s \int \frac{\mathrm{d}l}{B} \left(\int \frac{T_s}{F_{Ms}} |\hat{g}_{s,\boldsymbol{k}}|^2 \mathrm{d}^3\boldsymbol{v} - \frac{q_s^2 n_s}{T_s} |\phi_{\boldsymbol{k}}|^2\right) = \\ &\sum_{\boldsymbol{k}} \mathrm{Im}\left[\sum_s q_s \int \frac{\mathrm{d}l}{B} \hat{\phi}^*_{\boldsymbol{k}} \int \mathrm{d}^3\boldsymbol{v} \hat{g}_{s,\boldsymbol{k}} \omega^T_{\star s} J_0\right] + \sum_{\boldsymbol{k}} \mathrm{Re}\left[\sum_s \int \frac{\mathrm{d}l}{B} \int \mathrm{d}^3\boldsymbol{v} \frac{T_s}{F_{Ms}} \hat{g}^*_{s,\boldsymbol{k}} \left\langle \hat{C}_{\boldsymbol{k}} \right\rangle_{\boldsymbol{R}}\right]\end{aligned} \tag{Q.5}$$

where all terms involving the growth rate have been collected on the left-hand side.

[90] Alternatively, rather than imposing periodic boundary conditions, the the contribution of this integral to the total free energy will vanish as long as $|\hat{g}_{s,\boldsymbol{k}}|^2$ remains bounded, as the free energy formally involves a normalisation along the field line $/\oint \mathrm{d}l/B$ [195].

Q.1.2 Derivation of field energy evolution equation

Moving on to the field energy-like quantity, multiplying Equation (34) with $q_s J_0 \hat{g_s}$, adding the integrals/summations and taking the real parts gives

$$\sum_s \sum_{\boldsymbol{k}} \mathrm{Re}\left[\int \mathrm{d}^3\boldsymbol{v} \int \frac{\mathrm{d}l}{B} q_s J_0 \hat{\phi}^*_{\boldsymbol{k}} v_\parallel \boldsymbol{\nabla}_\parallel \hat{g}_{s,\boldsymbol{k}} - q_s J_0 \hat{\phi}^*_{\boldsymbol{k}} i\left(\omega_{\boldsymbol{k}} - \omega_{d,s}\right) \hat{g}_{s,\boldsymbol{k}} - q_s J_0 \hat{\phi}^* \hat{C}_{\boldsymbol{k}}\right] = \\ -\sum_s \mathrm{Re}\left[\int \mathrm{d}^3\boldsymbol{v} \int \frac{\mathrm{d}l}{B} i q_s J_0 \hat{\phi}^*_{\boldsymbol{k}} \frac{q_s}{T_s} J_0 \phi_{\boldsymbol{k}} \left(\omega_{\boldsymbol{k}} - \omega^T_{\star,s}\right) F_{Ms}\right] \quad . \tag{Q.6}$$

Working again on a term-by-term basis, the parallel dynamics term on the left-hand side of Equation (Q.6) cannot be simplified like before with the entropy evolution equation because it involves a mixing between $\hat{\phi}_{\boldsymbol{k}}, \hat{g_s}$ which cannot be rewritten in terms of the quasi-neutrality condition to eliminate the unknown phase. Specifically if the same trick of integration by parts along the field line would be performed than one would obtain

$$\int_{-\infty}^{\infty} \mathrm{d}l\, \hat{\phi}^*_{\boldsymbol{k}} \boldsymbol{\nabla}_\parallel \hat{g}_{s,\boldsymbol{k}} = \hat{\phi}^*_{\boldsymbol{k}} g_{s,\boldsymbol{k}}\Big|_{l=-\infty}^{l=+\infty} - \int_{-\infty}^{\infty} \mathrm{d}l\, \hat{g}^*_{s,\boldsymbol{k}} \boldsymbol{\nabla}_\parallel = -\int_{-\infty}^{\infty} \mathrm{d}l\, \hat{g}^*_{s,\boldsymbol{k}} \boldsymbol{\nabla}_\parallel \hat{\phi}^*_{\boldsymbol{k}} \tag{Q.7}$$

where the boundary vanishes again because they correspond to the points where the field line bites its own tail. Unlike before, the "new" integral obtained by integration by parts is not the complex conjugate of the "old" integral, and thus the parallel dynamics will contribute to the evolution of the free energy since it must have a real part. Equation (Q.7) will be useful later when the resulting evolutions are interpreted as it shows one can swap the derivative between $\hat{\phi}$ and g_s at the cost of a minus sign. The second term on the left-hand side (drift frequency $\omega_{\boldsymbol{k}} - \omega_{ds}$ term) will also involve the phase between the perturbations, however just like with the diamagnetic frequency term above $\omega_{\boldsymbol{k}} - \omega^T_{\star s}$, this can be partially recast in terms of the quasi-neutrality condition since $\omega_{\boldsymbol{k}}$ is independent of velocity

$$\sum_s \mathrm{Re}\left[\int \mathrm{d}^3\boldsymbol{v} \int \frac{\mathrm{d}l}{B} q_s J_0 \hat{\phi}^*_{\boldsymbol{k}} i\omega_{\boldsymbol{k}} \hat{g}_{s,\boldsymbol{k}}\right] = \mathrm{Re}\left[i\omega_{\boldsymbol{k}} \int \frac{\mathrm{d}l}{B} \hat{\phi}^*_{\boldsymbol{k}} \sum_s q_s \int \mathrm{d}^3\boldsymbol{v} J_0 \hat{g}_{s,\boldsymbol{k}}\right] = -\gamma_{\boldsymbol{k}} \sum_s \int \frac{\mathrm{d}l}{B} \frac{\mathrm{d}l}{B} \frac{n_s q_s^2}{T_s} \left|\hat{\phi}_{\boldsymbol{k}}\right|^2$$

where Equation (37) is used once more. The same simplification cannot be made for the drift frequency term however because of the dependence of the magnetic drift velocity Equation (27) on particle velocity, and is therefore also left as is.

Also much like before the term involving the collision operator cannot be simplified without first specifying a specific form of the collision operator, such that all that is left to simplify is the left-hand side term of Equation (Q.6). Fortunately, since side of the GKE is proportional to $\hat{\phi}_{\boldsymbol{k}}$ rather than $g_{\hat{s},\boldsymbol{k}}$ the phase between the perturbations is not involved for the remaining and the simplification procedure is straightforward

$$\sum_s \mathrm{Re}\left[\int \mathrm{d}^3\boldsymbol{v} \int \frac{\mathrm{d}l}{B} i \frac{q_s^2}{T_s} J_0^2 |\phi_{\boldsymbol{k}}|^2 \left(\omega_{\boldsymbol{k}} - \omega^T_{\star,s}\right) F_{Ms}\right] = \sum_s \mathrm{Re}\left[i\omega_{\boldsymbol{k}} \int \frac{\mathrm{d}l}{B} \frac{q_s^2}{T_s} |\phi_{\boldsymbol{k}}|^2 \int \mathrm{d}^3\boldsymbol{v} J_0^2 F_{Ms}\right] + 0$$

where the contribution from the diamagnetic drift vanishes as all terms are purely real valued. The remaining integral over the square of the Bessel function has been encountered before during the perturbative calculation in Section 3.3 and by using the integrals from Equation (I.1) it follows that $\int \mathrm{d}^3\boldsymbol{v} J_0^2 F_{Ms} = n_s I_0\left(\frac{(k_\perp \rho_{Ts})^2}{2}\right) \exp\left(-\frac{(k_\perp \rho_{Ts})^2}{2}\right) = n_s \Gamma_{0s}$ using the same shorthand notation as in Section 3.3 but with the index s added as a reminder that the argument of the modified Bessel and exponential functions should be taken with the thermal gyroradius of each species.

Compiling all of these intermediate results and substituting them back in Equation (Q.6) then leads to the "evolution" equation

$$\begin{aligned}\sum_{\boldsymbol{k}}\gamma_{\boldsymbol{k}}\sum_s\int\frac{\mathrm{d}l}{B}\frac{n_s q_s^2}{T_s}\left|\hat{\phi}_{\boldsymbol{k}}\right|^2(1-\Gamma_{0s}) &= \sum_{\boldsymbol{k}}\mathrm{Re}\left[\sum_s q_s\int\frac{\mathrm{d}l}{B}\int\mathrm{d}^3\boldsymbol{v}J_0\hat{\phi}^*_{\boldsymbol{k}}\hat{C}_{\boldsymbol{k}}\right]\\ &\quad-\sum_{\boldsymbol{k}}\mathrm{Re}\left[\sum_s q_s\int\frac{\mathrm{d}l}{B}\int\mathrm{d}^3\boldsymbol{v}J_0\hat{\phi}^*_{\boldsymbol{k}}\left(v_\parallel\boldsymbol{\nabla}_\parallel+i\omega_{ds}\right)\hat{g}_{s,\boldsymbol{k}}\right]\end{aligned} \tag{Q.8}$$

where all terms involving the growth have again been collected on the left-hand side.

Q.2 Interpretation of free energy evolution equations

Just as with the derivation of the free energy evolution equations, their interpretation is best done independently and on a term-by-term basis.

Q.2.1 Interpretation of the entropy evolution equation

The term on the left-hand side of Equation (Q.5) is best interpreted by not consdidering the kinetic and adiabatic responses separately, but by considering the total perturbation to the distribution function of the distribution function Equation (24) in Fourier space instead. By doing so the integrand along the field line can be written as

$$\int\frac{T_s}{F_{Ms}}|\hat{g}_{s,\boldsymbol{k}}|^2\mathrm{d}^3\boldsymbol{v}-\frac{q_s^2n_s}{T_s}|\phi_{\boldsymbol{k}}|^2=\int\frac{T_s}{F_{Ms}}\left|\hat{\delta f}_{s,\boldsymbol{k}}\right|^2\mathrm{d}^3\boldsymbol{v}+\hat{\phi}^*_{\boldsymbol{k}}q_s\int\hat{\delta f}_{s,\boldsymbol{k}}\mathrm{d}^3\boldsymbol{v}+\hat{\phi}_{\boldsymbol{k}}q_s\int\hat{\delta f}^*_{s,\boldsymbol{k}}\mathrm{d}^3\boldsymbol{v}$$

which follows by writing $\hat{g}_{s,\boldsymbol{k}}=\hat{\delta f}_{s,\boldsymbol{k}}+q_sF_{Ms}\hat{\phi}_{\boldsymbol{k}}/T_s$ and performing the velocity integrals over the Maxwellian. When performing the sum over species the latter two terms will cancel as they reduce to the quasi-neutrality condition $\sum_s q_s\delta n_s=0$. Consequently the left-hand side of Equation (Q.5) can be interpreted as a time derivative of the amplitude in perturbation in distribution function

$$\sum_{\boldsymbol{k}}\gamma_{\boldsymbol{k}}\sum_s\int\frac{\mathrm{d}l}{B}\int\frac{T_s}{F_{Ms}}\left|\hat{\delta f}_{s,\boldsymbol{k}}\right|^2\mathrm{d}^3\boldsymbol{v}=\frac{\partial}{\partial t}\sum_{\boldsymbol{k}}\sum_s\int\frac{\mathrm{d}l}{B}\int\mathrm{d}^3\boldsymbol{v}\frac{T_s}{2F_{Ms}}\left|\hat{\delta f}_{s,\boldsymbol{k}}\right|^2$$

which follows from recalling that the perturbations have an $\exp(-i\omega_{\boldsymbol{k}}t)$ time dependence with a complex mode frequency $\omega_{\boldsymbol{k}}=\omega_{R,\boldsymbol{k}}+i\gamma_{\boldsymbol{k}}$ such that the squared amplitude $\left|\hat{\delta f}_{s,\boldsymbol{k}}\right|^2$ has a growth rate of $2\gamma_{\boldsymbol{k}}$. This defines the first free energy quantity $\mathcal{E}_{\delta f}$, whose physical significance is related to the continuous extension of the Gibbs entropy to phase-space $S_s=-\iint f_s\ln f_s\mathrm{d}^3\boldsymbol{v}\mathrm{d}^3\boldsymbol{x}$ [111]. By inserting $f_s=F_{Ms}+\delta f_s$ and expanding the entropy for $\delta f_s/F_{Ms}\ll 1$

$$\begin{aligned}S_s&=-\iint(F_{Ms}+\delta f_s)\ln(F_{Ms}+\delta f_s)\mathrm{d}^6\Lambda\approx-\iint(F_{Ms}+\delta f_s)\left[\ln(F_{Ms})+\frac{\delta f_s}{F_{Ms}}-\frac{1}{2}\frac{\delta f_s^2}{F_{Ms}^2}+\mathcal{O}\left(\delta^3\right)\right]\mathrm{d}^6\Lambda\\ &=-\left(\iint F_{Ms}\ln(F_{Ms})\mathrm{d}^6\Lambda+\iint\delta f_s\ln(F_{Ms})\mathrm{d}^6\Lambda+\iint\delta f_s\mathrm{d}^6\Lambda+\frac{1}{2}\iint\frac{\delta f_s^2}{F_{Ms}}\mathrm{d}^6\Lambda\right)\\ &=-\iint F_{Ms}\ln(F_{Ms})\mathrm{d}^6\Lambda-\frac{1}{2}\iint\frac{\delta f_s^2}{F_{Ms}}\mathrm{d}^6\Lambda\equiv S_{0,s}+\delta S_s\end{aligned}$$

where the perturbations must satisfy $\int\delta f_s\mathrm{d}^3\boldsymbol{x}$ to have a zero net contribution to the number of particles in the system, it follows that $\mathcal{E}_{\delta f}=-\sum_s T_s\delta S_s$ is in fact the energy stored in the fluctuation entropy (as already hinted to by the names of the sections).

The identification of $\mathcal{E}_{\delta f}$ as entropy also helps to identify the second term on the right-hand of Equation (Q.5), since in absence of equilibrium profile gradients $\omega_{\star s}^T = 0$ and Equation (Q.5) reduces to

$$\frac{\partial}{\partial t}\sum_s\sum_{\boldsymbol{k}} -\delta S_{s,\boldsymbol{k}} = \sum_{\boldsymbol{k}} \mathrm{Re}\left[\sum_s \int \frac{\mathrm{d}l}{B}\int \mathrm{d}^3\boldsymbol{v}\frac{T_s}{F_{Ms}}\hat{g}^*_{s,\boldsymbol{k}}\left\langle \hat{C}_{\boldsymbol{k}}\right\rangle_{\boldsymbol{R}}\right]$$

which is the extension of Boltzmann's H-theorem for the perturbation to the distribution function, and consequently this represents irreversible dissipation of the perturbations by particle collisions such that collisions have a damping effect on the growth rate (as $\mathcal{E}_{\delta f}$ is positive definite) [8]. This is most readily seen by substituting the linearised BGK collision operator Equation (46) such that the term on the right-hand side $-\sum_{\boldsymbol{k}}\mathrm{Re}\left[\sum_s\int\frac{\mathrm{d}l}{B}\int\mathrm{d}^3\boldsymbol{v}\nu_s\frac{T_s}{F_{Ms}}|\hat{g}_{s,\boldsymbol{k}}|^2\right]$ is negative definite, but the same property also holds for more advanced collision operators used in gyrokinetic simulation codes [87–90].

Lastly the first term on the right-hand side of Equation (Q.5) must contains the role of the plasma gradients through the diamagnetic frequency Equation (30) and must represent the driving factors of the instability to balance the dissipation provided by collisions. According to the simple waveform model of drift waves from Section 2.1 it are the density and temperature gradients that are responsible for driving the perturbations unstable if there is an unfavourable phase-shift between the potential perturbations and the density/temperature perturbations. As the temperature and density perturbations follow from velocity moments of g_s, the phase-shift in the potential perturbation can be incorporated as $\phi = \sum_{\boldsymbol{k}}\hat{\phi}'_{\boldsymbol{k}}e^{i(\boldsymbol{k}\cdot\boldsymbol{x}-\omega_{\boldsymbol{k}}t-\varphi_{s,\boldsymbol{k}})}$, which affects the actual amplitude of the Fourier amplitude $\hat{\phi}_{\boldsymbol{k}} = \hat{\phi}'_{\boldsymbol{k}}\exp(-i\varphi_{\boldsymbol{k}})$ which is defined on an expansion of the perturbation in an $e^{i(\boldsymbol{k}\cdot\boldsymbol{x}-\omega_{\boldsymbol{k}}t)}$ basis. With such a phase-shift the first term on the right-hand side of Equation (Q.5) becomes

$$\begin{aligned}\sum_{\boldsymbol{k}}\mathrm{Im}\left[\sum_s q_s\int\frac{\mathrm{d}l}{B}\hat{\phi}^*_{\boldsymbol{k}}\int\mathrm{d}^3\boldsymbol{v}\hat{g}_{s,\boldsymbol{k}}\omega_{\star s}^T J_0\right] &= \sum_{\boldsymbol{k}}\sum_s q_s\int\frac{\mathrm{d}l}{B}\int\mathrm{d}^3\boldsymbol{v}\,\mathrm{Im}\left[\hat{\phi}^*_{\boldsymbol{k}}\hat{g}_{s,\boldsymbol{k}}\right]\omega_{\star s}^T J_0\\ &= \sum_{\boldsymbol{k}}\sum_s q_s\left(\int\frac{\mathrm{d}l}{B}\int\mathrm{d}^3\boldsymbol{v}\left|\hat{\phi}_{\boldsymbol{k}}\right||\hat{g}_{s,\boldsymbol{k}}|\omega_{\star s}^T J_0\right)\sin(\varphi_{s,\boldsymbol{k}})\end{aligned}$$

and consequently a phase shift of $\varphi_{s,\boldsymbol{k}}\in(0,\pi)$ results in a destabilising influence with a maximum destabilisation for $\pi/2$, while a phase shift of $\varphi_{s,\boldsymbol{k}}\in(-\pi,0)$ results in a stabilising influence and in the special case that the perturbations are completely in phase the basic collisionless drift wave from Section 2.1.1 is recovered. A novelty from the free energy formalism is that the different species can exert a different influence on the growth rate, while the basic models from from Section 2.1 only highlighted the main instability driving mechanism.

Q.2.2 Interpretation of field energy evolution equaiton

Completely analogous to the interpretation of Equation (Q.5) the term on the left-hand side of Equation (Q.8) identifies the growth of a free-energy quantity $\mathcal{E}_{\phi,\boldsymbol{k}} = \int\frac{\mathrm{d}l}{B}\frac{n_s q_s^2}{2T_s}\left|\hat{\phi}_{\boldsymbol{k}}\right|^2(1-\Gamma_0)$ which is quadratic the perturbations and also positive definite since $0\leq\Gamma_0\leq 1$. The second free energy quantity $\mathcal{E}_\phi$ is essentially the gyrokinetic generalisation of the kinetic energy due to the $\boldsymbol{E}\times\boldsymbol{B}$ flow [190, 191]. This can be seen by an analogy with the fluid model[91] of the plasma

[91]The extension to the kinetic picture is straightforward, with the total kinetic energy being $\sum_s\int\frac{m_s v_s^2}{2}f_s\mathrm{d}^3\boldsymbol{v_s}\mathrm{d}^3\boldsymbol{x}$. In the limit in which the fluid picture holds, collisionality is sufficiently large to establish equilibrium such that the distribution function $f_s\rightarrow F_{Ms}(\boldsymbol{v}-\boldsymbol{u_E})$ becomes a shifted Maxwellian around the $\boldsymbol{E}\times\boldsymbol{B}$ velocity. The integral then results in a thermal component and a bulk component as a result of the mean flow $\boldsymbol{u_E}$, the latter which is being used here.

where both electrons and ions will move with a bulk flow velocity which has a kinetic energy of

$$\sum_s \int \frac{1}{2} n_s m_s \boldsymbol{u}_{\boldsymbol{E}}^2 \mathrm{d}^3\boldsymbol{x} = \sum_s \int \frac{1}{2} n_s m_s \frac{\phi^2}{B^2} \|\boldsymbol{e_b} \times \boldsymbol{\nabla} \ln \phi\|^2 \mathrm{d}^3\boldsymbol{x} \sim \sum_s \int \frac{1}{4} \frac{n_s q_s^2}{T_s} \phi^2 \left(\frac{\rho_{Ts}}{L_{\phi,\perp}}\right)^2$$

where the last step follows from writing the magnetic field strength in terms of the gyrofrequency of a thermal particle $B = m_s v_{Ts}/q_s\rho_{Ts}$, the fact that $\boldsymbol{e_b}$ is a unit vector and an characteristic perpendicular length scale of the electrostatic potential fluctuations has been introduced similar to L_{ns}, L_{Ts}. To compare this fluid picture with $\mathcal{E}_\phi$ the appropriate long wavelength limit for the fluctuations $k_\perp\rho \ll 1$ has to be taken, for which $\Gamma_{0s} \approx 1 - (k_\perp\rho_{Ts})^2/2 + \mathcal{O}((k_\perp\rho_{Ts})^4)$ resulting in

$$\lim_{k_\perp\rho_{Ts}\to 0} \mathcal{E}_{\phi,\boldsymbol{k}} \approx \sum_s \int \frac{\mathrm{d}l}{B} \frac{n_s q_s^2}{2T_s} \left|\hat{\phi}_{\boldsymbol{k}}\right|^2 \frac{(k_\perp\rho_{Ts})^2}{2}$$

which by identifying the wavenumber as the inverse correlation length of the fluctuations $k_\perp \sim 1/L_{\phi,\perp}$ completely matches the fluid picture. Consequently $\mathcal{E}_\phi$ represents the energy stored in the fluctuating electric field in a gyrokinetic way.

The second term on the right-hand side of Equation (Q.8) requires some more effort to identify, but fortunately the tricky part has already been done in Appendix Q.1. The drift term can be rewritten by recalling that the magnetic drift frequency is defined as $\omega_{ds} = \boldsymbol{k}_\perp \cdot \boldsymbol{v_{ds}}$ such that

$$\sum_{\boldsymbol{k}} \mathrm{Re}\left[\sum_s q_s \int \frac{\mathrm{d}l}{B} \int \mathrm{d}^3\boldsymbol{v} J_0 \hat{\phi}_{\boldsymbol{k}}^* \left(v_\parallel \boldsymbol{\nabla}_\parallel + i\omega_{ds}\right) \hat{g}_{s,\boldsymbol{k}}\right] = -\sum_{\boldsymbol{k}} \mathrm{Re}\left[\sum_s q_s \int \frac{\mathrm{d}l}{B} \int \mathrm{d}^3\boldsymbol{v} \hat{g}_{s,\boldsymbol{k}}^* \left(v_\parallel \boldsymbol{\nabla}_\parallel + i\boldsymbol{k}_\perp \cdot \boldsymbol{v_{ds}}\right) J_0 \hat{\phi}_{\boldsymbol{k}}\right]$$

where Equation (Q.7) is used to rewrite the parallel dynamics in favour of a derivative of $\hat{\phi}$ and the complex conjugation of the drift term is allowed as it does not alter the real part of the integral. Now recalling that in Fourier space $i\boldsymbol{k}_\perp$ is equivalent to $\boldsymbol{\nabla}_\perp$ in real-space it follows that the second term on the right-hand side of Equation (Q.8) is the Fourier analogue to the $\boldsymbol{J} \cdot \boldsymbol{E}$ Joule heating that the gyroaverage perturbed electric field exerts on the plasma[92] which can either draw away energy from the electric field or provide energy to it corresponding to a stabilising/destabilising effect on the growth rate respectively.

The first term on the right-hand side of Equation (Q.8) does not have a straightforward interpretation by rewriting it and making an analogy with a familiar branch of physics. Rather if the collisions are interpreted as pitch-angle scattering, then the net result of a collision will be to "reset" the particle gyration and have it continue on a new orbit with a displaced gyrocenter, as a change in $v_\perp$ affects the gyroradius such that the average particle position during a gyration will be shifted w.r.t. the situation before the collision. As a particle effectively only feels the gyroaverage of the potential over its orbit, this scattering will result in a change of its potential energy $q_s \langle\phi\rangle_{\boldsymbol{R}}$. Therefore $\sum_{\boldsymbol{k}} \mathrm{Re}\left[\sum_s q_s \int \frac{\mathrm{d}l}{B} \int \mathrm{d}^3\boldsymbol{v} J_0 \hat{\phi}_{\boldsymbol{k}}^* \hat{C}_{\boldsymbol{k}}\right]$ can be interpreted as "potential energy scattering", which can either withdraws energy from the particles which has to be deposited in the perturbed electric field corresponding to growth or vice versa instill energy to the particles corresponding to damping. In the simple case of a BGK operator, and proposing a similar phase shift $\varphi_{s,\boldsymbol{k}}$ between the electrostatic potential and density/temperature perturbations this term becomes

$$\sum_{\boldsymbol{k}} \mathrm{Re}\left[\sum_s q_s \int \frac{\mathrm{d}l}{B} \int \mathrm{d}^3\boldsymbol{v} J_0 \hat{\phi}_{\boldsymbol{k}}^* \hat{C}_{\boldsymbol{k}}\right] = -\sum_{\boldsymbol{k}} \sum_s q_s \int \frac{\mathrm{d}l}{B} \int \mathrm{d}^3\boldsymbol{v} \nu_s J_0 \left|\hat{\phi}_{\boldsymbol{k}}\right| |\hat{g}_{s,\boldsymbol{k}}| \cos(\varphi_{s,\boldsymbol{k}})$$

[92] This is by considering the current carried by each species in a statistically as $\boldsymbol{j_s} = \int q_s \boldsymbol{v_s} f_s$, which vanishes for both the Maxwellian due to isotropy and the adiabatic response when integrating over the gyrophase [67].

which seems to predict that for the most unstable perturbations with a phase shift close to $\pi/2$ this "potential energy scattering" would have little effect on the field free energy $\mathcal{E}_\phi$, a feature which has also been observed in simulations by Navarro et al using a realistic collision operator instead [194].

The two evolution equations for the free energy quantities $\mathcal{E}_{\delta f}, \mathcal{E}_\phi$ Equations (Q.5) and (Q.8) are not independent, after all both free energy quantities are proportional to $|\phi_{\boldsymbol{k}}|^2$. Furthermore in the limit of a "monochromatic" perturbation which is characterised by just a single $\boldsymbol{k}$, the sums in Equations (Q.5) and (Q.8) would disappear giving two equations for the growth rate of the same perturbations, which would have to be consistent. This is not a feature caused by neglecting the $\boldsymbol{E} \times \boldsymbol{B}$ non-linearity in the derivation since Equation (Q.3) vanishes if the perturbation is "monochromatic" [111], showing that there are no unaccounted sources/sinks for both free energy forms in the "monochromatic" limit. Therefore the free energy should strictly be interpreted as the total $\mathcal{E} = \mathcal{E}_{\delta f} + \mathcal{E}_\phi$, which together with the identification of $\mathcal{E}_{\delta f}$ as the perturbation entropy and $\mathcal{E}_\phi$ as the "internal" energy of the perturbed electric field reveals that $\mathcal{E} = U - \sum_s T_s \delta S_s$ is essentially the Helmholtz free energy of the perturbations [191].

Q.3 Application to TEMs

In the "monochromatic" limit discussed above, the free energy framework can be found to obtain the growth rate of TEMs. The rationale for this approach is that each evolution equation for the free energy of each Fourier mode takes the form of

$$\frac{\partial \mathcal{E}_{\boldsymbol{k},\{\delta f,\phi\}}}{\partial t} = 2\gamma_{\boldsymbol{k}} \mathcal{E}_{\boldsymbol{k},\{\delta f,\phi\}} = [\text{Sources/sinks}]_{\boldsymbol{k},\{\delta f,\phi\}}$$

however in the "monochromatic" limit the $\boldsymbol{E} \times \boldsymbol{B}$ non-linearity cannot reshuffle energy between different Fourier modes, such that the sources and sinks will simply given by the corresponding Fourier component from the right-hand sides of Equations (Q.5) and (Q.8). As both contributions to the Helmholtz free energy are strictly positive $\mathcal{E}_{\boldsymbol{k},\{\delta f,\phi\}} > 0$ this means that the net sign of the sources/sinks determines whether the instability will be unstable ($\gamma_{\boldsymbol{k}} > 0$) or damped ($\gamma_{\boldsymbol{k}} < 0$). As in the "monochromatic" limit the perturbation consists of only a single Fourier mode, the subscript on the wavenumber will be omitted from now on.

This method has been used in the past to determine the maximum growth rates of linear eigenmodes [125, 191, 195] but using a different definition of the adiabatic response which leads to an evolution for the free energy that does not include the $\boldsymbol{J} \cdot \boldsymbol{E}$ or potential energy scattering work (see explanation under Footnote 88). Furthermore, free energy transfer has been used to assess that max-$\mathcal{J}$ configurations are stable against TEMs [95, 126], but this assessment only considers the collisionless case and the $\boldsymbol{J} \cdot \boldsymbol{E}$ work. It is therefore interesting to see if (even qualitatively) it could be assessed how collisions affect the growth rate of TEMs using this method.

To evaluate the sources and sinks of Equations (Q.5) and (Q.8) for TEMs, the approximate solutions for the kinetic responses of ions and electrons Equations (48) and (51) in the TEM are used again, and the simplified BGK collision operator $\langle C_{\boldsymbol{k}} \rangle_{\boldsymbol{R}} = -\nu_s \hat{g}_s$ is employed. The process is mostly a straightforward substitution of these expressions in the right-hand sides of Equations (Q.5) and (Q.8), and determining which factors are real/imaginary which can be done on a per-species basis. For example, starting with the ions direct substitution of Equation (48)

in the gradient drive term of Equation (Q.5) gives

$$\begin{aligned}\mathrm{Im}\left[\frac{e^2}{T_i}\int\frac{\mathrm{d}l}{B}\left|\hat{\phi}\right|^2\int\mathrm{d}^3\boldsymbol{v}\frac{\left(\omega-\omega_{\star i}^T\right)\omega_{\star i}^T}{\omega-\omega_{di}+i\nu_i}J_0^2F_{Mi}\right]&=\frac{e^2}{T_i}\int\frac{\mathrm{d}l}{B}\left|\hat{\phi}\right|^2\int\mathrm{d}^3\boldsymbol{v}\,\mathrm{Im}\left[\frac{\left(\omega-\omega_{\star i}^T\right)\omega_{\star i}^T}{\omega-\omega_{di}+i\nu_i}\right]J_0^2F_{Mi}\\&=\frac{e^2}{T_i}\int\frac{\mathrm{d}l}{B}\left|\hat{\phi}\right|^2\int\mathrm{d}^3\boldsymbol{v}\frac{\omega_{\star i}^T\left[\gamma\left(\omega_{\star i}^T-\omega_{di}\right)+\nu_i\left(\omega_{\star i}^T-\omega_R\right)\right]}{\left|\omega-\omega_{di}+i\nu_i\right|^2}J_0^2F_{Mi}\end{aligned}\tag{Q.9}$$

where $\hat{\phi}$ is extracted from the velocity integral since it only depends on position and the fraction of all frequencies is the only non-real valued term, which has been explicitly expanded with a complex mode frequency $\omega=\omega_R+i\gamma$ in the last step by multiplying with the conjugate of the denominator. Doing similarly for the dissipation term with a BGK operator gives

$$\mathrm{Re}\left[-\int\frac{\mathrm{d}l}{B}\int\mathrm{d}^3\boldsymbol{v}\frac{T_i}{F_{Mi}}\nu_i|\hat{g}_i|^2\right]=-\frac{e^2}{T_i}\int\frac{\mathrm{d}l}{B}\left|\hat{\phi}\right|^2\int\mathrm{d}^3\boldsymbol{v}\frac{\nu_i\left(|\omega|^2+\omega_{\star i}^2-2\omega_R\omega_{\star i}^T\right)}{\left|\omega-\omega_{di}+i\nu_i\right|^2}J_0^2F_{Mi}$$

which shares much a similar structure of the integrand, such that both contributions can be neatly combined to give the total change in entropy due to ions

$$\left(\frac{\partial\mathcal{E}_{\delta f}}{\partial t}\right)_{ions}=\frac{e^2}{T_i}\int\frac{\mathrm{d}l}{B}\left|\hat{\phi}\right|^2\int\mathrm{d}^3\boldsymbol{v}\frac{\gamma\omega_{\star i}^T\left(\omega_{\star i}^T-\omega_{di}\right)-\nu_i\left(|\omega|^2-\omega_R\omega_{\star i}^T\right)}{\left|\omega-\omega_{di}+i\nu_i\right|^2}J_0^2F_{Mi}.\tag{Q.10}$$

The procedure for the electron is much the same, but has a slight subtlety. The approximate solution for the electron kinetic response Equation (51) describes the response of trapped particles and vanishes in regions of velocity space corresponding to passing particles. This is best handled by using pitch-angle coordinates for velocity space such that e.g. the gradient drive term becomes

$$\begin{aligned}&\mathrm{Im}\left[\frac{e^2}{T_e}\int\frac{\mathrm{d}l}{B}\hat{\phi}^*\int\mathrm{d}^3\boldsymbol{v}\frac{\omega_{\star e}^T\left(\omega-\omega_{\star e}^T\right)}{\omega-\overline{\omega_{de}}+i\nu_e}\overline{J_0\hat{\phi}}J_0F_{Me}\right]=\mathrm{Im}\left[\frac{e^2}{T_e}\int\frac{\mathrm{d}l}{B}\hat{\phi}^*\int_{v_{cut}}^{\infty}\mathrm{d}v\int_{B_{max}}^{1/B}\mathrm{d}\lambda\,\frac{2\pi v^2B}{\sqrt{1-\lambda B}}\frac{\omega_{\star e}^T\left(\omega-\omega_{\star e}^T\right)}{\omega-\overline{\omega_{de}}+i\nu_e}\overline{J_0\hat{\phi}}J_0F_{Me}\right]\\&=\mathrm{Im}\left[2\pi\frac{e^2}{T_e}\int_{1/B_{max}}^{1/B_{min}}\mathrm{d}\lambda\sum_{w(\lambda)}\int_{v_{cut}}^{\infty}\mathrm{d}v\,\frac{\omega_{\star e}^T\left(\omega-\omega_{\star e}^T\right)}{\omega-\overline{\omega_{de}}+i\nu_e}\left|\overline{J_0\hat{\phi}}\right|^2L_{eff,[w]}v^2F_{Me}\right]\end{aligned}$$

where Equation (64) has been used to revert the order of integration and turn all remaining field line depending quantities into bounce averages. A comparison with Equation (Q.9) shows that the electron and ion gradient drive terms are isomorphic, by replacing all quantities that depend on the position along the field line with their bounce average, using pitch-angle velocity coordinates and replacing the integral along the field line with the "effective well" length. It is straightforward to show that this isomorphism between ion and electron free energy sources/sinks also carries over to the other terms, such that the total change in entropy due to electrons becomes

$$\left(\frac{\partial\mathcal{E}_{\delta f}}{\partial t}\right)_{electrons}=2\pi\frac{e^2}{T_e}\int_{1/B_{max}}^{1/B_{min}}\mathrm{d}\lambda\sum_{w(\lambda)}\int_{v_{cut}}^{\infty}\mathrm{d}v\,\frac{\gamma\omega_{\star e}^T\left(\omega_{\star e}^T-\overline{\omega_{de}}\right)-\nu_e\left(|\omega|^2-\omega_R\omega_{\star e}^T\right)}{\left|\omega-\overline{\omega_{de}}+i\nu_e\right|^2}v^2\left|\overline{J_0\hat{\phi}}\right|^2F_{Me}L_{eff,[w]}.\tag{Q.11}$$

The sources/sinks for the field energy $\mathcal{E}_\phi$ largely follow in a largely analogous way by direct substitution of the approximate solutions for $\hat{g}_i,\hat{g}_e$ in the right-hand side of Equation (Q.8), except for the parallel $\boldsymbol{J}\cdot\boldsymbol{E}$ work which requires some careful deliberation. The free energy evolution equations are derived for the most general case of the linearised GKE and is exact, whereas the approximate solutions for $\hat{g}_i,\hat{g}_e$ are obtained by asymptotic limits for the parallel dynamics term in the GKE based on the frequency ordering Equation (47). For the ions this

simply means that the $v_\parallel \boldsymbol{\nabla}_\parallel$ term can be completely neglected such with regard to the free energy $J_\parallel E_\parallel \approx 0$. Direct substitution of Equation (48) in Equation (Q.8) then gives the field energy source/sink for the ions

$$\left(\frac{\partial \mathcal{E}_\phi}{\partial t}\right)_{ions} = -\frac{e^2}{T_i}\int \frac{\mathrm{d}l}{B}\left|\hat{\phi}\right|^2 \int \mathrm{d}^3\boldsymbol{v} \frac{\nu_i\left(|\omega|^2 + \gamma\nu_i - \omega_R\omega_{\star i}^T\right) + \gamma\omega_{di}\left(\omega_{di} - \omega_{\star i}^T\right)}{|\omega - \omega_{di} + i\nu_i|^2} J_0^2 F_{Mi} \quad \text{(Q.12)}$$

For the electrons however the $v_\parallel \boldsymbol{\nabla}_\parallel$ term actually dominates and the approximate solution Equation (51) is obtained by taking the bounce average of the GKE to filter out the parallel dynamics, and only describes the trapped electrons (as described in Section 3.1.2). The passing electrons, which would only enter through the small correction $\hat{g}_{e,1}$ to the kinetic response can however carry a substantial parallel current which cannot be neglected. This can be accounted for by solving the GKE "iteratively", that is using Equation (49) to obtain an expression for the parallel dynamics from passing electrons $v_\parallel \boldsymbol{\nabla}_\parallel \hat{g}_{e,1}$ in terms of the approximate solution Equation (51) describing trapped electrons. With this "iterative" approach the $\boldsymbol{J}\cdot\boldsymbol{E}$ work due to electrons becomes

$$\mathrm{Re}\left[-e\int\frac{\mathrm{d}l}{B}\int \mathrm{d}^3\boldsymbol{v} J_0\hat{\phi}^*\left(v_\parallel\boldsymbol{\nabla}_\parallel + i\omega_{de}\right)\hat{g}_e\right] \approx \mathrm{Re}\left[-e\int\frac{\mathrm{d}l}{B}\int \mathrm{d}^3\boldsymbol{v} J_0\hat{\phi}^*\left(v_\parallel\boldsymbol{\nabla}_\parallel\hat{g}_{e,1} + i\omega_{de}\hat{g}_{e,0}\right)\right]$$

$$= \mathrm{Re}\left[i\frac{e^2}{T_e}\int\frac{\mathrm{d}l}{B}\int \mathrm{d}^3\boldsymbol{v}\frac{\left(\omega-\omega_{\star e}^T\right)\left(\omega+i\nu_e\right)}{\omega-\overline{\omega_{de}}+i\nu_e} J_0\hat{\phi}^*\overline{J_0\hat{\phi}}F_{Me}\right] - \mathrm{Re}\left[i\frac{e^2}{T_e}\int\frac{\mathrm{d}l}{B}\int \mathrm{d}^3\boldsymbol{v}\left|\hat{\phi}\right|^2 J_0^2\left(\omega-\omega_{\star e}^T\right)F_{Me}\right]$$

where the first term will vanish for passing electrons because of the bounce average, but the second term contains contributions from both passing and trapped electrons. For the potential energy scattering however, this distinction between passing and trapped electrons does not matter and retaining only the approximate solution Equation (51) is sufficient. Working out the $\mathrm{Re}[\cdots]$ operator by expanding the complex frequency fraction for each term like before then gives the total field energy source/sink for electrons as

$$\left(\frac{\partial \mathcal{E}_\phi}{\partial t}\right)_{electrons} = -2\pi\frac{e^2}{T_e}\int_{1/B_{max}}^{1/B_{min}}\mathrm{d}\lambda\sum_{w(\lambda)}\int_{v_{cut}}^{\infty}\mathrm{d}v\,\frac{\nu_e\left(|\omega|^2+\gamma\nu_e-\omega_{\star e}^T\omega_R\right)+\gamma\overline{\omega_{de}}\left(\overline{\omega_{de}}-\omega_{\star e}^T\right)}{|\omega-\overline{\omega_{de}}+i\nu_e|^2}v^2F_{Me}\left|\overline{\hat{\phi}J_0}\right|^2 L_{eff,[w]}$$

$$-\frac{e^2}{T_e}\gamma\left[\int\frac{\mathrm{d}l}{B}\int\mathrm{d}^3\boldsymbol{v}\left|\hat{\phi}\right|^2J_0^2F_{Me} - 2\pi\int_{1/B_{max}}^{1/B_{min}}\mathrm{d}\lambda\sum_{w(\lambda)}\int_{v_{cut}}^{\infty}\mathrm{d}v\left|\overline{J_0\hat{\phi}}\right|^2v^2F_{Me}L_{eff,[w]}\right] \quad \text{(Q.13)}$$

where the term is again the isomorphic electron equivalent to the ion term from Equation (Q.12), and the second term which is absent for the ions describes the non-negligible $J_\parallel E_\parallel$ work. One would expect this additional term to be mainly due to passing electrons rather than trapped electrons which at first sight also give a contribution. Rather by explicitly splitting the velocity integral of the first term in a passing and trapped contribution it follows that

$$\int\frac{\mathrm{d}l}{B}\int\mathrm{d}^3\boldsymbol{v}\left|\hat{\phi}\right|^2J_0^2F_{Me} - 2\pi\int_{1/B_{max}}^{1/B_{min}}\mathrm{d}\lambda\sum_{w(\lambda)}\int_{v_{cut}}^{\infty}\mathrm{d}v\left|\overline{J_0\hat{\phi}}\right|^2v^2F_{Me}L_{eff,[w]} =$$

$$\int\frac{\mathrm{d}l}{B}\int_P\mathrm{d}^3\boldsymbol{v}\left|\hat{\phi}\right|^2J_0^2F_{Me} + 2\pi\int_{1/B_{max}}^{1/B_{min}}\mathrm{d}\lambda\sum_{w(\lambda)}\int_{v_{cut}}^{\infty}\mathrm{d}v\left\{\overline{\left|J_0\hat{\phi}\right|^2} - \left|\overline{J_0\hat{\phi}}\right|^2\right\}v^2F_{Me}L_{eff,[w]}$$

where the subscript P has been used to indicate the passing particle region[93] and the trapped particle particles have been described by pitch-angle coordinates as usual. The term in the curly

[93] Using e.g. pitch-angle velocity coordinates these would be characterised by $v\in[0,\infty), \lambda\in[0,1/B_{max})$ and the integral along the field line would wind completely around the torus. However to keep the notation compact this has not been written out explicitly.

brackets is essentially the extension of the usual definition of the variance of $J_0\hat{\phi}$ along the orbit of a trapped electron. In case the perturbations are relatively elongated compared w.r.t. the effective well length $k_\parallel L_{eff}[w] \ll 1$ then a trapped particle will hardly experience changes to the electrostatic potential along its orbit and the contribution from trapped electrons will approach zero such that the $J_\parallel E_\parallel$ work is largely due to passing particles as expected. One intricacy is that the $J_\parallel E_\parallel$ work is proportional to the growth $-\gamma$, which means that it will exert a stabilising influence to unstable modes and vice versa. Both of these observations match the result from Manas et al [76] who separately looked to contributions from parallel and perpendicular electron dynamics to the TEM growth rate in simulations and found that the parallel dynamics were uniformly stabilising and concentrated in the passing particle region of velocity space.

With all four sources/sinks to the total Helmholtz free energy $\mathcal{E} = \mathcal{E}_{\delta f} + \mathcal{E}_\phi$ identified, the growth rate can be determined by adding the evolution equations Equations (Q.5) and (Q.8) in an attempt to find the growth rate of TEMs

$$\begin{aligned}\frac{\partial \mathcal{E}}{\partial t} = 2\gamma\mathcal{E} = &-\frac{e^2}{T_i}\int \frac{\mathrm{d}l}{B}\int \mathrm{d}^3\boldsymbol{v}\frac{2\nu_i\left(|\omega|^2 - \omega_R\omega_{\star i}^T\right) + \gamma\nu_i^2 + \gamma\left(\omega_{di}^2 - \omega_{\star i}^2\right)}{|\omega - \omega_{di} + i\nu_i|^2}J_0^2F_{Mi} \\ &- \frac{e^2}{T_e}2\pi\int_{1/B_{max}}^{1/B_{min}}\mathrm{d}\lambda\sum_{w(\lambda)}\int_{v_{cut}}^{\infty}\mathrm{d}v\,\frac{2\nu_e\left(|\omega|^2 - \omega_R\omega_{\star e}^T\right) + \gamma\nu_e^2 + \gamma\left(\overline{\omega_{de}}^2 - {\omega_{\star e}^T}^2\right)}{|\omega - \overline{\omega_{de}} + i\nu_e|^2}v^2F_{Me}\left|\overline{\hat{\phi}J_0}\right|^2L_{eff,[w]} \\ &- \gamma\frac{e^2}{T_e}\left(\int\frac{\mathrm{d}l}{B}\int_P\mathrm{d}^3\boldsymbol{v}\left|\hat{\phi}\right|^2J_0^2F_{Me} + 2\pi\int_{1/B_{max}}^{1/B_{min}}\mathrm{d}\lambda\sum_{w(\lambda)}\int_{v_{cut}}^{\infty}\mathrm{d}v\left\{\overline{\left|J_0\hat{\phi}\right|^2} - \left|\overline{J_0\hat{\phi}}\right|^2\right\}v^2F_{Me}L_{eff,[w]}\right)\end{aligned} \tag{Q.14}$$

where Equations (Q.10) to (Q.13) were substituted and the all terms with the same denominator were brought together. There is one major problem with Equation (Q.14): it is impossible to determine the right-hand side without knowing the growth rate γ! This means that the free energy transfer cannot be used to assess the growth rate based on the rationale that the free energy itself $\mathcal{E}$ is always positive such that the sign of the source/sinks can be used to determine the growth rate. Ideally, Equation (Q.14) could be rewritten in the form $\gamma(2\mathcal{E}+\mathcal{G}) = \mathcal{F}$ where $\mathcal{G}$ contains all term on the right-hand side which are proportional to γ such that the growth could still be determined, however the terms in $\mathcal{G}$ are not strictly positive such that whether there will be an instability would no longer depend just on the sign of $\mathcal{F}$.

Nevertheless some rudimentary qualitative information about the influence of collisions on TEMs can be extracted from Equation (Q.14). Reasoning similarly as for the $J_\parallel E_\parallel$ term which has a stabilising influence on instabilities, by assuming the growth rate to be $\gamma > 0$ the collisions will have a directly stabilising effect from both the $\gamma\nu_s^2$ and $2\nu_s|\omega|^2$ terms in Equation (Q.14) regardless of the real frequency. The real frequency is however crucial in determining the sign of the $2\nu_s\omega_R\omega_{\star s}^T$ terms, which is independent of the growth rate, such that collisions exert a destabilising effect if $\omega_R\omega_{\star s}^T > 0$, which in absence of temperture gradients is exactly the same criterion as for the collisionless TEM resonance. As the electron collision frequency is typically higher than the ion collision frequency, this means that collisions could further destabilise an already resonant TEM. However this analysis only allows to assess the qualitative effects of each term involving the collision frequency, the net effect of collisions will be determined by the imbalance among them which is impossible to assess.

R Preliminary work on the variational principle for growth rates

The basis of all variational principles rely on the calculus of variations, which is first briefly outlined in Appendix R.1 before diving into its application towards finding the generally complex

mode frequency for gyrokinetic instabilities, with in particular TEMs in Appendix R.2. After deriving the corresponding Euler-Lagrange equations their consistency issue is highlighted and some first steps towards their resolvement are taken in Appendix R.3.

R.1 Introduction to variational principle

The following exerpt is based on the classical textbook on the subject by Gelfand and Fomin [225] on the subject.

Calculus of variations concerns itself with finding extrema of a functional $S[y]$, where most functionals encountered in physics take the form

$$S[y] = \int_a^b \mathcal{L}(x, y, y')\,\mathrm{d}x \tag{R.1}$$

where $y' = \frac{\mathrm{d}y}{\mathrm{d}x}$. Such a funtional $S[y]$ can be considered as "a function of the function $y(x)$", or formally it expresses a mapping of some curve $y(x)$ to the set of real numbers. Much of functional analysis follows by analogy with the analysis of "normal" functions $f(x)$. In particular of importance in optimisation problems is to find where Equation (R.1) has an extremum. For a regular function $f(x)$ this happens when its variation $df = 0$, and the subsequent analogue for functionals is that the variation $\delta S = 0$. Consider two curves $y(x)$ and $\tilde{y}(x) = y(x) + h(x)$ with $h(x)$ such that $y(x)$ and $\tilde{y}(x)$ are "neighbouring curves" in function space[94] with the same end-points such that $h(a) = h(b) = 0$. Then the difference in $S[y]$ between the two curves is

$$\Delta S[y] = S[\tilde{y}] - S[y] = \int_a^b \frac{\partial \mathcal{L}}{\partial y} h(x) + \frac{\partial \mathcal{L}}{\partial y'} h'\,\mathrm{d}x + \mathcal{O}(h^2, hh', (h')^2)$$

where a Taylor expansion of the integrand is made and the first part linear in $h(x), h'(x)$ is referred to as the variation δS. Integrating the latter by parts gives

$$\delta S[y] = \int_a^b \left[\frac{\partial \mathcal{L}}{\partial y} - \frac{\mathrm{d}}{\mathrm{d}x}\left(\frac{\partial \mathcal{L}}{\partial y'}\right)\right] h(x)\,\mathrm{d}x + \underbrace{\frac{\partial F}{\partial y'} h(x)\Big|_{x=a}^{x=b}}_{=0}$$

where the boundary term vanishes since the two curves $\tilde{y}(x), y(x)$ have the same end points. For the functional $S[y]$ to have an extremum for the curve $y(x)$ its variation must vanish $\delta S[y] = 0$ for any arbitrary choice of $h(x)$, which can only happen if

$$\frac{\partial \mathcal{L}}{\partial y} - \frac{\mathrm{d}}{\mathrm{d}x}\left(\frac{\partial \mathcal{L}}{\partial y'}\right) = 0$$

which is referred to as the Euler-Lagrange (EL) equation for the functional Equation (R.1),whose integrand $\mathcal{L}$ is then referred to as the Lagrangian density (or just Lagrangian depending on the field of application). The EL equation is readily generalised for a functional $S[y_1, y_2, \cdots, y_N]$ depending on multiple curves as

$$\frac{\partial \mathcal{L}}{\partial y_j} - \frac{\mathrm{d}}{\mathrm{d}x}\left(\frac{\partial \mathcal{L}}{\partial y_j'}\right) = 0 \quad \text{for } j = 1, 2, \cdots, N. \tag{R.2}$$

Additional generalisations such as non-fixed end point problems, functionals depending on higher order derivatives, etc can be found in [225], but Equation (R.2) is already more than sufficient for its application to gyrokinetics.

[94] This can be defined by means of a suitable norm depending on the type of functional. For the common example of Equation (R.1) where the functional depends both on y and its derivative, this means that the absolute deviation of the curve and their slopes have to stay within some prescribed bound for which $S[y]$ is continuous.

R.2 Quadratic form functional for TEMs

As the main difficulty of the trapped electron mode is that the qausi-neutrality condition is in an equation in both the mode structure $\hat{\phi}$ and its integral because of the bounce averaging (called a Fredholm equation in mathematics). As the main interest is not so much the mode structure but rather the complex mode frequency, in particular its imaginary part giving the instability growth rates. This problem can be circumvented by multipyling the quasi-neutrality condition, in the form of Equation (54) with the approximate solutions for the kinetic responses $\hat{g}_e, \hat{g}_i$ of electrons and ions substituted, with $\hat{\phi}^*$ and integrating over the field line [43, 93], resulting in[95]

$$\begin{aligned}\oint (1+\tau)\left|\hat{\phi}\right|^2 \frac{\mathrm{d}l}{B} = \oint \frac{\mathrm{d}l}{B} \int \mathrm{d}^3\boldsymbol{v_i} \frac{\omega-\omega^T_{\star i}}{\omega-\omega_{di}+i\nu_i} J_0^2 \left|\hat{\phi}\right|^2 \frac{F_{Mi}}{n_0} \\ + \tau \oint_{1/B_{max}}^{1/B_{min}} \mathrm{d}\lambda \sum_{w(\lambda)} \int_{v_{cut}}^{\infty} \mathrm{d}v_e \, \frac{\omega-\omega^T_{\star e}}{\omega-\overline{\omega}_{de}+i\nu_e} \frac{2\pi v_e^2 F_{Me}}{n_0} \left|\overline{\hat{\phi}}\right|^2 L_{eff[w]}\end{aligned} \tag{R.3}$$

where pitch-angle velocity coordinates for the trapped electrons are used for the velocity integration and the trick of Equation (64) has been used to change the order of integration over pitch angle and field line. Equation (R.3) is the so called quadratic form and has the benefit that it depends on integrals of the absolute magnitude of ϕ which are always positive and real-valued, and the mode frequency ω which is constant w.r.t. all integrals. Although it is still not possible to solve Equation (R.3) for the mode structure and the mode frequency ω, one could make an educated guess for the mode structure and calculate what the corresponding mode frequency would be. In general the resulting guess of the mode frequency will be off from the "true" mode frequency ω_0 belonging to the "true" electrostatic potential $\hat{\phi}_0$. The idea is now that if Equation (R.3) can be recast into a functional $S[\omega, \hat{\phi}] = 0$ and the variational principle can be used to find stationary solutions $\delta S[\omega, \hat{\phi}] = 0$, then the guess for the mode frequency will be a close proxy to the actual frequency of the TEM. Because Equation (R.3) is quadratic in $\hat{\phi}$ but "linear" in ω this technique will be a double-edged sword as it means any error $\delta\hat{\phi} = \hat{\phi} - \hat{\phi}_0$ made in the initial guess for the mode structure will propagate as δ^2 into the error for the guess of the mode frequency $\delta\omega = \omega - \omega_0$, such that the proxy for the TEM frequency will be either very good if $\delta \ll 1$ or very poor if $\delta > 1$. In the latter case of course the EL equations will not be valid as the assumption in their derivation was that the deviations are small such that $\Delta S[y]$ is accurately given by its linear variation $\delta S[y]$ and the quadratic and higher corrections are negligible.

To be suitable for the variational principle the functional $S[\omega, \phi]$ has to be written in the form of Equation (R.1) with a single integration variable. This can be achieved by sacrificing the symmetry in the trap electron obtained by reversing the order of the pitch-angle and field line integrals, such that the instruction of multiplying the quasi-neutrality by $\hat{\phi}$ and integrating along the field line not further simplified than by introducing pitch-angle coordinates for $\mathrm{d}^3\boldsymbol{v_e}$, leading to the functional

$$S[\omega, \hat{\phi}] = \oint \left[f(\omega, l)\left|\hat{\phi}\right|^2 / B(l) - \left\{ \int_{1/B_{max}}^{1/B(l)} g(\omega, \lambda, l)\overline{\hat{\phi}}(\lambda)\,\mathrm{d}\lambda \right\} \hat{\phi}^* / B(l) \right] \mathrm{d}l$$

[95] Note that is essentially the same as the last step of the perturbative calculation of Section 3.2 except that the electron response is treated in a non-perturbative way from the get-go.

where the functions

$$\begin{aligned} f(\omega,l) &= (1+\tau) - h(\omega,l) \\ h(\omega,l) &= \int \mathrm{d}^3\boldsymbol{v_i} \frac{\omega-\omega_{\star i}^T}{\omega-\omega_{di}+i\nu_i} J_0^2 \frac{F_{Mi}}{n_0} \\ g(\omega,\lambda,l) &= \int_{v_{cut}}^{\infty} \mathrm{d}v_e \, \frac{\omega-\omega_{\star e}^T}{\omega-\overline{\omega}_{de}+i\nu_e} \frac{2\pi v_e^2 B(l)}{\sqrt{1-\lambda B(l)}} \frac{F_{Me}}{n_0} \end{aligned} \tag{R.4}$$

are defined for convenient shorthand notation and $S[\omega,\hat{\phi}]$ is here liberally interpreted as a general functional which maps the "curve" of $\hat{\phi}(l)$ to a complex number, with the special case of $S[\omega,\hat{\phi}]=0$ corresponding to the solution of Equation (R.3). Thus the Lagrangian density to use for the variational principle is then recognised as

$$\mathcal{L}(\omega,\hat{\phi},l) = f(\omega,l)\hat{\phi}\;\hat{\phi}^*/B(l) - \int_{1/B_{max}}^{1/B(l)} g(\omega,\lambda,l)\overline{\hat{\phi}}\,\mathrm{d}\lambda\,\hat{\phi}^*/B(l)$$

which depends on both $\hat{\phi}$ and its complex conjugate. Such a situation also typically occurs in the variational formulation of quantum-mechanics where both the wavefunction ψ and its complex conjugate enter the Lagrangian density and they are treated as independent variables for the variations of the EL equations which lead to the Schrödinger equation for ψ and ψ^* respectively [198, 203, 226]. This is essentially because the wavefunction is a complex number which can be represented by two independent real numbers; either its real and imaginary parts or more physically relevant its phase and magnitdue which can be constructed from combinations of ψ and ψ^*. The same also applies to the Fourier coefficent-like electrostatic potential $\hat{\phi}$, such that actually $S[\omega,\hat{\phi},\hat{\phi}^*] = \int \mathcal{L}(\omega,\hat{\phi},\hat{\phi}^*,l)\,\mathrm{d}l$ which leads to the following system of EL equations

$$\frac{\partial\mathcal{L}}{\partial\omega}=0 \quad \frac{\partial\mathcal{L}}{\partial\hat{\phi}}=0 \quad \frac{\partial\mathcal{L}}{\partial\hat{\phi}^*}=0$$

as a result of applying Equation (R.2) to a Lagrangian density which does not depend on any derivative. Technically Equation (R.2) is derived for a real-valued functional which maps a collection of curves along the real line to a real-valued number, but this can be naturally extended to functionals which map a curve in the complex plane to a complex number resulting in the same set of (complex) EL equations [202]. Although the derivatives of $\mathcal{L}$ w.r.t. $\hat{\phi},\omega$ are straightforward to obtain, the derivative w.r.t. $\hat{\phi}$ is less obvious because of the bounce averaging. Here the quadratic form of this term in Equation (R.3) provides a clever way of calculating the derivative by (re)writing it as

$$\int_{1/B_{max}}^{1/B_{min}} \mathrm{d}\lambda \sum_{w(\lambda)} (\cdots)\,\overline{\hat{\phi}}\;\overline{\hat{\phi}}^* \int_{l1[w]}^{l2[w]} \frac{\mathrm{d}l}{\sqrt{1-\lambda B(l)}} = \oint \mathrm{d}l \int_{1/B_{max}}^{1/B(l)} \mathrm{d}\lambda\,(\cdots)\,\overline{\hat{\phi}}\frac{\hat{\phi}^*}{\sqrt{1-\lambda B}} = \oint \mathrm{d}l \int_{1/B_{max}}^{1/B(l)} \mathrm{d}\lambda\,(\cdots)\,\overline{\hat{\phi}^*}\frac{\hat{\phi}}{\sqrt{1-\lambda B}}$$

where $L_{eff[w]}$ has been written out explicitly in the first line, and the two steps below follow reversing the order of integration between λ and l again by means of Equation (64), applying the definition of the bounce average Equation (52) once to the product of $\overline{\hat{\phi}}L_{eff[w]}$ and once to the complex conjugate instead and recognising that during any of the integrals the pitch angle never exceeds $\lambda B \geq 1$ such that $\overline{\hat{\phi}}^* = \overline{\hat{\phi}^*}$. The fact that these integrals are similar is of course because $\left|\overline{\hat{\phi}}\right|^2 L_{eff[w]} \in \mathbb{R}$ and must therefore equal its own conjugate. Consequently this means there are two equivalent Lagrangian densities $\mathcal{L}_1, \mathcal{L}_2$

$$\mathcal{L}_1(\omega,\hat{\phi},\hat{\phi}^*,l) = f(\omega,l)\hat{\phi}\;\hat{\phi}^*/B(l) - \int_{1/B_{max}}^{1/B(l)} g(\omega,\lambda,l)\overline{\hat{\phi}}\,\mathrm{d}\lambda\,\hat{\phi}^*/B(l)$$

$$\mathcal{L}_2(\omega,\hat{\phi},\hat{\phi}^*,l) = f(\omega,l)\hat{\phi}\;\hat{\phi}^*/B(l) - \int_{1/B_{max}}^{1/B(l)} g(\omega,\lambda,l)\overline{\hat{\phi}^*}\,\mathrm{d}\lambda\,\hat{\phi}/B(l)$$

which lead to exactly the same functional $S[\omega, \hat{\phi}, \hat{\phi}^*]$, such that for the EL equations one has the freedom to pick which Lagrangian density to use for the derivatives[96] such that the EL equations for the variational principle are

$$\frac{\partial \mathcal{L}}{\partial \hat{\phi}} = f(\omega, l)\hat{\phi}^*/B - \int g(\omega, \lambda, l)\overline{\hat{\phi}^*}\,\mathrm{d}\lambda\,/B = 0 \tag{R.5a}$$

$$\frac{\partial \mathcal{L}}{\partial \hat{\phi}^*} = f(\omega, l)\hat{\phi}/B - \int g(\omega, \lambda, l)\overline{\hat{\phi}}\,\mathrm{d}\lambda\,/B = 0 \tag{R.5b}$$

$$\frac{\partial \mathcal{L}}{\partial \omega} = \frac{\partial f(\omega, l)}{\partial \omega}\left|\hat{\phi}\right|^2/B - \int \frac{\partial g(\omega, \lambda, l)}{\partial \omega}\overline{\hat{\phi}}\,\mathrm{d}\lambda\,\hat{\phi}^*/B = 0 \tag{R.5c}$$

where the boundaries of the pitch-angle integration have been suppressed.

R.3 The consistency issue of the Euler-Lagrange equations

All EL equations of Equation (R.5) take the form of $(\cdots)/B = 0$ which have to be satisfied everywhere along the field line where the magnetic field strength remains finite, such that all EL equations can only be satisfied by $(\cdots) = 0$. Interestingly the EL equation Equation (R.5b) for variation w.r.t. $\hat{\phi}^*$ reduces exactly to the quasi-neutrality equation for TEMs (Equation (54)) after substituting Equation (R.4), despite the general interpretation of $S[\omega, \hat{\phi}, \hat{\phi}^*]$ as a general mapping of some complex curve $\hat{\phi}(l)$ to a complex number which may be other than zero if the electrostatic potential does not satisfy quasi-neutrality. One is tempted to interpret this result that the extrema of S thus correspond to solutions to the quasi-neutrality condition. This is however problematic as a comparison between Equations (R.5a) and (R.5b) shows that $\hat{\phi}$ and $\hat{\phi}^*$ should satisfy exactly the same equation which can only be true if $\hat{\phi} = \hat{\phi}^*$ because both f, g are complex-valued. Mathematically this would strictly limit the WKB amplitude functions $\hat{\phi}$ to be real-valued since the conjugate should satisfy $\mathrm{Im}[\hat{\phi}^*] = -\mathrm{Im}[\hat{\phi}]$. Physically however the interpretation that the extrema of the functional correspond to solutions of the quasi-neutrality breaks down, since the electrostatic potential is real-valued such that

$$\phi(\boldsymbol{x}, t) = (\phi(\boldsymbol{x}, t))^* = \hat{\phi}^*(\boldsymbol{x})\exp(-i(S(\boldsymbol{x})/\delta - \omega^* t))$$

by invoking Equation (28) for the electrostatic potential, which shows that $\hat{\phi}^*$ corresponds to a "mirror image" of $\hat{\phi}$ which is going in the opposite direction with a corresponding vector $\boldsymbol{k}_\perp^* = \boldsymbol{\nabla}\phi/i\phi \to -\boldsymbol{k}_\perp$ and oscillation frequency $\omega_R^* \to -\omega_R$ but the same growth rate $\gamma^* = \gamma$. Consequently this would introduce sign change to the appropriate diamagnetic frequency $\omega_{\star s}^T$ and magnetic drift frequency ω_{ds} as well such that the corresponding quasi-neutrality condition for $\hat{\phi}^*$ would be described by functions $f^*(\omega, l), g^*(\omega, \lambda, l)$ other than the ones from Equation (R.4) which appear in Equation (R.5a).

This prevents a consistent interpretation of extrema of $S[\omega, \hat{\phi}, \hat{\phi}^*]$ as solutions to the quasi-neutrality condition since $\hat{\phi}^*$ would no longer be the conjugate of $\hat{\phi}$ which solves the quasi-neutrality condition. This problem does not occur in the "normal" variational principle of the Schrödinger equation because the corresponding Lagrangian density is real-valued and so the corresponding EL equations are each other's complex conjugate[97] and a consistent interpretation

[96] This is because one could formulate the EL equations once by expressing $S[\omega, \hat{\phi}, \hat{\phi}^*]$ in $\mathcal{L}_1$ and once by expressing S in $\mathcal{L}_2$ which does not introduce an additional term to the EL equations since $\mathcal{L}_2$ still does not depend on any derivative and arrive at $\frac{\partial \mathcal{L}_\infty}{\partial \hat{\phi}} = 0 = \frac{\partial \mathcal{L}_\in}{\partial \hat{\phi}}$.

[97] Formally speaking, in the quantum mechanics the formulation is in terms Hilbert spaces where $\langle\psi|, |\psi\rangle$ are used instead and the EL equations are each other's adjoint in the respective Hilbert space because the Lagrangian density is a Hermittian operator with real eigenvalues corresponding to energy E of the quantum system [226]. In terms of the TEM problem, the "eigenvalue" would be the frequency ω which is complex and the Lagrangian density is not Hermitian because of the reasons argued above.

as ψ^* and ψ is possible [203]. This problem also does not arise in previous applications of the variational principle to TEMs [126, 182] which are done in the collisionless limit ($\nu \to o$) at marginal stability ($\gamma \downarrow 0$) such that the functions $f(\omega, l), g(\omega, \lambda, l)$ become real-valued again and all the sign changes to the frequencies would neatly cancel, such that the EL equations for $\hat{\phi}^*$ and $\hat{\phi}$ become each others complex conjugate and a consistent intepretation of $\hat{\phi}^*$ as the complex conjugate is possible again.

In an attempt to remedy this issue, the constraint that $S[\omega, \hat{\phi}] = 0$ is satisfied for proper solutions to the quasi-neutrality condition. A similar approach is used in Reference [201] to use the variational approach for the growth rate in the fluid limit of kinetic-ballooning modes, where the fact that $S = 0$ results in an two equations for the real and imaginary part which could be solved independently. With the quasi-neutrality expressed in the quadratic form of Equation (R.3) where only $|\phi|^2$ and $\left|\overline{\phi}\right|^2$ taking the real and imaginary part are straightforward, resulting in the two equations

$$\oint (1+\tau)\,|\phi|^2 \frac{\mathrm{d}l}{B} = \oint \mathrm{Re}[h(\omega,l)]|\phi|^2 \frac{\mathrm{d}l}{B} + \tau \int_{1/B_{max}}^{1/B_{min}} \mathrm{d}\lambda \sum_{w(\lambda)} \mathrm{Re}[G(\omega,\lambda,[w])]\left|\overline{\hat{\phi}}\right|^2 L_{eff[w]}$$

$$0 = \oint \mathrm{Im}[h(\omega,l)]|\phi|^2 \frac{\mathrm{d}l}{B} + \tau \int_{1/B_{max}}^{1/B_{min}} \mathrm{d}\lambda \sum_{w(\lambda)} \mathrm{Im}[G(\omega,\lambda,[w])]\left|\overline{\hat{\phi}}\right|^2 L_{eff[w]}$$

where temporarily $G(\omega, \lambda, [w]) = \int_{v_{cut}}^{\infty} \mathrm{d}v_e \, \frac{\omega - \omega_{*e}^T}{\omega - \overline{\omega}_{de}[w] + i\nu_e} \frac{2\pi v_e^2 F_{Me}}{n_0}$ has been used for short hand-notation. Focussing on the latter, and reverting the order of integration between pitch-angle and arc length yields

$$\oint \mathrm{Im}[h(\omega,l)]\left|\hat{\phi}\right|^2 \frac{\mathrm{d}l}{B} + \oint \int \mathrm{d}\lambda \,\mathrm{Im}[g(\omega,\lambda,l)]\overline{\hat{\phi}}\hat{\phi}^* \,\mathrm{d}l\,/B = \oint \left(\mathrm{Im}[h(\omega,l)]\hat{\phi} + \int \mathrm{d}\lambda \,\mathrm{Im}[g(\omega,\lambda,l)]\overline{\hat{\phi}}\right)\hat{\phi}^* \frac{\mathrm{d}l}{B} = 0$$

which can be satisfied only if either $\hat{\phi}^* = 0$ or $\mathrm{Im}[h(\omega,l)]\hat{\phi} + \int \mathrm{d}\lambda \,\mathrm{Im}[g(\omega,\lambda,l)]\overline{\hat{\phi}} = 0$. The first solution would however imply $\hat{\phi} = 0 = \overline{\phi}$ and corresponds to the trivial solution of no turbulence, such that the second equation provides the proper constraint. As assessed in Appendix R.2 there is some freedom in how $\left|\overline{\hat{\phi}}\right|^2 L_{eff[w]}$ is converted from a sum over wells to an integral along the arc length of the field line which leads to two equivalent Lagrangian densities corresponding to the same functional S¿ Completely analogous as shown above where the choice was made to convert $\overline{\hat{\phi}}^* L_{eff[w]}$, the condition of $\mathrm{Im}[h(\omega,l)]\hat{\phi}^* + \int \mathrm{d}\lambda \,\mathrm{Im}[g(\omega,\lambda,l)]\overline{\hat{\phi}}^* = 0$ would be obtained instead if $\overline{\hat{\phi}} L_{eff[w]}$ were converted, which is just the complex conjugate of the previous constraint. This should be expected since the fact that $\hat{\phi}$ and $\hat{\phi}^*$ are each others complex conjugates have been extensively used to arrive at the constraints.

This constraint can now be applied to the EL equations of Equation (R.5) by complex expanding the functions $f = \mathrm{Re}[f] + i\,\mathrm{Im}[f]$ and similarly for g, where from Equation (R.4) it follows that $\mathrm{Im}[f] = -\mathrm{Im}[h]$, which results in

$$\frac{\partial \mathcal{L}}{\partial \hat{\phi}} = \mathrm{Re}[f(\omega,l)]\hat{\phi}^*/B - \int \mathrm{Re}[g(\omega,\lambda,l)]\overline{\hat{\phi}^*}\,\mathrm{d}\lambda\,/B = 0 \tag{R.6a}$$

$$\frac{\partial \mathcal{L}}{\partial \hat{\phi}^*} = \mathrm{Re}[f(\omega,l)]\hat{\phi}/B - \int \mathrm{Re}[g(\omega,\lambda,l)]\overline{\hat{\phi}}\,\mathrm{d}\lambda\,/B = 0 \tag{R.6b}$$

$$\frac{\partial \mathcal{L}}{\partial \omega} = \frac{\partial\,\mathrm{Re}[f(\omega,l)]}{\partial \omega}\left|\hat{\phi}\right|^2/B - \int \frac{\partial\,\mathrm{Re}[g(\omega,\lambda,l)]}{\partial \omega}\overline{\hat{\phi}}\,\mathrm{d}\lambda\,\hat{\phi}^*/B = 0 \tag{R.6c}$$

as a result of the linearity of the integral and derivative operators. At a first glance Equations (R.6a) and (R.6b) still imply that $\hat{\phi} = \hat{\phi}^*$ must solve the quasi-neutrality condition. However, since only $\mathrm{Re}[f], \mathrm{Re}[g]$ instead of f, g appear these new constrainted EL equations now do satsify the equations for $\hat{\phi}$ and $\hat{\phi}^*$ are each others complex conjugate such that $\hat{\phi}^*$ can be consistently interpreted as the conjugate of $\hat{\phi}$. This gives a first improvement which is necessary to be able to extent the variational principle for TEMs to be applicable to their growth rates and without neglecting collisions, however the issues with Equation (R.5) are not completely resolved yet. It remains to be shown in future work that the new EL equations of Equation (R.6) can still be interpreted as the quasi-neutrality condition for $\hat{\phi}$ and $\hat{\phi}^*$ as the imaginary imagination about f, g is lost. Once this has been established some effort can be put to interpreting what physics Equation (R.6c) represents, e.g. could it already give a simpler equation than the original quasi-neutrality condition for finding an analytical expression for the growth rate?, and then finally the variational machinery could be put to work by using trial functions $\hat{\phi}$ for the potential and see how well the resulting real frequency and growth rates do correspond to the results of simulations to see if the variational method would correspond to a cheaper but good alternative to gyrokinetic simulations.